THÈSE DE DOCTORAT

Présentée à

L'Université de Lille

Pour l'obtention du

GRADE DE DOCTEUR

Ecole Doctorale : Sciences de la Matière, du Rayonnement et de l'Environnement

Discipline : Energétique, génie des procédés, combustion

Par

Carolina S. MERGULHÃO

Étude Expérimentale de la Cinétique de Combustion de Biocarburants Issus de la Biomasse Lignocellulosique à Hautes Pressions

Soutenue le 14 Décembre 2020 devant la commission d'examen :

Frédérique Battin-Leclerc	Directeur de recherche CNRS, Laboratoire réactions et génie des procédés (LRGP), Nancy	**Rapportrice**
Guillaume Dayma	Professeur, ICARE, Université d'Orléans	**Rapporteur**
Laurent Gagnepain	Ingénieur expert transport et environnement, ADEME, Nice	**Examinateur**
Pascale Desgroux	Directrice de recherche CNRS, PC2A, Université de Lille	**Examinatrice**
Mickaël Matrat	Ingénieur de recherche, IFP Energies nouvelles, Paris	**Examinateur**
Luis Fernando Figueira da Silva	Associate Professor, PUC-Rio, Universidade Católica do Rio de Janeiro	**Examinateur**
Guillaume Vanhove	Maître de Conférences CNRS, PC2A, Université de Lille	**Directeur de thèse**

"This work is dedicated to my Brazilian family, who supported me when I was just a little girl dreaming about becoming a Scientist and, to my German family, who supported me when this dream was coming true."

Abstract

In 2019, nearly 30% of the CO_2 emissions in the EU come from the transport sector. Electrification is one of the possible and stringent alternatives towards reducing CO_2 emissions from the mobility; nevertheless, its wide availability would cost an enormous budget and decades to replace more than 300 million passenger cars powered by internal combustion engines. Moreover, some domains such as aviation and marine transport are still far from adopting electrification due to the comparably lower energy density of the batteries and carbon-free energy provision. Considering these situations and limitations, renewable biofuels emerge as a promising way to decarbonize the transport sector promptly. Biofuels are currently blended as additives, and can be produced by transformation of lignocellulosic biomass; inedible and renewable feedstock utilized for second-generation biofuel production. The newly introduced biofuels would demonstrate different combustion characteristics than the conventional fossil-based fuels, which need to be investigated in detail. The implementation of such substances requires precise operation strategy to avoid engine knock from spark-ignition (SI) engines, which is a major obstacle against increasing the thermal efficiency in highly turbocharged engines. Taking into account that the engine knock, or in general the autoignition of the unburned end-gas under low temperature conditions, is governed by the autoignition chemistry of fuel, it is, necessary to ensure their compatibility with the new engines by looking into their reaction pathways in engine-relevant conditions. This study aims to present a benchmark of potential new biofuels and/or additives to be used in (SI) engines, as well as provide useful discussions from a kinetics perspective on the co-oxidation of these compounds along with conventional fuels. Four oxygenated lignocellulosic derived compounds (LDCs) were investigated; anisole, o-cresol, prenol, and cyclopentanone (CPN), which are either potential automotive fuels or additives. Isooctane, which has often been used as the reference gasoline surrogate, was also tested to compare the acquired data with literature and validate the methodology used in this study. Ignition delay times (IDTs) were measured using ULille Rapid Compression Machine (RCM), and the mixtures of isooctane/LDC/O2/inert were evaluated at stoichiometric fuel-in-air conditions. The composition effect was investigated, varying the amount of LDC within isooctane mixtures and also varying the compression pressure from 14 to 25 bar. The effect of temperature on the IDT was investigated at 20 bar, and core gas temperatures from 665 to 870 K. The surrogates were formulated at stoichiometric conditions and prepared until the LDC fraction reached the maximum reasonable value given their volatility. The limits were 20% for o-cresol, 40% for anisole and CPN, and 50% for prenol. Overall, the LDC addition inhibits the isooctane reactivity, which can be ranked in descending order for reactivity: pure isooctane, o-cresol, anisole, and cyclopentanone. On the other hand, prenol surrogate was the only one to show limited reactivity at low temperatures and promote the isooctane reactivity at high temperatures, i.e., from 800 to 870 K.

Contents

1. Context

The current work is part of a context that includes the development of alternative fuels as well as new engine technologies through the construction of kinetic models that describe the chemistry behind the fuel's combustion. These aspects will be exposed briefly in this chapter in order to enable the application of the results herein presented to "realistic" combustion problems.

Introduction

The transport sector is constantly evolving and faces environmental problems, since the emissions of internal combustion engines, in addition to being harmful to health, contribute actively to global warming. The significant growth of the world's economy and of the population is the essential driver of the increase in energy demand. This growth is naturally accompanied by growing energy needs, which require increasing production capacity. The transport sector alone accounts for more than half of the demand for liquid fuels, with a very significant increase due in particular to the expansion of the global vehicle fleet. This increase can be attributed to the improvement of living standards in developing countries, where the purchase of personal vehicles is gaining momentum. It can also be correlated again with the increase of the world population. Vehicles manufacturers face significant technological challenges and are forced to find solutions to continue to market their vehicles. In recent years, after-treatment technologies, such as the dust particle filter or the exhaust gas recirculation, have made it possible to meet the current regulations, but have also demonstrated inefficient in real-driving conditions. Future suggested solutions feature new concepts derived from the HCCI (Homogeneous Charge Compression Ignition) engine or the use of alternative renewable fuels likely to produce smaller quantities of pollutants (1).

Biofuels are fuels that can be produced from the transformation of plant products (2). It gives them the major advantage of being renewable. They can also help reduce carbon dioxide emissions (3). These alternative fuels are currently used in Europe as additives, with incorporation targets set by the European Commission, to encourage the transition to renewable fuels (4). The implementation of such technologies makes the development of engines dependent on the development of knowledge on the combustion kinetics of such hydrocarbons under the conditions of low temperature (that is to say below 1000 K). This temperature range is known to give rise to cool flames and to be related to indirect chain-branching involving peroxyl radicals and hydroperoxides. These mechanisms are responsible for fuel autoignition in those new modes of combustion. This reactivity is also responsible for engine knock (5) in spark-ignition conditions (or "gasoline" engines). This phenomenon is a major obstacle to increasing the thermal efficiency of these engines, especially for highly turbocharged engines (6). This area of research has therefore been of increasing interest for the last ten years, as the recent rise in the number of publications testifies (7,8). In order to introduce new biofuels, it is necessary to ensure their compatibility with such new engines through a study of these kinetic mechanisms. The construction of a predictive model of this reactivity is an asset for introducing these species into commercial fuels. Furthermore, a commercial fuel such as gasoline is a mixture composed of hundreds of hydrocarbons, the kinetic modeling of the combustion of one of these hydrocarbons involving thousands of elementary reactions. Therefore, to represent its combustion properties, a simpler fuel surrogate containing a limited number of components can be used. Isooctane has often been used as the simplest gasoline surrogate, and its binary blends with *n*-heptane to represent a variable octane number fuel. These types of blends are known as primary reference fuels (PRF). Ternary mixtures as isooctane, *n*-heptane, and toluene, known as Toluene Reference Fuels (TRF), have been proposed to study the effect of fuel composition on combustion properties, such as emissions (9). Besides that, the choice of potential additives to formulate a gasoline-like fuel depends on different combustion properties as the antiknock tendency. The Research Octane Number (RON) and the Motor Octane Number (MON) are the ASTM tests which evaluate the resistance to autoignition and knock (10). These tests are performed at specific conditions which are not anymore relevant to new engine operating conditions. The benefits of high octane number include increasing the volumetric compression ratio of the engine (and therefore its thermal efficiency), increasing turbocharging, and reducing carbon monoxide and soot emissions (11). Many efforts have been made to understand the effect of blending on the autoignition tendency by investigating the octane rating of net components and mixtures. It has been observed that a mixture can have higher octane values than the net value of each component of the mixture (12). However, the reason why some mixtures depict such a synergetic blending behavior is very often still unclear and can result from physical (evaporative cooling) or chemical reasons. Therefore, the blending effect on the reactivity of new potential biofuel candidates, at relevant conditions to knock investigation in SI engines is investigated in the current work.

1.1. Environmental concerns and the transport sector

One of the biggest challenges in the 21st century could be supplying the ever-growing global energy demand while mitigating the climate change triggered by the emissions of Green House Gases (GHG). According to the report presented by the Intergovernmental Panel on Climate Change (IPCC) in 2018 (13), the human-induced global warming, in 2017, reached approximately 1 ± 0.2°C above pre-industrial levels and currently continues to increase by 0.2 ± 0.1°C every decade. Besides that, NOAA (National Oceanic and Atmospheric Administration) and NASA (National Aeronautics and Space Administration) recently revealed that the heat content of oceans was the highest in recorded history and that the decade from 2010 to 2019 was the hottest ever recorded (14). The temperature data follows the historical trend: since the 1980s, each ten-year cycle has been warmer than the previous corresponding interval. Between 2010 and 2019, the average was 0.2°C warmer than that recorded between 2000 and 2009. Only the year 2016 and, for some data, the year 2015, were hotter than 2019. Therefore, at the end of 2019 more than 11,000 scientists from 153 countries signed an article based on historical data of 15 indicators of human activities and 14 of actual climatic impacts, declaring a clear and unequivocal climate emergency (15).

This increase in global temperature is accompanied by the growing concern for the consequences of atmospheric pollution, a by-product of growing urbanization and industrialization. Several pollutants contribute the most to this phenomenon, including sulfur dioxide (SO_2), nitrogen oxides (NOx), ozone (O_3), particulate matter (PM), volatile organic compounds (VOCs) and carbon monoxide (CO) (16). Atmospheric pollution has many negative impacts on human health, ecosystems, food crops, and the environment more generally. The World Health Organization (WHO) estimates that it constitutes the most considerable environmental risk to human health. It is estimated to be the cause of seven million premature deaths each year (17). Figure 1 represents the contribution of the transport sector to the worldwide emission of certain pollutants, as reported by the European Environment Agency (EEA) (18).

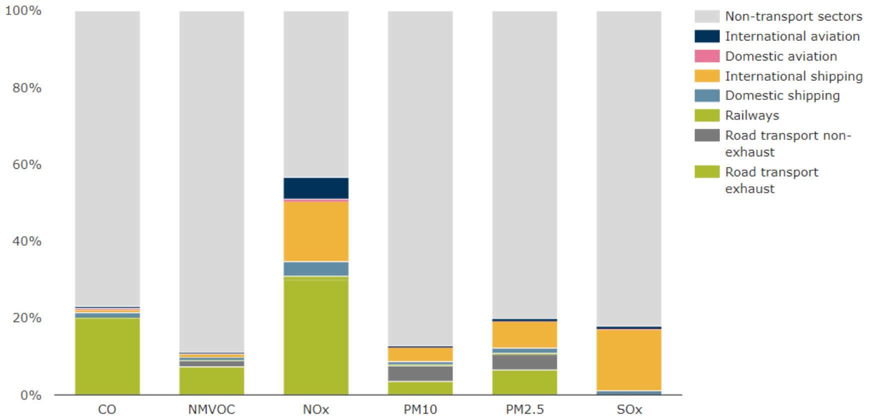

Figure 1 - Contribution of the transport sector to total emissions of major atmospheric pollutants (18).

Figure 1 shows that the transport sector is responsible for more than half of NO_x emissions and contributes significantly (around 13% or more) to the total emissions of other pollutants. In terms of CO_2 emissions, the transport sector represents 23% of global emissions and in the period between 2010 and 2015, it has increased by 2.5% per year (18). In France, CO_2 emissions have decreased over the last decade. Nevertheless, the transport sector is the major responsible for energy-related CO_2 emissions (40%), followed by buildings (23%) and industries (20%) (19).

To reduce the emission of pollutants, governments around the world have gradually imposed stricter standards on emission levels and quality standards for the composition of fuels. Emission laws regulate polluting species such as (NOx), unburnt hydrocarbons, CO, and PM. These pollutants are often referred to as "regulated pollutants." Moreover, NH_3 and specific organic compounds such as aldehydes could be possibly regulated in the future due their toxicity. Vehicle emission standards are specified in terms of the mass of pollutants per unit of distance traveled (mg/km). For light vehicles, emission standards are based on driving cycles representing a typical driving pattern in a given country. Recent events have shown that driving cycles are sometimes not representative of current driving methods, or that some manufacturers have implemented systems to evade these checks (20). Figure 2 depicts the limits of the emissions standards by region and their respective driving tests.

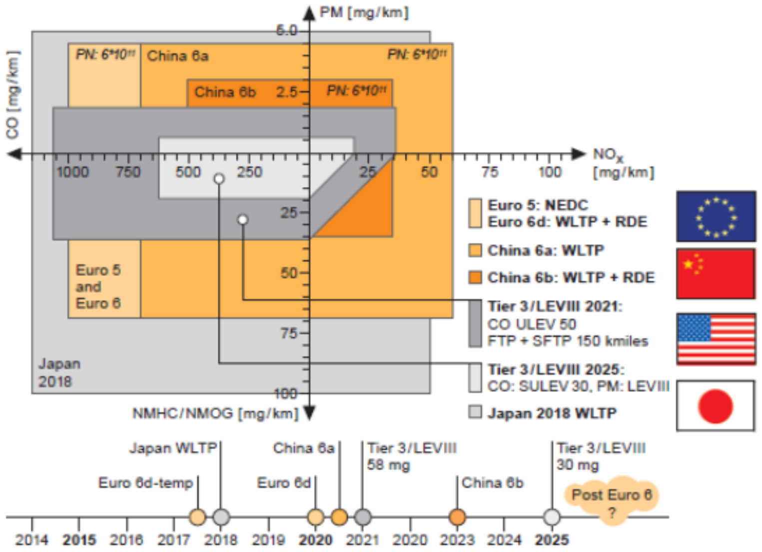

NEDC (New European Driving Cycle)
WLTP (World LDV Test Procedure)
RDE (Real Driving Emission test)
FTP (Federal Test Procedure)
LEV (Low Emission Vehicle)
ULEV (Ultra Low Emission Vehicle)
SULEV (Super Ultra Low Emission Vehicle)
NMHC (Non-Methane Hydrocarbons)
NMOG (Non-Methane Organic Gases)

Figure 2 - Emission standards by world region (21).

The CO_2 emissions policies were driven by international agreements focused on regulating and setting targets on the reduction of GHG emissions in the next decades. Table 1 summarizes the main agreements which drive EU CO_2 emissions regulations as well as EU measurements to mitigate such emissions.

Table 1 - Measures taken to reduce CO_2 emissions worldwide adapted from (21).

	Year	Description
United Nations Framework Convention on climate Change (UNFCC)	1992	- Agreement on cooperation and reporting, installation of regular conferences - Decision making: conference of the parties (COP)
Kyoto Protocol (COP 3)	1998	- Phase 1 (2008-2012): EU 8% reduction target compared to 1990, (EU-15 has achieved an overall cut of 11.7% domestically) - Phase 2 (2013-2020): EU 20% reduction target compared to 1990
Paris Agreement (COP 21)	2015	- Global average temperature increase < 2 °C above pre-industrial levels, efforts to limits to 1.5 °C (COUNCIL DECISION (EU) 2016/1841) - Intended Nationally Determined Contribution (INDC) of the EU and its member states - Definition of individual CO_2 emissions target for each member state - 197 countries signed the agreement and 189 Parties have ratified. In 2020, the American government notified the intention to withdraw the United States from the Agreement.
Measure taken at EU level	-	- Road transport - Reducing CO_2 emissions from vehicles - Fuel quality: GHG intensity of vehicle fuels to be cut by up to 10% by 2020

In addition to these measurements, in december 2019 the EU presented the European Green Deal providing action plans in order to improve the use of sources moving forward to a clean and circular economy as well as restore the biodiversity and mitigate pollution (22). Figure 3 shows the historical EU CO_2 emissions as well as the projections up to 2050. These projections included the projections with existing measures (WEM) scenario, which consider existing policies and measures, and the projections with additional measures (WAM) scenario, additional effects of planned measures annouced by Member States. Both cases reveil a trend that may not lead to the ambitious European target established by 2030, which predicts a reduction of GHG emissions of 40% in comparison with 1990 levels (23).

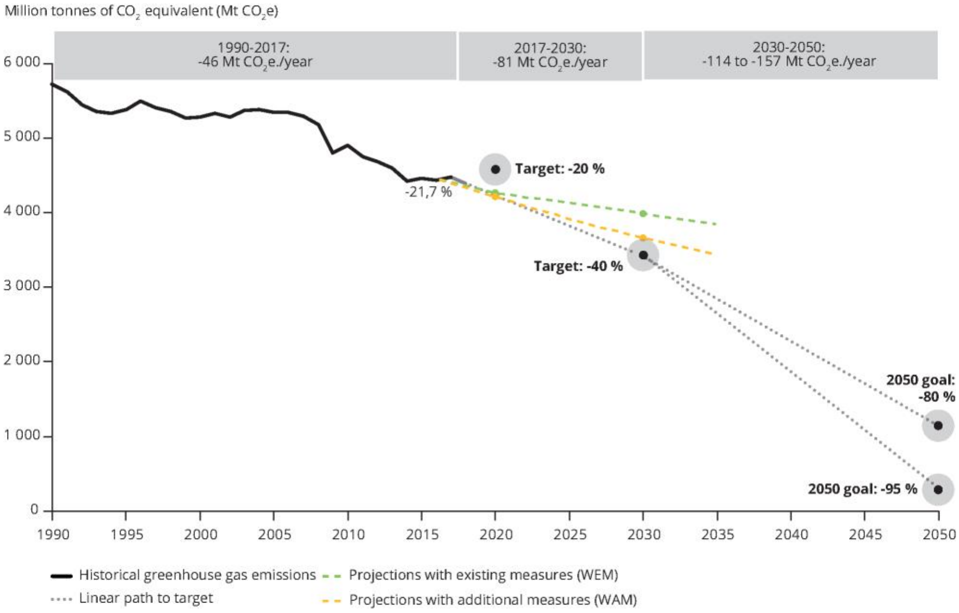

Figure 3 – Historical European CO_2 emissions and projections by 2050 (23).

The slight increase in CO_2 emissions from 2015 to 2018 was leaded by Germany, which has, in 2018, the highest global CO_2 emissions level, accounting for 23 % of the EU-27 total, i.e., 889 million tons of CO_2-eq, ahead of France and Italy. In this context, in November 2019, Germany's parliament approved the climate protection bill which aims to cut Germany's greenhouse gas emissions to 55% of the 1990 levels by 2030.

There are two possible approaches to reducing the impact of internal combustion engines on pollutants and greenhouse gas emissions.

- The first one consists of developing engine technologies, post-treatment systems, and traction systems (hybridization, electrification), which is a long-term approach, and therefore its effects will only be visible after a substantial renewal of the vehicle fleet.

- The second mode of action is aimed to change the formulation of fuels, taking into account other energy vectors. Therefore, it has a shorter-term effect, as long as the new fuels remain compatible with existing engines.

The following section covers fundamental concepts related to the internal combustion engine technologies, in order to understand the application of the kinetic models, considering that the potential new alternative fuels investigated in the current work are gasoline-like fuels, i.e., fuels to be used in spark-ignition engines.

1.2. IC Engine technologies

The types of conventional Internal Combustion Engines (ICE) are compression ignition (CI) and spark-ignition (SI) engines, but new engine technologies have also emerged in order to mitigate harmful gas emissions directly at the source. The operational conditions of some of these engines are summarized in the equivalence-ratio/temperature diagram shown in Figure 4 (24).

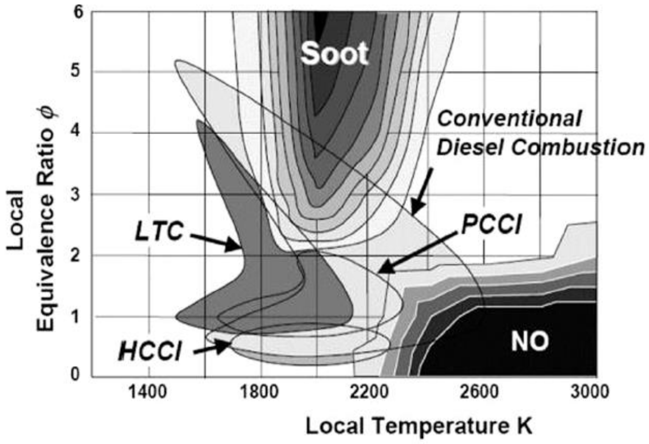

Figure 4 - Temperature and fuel content effect on emissions (25).

Table 2 - Overview of engine/fuel technologies available for vehicles (26) .

	Fuel	Engine technology
Conventional	Gasoline Diesel	SI- spark ignition CI – compression ignition
Alternatives	**Compression ignition:** Biodiesel GTL (Gas-to-Liquid), DME (dimethylether), FTD (Fischer -Tropsch diesel), DEE (diethyl ether) **Spark-ignition:** - fossil fuels: GTL (Gas-to-Liquid), CNG (Compressed Natural Gas), LPG (liquefied petroleum gas), H_2 (from coal or natural gas) - Biofuels: alcohols, DMF (2-5-dimethylfuran), syngas, biogas, H_2	HCCI - Homogeneous charge compression ignition PPCI - Partially premixed compression ignition SPCCI - Spark Controlled Compression Ignition GDI – Gasoline Direct Injection RCCI - Reactivity Controlled Compression Ignition SACI - spark assisted compression ignition Electric vehicles (hybrid, plug-in hybrid, battery, cell-fuel)

This diagram has, for example, motivated the implementation of EGR (Exhaust Gas Recirculation) valves on current diesel engines, but also recent developments in engine technologies of the "compression ignition of a quasi-homogeneous mixture" such as HCCI and PPCI (Partially Premixed Compression Ignition) (27). Table 2 summarizes engine technologies and fuels associated to conventional and alternative ICE.

1.2.1. Conventional technologies

The most common types of IC engines, CI and SI, are four-stroke, i.e., four distinct strokes in a complete CI/SI engine cycle: intake, compression, combustion-expansion, and exhaust. (28). In IC engines, the displacement of the piston takes place between two limits called respectively the Top Dead Center (TDC) and the Bottom Dead Center (BDC). The most relevant parameters are the geometric parameters, the operating cycle (two-stroke or four-stroke), ignition timing, and fuel and combustion type.

The geometric parameters characterize the construction of the engine and generally remain unchanged for an engine already during its entire service life. Among these parameters, the parameter D is the nominal diameter of the cylinder, the piston stroke S is the path traveled by the piston between TDC and BDC and the volumetric compression ratio (or compression ratio) is the ratio between the maximum volume cylinder pressure (V_{max}) and minimum volume (V_{min}). Regarding the operating cycles, the characteristic times of a four-stroke SI engine are presented below:

Intake: In this stage the intake valve is open. The cylinder is filled with the fuel-oxidant mixture as the piston moves down;

Compression: The piston compresses the air-fuel mixture, then a spark is produced by the spark plug which ignites the mixture;

Combustion-expansion: In this stage the combustion takes place, transforming the chemical energy contained in the fuel-oxidant mixture into mechanical energy. With the expansion of the burnt gases, the piston is pushed down;

Exhaust: This step corresponds to the escape of the burnt gases from the cylinder. The exhaust valve is open, the piston rises and ejects the burnt gases.

The injection modes can be either indirect or direct. In the indirect injection mode, fuel is injected upstream of the intake valve and then mixed with air. The operation of the direct injection mode is based on the introduction of fuel directly into the combustion chamber (28). The advantages of this injection mode lie in the reduction of fuel losses between the valve and the combustion chamber, especially when using lean mixtures, and therefore a more precise metering of fuel is possible. However, the formation of unburned hydrocarbons and particles is favoured following the emergence of stratification zones by the late injection of fuel (29).

Engine knock is one of the major hindrances for enhancing the performance of SI engines. Indeed, during the combustion stroke, a flame front is formed from the fuel/oxidant mixture in the combustion chamber triggered by the spark plug. This flame front and the resulting pressure wave increase the temperature of the unburned fuel/oxidant mixture, which can then auto-ignite. This autoignition can generate a local detonation, which causes pressure oscillations at high frequencies accompanied by a characteristic metallic noise. The consequences of this phenomenon are a loss of power, vibrations, but above all deterioration of certain parts due to heating, and in the long-term permanent damage to the engine. Since the 1990s, the standard use of knock sensors has prevented this phenomenon by altering the ignition timing, which, however, results in a loss of efficiency. The arrival on the market of new so-called downsized and supercharged engines has put this phenomenon back in the center of attention: In these engines, what has been called "super-knock" has been observed (30) which can cause permanent damage to the engine in a single cycle, and therefore cannot be avoided with sensors.

The risk of knocking increases as the compression ratio increases due to the temperature and pressure conditions at the TDC, which are more severe. Therefore, it is necessary to understand the reactivity of fuel components to autoignition to reduce this abnormal combustion. The octane number traditionally measures the fuel anti-knock propensity at a given condition. Compounds that are highly reactive auto-ignite easily and have a low octane number. There are two methods of measuring this index: Research Octane Number (RON) and Motor Octane Number (MON). The difference between them lies in the conditions to which the fuel/air mixtures are subjected during testing, summarized in Table 3. The octane number is a typical characteristic of fuel, which depends on its chemical structure.

Table 3 - Engine conditions for the RON and MON tests (31).

Parameters	**RON**	**MON**
Inlet air temperature	52 °C	38 °C
Inlet mixture temperature	Not specified	149 °C
Intake air pressure	Atmospheric	Atmospheric
Coolant temperature	100 °C	100 °C
Engine speed	600 rpm	900 rpm
Spark timing	13 ° bTDC*	14- 26 ° bTDC*
Compression ratio	4 - 18	4 - 18

*bTDC(before Top Dead Center)

In the case of CI engines, whose characteristic times are similar to those of the SI engine, the piston compresses the air only until it reaches a sufficiently high temperature. When the piston approaches TDC, fuel is injected and reacts spontaneously with the oxygen present in the hot air by autoignition. The operating cycle strokes shown above are still valid, except for the ignition, which corresponds to the fuel injection. The limiting factor for the heat released during this engine cycle is the mixture between the evaporating fuel and the air, not the propagation of a flame.

According to the CCFA (Comité des Constructeurs Français d'Automobiles), the future of the diesel engine seems uncertain. Following a series of political decisions related to the issue of emissions of soot particles and nitrogen oxides, a drop of more than 30% in purchases of new diesel vehicles signals a trend that should continue in the coming years (32).

1.2.2. Alternative technologies

Recent developments in conventional SI and CI engines have shown improved fuel economy and exhaust pollutant emissions. However, the compression ratio of SI engines is limited by the knocking phenomenon, which causes a reduction in thermal efficiency. Also, it is not possible to operate SI engines at lean conditions without deteriorating the efficiency of the three-way catalyst at the exhaust, limiting the possible gains in efficiency in this operating mode. To overcome some of the drawbacks of conventional engines, alternative technologies for lean combustion engines are proposed. Lean combustion has a thermodynamically higher efficiency due to the higher ratio of heat capacities (γ) and, consequently, lower combustion temperature, thus reducing heat losses and nitrogen oxides formation. Unfortunately, there is a limit to the ability to ignite or autoignite in lean conditions. The main alternative combustion concepts are briefly described below:

- The principle of the HCCI (Homogeneous Charge Compression Ignition) engine is based on the combustion by homogeneous autoignition of lean mixtures using high compression ratios, in order to obtain high efficiency. Significant dilution with excess air or burnt gases makes it possible to reduce the maximum temperature of the mixture and thus the NOx emissions (33). The major drawback of the HCCI engine is the difficulty in controlling the ignition timing, and its limited power.

- The partially stratified charge engines PCCI (Premixed Charge Compression Ignition), with diesel fuel, and PPC (Partially premixed combustion), with petrol fuel, have thus been proposed in order to increase the engine load while maintaining the advantages of the HCCI combustion mode.

- RCCI (Reactivity Controlled Compression Ignition) technology also allows higher power output, better combustion phasing, and better control of combustion time. To that end, diesel fuel is premixed to increase the reactivity of the load and improve the distribution of the reactivity in the engine cylinder, thus providing an intermediate combustion process between the CI mode and the HCCI mode. (34). The so-called “dual-fuel” engines offer an intermediate process between the CI and SI modes.

- SACI (Spark-assisted compression ignition) engines are intermediate between the SI and the HCCI. In this type of engine, homogeneous combustion is triggered by using an external ignition source. This technique is an essential asset for the SI-HCCI hybrid system. The engine starts in SI mode to resolve the HCCI cold start problem, then switches to HCCI mode for low engine load operations. When the load requirements of the motor are higher, the motor can be put back into SI operation mode. (35).

In 2019, Mazda launched the world's first SPCCI (SPark Controlled Compression Ignition) engine, a technology very close to SACI. The Skyactiv-X combines both SI and CI combustion methods, promising more efficient and less polluting combustion (36). The Skyactiv-X M Hybrid was also announced, including an alternative system in which the integrated starter motor generator produces electricity during the deceleration, this electricity is then stored in a battery and deployed as needed (37). Other engines using the HCCI combustion mode were previously presented such as the prototype developed by Oxy-Gen Combustion in partnership with Michelin and Shell (38), by

Volkswagen (39) and by General Motors (40), however they were not introduced in the market. Furthermore, HCCI engines powered by biofuels are still at research level: experimental studies have been focused on the usage of ethanol (41–43), blends of diethyl ether/ethanol (44), dimethyl ether/ethanol (45), ethanol/n-heptane (46,47), methanol (48–50) and butanol (51,52).

Figure 5 shows schematically the relationship between the different engine technologies previously described.

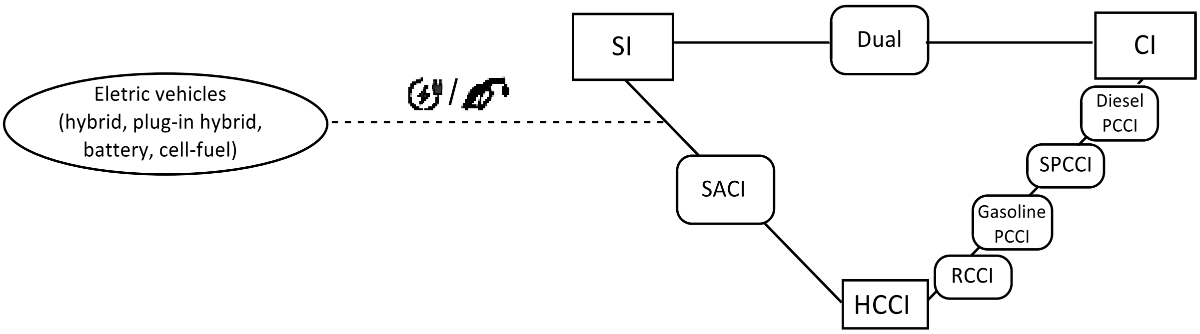

Figure 5 - Schematic representation of the three main combustion modes, and the 5 alternative combustion concepts for internal combustion engines adapted from (33).

In addition to the techniques mentioned, the development of control systems which allow the use of different fuel technologies on the same engine, is one of the great current challenges (26) of automotive engineering. It includes therefore adapting the composition of the injected fuel in order to meet the needs of the engine, according to the operating conditions described in Figure 4.

1.3. Fuel technologies

1.3.1. Conventional fuels

The properties of the fuel affect the performance, combustion, and emission characteristics of the engine. Mixture injection and preparation systems are strongly dependent on physical parameters such as phase-change characteristics, density, lubricity, viscosity, and electrical conductivity. The physical and chemical properties of fuels depend on their chemical composition, and modern automotive fuels are typically made up of hundreds of pure and oxygenated hydrocarbons, to which additives are added. The following table shows a typical composition of gasoline. Additives are generally present in volume fractions inferior to 1.0% (53).

Among the combustion properties, we can mention the propensity for autoignition, calorific value, and the formation of pollutants. To facilitate the adaptation of fuels to new combustion modes, it is essential to characterize the first of these properties precisely. As noted above, the ON is used to describe the propensity of fuels to auto-ignite in SI engines. There is an equivalent for the CI engine: the Cetane Number (CN). Unlike ON, it is high if the fuel ignites easily. Octane and cetane numbers are still used in industry, although it is well-accepted that it is difficult to relate these values to the chemical mechanisms responsible for autoignition and therefore, to preclude the characterization of the phenomenology of ignition.

Table 4 - Typical volumetric composition of a gasoline (53). *Species present at a fraction less than 1 vol% are not included.*

	Total amount (vol%)	Compound	Amount (vol%)
n-alkanes (C_nH_{2n+2})	9	*n*-Butane	4,3
		n-Pentane	1,9
		n-Hexane	1,5
		Other linear alkanes	1,3
Iso-alkanes (C_nH_{2n+2})	43	2-Methylpentane	14,3
		Iso-pentane	5,8
		3-Methylpentane	4,1
		Isooctane	3,5
		2-Methylhexane +2,3-Methylpentane	3,5
		2,3-dimethylbutane	3,3
		Other iso-alkanes	8,5
Aromatics	34	Xylene	10,2
		Toluene	8,0
		1,2,3-Trimethylbenzene	2,6
		Ethylbenzene	2,2
		Xylenes	1,7
		Other aromatics	9,3
Alkenes (C_nH_{2n})	11	2-Methylbut-2-ene	1,9
		Pent-2-ene	1,5
		Other alkenes	7,6
Cyclo-alkanes (C_nH_{2n})	3	Cyclohexane Cyclopentane	-

For certain compounds, such as alkanes, ethers, and compounds with a long alkyl chain, a two-stage auto-ignition can be observed. In this case, the first stage is intimately linked to the chemical chain-branching leading to cool flames. These phenomena are often observed at temperatures below 850 K, at typical engine pressures. When two-stage ignition occurs, the first stage has an essential influence on the duration of the second stage, which depends on the heat release and the intermediate species formed during the first stage. The end of this first-stage and transition to the second stage is in turn correlated to the negative temperature coefficient (NTC - Negative Temperature Coefficient) (54). This phenomenon is strongly correlated with the difference in reactivity of gasoline fuels under RON and MON conditions (55). In order to be able to predict the reactivity of fuels in the large temperature and pressure ranges typical of commercial engines, predictive kinetic models are used. More details on the chemical causes for the first-stage ignition and NTC behaviour are given in Chapter 2.

1.3.2. Biofuels

As mentioned earlier, environmental concerns and increasing global demand for oil are leading to efforts to reduce global dependence on this resource. The use of biomass as an abundant and renewable energy source is increasingly becoming a potential alternative (56), with many applications such as the production of heat, electricity, fuels, and the production of chemicals (57). Biomass fuels can play an important role in reducing greenhouse gas emissions and dependence on fossil fuels by limiting or reducing its consumption (58).

Biofuels are fuels obtained from biomass, which is defined as the biodegradable fraction of products, waste and residues from agriculture, including plant and animal substances from land and sea, forestry and related industries, as well as the biodegradable fraction from industrial and household waste (59). It can also be understood as the material produced by photosynthesis or biological processes that consume CO_2. This material, in turn, when burned, converts the biomass back to CO_2. Biofuel are therefore often referred as renewable or carbon-neutral fuels (60).

Biofuels can be divided into three main categories according to the type of biomass resource. First-generation biofuels are synthesized from food crops such as wheat, sugarcane, soybeans, rapeseed, and many other edible crops. They are obtained using traditional biochemical conversion technologies (fermentation/hydrolysis). This first generation of biofuels raised concerns about the potential competition between the production of crops for bioenergy and food supply, which could lead to an increase on food prices (3). However, several studies have shown that the biofuel feedstock production does not necessary affect food security in specific conditions (61,62); it could even lead to a positive impact due to the better access to inputs and technical assistance (63,64). The land-use change also has to be considered on the trade-off of biofuels production expansion, and, regarding that, recent studies have shown the potential of marginal lands for bioenergy supply as well as food security (65,66). Marginal lands can be defined as non-profitable lands for crop cultivation, i.e., the poor soil quality and climate conditions leading to low productivity (67). A detailed list of potential crops for cultivation in marginal lands for biomass/bioenergy production can be found in (68).

The second generation of biofuels emerged to overcome the problems associated with the use of arable land and food crops. This type of biofuel is obtained from non-food sources such as wood, agricultural residues, forest waste and certain municipal and industrial waste. They contain lignin and cellulose and are known as lignocellulosic biomass. They are produced using thermochemical (69) or biochemical (70) routes . The use of waste as a source leads to more sustainable processes, with less negative environmental impacts compared to first generation biofuels (71,72).

Third-generation biofuels come from algae, which are the most abundantly available potential raw materials. These do not require arable land for cultivation and do not constitute an edible crop, with the inherent advantage of producing oils that can be easily refined into diesel and some components of gasolines. However, this approach is still in its early stage (73), and the potential impacts due to large scale production on the ecology and marine fauna are still unknown. Fourth generation biofuels are produced using genetically modified microorganisms such as microalgae, yeast, fungi or cyanobacteria as source (3). It includes technologies such as pyrolysis, gasification, upgrading, solar-to-fuel and electro-fuel.

Lignocellulose is the most abundant form of biomass, with an annual production of approximately 170 billion metric ton (74). It is composed of three fractions which are shown in Figure 6. Cellulose is a polymer with linear chains of 1,4-D-glucopyranose units, with an average molecular weight of approximately 100,000 Da. (75). Hemicellulose is a complex polysaccharide, composed almost entirely of branched structures of glucose, mannose, xylose and arabinose present in the cell wall, with an average molecular weight of 3000 Da (76). Lignin is an aromatic polymer composed of three monomers based on the phenolic backbone and linked mainly by C-O-C ether bonds (77), and often adjacent to cellulose fibers to form a lignocellulosic complex (78).

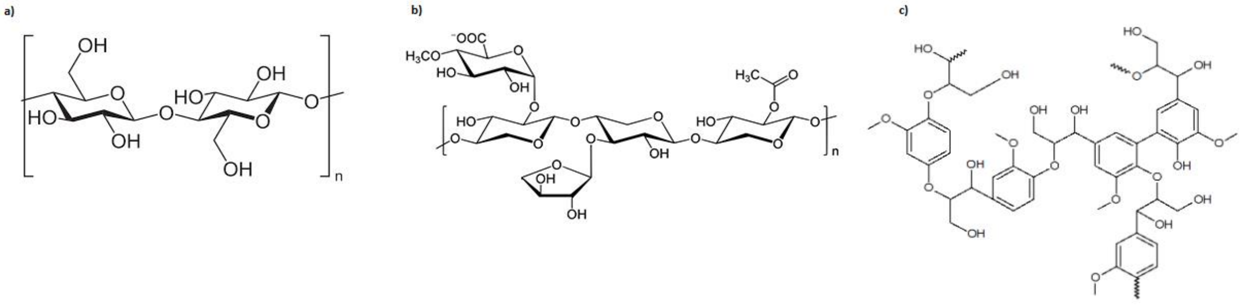

Figure 6 – Illustration of the composition of lignocellulosic biomass (79)*, a) cellulose, b) : hemicellulose et c) : lignin.*

Cellulose is commonly the largest fraction of the lignocellulosic biomass, followed by hemicellulose and lignin, although this distribution is dependent on the type of source (80). A summary of biomass composition analysis, depending on the type of source, is given by different studies (81–83). In addition, a recent study (84) presents different sources of biomass and many parameters associated with the production of liquid fuels. Lignin, the fraction of interest in this study, is a polymer of three typical monomers: coumaryl, coniferyl and sinapyl alcohols (85).

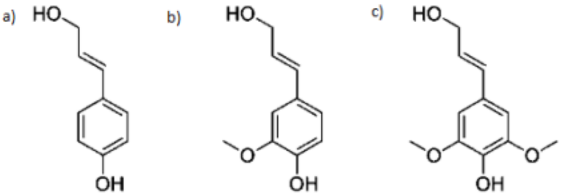

Figure 7 - Three typical monolignols which constitute the characteristic monomer units of lignin: a) para-coumaryl alcohol; b) coniferyl alcohol; and c) sinapyl alcohol.

Biorefineries that convert cellulosic biomass into biofuels generate much more lignin than needed. Among the fractions of biomass, it is usually considered the least valuable, cellulose and hemicellulose being widely used to synthesize platform molecules in biorefinery processes. Examples of recovery routes include low-cost carbon fiber, thermoplastic elastomers, polymer foams, and membranes, as well as various fuels and chemicals currently coming from the petroleum industry (86). The annual world production is between 40 and 50 million tons of lignin (87), and it is positioned as one of the types of industrial solid waste produced in large quantities by the transformation of wood and the production of paper.

The use of biomass as an energy source can be achieved after thermal, biological or mechanical pre-treatment processes. Thermochemical conversion processes are an excellent solution, both in terms of economics and efficiency (69,88). The thermochemical route converts biomass through pyrolysis or gasification, while biochemical processes convert the biomass into sugar, and further, the sugar is subjected to microbial fermentation. A state-of-the-art review on such biofuel production technologies can be found in (89). Figure 8 presents the main ways of recovering energy from biomass.

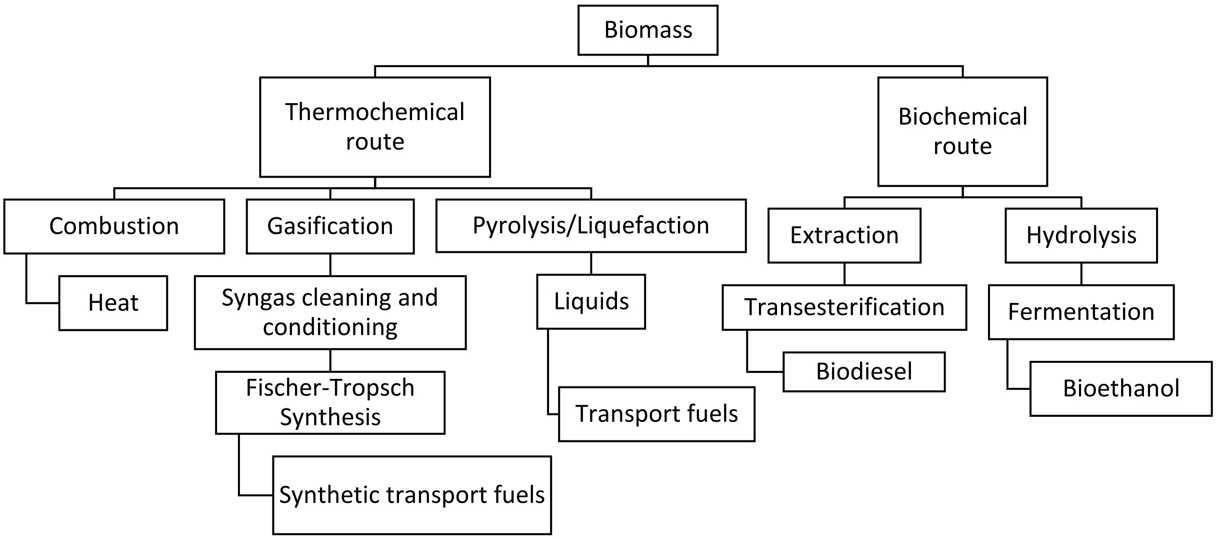

Figure 8 - Thermochemical and biochemical conversion routes for biomass to biofuels (73).

The bio-oil obtained after pyrolysis of lignocellulosic biomass is a mixture of large size oxygenated molecules, involving almost all oxygenated organic molecule classes, such as esters, ethers, aldehydes, ketones, carboxylic acids, alcohols, and phenols. This bio-oil generally contains significant amounts of methoxyphenols (~ 30% by weight (90)), which are typical decomposition products of the components of lignin. Numerous studies demonstrate the feasibility of obtaining aromatics from lignin (91–94) with yields between 12 and 17%. Various routes have been explored to depolymerize lignins including pyrolysis, catalytic hydrogenation, oxidation, hydrolysis and hydrocracking and a two-step catalytic process using base-catalyzed depolymerization followed by selective hydrocracking (95).

In addition to the aforementioned controversial aspects of renewable fuels production, uncertainties on biofuel policies have been revealed as the most important impediment to investments in this sector (96) and consequently slowing its expansion. The European Union has, therefore, strengthened its biofuel legislation in order to achieve the ambitious climate targets as well as address the ever-growing transport demand.

1.3.2.1. Biofuel policy

Although efforts has been made in order to unify the implementation of biofuels across Europe, the application of the regulations, mentioned above, can differ among EU member states due a co-decision procedure, which allows EU countries to implement these mandates as part of the compromise negotiations of the EU’s Energy Council (97). Consequently, the differences on biofuel blending regulations affect the share of renewable energy source in transport, as shown in Figure 9.

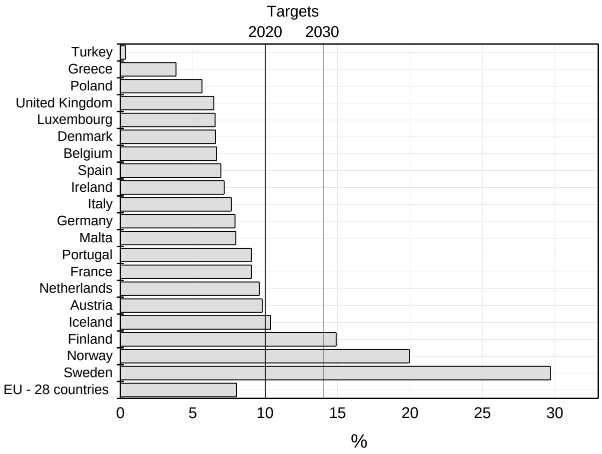

Figure 9 – Shares of renewable energy sources in transport in 2018 (98).

The high shares of renewable energy source in transport in Sweden can be attributed to its high availability of moving water to produce energy and biomass, but also through the exemption of fuel taxes for pure biofuels and high-biofuel content blends (99). On the other hand, even though France has made progress on GHG emissions, dropping 15% from 1990 to 2016 (19), the 14% share of renewable energy in transport aimed by 2030 is still far from being achieved. In Latin America, Brazil and Argentina are the biggest markets and, in 2017, were responsible for 23% of global biofuel demand (100). The high production and consumption of biofuels in Brazil is driven by ethanol policies implemented since 1975 and, which are current under the RenovaBio program, including reduction in GHG emissions of 10% in transport up to 2028 and, share of biofuels of 18% in the final energy by 2030 (101). Finally, the high share of flex-fuel engines in Brazilian vehicle fleet, 70% in 2017, improve the consumption of blended and unblended ethanol (100).

On July 2020, in addition to the suggestions of the National Energy and Climate Plan (NECP) (102), the German federal bioenergy market detailed a series of recommendations in order to de-carbonize the transport sector through the use of biofuels (103). These recommendations include an increase in the share of renewable energies in transport as well as an increase of the cap for biofuels from edible biomass; increasing GHG reduction minimum quota for fuel distributors; define conditions for higher blending regulations; crediting biofuels to the CO_2 limit values of newly-sold vehicles; Toughen regulations for sustainability certification and documentation obligations and, finally, provide funds for biofuel system research and model regions.

1.3.2.2. Impacts of COVID-19 on biofuels market

With the duration of three years, the current work began in 2017. Between this time, a dramatic health crisis unprecedented in the modern era emerged, caused by COVID-19. This crisis has strongly affected the global oil industry, creating a unique set of challenges for the biofuel sector. In a preliminary analysis, biofuels' decreased demand is associated with the contraction in global fuel demand, which was triggered by lockdown measures. The drop in oil prices results in a loss of competitivity of renewable fuels and a potential loss in market share, considering that biofuels are often implemented blended into gasoline and diesel. After reaching a record year in biofuel production in 2019, counting of 162 billion litres, a contraction of around 13%, in 2020, is expected on the production to reach 2017 levels (104), thus lower levels than those predicted by the IEA in a pre-pandemic period.

In 2018, 2.1 million jobs worldwide were identified in the biofuel sector (105), which are currently threatened by the uncertainties caused by the contraction of the demand in biofuels and the resulting closure of several plants or reduction of the production rates in different countries. In France, Cristalco, the European Union's third-largest ethanol producer, has temporarily reduced its bioethanol production (106). Also, the Cristal Union group (107) and Vertex announced a temporary shutdown of a bioethanol production unit in favor of hand sanitizer production. In the USA, Poet Biofuels, the world's largest ethanol producer, stopped production at Chancellor, Ashton, Coon Rapids and postponed the start-up of its new plant in Shelbyville (108); other companies have been idling their biofuel production or definitely stopped (109).

A series of measures have been proposed in order to mitigate the Covid-19 impact on biofuels (110), due to the strong potential for job creation, especially in rural areas, and to decarbonize the transport sector. These measurements including improve the sales of fuel-efficient vehicles and the implementation of advanced biofuel for aviation and shipping, through exemption of taxes; regulate minimum standards for energy efficiency, emissions and biofuel blend mandates; propose specific loans for biofuel production; and also support the R&D to enable future more efficient solutions.

1.4. Development of new fuels and the importance of kinetic modeling

Ethanol is the most used renewable fuel worldwide, counting of 70% by volume of total biofuel consumption (111). The Fiat 147 was the first ethanol-powered vehicle, created in 1978 by the Brazilian engineer Urbano Ernest Stumpf. He also contributed to the creation of "Proálcool" program, implemented in 1975, which became the first implemented biofuel policy including blending mandate, subsidies and, the entire biofuel production chain and consumption (112). Only in 1981 the first ethanol oxidation mechanism (113) was proposed, combining experimental data and estimated rate coefficients for unknown reactions. The improved understanding of the combustion of ethanol allowed the improvement of fuel/engine performance and consequently, its consolidation on the market.

The ability to simulate in-cylinder combustion permits increasing the engine efficiency as well as reducing emissions caused by internal combustion engines. Kinetic models are, therefore, crucial to automotive engineering, considering that these models are used to predict the formation of harmful emissions precursors and also the performance of engines. The advantage of having a kinetic model that is capable of predicting detailed production and conversion of intermediates, as well as global parameters such as flame speed, heat release and ignition delay, also relates to Computational Fluid Dynamics (CFD), which can be used to simulate combustion phenomena at engine conditions without building a new device or formulate a real fuel. As a result, the development of detailed kinetic mechanisms requires validation in a wide variety of regimes.

Modeling the kinetics of a fuel's combustion is challenging due to the complexity of real fuels, which contain hundreds of components. (114). Developing a kinetic model capable of simulating the autoignition of all the components inside a fuel is therefore difficult. Hence, model fuels composed of a limited number of hydrocarbons are commonly used to reproduce the autoignition kinetics of real fuels such as gasoline. The development of a surrogate and the modeling of its combustion kinetics usually process through several steps which include the selection of a minimum number of representative species, one of each chemical family, presented in the fuel to formulate the surrogate; by targeting the physicochemical properties and the combustion behavior of real fuels. Next, a large amount of experimental data is needed (laminar flame speeds, flame extinction, ignition delay, reactivity and species mole fraction profiles, etc.) for each primary component as well as the surrogate itself, at different experimental conditions. A detailed chemical kinetic mechanism is then built by coupling the sub-mechanisms for each primary species present in the surrogate. The model is validated by comparing the simulated results against the experimental data. According to the level of agreement between the experiments and the simulations, the kinetic mechanism is modified if necessary, by using other values of rate constants of specific reactions available in the literature, estimated or calculated. Finally, the developed model can be reduced for specific applications such as complex turbulent combustion modeling, in the same way as described above for pure components.

1.5. General properties of studied biofuels

The molecules chosen to perform this study are oxygenated molecules that are either potential automotive fuels, or model molecules which can be used to understand the chemical kinetics of combustion of similar fuels. An effort was made to choose systems with various structures and the compounds studied during this work belong to the families of aromatics, alcohols and ketones. One representative of each family is chosen and its ignition properties are studied using a Rapid Compression Machine (RCM). Some of the molecules' properties, shown in Table 5, make them potential biofuels. Intermediate stable species formed during the ignition delay are then identified and quantified after sampling by gas chromatographic analysis. The obtained results are used to develop and validate combustion kinetic models. This modeling work can be supported by theoretical chemistry work, which makes it possible to provide thermodynamic data or rate constants for key reactions. The molecules studied during this thesis are:

- **Anisole** (methoxybenzene) is the simplest aromatic with a methoxy group and it is investigated due to its potential octane booster properties and interest as a lignin pyrolysis and oxidation surrogate.
- ***O*-cresol** is a substituted phenol with anti-knock properties owing its aromaticity and a potential gasoline additive. It is also one of the main products of anisole oxidation (115) thus understanding its kinetics helps to clarify anisole oxidation mechanism.
- **Prenol**, while not being directly synthesized from lignocellulose but rather from sugars, is an unsaturated alcohol with an energy density higher than ethanol (12) and which shows an “octane hyperboosting” effect, thereby it is an interesting fuel additive.
- **Cyclopentanone** is a cyclic ketone and due to its high RON value, (see Table 7) it is also a potential biofuel.

The choice of the molecules of interest for this study depends not only on the properties inherent to the fuel formulation but also on the limitations attached to the experimental conditions. Currently available experimental devices impose operating temperature limits due to the risk of mixture condensation during their preparation which can also occur in real engines. Therefore, the Figure 10 shows the vapor pressure as a function of the temperature for the five molecules studied and a comparison with ethanol. It should be noted that fuel formulation also imposes sufficient volatility for operation inside a SI engine.

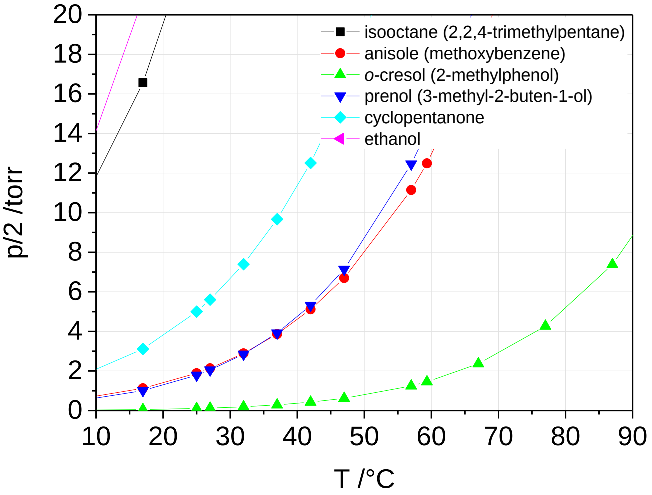

Figure 10 - Vapor pressure of studied fuels (116).

Table 5 - Properties of fuels relevant to modern SI engines.

Molecular structure	Name	Chemical formula	RON	MON	S = RON - MON	Lower heating value [MJ/L]	Heat of vaporization [kJ/kg]	Water solubility [mg/L]	Safety information
-	gasoline	-	85–95[*] (117)	80–88 (114)	-	31.9 (118)	373 (118)	<0.1 (119)	-
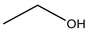	ethanol	C_2H_6O	109 (120)	90 (120)	19	20.2 (120)	918.2 (120)	789.3 (120)	🔥
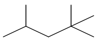	isooctane (2,2,4-triméthylpentane)	C_8H_{18}	100 (121)	100 (121)	-	30.7 (118)	308 (118)	2.2 (122)	🔥
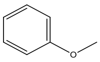	anisole (methoxybenzene)	C_7H_8O	103 (120)	92 (120)	11	33.2 (120)	428.2 (120)	1040 (120)	🔥
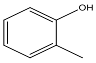	*o*-cresol (2-methylphenol)	C_7H_8O	96.9[**] (123)	NF[***]	NF	NF	NF	NF	☠
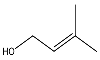	prenol (3-methyl-2-buten-1-ol)	$C_5H_{10}O$	93.5 (124)	74 (124)	19.3 (124)	29.6 (124)	512 (12)	41000 (12)	🔥 ❗
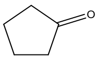	cyclopentanone	C_5H_8O	101 (120)	89.4 (120)	11.6 (120)	31.99 (120)	504 (120)	60000 (120)	🔥 ❗

[*] Typical gasoline available in the EU market.
[**] Experimental blended RON - standard RON engine-like simulations with 2% mole fraction *o*-cresol additive in butane (RON of 93.6 (125)).
[***]NF – not found.

1.6. Thesis outline and objectives

Chapter 2: This chapter begins with a brief review of the theoretical fundamentals of the combustion of hydrocarbon fuels. Subsequently, the specifics of combustion chemistry for each family, alkanes, alkenes, aromatic, alcohols, and ketones, are discussed by reviewing previous works, to offer insights into the chemistry behind the studied LDCs. The last section is dedicated to the combustion of gasoline surrogates.

Chapter 3: In this chapter, the experimental facility and the methodologies employed in this work are presented. These include the experimental devices used to study the autoignition propensity of the lignocellulosic biomass derived compounds, as well as the sampling and the analysis system. Finally, the numerical approach used to simulate the experimental data is discussed.

Chapter 4: In this chapter a framework of the reactivity of the studied LDCs is presented. For each surrogate, RCM experiments were performed at low to intermediate temperatures, and sampling experiments with the aid of chemical kinetic support the proposed discussion regarding the possible oxidation pathways of these compounds and the differences in their reactivity.

Chapter 5: A summary of experimental results and a discussion from a global point of view is presented in this chapter as well as suggestions for future research.

The objectives of the current work are listed below:

- Provide a benchmark of new potential biofuels through the study of their reactivity at engine relevant conditions;
  - To ensure experimental reliability using U. Lille RCM by investigating isooctane reactivity and comparing with previous results;
  - Investigate the reactivity, from low to intermediate temperatures, of four Lignocellulosic Derived Compounds (LDC´s): anisole, *o*-cresol, prenol and cyclopentanone;

- Investigate the blending effect of the studied biofuels inside a gasoline surrogate;

- Investigate the species formed during the combustion of surrogates containing anisole and cyclopentanone;
  - Sampling the reactant mixture and analyze the species formed and consumed before and during the combustion;

- Develop a combustion kinetic model of anisole co-oxidation inside a chosen surrogate.

2. Combustion of Hydrocarbon Fuels

This chapter begins with a brief review of the theoretical fundamentals of the combustion of hydrocarbon fuels. Subsequently, the specifics of combustion chemistry for each family, alkanes, alkenes, aromatic, alcohols, and ketones, are discussed by reviewing previous works, to offer insights into the chemistry behind the studied LDCs. The last section is dedicated to the combustion of gasoline surrogates.

Introduction

As discussed in the previous chapters, the development of modern engine technology is strictly dependent on the knowledge of the kinetic models responsible for the combustion chemistry of the fuel. Hence, in this chapter, a non-exhaustive literature review of the combustion of hydrocarbon fuels is provided. The first section discusses the general aspects of combustion chemistry at low and high temperatures. The following section summarizes the previous works concerning the chemical kinetics of isooctane and the four studied LDCs, anisole, *o*-cresol, prenol, and cyclopentanone (CPN) as well as 2-methyl-2-butene (2M2B), to shed some light on the influence of the molecular structure on the fuel´s reactivity.

Moreover, considering that some compounds (e.g. aromatics and alkenes) depict different combustion properties within a mixture, the last section of this chapter includes a discussion about the combustion characteristics of gasoline surrogates, providing useful discussions from a kinetics perspective on the co-oxidation of the LDCs, blended with conventional fuels.

2.1. Theoretical fundamentals

2.1.1. Chemical kinetics

Methane is the simplest hydrocarbon fuel and its global combustion reaction is given by:

$$CH_4 + O_2 \rightarrow CO_2 + 2H_2O \qquad (1)$$

However, the kinetics of a fuel´s combustion rarely proceed in such a simple manner. The global reaction represents a molar relation between reactants and products, and it cannot provide a detailed description of the chemistry. On the other hand, the same global reaction can be represented by a system of reactions, where intermediate species are formed and contribute to the final products. These reactions are known as elementary reactions, and are defined as one that occurs on a molecular level exactly in the way described by the Reaction (2) (126). Reaction (1) is the global reaction representing the complete combustion of methane, and Reaction (2) is the elementary reaction where molecules of methane and oxygen react to form two radicals (127):

$$CH_4 + O_2 \rightarrow \dot{C}H_3 + H\dot{O}_2 \qquad (2)$$

Hence, to better understand radical chain branched kinetics, some additional fundamentals are discussed here. Considering a system, with a volume V, where the mass inside the system is conserved, and the concentration gradients can be neglected; a series of reactions occur inside this system simultaneously, involving n species $(n = N + M)$. This series of elementary reactions describes the global reaction in detail. These reactions can be reversible or irreversible and each one of them can be represented by the general form:

$$\sum_{i=1}^{N} \upsilon_i{}' \, R_i \rightarrow \sum_{i=1}^{M} \upsilon_i{}'' \, P_i \qquad (3)$$

Where R_i and P_i are the reactants and the products and $\upsilon_i{}'$ and $\upsilon_i{}''$ are the associated stoichiometric coefficients, respectively. These coefficients represent the quantitative relationship among the species as they participate in the reaction. On the other hand, the relationship between the molar concentration of species and the rate of a reaction is represented by the rate law, which indicates how fast a reaction takes place. For forward reaction in Equation (3), the rate law can be expressed, under the assumption of the law of mass action, as:

$$r_f = \left(\frac{d[R_i]}{dt}\right)_f = \upsilon_{i,f} k_f \prod_{i=1}^{N} [R_i]^{\upsilon_i'} \qquad (4)$$

Where the concentration of the reactants is expressed by $[R_i]$; $\upsilon_{i,f} = \upsilon_i'' - \upsilon_i'$ and k_f is the forward rate coefficient. Similarly, for the backward reaction, the rate constant can be expressed as:

$$r_b = \left(\frac{d[P_i]}{dt}\right)_b = \upsilon_{i,b} k_b \prod_{i=1}^{M} [P_i]^{\upsilon_i''} \qquad (5)$$

where the concentration of the products is expressed by $[P_i]$; $\upsilon_{i,b} = \upsilon_i' - \upsilon_i''$ and k_b is the backward rate coefficient.

Besides that, in a reversible reaction, when the thermodynamic equilibrium is reached, the concentrations reach a steady state and therefore the rates of the direct (r_f) and the reverse (r_b) reactions are the same, i.e., no net reaction change on the macroscopic level is observed, which implies:

$$\upsilon_{i,f} k_f \prod_{i=1}^{N} [R_i]^{\upsilon_i'} + \upsilon_{i,b} k_b \prod_{i=1}^{M} [P_i]^{\upsilon_i''} = 0 \tag{6}$$

The equilibrium constants, which represent the ratio between the two rate constants k_f and k_b, can be written in terms of the molar concentration or the pressure of the species:

$$K_C = \frac{\prod_{i=1}^{M} [P_i]^{\upsilon_i''}}{\prod_{i=1}^{N} [R_i]^{\upsilon_i'}} \tag{7}$$

$$K_P = \frac{\prod_{i=1}^{M} P_{P_i}^{\upsilon_{x,i}}}{\prod_{i=1}^{N} P_{R_i}^{\upsilon_{y,i}}} \tag{8}$$

From this knowledge, the relation between kinetics and the thermodynamics can be obtained, by considering the following equations:

$$\frac{K_P}{K_C} = (RT)^{\sum_{i=1}^{M} \upsilon_i'' - \sum_{i=1}^{N} \upsilon_i'} \tag{9}$$

In the equilibrium the relation between the standard molar Gibb's free energy $\Delta G^{\circ}(T)$ and the equilibrium constant is given by:

$$\Delta G^{\circ}(T) = -RT \ln K_p \tag{10}$$

$\Delta G^{\circ}(T)$ can be calculated by the following equation:

$$\Delta G^{\circ}(T) = \Delta_R H(T) - T.\Delta_R S(T) \tag{11}$$

Where $\Delta_R H(T)$ is the molar enthalpy of the reaction and $\Delta_R S(T)$ is the molar entropy of the reaction, both at temperature T. Moreover, the variation of the rate constant as a function of temperature, for an elementary reaction, is represented by the modified Arrhenius law:

$$k_i = AT^n(-\frac{E_a}{RT}) \tag{12}$$

Where A is the pre-exponential factor, n is a factor reflecting the deviation from the original Arrhenius formalism and E_a is the activation energy.

In reactions in which the rate constant is pressure-dependent, such as unimolecular decompositions and recombination reactions, three regimes can be defined: the low-pressure regime, where the rate constant is proportional to the pressure, and it increases linearly within the pressure; the fall-off zone, between the low and high-pressure zones, in which the rate constant increases within the pressure, however, in a non-linear way; and the last regime, that is independent of the pressure and it is located at its high-pressure limit. These pressure-dependent reactions require a collision partner M, that is an unspecified species present in the reactant gas-phase mixture. It is responsible for carrying the excess energy released or the required energy by the pressure-dependent reactions. The efficiency of the collision partner is variable, and is characterized by a coefficient. Different methods can be used to represent the fall-off zone, such as the Lindemann-Hinshelwood theory and the Troe formalism (127).

Considering the aforementioned closed system with volume V, by writing the conservation of energy, it is possible to evaluate the evolution of the temperature as a function of time and thermodynamic properties of the mixture:

$$\sum_{i=1}^{n} n_{I_i} c_P^{I_i}(T) \frac{dT}{dt} + \sum_{i=1}^{n} \left[\frac{dn_{I_i}}{dt} \Delta_f H_{I_i}^{\circ}(T) \right] = hA\Delta T \qquad (13)$$

Where ΔT is the temperature differences inside the system, if the considered system is a closed reactor, these temperatures are the reactor core temperature and the reactor walls temperature; A is the surface area where the heat transfer takes place; h is heat transfer coefficient; and $\Delta_f H_{I_i}^{\circ}$ and $c_P^{I_i}$ are the standard enthalpy of formation and the molar heat capacity at constant pressure, respectively, of the component I_i, at the temperature T. Therefore, the system of differential equations for the concentration of the species and also for the energy and momentum variables, together with the physical and chemical quantities such as heats of formation, molecular transport coefficients, and specific heats, can be solved to describe the evolution of a given system.

The solution of these n differential equations provides, for each species, the time-dependent concentration profile as well as illustrates how fast the amounts of reactants and products change during the reaction.

2.1.2. Reaction mechanisms

During the pyrolysis and oxidation of organic compounds, there are four types of elementary chain reactions: initiation, branching, propagation, and termination or recombination. The hydrogen oxidation mechanism is used here to illustrate these types of reactions due to its relevance in the mechanism of every hydrocarbon or oxygenate, considering that the combustion of larger hydrocarbon fuels directly involves or eventually leads eventually to the formation of species involved in the kinetic model of hydrogen. A comprehensive model that describes the oxidation of hydrogen can be found in (128). The combustion of hydrogen can be described overall by the stoichiometric relation (129) given below:

$$H_2 + \frac{1}{2}O_2 \rightarrow H_2O \qquad (14)$$

However, a set of elementary reactions is used to describe hydrogen combustion in detail. The initiation of the combustion reaction occurs through chain initiation reactions such as:

$$H_2 + M \rightarrow \dot{H} + \dot{H} + M \qquad (15)$$

$$O_2 + M \rightarrow \text{Ő} + \text{Ő} + M \qquad (16)$$

These types of reactions have high activation energies, and therefore they are essential at high-temperature conditions. The second type of reactions is chain branching reactio*ns, which* can be illustrated by the following reaction:

$$\dot{H} + O_2 \rightarrow \dot{O}H + \text{Ő} \qquad (17)$$

In this case, the reactions produce more radical-species than they consume. They are therefore responsible for the explosive nature of combustion by increasing the pool of radicals rapidly. In other words, the ignition phenomena can be understood as events taking place in a chain-branching environment. On the other hand, in chain propagating reactions, the same number of radicals is produced that have been consumed, i.e., the total number of radicals remains unchanged. The reactions below are examples of chain propagation reaction:

$$H_2 + \dot{O}H \rightarrow H_2O + \dot{H} \qquad (18)$$

$$\dot{H} + O_2 + M \rightarrow H\dot{O}_2 + M \qquad (19)$$

Finally, recombination reactions are chain-terminating processes that take place when the concentration of radicals is sufficient to react among themselves, forming stable species. As a consequence, the radical pool decreases. These reactions compete against chain branching reactions, and if chain termination exceeds chain branching reactions, the combustion process is quenched. The following reactions depict examples of chain termination and recombination reactions:

$$\text{Ő} + \dot{H} + M \rightarrow \dot{O}H + M \qquad (20)$$

$$\dot{H} + \dot{O}H + M \rightarrow H_2O + M \qquad (21)$$

Besides that, chain branching reactions are endothermic reactions that produce radicals, i.e., with a high enthalpy. In contrast, chain termination reactions are exothermic reactions that release energy to the system. When radicals accumulate in sufficient amount for bimolecular or termolecular chain termination reactions to occur, the energy released to the system causes an increase in temperature. The increased temperature may help chain branching if the temperature achieved is enough to overcome the energy barrier for such reactions. In contrast, termination reactions deplete the radical pool and increase the temperature.

This competition takes place until the thermodynamic equilibrium of the system is reached. In the case of ignition, chain-branching often takes place through the formation of an indirect chain branching agent, i.e. a non-radical species, for example ketohydroperoxides in the case of LTC, and H_2O_2 in the case of Intermediate temperatures. While this species is not a radical, it will eventually decompose and form 2 radicals, therefore initiating chain branching.

2.1.3. Temperature regimes

As mentioned earlier, combustion is initiated by chain initiation reactions. Once reactivity has started, small radicals are quickly formed and attack the fuel. The following reactions strongly depend on the temperature regime of the system. Figure 11 shows a typical evolution of the ignition delay as a function of temperature for a fuel that shows NTC behavior (i.e. a long alkyl chain paraffin) and one that does not (i.e., a short alkyl chain aromatic). The Ignition Delay Time (IDT) is defined as the time necessary to reach autoignition at a given temperature and pressure. Hence, the shorter the IDT of a given fuel is, the more reactive it is. The autoignition results from the conjunction of two phenomena previously discussed:

- Indirect chemical branching, which multiplies the number of radicals. These radicals can take part in the initiation and branching reactions therefore growing exponentially;

- Thermal runaway, which results from the increase in the temperature of the medium following the exothermic reactions which take place. As reaction rates usually increases as the temperature increases, this creates a loop that leads to autoignition.

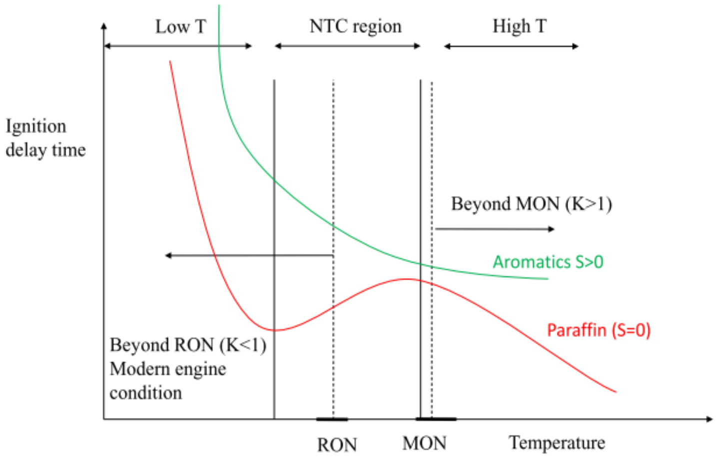

Figure 11- Schematic representation of the fuel´s reactivity as a function of temperature (130).

The mechanism responsible for chemical branching is however different depending on the range of temperature. A distinction is thus made between three temperature regions. The first region is the high temperature, commonly accepted as above about 1200 K. In this region the reactivity increases as the temperature increases, according to the Arrhenius´ Law with a positive activation energy. Sensitivity analyses show that for many different hydrocarbon fuels (131), at high temperatures, Reaction (17) is the most sensitive reaction. The region from 850 to 1200 K is known as intermediate temperature zone. This temperature domain is separated from the low-temperature combustion domain by the Negative Temperature Coefficient (NTC) zone. This last zone is characterized by a decrease in reactivity, along with an increase in temperature, in contrast with the Arrhenius law.

The low-temperature regime operates according to a peroxidation-isomerization process. The chemistry behind this regime is complex due to the large number of associated reactions. The energy content of the system being lower than in the high temperature regime, radical reactions tend to be more selective, and the structure of the fuel has more influence on its reactivity. The chemistry of these compounds dictates commonly observed phenomena at low temperatures for certain species such as long-chain hydrocarbons and ethers: cool flames (132). In closed systems, the further extinction of this cool flame is often observed, because of the NTC. This is mainly due to the fact that, when the temperature rises, the reactions responsible for chemical branching at low temperatures are no longer competitive with other reactions which do not lead to chemical branching (133). Therefore, the change in the kinetic mechanism as a function of temperature can also be described as a change in the reaction pathways for hydrocarbon combustion.

The presence of the NTC region and its characteristics are relevant criteria for the evaluation of fuel viability, since properties such as octane numbers and, consequently, fuel octane sensitivity (as defined by S = RON - MON) are related to this NTC behavior, as seen in Figure 11. In fact, fuels that do not exhibit NTC behavior are the most promising for working with high compression ratio, turbocharged engines, as they lead to a reduction of the incidence of autoignition and detonation during combustion processes (134). Kinetic models designed to describe combustion, should therefore include specific mechanisms for the high-, intermediate-, and low-temperature regime, to correctly predict information such as performance and formation of pollutants at all engine-relevant temperature ranges.

2.2. State-of-the-art of combustion chemistry

The chemical families of compounds found in commercial fuels, and that best represent them are alkanes, alkenes, and aromatics. Meanwhile, biofuels are composed of oxygenated hydrocarbons. Alcohols and methyl esters were the first candidates used as substitutes for conventional fuels and they have been widely studied. The database on the oxidation of such molecules is therefore large (135), and shows that these compounds have significantly different reaction pathways under combustion conditions. It is also probable that interactions between molecules can occur in a complex environment such as gasoline or diesel. For example, measurements of RON and MON of mixtures have shown that a mixture can have eventually a reactivity higher or lower than each of the pure hydrocarbons present in such mixture (12). In the case of prenol, an increase in the reactivity of the mixture is observed comparing against pure prenol; this phenomenon is known as octane "hyperboosting."

Before investigating a mixture of hydrocarbons that can potentially be used as a surrogate fuel, it is necessary to examine how each one of its components behaves. Therefore, this section discusses previous works dedicated to the chemical families mentioned above (alkanes, alkenes, aromatics, alcohols, and ketones), which can be found in different generations of fuels (3). The general concepts concerning the oxidation of these hydrocarbons are discussed. Subsequently, a non-exhaustive review is presented for examples including the LDCs and other relevant molecules: isooctane, 2-methyl-2-butene (2M2B), anisole, *o*-cresol, prenol, and cyclopentanone. Based on this knowledge, a review presents relevant experimental and numerical combustion studies available, in order to better understand the blending effect of the molecules present in alternative fuels. The focus is on potential co-oxidation reactions that can take place between the components inside the mixture, allowing the development and use of simpler mixtures to mimic properties of real fuels. The brief analysis presented herein allows us to conclude that despite recent progress in combustion research concerning gasoline surrogates as well as the molecules present in biofuels, there are still significant gaps in the study of the interaction between them.

2.2.1. Alkanes

Detailed kinetic mechanisms are often built following a hierarchical structure consisting of several successive layers. The core of this mechanism is known as the C_0 part, and it contains reactions relating to the combustion of hydrogen. The following layer concerns C_1 (carbon monoxide, methane, methanol, formaldehyde) and up to C_4. This sub-mechanism constitutes the basis. Very often, the sub-mechanism of the molecule to be studied is added to the base to form the model. When this molecule decomposes, it generates smaller fragments that react subsequently. The numerical approach used to develop detailed kinetic models will be discussed in the next chapter.

In the engine-relevant case of globally lean to stoichiometric mixtures, the combustion of large hydrocarbon fuels often leads to the formation of CO_2, H_2O, and other stable species such as carbon monoxide in the same sequential way as smaller hydrocarbons, i.e., the final combustion products of large hydrocarbons are often similar to those of smaller ones. Similarly, the combustion of ethane forms ethyl radical, which then generate ethene and subsequently formaldehyde, CO, and CO_2. The core mechanism is common to all larger hydrocarbon fuels, whether petrol or alternative fuels. Core mechanisms from different research groups can be found in (136–142).

Methane is the simplest alkane, and due to the simplicity of this molecule, its combustion kinetic differs from conventional hydrocarbon fuels. The first kinetic model used to describe the combustion of methane was published in 1936 (143) and a recent review, including the recent progress made in methane mechanism can be found in (144). The comparison of the kinetic models of hydrogen and methane shows that the number of reactions and species increases very fast with the complexity of the fuel´s molecular structure (145). Therefore, different classes of elementary reactions have been proposed (7,60) in order to describe the oxidation of hydrocarbons in a systematic way. The main classes of reactions considered in the current work are summarized in the next table:

Table 6 - Classes of elementary reactions considered during the oxidation of hydrocarbon fuels.

A: unimolecular decomposition	Bond rupture, forming two radicals. High activation energy is required (7).
B: H-atom abstraction	Abstraction of a H-atom by small radicals $(\ddot{O}, \dot{H}, \dot{O}H, \dot{C}HO, \dot{C}H_3, \dot{C}_3H_5)$. Different chemical features rule this class of reaction depending on the type of the bond cleavage to produce an $(\dot{H})$ radical. This is, in general, the most important class of reaction for the fuel consumption (145).
C: decomposition β-scission	Bond cleavage of a radical forming olefin or aldehyde, and a small radical, preferentially at the β position to the atom with the unpaired electron. This reaction requires high activation energy and is therefore favored at high temperatures (7).
D: isomerization	Transfer of a hydrogen atom from the molecule to the atom which carries the unpaired electron (7). Peroxyalkyl radicals $(\dot{R}\mathrm{O}_2)$ undergo internal isomerization to form the hydroperoxyalkyl radical $(\dot{Q}O_2H)$. Peroxyhydroperoxyalkyl radicals $(\dot{O_2}QO_2H)$ reacting through internal isomerization will quickly yield a ketohydroperoxide (OQO_2H) and an OH radical.
E: formation of alkenes from alkyl radicals	The formation of an olefin, for example through the addition of an alkyl radical to an oxygen molecule. This reaction has high activation energy and its occurrence depends on the fuel molecular structure. This reaction competes with the intermediate temperature reactions (7).
F: addition of radicals to the double bond	Exothermic reactions that reduce the presence of certain radicals $(\ddot{O}, \dot{H}, \dot{O}H, \dot{C}HO, \dot{C}H_3, \dot{C}_3H_5)$. The formed radical can easily decompose, at high temperatures, to products, and at low temperatures it can react by successive oxidative reactions (146).
G: decomposition of unsaturated radicals	If the initial radical is an allylic or a vinylic radical, the reaction product will be an olefin with two unsaturations (7).
H: concerted elimination	In this reaction an unsaturated bond is formed by removing the substituents in a single step.
I: recombination	Exothermic reactions between two radicals forming a stable species. This type of reaction can occur both at high or low temperature due the low activation energy required (130).
K: Addition to O_2	The addition of an alkyl radical $(\dot{R})$ to oxygen forms the peroxyalkyl radical $(\dot{R}\mathrm{O}_2)$, which is not stable at high temperatures. Hydroperoxyalkyl radicals $(\dot{Q}O_2H)$ can also undergo addition to O_2 to form a peroxyhydroperoxyalkyl radical $(\dot{O_2}QO_2H)$.
L: peroxyl radical reactions	Peroxyalkyl radicals $(\dot{R}\mathrm{O}_2)$ can react by hydrogen abstraction on another molecule or radical to form the corresponding hydroperoxide $(ROOH)$.
M: decomposition of hydroperoxides	Hydroperoxide $(ROOH)$ can decompose due to the breaking of the O-O bond, producing two radicals $(R\dot{\mathrm{O}})$ and $(\dot{O}H)$. The alkoxy radical formed $(R\dot{\mathrm{O}})$ is highly unstable and thus it can decompose to form mostly aldehydes or ketones (7).
N: radical cyclization	Formation of cyclic products from hydroperoxyalkyl radical $(\dot{Q}OOH)$ (7).
O: ipso-substitution	Addition followed by elimination in the same site. This reaction class is favored at intermediate and high temperatures.

These classes of reactions are present in the oxidation and pyrolysis mechanisms of alkanes but also of other chemical families: alkenes, aromatics, alcohols, and ketones. However, some species such as prenol can fit within the kinetics of alkenes but also that of alcohols, due to the presence of the double bond and also the hydroxyl group attached to the primary carbon. This literature review was focused on studies of oxidation of hydrocarbons at low temperatures, taking into account that this temperature regime is representative of real conditions in modern engines (147). Several studies concerning the kinetics of oxidation of hydrocarbon fuels can be found in (144,148,149) and more specifically at low temperatures (7,8).

Based on the works of Curran et al. (126,150), a simplified reaction scheme for oxidation of alkanes, at low temperatures, is shown in Figure 12.

Figure 13 uses isooctane to exemplify this general kinetic mechanism as well as the aforementioned classes of reaction.

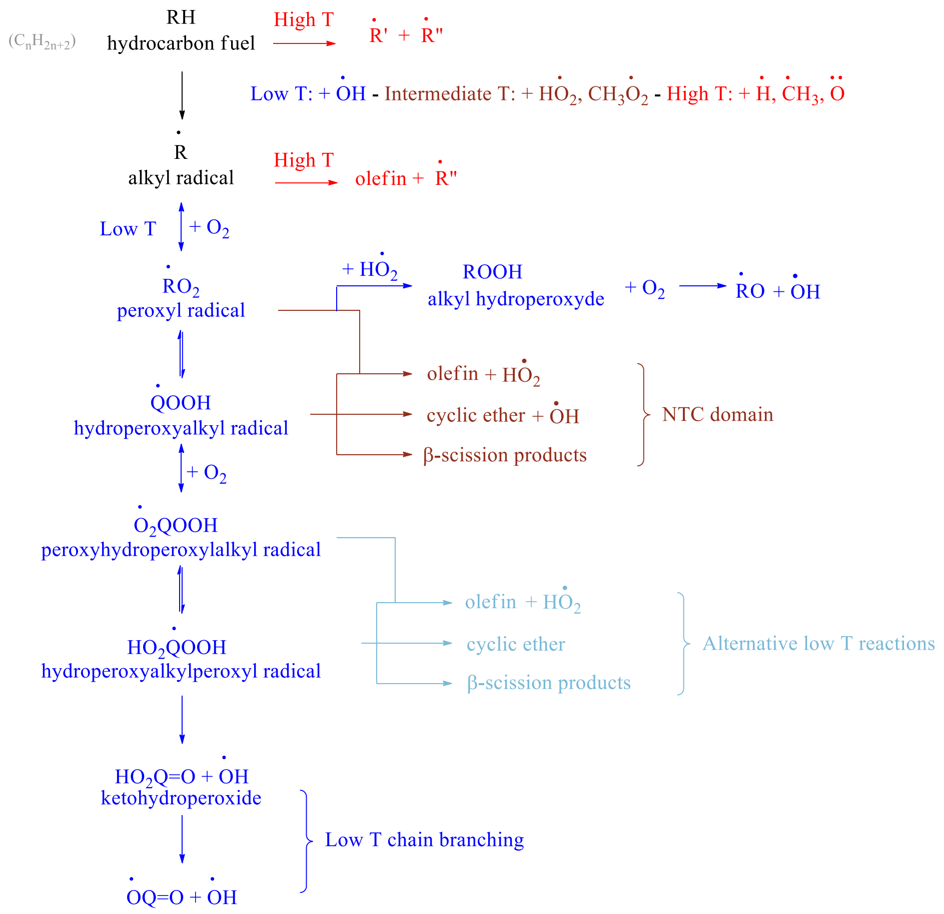

Figure 12 - Simplified reaction scheme for the oxidation of hydrocarbon fuels adapted from (60).

As discussed before, temperature dictates which reaction pathways are favored or inhibited, characterizing the mechanisms at low, intermediate and high temperatures. The high temperature oxidation mechanism of alkanes can be simplified and summarized by the following reactions:

$$RH + M \rightarrow \dot{R} + \dot{H} + M \qquad (22)$$

$$RH + M \rightarrow \dot{R}' + \dot{R}'' + M \tag{23}$$

The fuel decomposes into two radicals, therefore initiating the chain process through reactions of class A. This reaction pathway is favored at high temperatures due to the high energy required to break the original molecule. This decomposition can occur through different ways, depending on the type of bond-break. If a C-C bond is broken, two alkyl radicals will be produced, and if a C-H bond is broken, an alkyl radical and a hydrogen atom will be generated. Besides that, the Bond Dissociation Energy is superior for C-H bonds than for C-C bonds (127), and therefore it requires more energy to be broken. Among C-C bonds, the bonds involving primary carbons are stronger, followed by secondary carbons and, finally, tertiary carbons (151).

The alkyl radical can react to form unsaturated hydrocarbons through class C:

$$\dot{R} + M \rightarrow olefin + \dot{R}' + M \tag{24}$$

$$\dot{R}' + M \rightarrow conjugated\ alkene + \dot{H} + M \tag{25}$$

The fuel can also react with small radicals, as in class B:

$$RH + X \rightarrow \dot{R} + HX \tag{26}$$

Where X can be replaced by: $\dot{H}, \dot{O}H,$ Ő, $H\dot{O}_2, \dot{C}H_3, HC\dot{O}$or larger radicals.

These H-abstraction reactions can occur at low or high temperatures due the low energy required (127). They lead to the formation of four different iso-octyl radicals, in the case of isooctane, depending on the site where the hydrogen will be abstracted. The isooctyl radical can also decompose through elimination, where a methyl group will be lost, thereby forming a C_7 alkene. At low temperatures, the H-atom abstraction plays an important role in the initiation process when radicals are present due the relatively low activation energy associated to this reaction. H-atom abstraction can also take place with molecular oxygen, producing alkyl radical and hydroperoxyl radical ($H\dot{O}_2$).

$$RH + O_2 \rightarrow \dot{R} + H\dot{O}_2 \tag{27}$$

At low temperature (about 500–600 K), the alkyl radicals react rapidly by addition to the oxygen molecules to produce peroxyl radicals (class K),

$$\dot{R} + O_2 \rightleftharpoons R\dot{O}_2 \tag{28}$$

or by an abstraction:

$$\dot{R} + O_2 \rightarrow alkene + H\dot{O}_2 \tag{29}$$

In this chain reaction, hydroxy radicals are the main chain carriers. Peroxyl radicals can undergo internal isomerization (class D) to produce hydroperoxyalkyl radicals ($\dot{\mathrm{Q}}\mathrm{OOH}$).

$$R\dot{O}_2 \rightleftharpoons \dot{Q}OOH \tag{30}$$

These radicals can form oxygenated heterocycles, alkenes or aldehydes. In addition, the hydroperoxyalkyl radical can also add to another O_2 molecule, producing the hydroperoxyalkylperoxy radical ($O_2\dot{Q}OOH$):

$$\dot{Q}OOH \leftrightarrow oxygenated\ heterocycle + \dot{O}H \tag{31}$$

$$\dot{Q}OOH \leftrightarrow conjugated\ alkene + H\dot{O}_2 \tag{32}$$

$$\dot{Q}OOH \leftrightarrow alkene + aldehyde + \dot{O}H \tag{33}$$

$$\dot{Q}OOH + O_2 \leftrightarrow O_2\dot{Q}OOH \tag{34}$$

The oxygenated heterocycle formed in Reaction (31) may have a ring size from 3 to 6 atoms (60). The peroxyhydroperoxyalkyl radical can then undergo a second isomerization, which ultimately forms a ketohydroperoxide or an aldohydroperoxide (HO_2QO).

$$O_2\dot{Q}OOH \leftrightarrow HOO\dot{Q}_{-H}OOH \leftrightarrow \dot{O}H + HO_2QO \tag{35}$$

These indirect chain-branching agents can form another OH radical by dissociation:

$$HO_2QO \leftrightarrow \dot{O}H + O\dot{Q}O \tag{36}$$

The formation and decomposition of this ketohydroperoxide will therefore produce two ($\dot{\mathrm{O}}\mathrm{H}$) radicals and a ($O\dot{\mathrm{Q}}\mathrm{O}$) radical by consuming only the fuel, one radical and molecular oxygen, thus provoking the degenerate chain branching responsible for the cool flames and first-stage ignition. In a recently published study, Wang et al. (152) proposed that at low temperatures, a 3rd addition of oxygen is possible, and should be taken into account for *n*-alkanes with six or more carbon number in their structure. Hydrogen peroxide is also formed and decomposed through the following reactions:

$$RH + H\dot{O}_2 \leftrightarrow \dot{R} + H_2O_2 \tag{37}$$

$$H\dot{O}_2 + H\dot{O}_2 \leftrightarrow O_2 + H_2O_2 \tag{38}$$

$$H_2O_2 + M \leftrightarrow 2\dot{O}H + M \tag{39}$$

The decomposition of ($\mathrm{H_2O_2}$) into two ($\dot{\mathrm{O}}\mathrm{H}$) radicals requires higher temperatures than the decomposition of ketohydroperoxides, and is responsible for the second degenerate branching leading to the final ignition, especially in the NTC region. Once the system is ignited, direct chain branching takes place through this reaction:

$$\dot{H} + O_2 \leftrightarrow \ddot{O} + \dot{O}H \qquad (40)$$

Alkanes with a longer alkyl chain are often more reactive than those with a shorther alkyl chain, resulting in shorter IDTs. An experimental study on the autoignition properties of a series of linear and branched-chain alkanes at intermediate temperatures that illustrates such behaviour can be found in (153)' and also for smaller hydrocarbons in (148,154). Minetti et al. (153) used the ULille RCM to investigate the ignition properties as a function of temperature for *n*-butane, *n*-pentane and *n*-heptane. These results corroborate the fact that long alkyl chains lead to shorter ignition times and also emphasize that the kinetics at intermediate temperature plays an important role on the reactivity of alkanes, especially in the case of *n*-butane, which has a well-defined NTC region. It can be explained by the pathway (D) shown in

Figure 13, that corresponds to the formation of hydroperoxyalkyl radicals by intra-molecular isomerization. Hydrocarbons with longer alkyl chains have more suitable sites for these isomerization reactions, and consequently, they can easily lead to subsequent indirect chain-branching reactions at low temperatures. For the same reason, the effect of the side chain position on branched alkanes is to cause a decrease in the reactivity with a change of position of the side chain towards the center of the hydrocarbon molecule (155). Moreover, the increase of the number of branches also leads to an inhibition of the reactivity of alkanes. These three phenomena observed for branched alkanes are summarized in (6).

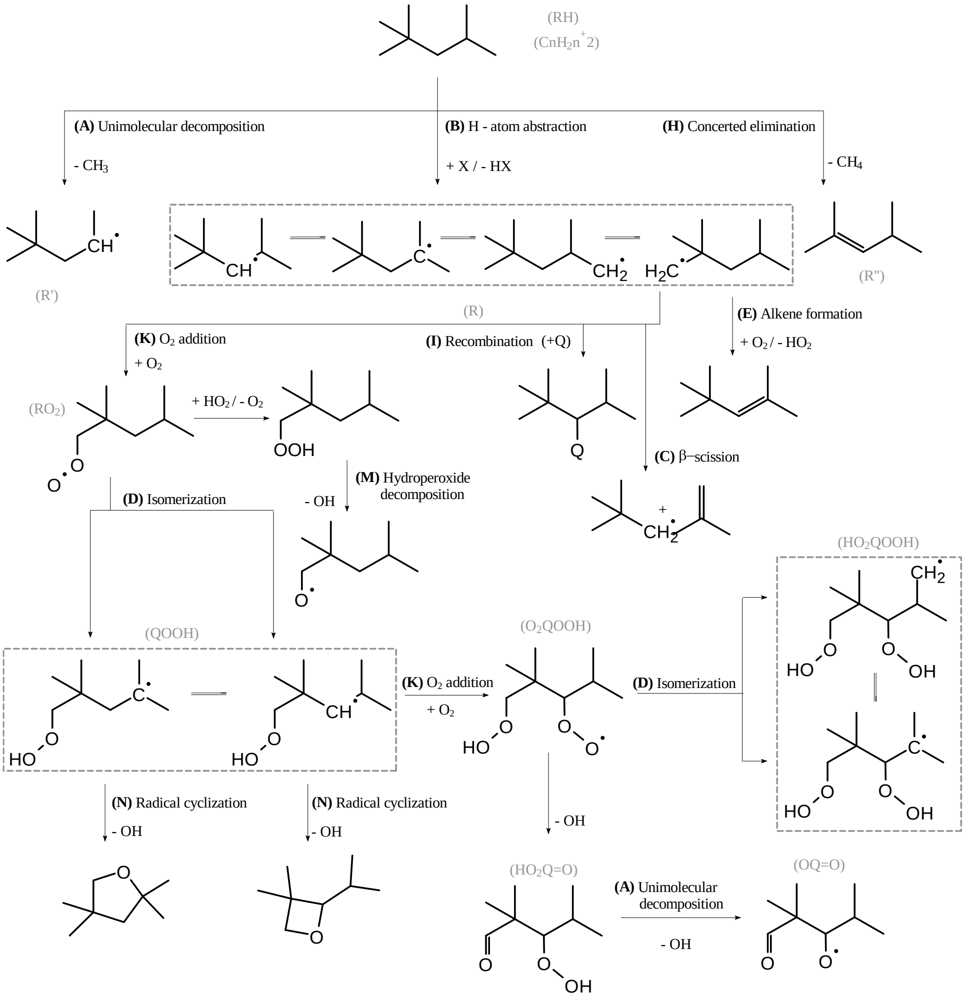

Figure 13 – Example of potential routes for isooctane oxidation.

2.2.1.1. Previous work on Isooctane

Isooctane (2,2,4-trimethylpentane) is one of the 18 octane isomers found in gasoline, diesel, and aviation fuels. It is, along with *n*-heptane, a constituent of reference fuels (PRF - Primary Reference Fuel) used in the measurement of the octane numbers (RON and MON), of which it is the reference 100 (156). Consequently, isooctane is an excellent representative of alkanes in gasoline fuels. This molecule has also been widely studied since it is considered the basic model for the oxidation of branched alkanes, and has therefore been studied experimentally extensively.

Detailed chemical kinetic models for hydrocarbon fuels have been developed since the early 1970s (157,158). One of the first mechanisms for the oxidation of isooctane was developed by Westbrook et al. (159) in 1988. This model includes 324 species and 1303 reactions and is able to predict the kinetics of isooctane only at high temperatures. This model was used by Chen et al. (160), in 2000, in order to simulate their experimental profiles obtained in a flow reactor, at high pressure, and in lean fuel conditions. In 2002, Curran et al. (150) used the model from Chen et al. (160) to generate a new mechanism systematically constructed according to the classes of elementary reactions discussed before. The mechanism of Curran et al. (150) was validated for many experimental conditions. This model was improved by Mehl et al. (161) in 2009 in order to better represent the ignition delay times of isooctane in STs and RCMs. In 2011 Mehl et al. (162) updated this mechanism to simulate surrogate mixtures of isooctane, toluene and 1-hexene relevant to gasoline. Experimental ignition delay data were used to validate the mechanism from different research groups including ULille. The improved mechanism is able to predict the experimental behaviour in a range from 3 to nearly 50 atm in both the low- and high-temperature domain. Both mechanisms form Curran et al. and from Mehl et al. show a good agreement between the experimental and simulated results. However, some works (163–165) indicated that the isooctane reactivity is underestimated using the models from Curran et al. (150) and Mehl et al. (162), especially at low- to intermediate temperatures and for lean mixtures.

Atef et al. (166) proposed in 2017, an experimental and modeling study of the combustion of isooctane at relevant conditions to the current study. The proposed model was based on works mentioned above from Curran and Mehl. The developed mechanism took into account new thermochemical and kinetic data available in the literature or calculated as part of this work. We can mention, among others, the inclusion of new alternative isomerization pathways for hydroperoxyperoxyalkyl radicals as an important contribution from this work. Thus, the updated kinetic model shows good performance in reproducing autoignition delays measurements in the RCM and high-pressure shock tube. These experiments were carried out at pressures of 20 and 40 atm, at $\phi = 0.4$ and 1.0, and at temperatures from 632 to 1060 K. Experimental data available in the literature from RCMs, STs, JSR, premixed laminar flame speeds and counterflow flame ignition measurements were also used to validate the mechanism.

Recently, Fang et al. (167) investigated the ignition characteristics of mixtures of isooctane/air and iso-dodecane/air, using a RCM. The measurements were performed at pressures 15, 20, and 30 bar, equivalence ratios 0.7, 1.0, and 2.0, and in a temperature range from 600 to 900 K. A detailed kinetic model, including iso-alkanes from C_8 up to C_{16} was developed hierarchically from the models by K. Zhang et al. (168) and AramcoMech2.0 (142) for the species up to C_2. The experimental ignition delay time measurements were compared against the results from Atef et al. (166) for isooctane at p_C = 20 bar, showing good agreement. The developed model matches well with the experimental data from this work, as well as the data available in the literature. Discrepancies were observed for stoichiometric mixtures at 20 bar and at 15 bar and 30 bar at high temperatures. The authors suggest that the observed ignition delay time crossover between the two studied branched iso-alkanes is due to the complex chemical kinetics in the NTC region.

Discrepancies between experimental results, using different RCMs can also be attributed to the composition of the used diluent gas, as suggested by Atef et al. (166). Di et al. (169) published the first experimental investigation on the effect of the buffer gas on the reactivity of isooctane and n-heptane at low to intermediate temperatures. The autoignition of stoichiometric mixtures of isooctane was investigated, using a RCM, temperatures ranging from 600 to 850 K, p_C = 20 bar and using 100% Ar, 100% N_2 and a mixture of Ar and CO_2 as buffer gas. At these conditions, the mixture using only Ar was found to be more reactive with IDTs around 40% shorter than in the other cases. In addition, the effect of third-body collision efficiencies was also investigated by testing a mixture of Ar and CO_2, which has almost the same heat capacity as of the mixture using N_2. The experimental results show no significant effect, at the studied conditions, on the total and first-stage ignition delay.

Zhang et al. (170) carried out an experimental study of the autoignition of isooctane in order to investigate the first-stage ignition delay in the NTC region behavior. Stoichiometric mixtures of isooctane/O_2/N_2/Ar were tested using an RCM at 20 bar, and from 675 to 792 K. The most relevant contribution from this work is the demonstration that the first-stage ignition delay is sensitive to the concentration of oxygen. In contrast, it is insensitive to the gas dilution and the concentration of the original molecule of fuel. Furthermore, numerical simulations were performed to better understand the effect of the first-stage ignition on the final ignition. The authors identified five competing reactions as important reactions for the first-stage NTC behavior: the reverse reaction of second O_2 addition, alkene and hydroperoxyl radical production from hydroperoxyalkyl radicals, the β-scission reaction of the alkyl radical, and both decomposition reactions of the hydroperoxyalkyl radical, the first one forming a cyclic ether and a hydroxyl radical and the second, an alkene and a hydroperoxyl radical.

Mittal et al. (171) measured the ignition delay times of mixtures of isooctane/O_2/Ar = 1/12.5/47 by mole, at temperatures from 680 to 940 K and compressed pressure of 15.5 and 20.5 bar. This work investigated the effect of the mass transfer to the crevice during multi-stage ignition. The authors proposed a “crevice containment” design in order to perform the experiments while mitigating mass transfer to crevice, using a ring placed between the piston and the chamber which prevents the tested mixture to flow through the crevice.

The experimental results revealed longer ignition delay times when the mass transfer to the crevice occurs, and thus it was suggested to take into account this phenomenon to model RCM IDTs. Additional isooctane ignition delay time measurements, using the same RCM and published earlier can be found in (172,173).

Most recently, Wu et al. (174) used ignition delay measurements to validate a new RCM facility. Fuels with and without NTC behave were investigated including a stoichiometric mixture of isooctane/air at 20 bar, and at temperatures from 600 to 900 K, in order to validate the use of the adiabatic core hypothesis in their apparatus. Furthermore, a dynamic mesh strategy was used to optimize the creviced piston. The authors suggest that the effect of the shape of the crevice on the temperature homogeneity is negligible as long as the volume is enough to suppress the vortex caused by the cold gases during the compression. Ignition delay time measurements were compared against results from RCM from KAUST, NUIG, Uconn (166) and UAkron (175), matching well, considering the complexity of these type of experiments. However the comparison of numerical simulations using Atef (166) and Mehl (162) models revealed considerable discrepancies at intermediate and low temperatures.

He et al. (176) investigated the autoignition of isooctane under HCCI engine conditions. Mixtures of isooctane using O_2, N_2 and Ar as diluent gas were tested in the University of Michigan RCM. The relation between autoignition and the addition of EGR species such as CO_2 and H_2O were also studied. It was found that CO_2 has no effect on the ignition delay measurements of isooctane however, the addition of H_2O proves to increase the reactivity of the mixture. A relation to calculate the IDTs based on the pressure, temperature, equivalence ratio and oxygen content, was proposed and it showed a strong dependence on the equivalence ratio and pressure. Numerical simulations at 20 bar, 970 K and 20.9 % O_2 are in good agreement with the model proposed by Curran (150). Later, the same machine was used to investigate OH time histories by narrow line absorption techniques during the ignition delay of isooctane.

Isooctane ignition delay times were measured for the first time using the ULille RCM in 1992 by Ribaucour (177) at temperatures from 650 to 850 K, at compressed pressure from 11 to 16 bar and equivalence ratios 0.8, 1.0 and 1.2. These experimental results were one of the first to show a reduction in IDTs and significant displacement towards low temperatures of the autoignition limits with the increase in the length of the hydrocarbon chain, reflecting a greater reactivity of long-chain hydrocarbons. Using the same RCM, Minetti et al. (178) measured the intermediate species profiles during the oxidation of isooctane. Thirty-two different products have been identified, among which we can mention: aldehydes (formaldehyde, acetaldehyde, acrolein, propanal, 2-methylpropanal, 2-methylpropenal, and 2,2-dimethylpropanal), alkenes (propene, isobutene, 2-methyl-1-butene, 1,3-pentadiene, 4,4-diethyl-1-pentene, 4,4-dimethyl-2-pentene, 2,4-dimethyl-2-pentene, 2,4-diethyl-1-pentene, 2,4,4-trimethyl-1-pentene and 2,4,4-trimethyl-2-pentene) and cyclic ethers (furan, pyran and oxetanes). Further isooctane autoignition measurements using ULille RCM were reported in the work of Vanhove et al. (179) in 2004, showing the highly non-linear behavior of adding small quantities of toluene or 1-hexene to isooctane, and in Goldsborough et al. in 2017 (175). The excellent agreement between all three datasets should be noted, while the small discrepancies can be attributed to the changes in piston geometry and RCM operating procedure over the years.

Figure 14 shows ignition delay time measurements from several research groups for isooctane at p_C = 20 bar, including results from the University of Connecticut RCM. This machine is considered as a reference in the autoignition studies and it is described in detail in (173). The experimental results show overall good agreement even though at low-temperature, small discrepancies are observed. RCMs can operate in a wide range of operating conditions such as initial pressure, temperature, mixture dilution and surface/volume ratio. As a consequence, the heat losses associated with these experiments can differ. All results for isooctane show the same behavior: increased reactivity with increasing temperature in the low and high-temperature regions, i.e., approximately until 700 K and over 900 K, respectively; and an NTC behaviour between these two regions, where the reactivity decreases with increasing temperature, in contrast to the Arrhenius law. The availability of a large number of comparable results allows, therefore, different research groups to validate their RCM facilities for ignition delay measurements of other fuels. Further work demonstrated that all the datasets could be reconciled within 30% with simulations taking into account the composition of the diluent, the compression phase and heat losses after compression.

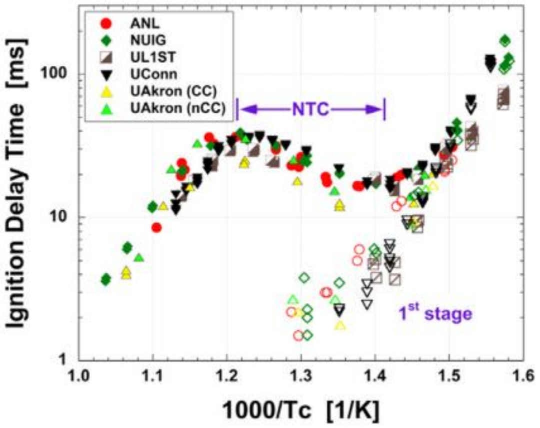

Figure 14 - Measurements from different RCM of ignition delay time as function of compressed temperature at p_C = 20 (±0.65) bar for isooctane (175).

In addition, interested readers can find additional works concerning the combustion of isooctane, including autoignition properties of isooctane at high-to-intermediate temperatures using STs in (180–186), species profile measurements using JSR in (187–189), premixed laminar flame speed in (190–197), ignition temperature using counterflow flames in (198,199), and finally thermochemistry and kinetics studies in (200–202). Table 7 introduces a list of the published works discussed above.

Table 7 - Synthesis of isooctane previous work and experimental conditions.

Reference	Type of study	Operational conditions

Fang et al., 2020 (167)	Oxidation Experimental study of autoignition	Rapid Compression Machine Numerical simulation	T: 600 - 900 K P: 15, 20, and 30 bar Φ: 0.7, 1.0, and 2.0
Wu et al., 2019 (174)	Validation of RCM facility: experimental study of autoignition and optimization of creviced piston design	Rapid Compression Machine Numerical simulation	T: 650 - 900 K P: 20 bar Φ: 1.0
Atef et al., 2017 (166)	Oxidation Experimental study of autoignition Thermochemistry and kinetic data calculations	Rapid Compression Machine Shock tube Numerical simulation	T: 632 - 1060 K P: 20.3 and 40.5 bar Φ: 0.4 and1.0
P. Zhang et al., 2016 (170)	Oxidation Experimental study of autoignition	Rapid Compression Machine Numerical simulation	T: 675 - 792 K P: 20 bar Φ: 1.0
Mittal et al., 2014 (171)	Experimental study of autoignition and crevice mass transfer	Rapid Compression Machine	T: 680–940 K P: 15.5 and 20.5 bar Φ: 1.0
Di et al., 2014 (169)	Study of the influence of buffer gas on the autoignition characteristics	Rapid Compression Machine Numerical simulation	T: 600 to 850 K P: 20 bar Φ: 1.0
Mehl et al., 2011 (162)	Pyrolysis, oxidation	Numerical simulation	T: 650 - 1200 K P: 3.0 – 50.7 bar Φ: 1.0
Mittal et al., 2008 (172)	Experimental study of autoignition and blending effect	Rapid Compression Machine	T: 740 -1060 K P: 15.0 – 45.0 bar Φ: 0.75
Walton et al., 2007 (203)	Experimental study of autoignition	Rapid Compression Machine	T: 868 - 1300 K P: 8.8 - 16.8 bar Φ: 0.20 - 1.98

Vanhove et al., 2006 (204)	Experimental study of autoignition and blending effect	Rapid Compression Machine	T: 900 - 650 K P: 12.6 – 16.1 bar Φ: 1.0
He et al., 2006 (205)	Experimental study of autoignition and OH time histories	Rapid Compression Machine Numerical simulation	T: 945 – 1020 K P: 8.6 – 15.2 bar Φ: 0.25 – 0.6
He et al., 2005 (176)	Experimental study of autoignition	Rapid Compression Machine Numerical simulation	T: 943 - 1027 K P: 5.2 – 23.3 bar Φ: 0.25 – 1.0
Curran et al., 2002 (150)	Pyrolysis, oxidation Experimental study of autoignition	Jet-stirred reactor Flow reactors Shock tube Motored engine Numerical simulation	T: 550 - 1700 K P: 1.0 – 45.6 bar Φ: 0.3 - 1.5
Minetti et al., 1996 (178)	Experimental study of autoignition	Rapid Compression Machine	T: 600 - 800 K P: 10.7 - 14.3 bar Φ: 1.0
Ribaucour, 1992 (177)	Experimental study of autoignition	Rapid Compression Machine	T: 650 - 850 K P: 11 - 16 bar. Φ: 0.5 - 1.2

2.2.2. Alkenes

Alkenes are present in conventional fuels as well as in alternative fuels; for example, gasoline is composed 15-20% olefins by volume (206). Due their higher octane sensitivities (OS) compared to alkanes of same carbon number, the unsaturated species are added to conventional fuels as gasoline to improve their octane ratings and allow engines to operate at higher compression ratios (130). They are also critical primary products of the combustion of most hydrocarbon fuels (7). Good knowledge of oxidation chemistry of alkenes is therefore essential to accurately model the reactivity of gasoline and biofuel surrogates, and furthermore the formation of primary pollutants in real engines.

The oxidation of alkanes has been largely studied in recent years as detailed in the previous section; in contrast, the modeling of the oxidation of branched alkenes at low temperatures has not received so much attention. To the author´s knowledge, 2-methyl-2-butene is the largest branched alkene with such a comprehensive model (207). Nevertheless, works concerning the combustion of linear alkenes can be found for ethylene (208–210), propene (211–213), 2-butene (142), 1-pentene (214–217), and 1-, 2-, 3-hexene (146,218,219).

The presence of a double bond in alkenes increases the potential number of elementary reactions involved in the global oxidation process, leading to a considerable increase in the number of species and reactions compared to saturated molecules. Indeed, the possibilities of radical addition to the double bond and the formation of radicals stabilized by resonance considerably complicate the chemistry. However, most of the reaction classes involved in the oxidation of alkanes remain calid for alkenes, as hydrogen abstraction, isomerization, the formation of cyclic ethers, β-scission, and oxygen additions. Thus, the kinetic models developed for alkenes are often derived from those of alkanes, the alkenes-specific pathways being added. Based on the work of Mehl et al. (146) and Tian et al. (130), a simplified reaction scheme for oxidation of alkenes, at low temperatures, is shown in Figure 15.

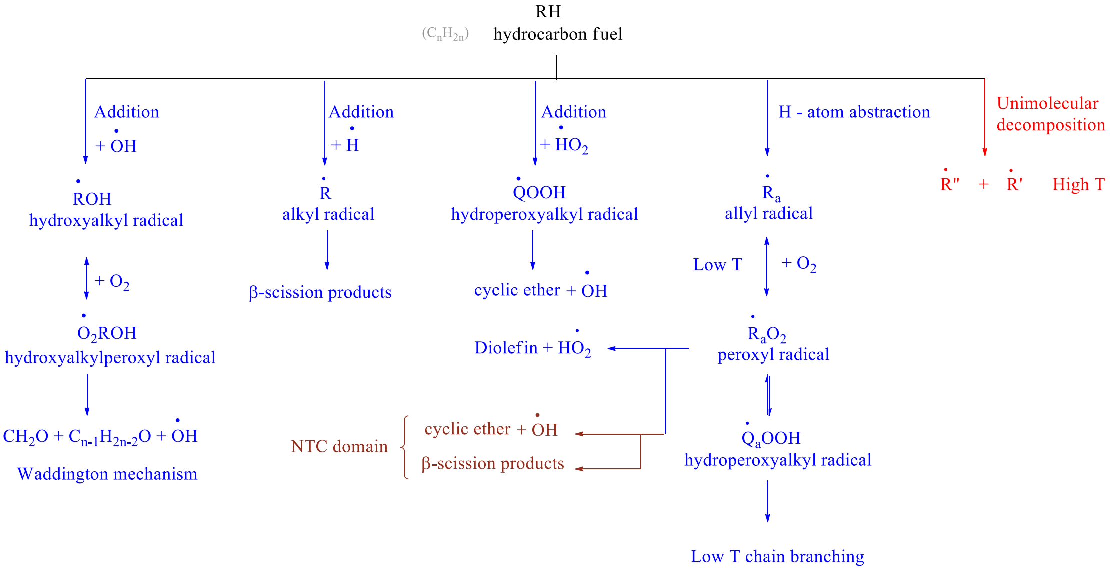

Figure 15 - Simplified reaction scheme for oxidation of alkenes.

Additional types of hydrogen atoms can be abstracted in alkenes, i.e. allylic and vinylic hydrogens, as illustrated in Figure 16 for the 2-methyl-2-butene (2M2B) molecule. The abstraction of allylic hydrogens, leads to the formation of a resonance-stabilized radical, therefore more stable radical than alkylic radicals. This stability is responsible for an inhibition of the subsequent reactions which lead to low temperature branching, and consequently slows down the overall reaction rate (7). Vinylic hydrogens, attached to the carbons that are part of the double bond, are less prone to H-abstraction than allylic hydrogens in the low- to intermediate-temperature regime because of the higher bond dissociation energy for vinylic C-H bonds. The further reactivity of alkylic hydrogens, located further away from the double bond, is also impacted by the presence of the double bond, because of the preferential reactivity on the allylic site during further H-abstraction or internal isomerization pathways.

Comparing alkenes to similar alkanes, the reactivity of unsaturated compounds is lower at low temperatures and higher at high temperatures (60). This can be roughly explained by the facility for these compounds to undergo unimolecular decompositions, forming alkyl radicals, at high temperature. At low temperatures, the stability of allylic radicals, which inhibits the low-temperature branching, decreases the overall reactivity and reduces the occurrence of cool flames and first-stage ignition. The position of the double bond in the alkyl chain plays a key role in the reactivity of alkenes. In general, it is inhibited as the double bond moves far away from the end of the alkyl chain (146). Meanwhile, at low temperatures, the reactivity of the fuel is increased along with the size of the saturated chain aside of the double bond (149), this case being most prone to alkane-like reactivity.

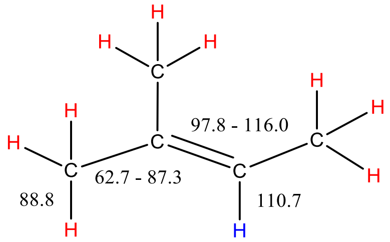

Figure 16 – Molecular structure and bond dissociation energies (kcal/mol) 2M2B, in detail allylic (red) and vinylic (blue) C-H bonds (220).

As mentioned before, the presence of the double bond enables the addition of radical $(\ddot{O}, \dot{H}, \dot{O}H, \dot{O}H_2, \dot{C}HO, \dot{C}H_3, \dot{C}_3H_5)$ to the double bond as described by the class (F), and shown in Figure 17, with the most important contributions originating from $(\dot{H}, \dot{O}H, H\dot{O}_2)$. The addition of hydroxyl radical to the fuel forms a hydroxyalkyl $(\dot{R}OH)$ radical which can undergo addition to oxygen and then decompose by Waddington mechanism (221), generating aldehydes or ketones and a hydroxyl radical. The further reactivity of the resultant $(O_2\dot{Q}OH)$ radicals has been suggested recently to be an important pathway in the description of the low-temperature reactivity of alkenes (222). $\dot{H}$ radical addition leads to the formation of an alkyl radical and subsequent β-scission decomposition products as small alkenes and alkyl radicals. Finally, the addition of hydroperoxyl radicals generates a hydroperoxyalkyl radical that can react further through the typical alkane LTC mechanism to form a cyclic ether and a hydroxyl radical, or undergo a second addition to O_2 as described in the case of alkanes. This pathway, in high-pressure conditions, results mostly in the formation of an oxirane and an OH radical.

Based on the brief review on the kinetic of oxidation of alkenes and also on 2-methyl-2-butene specific combustion works (126,150,207), the simplified reaction scheme for this molecule, at low temperatures, is shown in Figure 17 using the classes of reactions discussed previously.

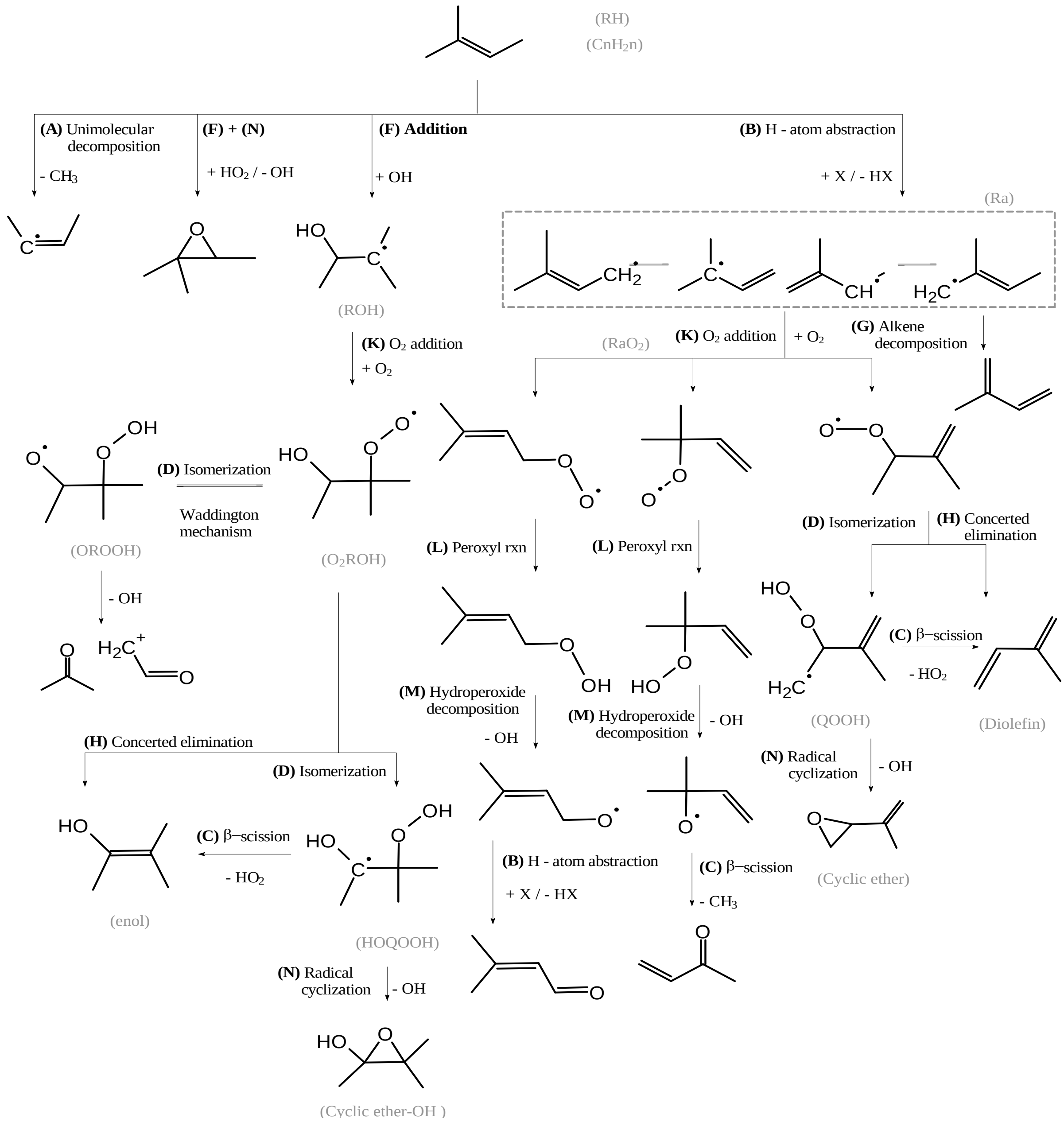

Figure 17- Example of potential routes for 2M2B oxidation.

2.2.2.1. 2-methyl-2-butene previous works

2-methyl-2-butene is a branched alkene and a promising fuel for Spark Ignition engines, due its values of RON and MON of 97.3 and 84.7 (207), respectively. These values lead to a strong octane sensitivity, as required in modern engines (11). Furthermore, its molecular structure with one vinylic and nine allylic C-H bonds, shown in Figure 16, make this molecule interesting from a kinetic point of view. Although this compound was not investigated in the current study, a review of previous studies concerning the combustion of 2M2B will be presented below to better understand the effect of the presence of the double bond, in a branched hydrocarbon, on the autoignition, and because of its structural similarity with prenol.

The most recent IDTs measurements of 2M2B were conducted by Song et al. (223) using the ULille RCM. The autoignition of stoichiometric methylbutene isomers/air mixtures was investigated in a range of temperatures from 700 to 890 K and compressed pressure of 15 and 20 bar and using Ar and N_2 as the diluent gas. It was found that the molecular fuel structure, i.e., the position of the double bond and thus the number of allylic C-H bonds, affects the IDTs and the presence of the NTC region. 2M2B, the species with the highest number of allylic C-H bonds, was the only of the studied methylbutene isomers to display single-stage ignition all along the investigated temperature range. The differences in the reactivity of the studied isomers were attributed to the different balance in the alkene-specific reaction pathways for all isomers. The low reactivity at low temperatures was associated with the reaction of allylic alkenyl radicals addition to O_2, which is not favored and therefore does not lead to chemical branching.

Westbrook et al. (207) developed a kinetic model to describe the oxidation of 2M2B. This model was validated using species mole fractions from JSR and IDTs measurements in a ST. Operational conditions applied in ST and JSR experiments are described in Table 8. It was found that at high temperatures 2M2B reacts in a similar way to alkanes. However, at low temperatures, the stability of allylic pentenyl radical inhibits the fuel reactivity. This stability is related to the radicals' inability to produce alkenylperoxy radicals that could lead to first-stage ignition. The absence of cool flame reactivity reported in this work, at studied conditions, is also consistent with Song´s results.

Furthermore, additional 2M2B previous works concerning premixed laminar flames can be found in (224–226) and species mole fraction profile measurements in non-premixed opposed flow diffusion flames in (227).

Table 8 - Synthesis of 2M2B previous work and experimental conditions.

Reference	Type of study		Operational conditions
Song et al., 2019 (223)	Oxidation Experimental study of autoignition	Rapid Compression Machine Numerical simulation	T: 700–890 K P: 15 and 20 bar Φ:1.0
Westbrook et al., 2015 (207)	Oxidation Experimental study of autoignition	Jet-stirred reactor Shock tube Numerical simulation	Jet-stirred reactor T: 600 - 1150 K P: 1.1 bar Φ:1.0 Shock Tube T: 1330 - 1730 K P: 1.7, 11.3, and 31.4 bar Φ: 0.5, 1.0 and 2.0

2.2.3. Aromatics

Since the elimination of lead tetraethyl in the early 1990s, and because of their high RON and low octane sensitivity, aromatic hydrocarbons have been widely used in automotive fuels. But the exceptional chemical stability which gives these species their properties of knock resistance also makes them as a source of emissions of aromatic unburnt hydrocarbons (228), although they seem to have an effect of reducing emissions of nitrogen oxides (NOx). It has been suggested that the addition of oxygenated aromatics (e.g., 2-phenyl-ethanol and anisole) can improve the trade-off between soot and NO$_x$ emissions (229).

Aromatics can also be formed from aliphatic compounds during combustion processes (230), especially in fuel-rich or diffusion flame conditions. Kinetic modeling of aromatic oxidation is, therefore, both important in the context of fuel formulation and emission reduction. A bibliographic summary of work on the oxidation of aromatics can be found in (231). Among the specific pathways relevant to aromatic reactivity, the formation of resonance-stabilized radicals should be noted, as in the case of the formation of the benzyl radical from toluene. Based on previous anisole kinetic modeling works, Figure 18 illustrates the potential routes for oxidation of anisole as well as the principal classes of reactions that governing this process. The kinetics governing the combustion of aromatics differ from those of alkanes and alkenes due to the presence of the benzene ring. The ring enables electrophilic ipso-substitutions by small radicals. This reactions class competes with H-atom abstraction on the ring or the side chain (231).

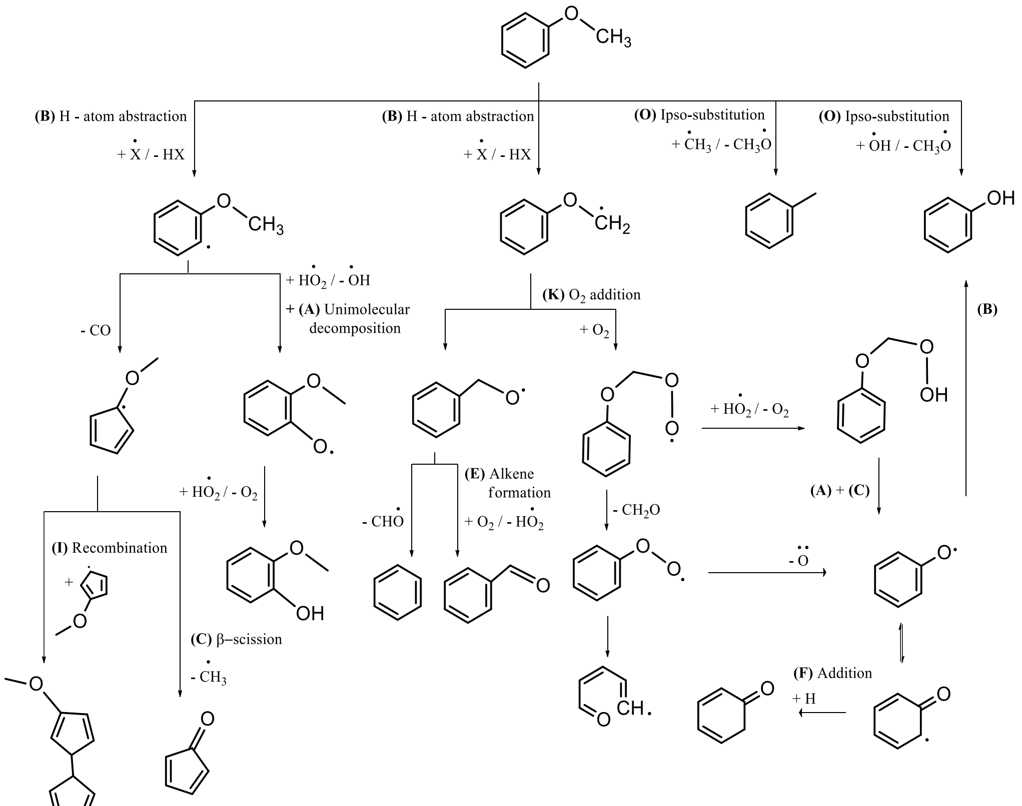

Figure 18 - Example of potential routes for anisole oxidation (232).

2.2.3.1. Anisole previous works

Among the aromatics obtained from lignin, anisole (methoxybenzene) was chosen as the starting point for the present study. In addition to the reasons set out in Section 1, it has been shown that anisole is a potential octane booster (130,230,233,234). This compound, unlike ethanol, also has an energy density compatible with commercial fuels.

The combustion properties of anisole have been widely studied due to its potential octane booster properties and interest as lignin pyrolysis and oxidation surrogate. It is an aromatic, which can be obtained from lignin, and due to its high-octane number (RON 103 and MON 92), it can be used as antiknock blending component in commercial fuels. There are however large uncertainties on the kinetic effects by which they alter the original fuel reactivity. Recent studies propose anisole detailed kinetic models which were validated at different conditions and thus they have different efficiency when they are used to simulate experimental results from different devices as Rapid Compression Machines, shock tubes or jet-stirred reactors. In contrast with previous works as in the work from Nowakowska et al. (115) in which the main reaction pathways of anisole oxidation at intermediate temperatures, lead to formation of benzoxyl radical and then to benzene and benzaldehyde formation, recent works proposed that the phenoxy and consequently cyclopentadienyl reaction pathways play a key role on the anisole oxidation, as described later.

In order to shed some light on the anisole pyrolysis and oxidation mechanism, Pelucchi et al. (235) have studied anisole pyrolysis in the flow reactor of Ghent University and proposed a kinetic mechanism of anisole pyrolysis and oxidation. This work also provides a comparison with anisole oxidation experimental data from Nowakowska et al. (236) using a jet-stirred-reactor, the ignition delay times of anisole/air mixtures measured by Shu et al. (237) and laminar flame speed measurements by Wagnon et al. (230). The anisole pyrolysis and oxidation mechanism proposed is a combination of the revised Baker-Hemings (238) model and CRECK kinetic scheme. It suggests that the thermal homolysis of C-O bond of methoxy group is the main route to decompose anisole, forming the phenoxy radical which is resonantly stabilized. Moreover, the formation of benzofuran through the combination of C_2 species and phenol is proposed and also dibenzofuran via phenoxy radical self-combination reactions. The experimental results from the Ghent flow reactor show a good agreement with the model with the exception of benzene which is overestimated by the model. The model shows a reasonable agreement with anisole oxidation experimental data from Nowakowska et al. (236). However, some deviations are observed in the experimental data from Shu et al. (237) associated with the experimental conditions. Finally, the model underestimates the laminar burning velocity, which could be related to phenol and cyclopentadiene sub-mechanisms, but also to phenoxy and cyclopentadienyl radical reactions.

A new detailed kinetic model for anisole was developed by Yuan et al. (239) and a flow reactor used to validate the model against experimental data. The model comprises of 432 species and 2563 reactions and it was developed revisiting previous models for aromatic fuels (230,236,240). In this work, the pyrolysis of anisole was studied at temperature from 850 K to 1160 K and at pressures 0.04 bar and at 1.0 bar and the speciation was performed using synchrotron vacuum ultraviolet photoionization mass spectrometry. In agreement with Pelucchi et al. (235), the authors also proposed that phenoxy and cyclopentadienyl radical reactions are particularly important to the anisole combustion model and they proposed improvements in this sub-mechanisms. Concerning phenoxy radical reactions, the main reactions are unimolecular decomposition of phenoxy radical forming cyclopentadienyl and recombination reactions forming cresol, phenol and dibenzofuran. Moreover, through hydrogen abstraction the anisyl radical can be formed producing the benzoxyl radical. The cyclopentadienyl reactions include recombination reaction with methyl radical forming methylcyclopentadiene and methylcyclopentadienyl radical. The unimolecular decomposition of cyclopentadienyl occurs through a hydrogen abstraction to produce fulvene and benzene. Lastly the recombination of cyclopentadienyl with ethyl radical, allyl radical and propargyl radical can also produce aromatic products. The last-mentioned reactions were revisited and the rate constants updated.

The validation of aforementioned detailed kinetic models at combustion conditions relevant to IC engines is strongly dependent on available experimental data. To the author´s knowledge, anisole ignition delay time measurements are limited to a few recent studies. Herzler et al. (241) studied the autoignition properties of aromatic LIF tracers anisole and 1,3,5-trimethylbenzene, in a shock tube at 10, 20 and 40 bar, at equivalence ratios of 0.5 and 1.0 and temperatures from 770 to 1600 K. The experimental results were compared against simulations using the kinetic models available in the literature, which showed good agreement in lean conditions using the Ranzi et al. (242) mechanism. At the same experimental conditions and using the Nowakowska et al. (236) mechanism, the ignition delay times are overpredicted. At stoichiometric conditions, the Nowakowska et al. (236) mechanism shows an acceptable agreement between experimental and simulated results at temperatures above 1250 K. This is also true, but at temperatures above 1100 K, for the Ranzi et al. (242) mechanism. Both mechanisms better predict the ignition delay times at lower pressures and are not able to reproduce the change of slope of the evolution of the ignition delays with temperature which is observed experimentally. This change of slope is however seen at the lowest temperatures, where the ignition delays become long in comparison with typical shock tube test times, and the possibility of interaction with the boundary layer increases.

With the same purpose of providing experimental data to validate an anisole detailed kinetic mechanism at engine-relevant conditions, Büttgen et al. (243) investigated the autoignition properties of different oxygenated aromatics using a Rapid Compression Machine. This study is also aimed at better understanding the substituent group effect on ignition delay times. In that regards, anisole, phenol, and their equivalent non-oxygenated aromatics, toluene and benzene were studied. Ignition delay times were measured and helped rank the reactivity, anisole being the most reactive followed by phenol, toluene, and benzene. The higher reactivity observed for anisole is explained by considering the weak C-O bond dissociation energy which allows the unimolecular decomposition and then lower activation energy for this bond scission when it is compared with the other aromatics studied. Moreover, H-atom abstractions from phenol and toluene lead to resonance-stabilized products, whose further reactivity is slow. These studies were conducted in stoichiometric conditions, at compressed pressures (p_C) of 10 and 20 bar and at temperatures (T_C) from 870 to 1100 K. The four molecules studied showed the characteristic Arrhenius behavior of aromatics (6), i.e., the reactivity of these compounds increases along with the increase of temperature leading to shorter ignition delay times. The ignition delay times were simulated using three detailed kinetic mechanisms: Nowakowska et al. (244), Wagnon et al. (230) and Pelucchi et al. (240). The model from Nowakowska et al. (244) shows the best agreement with experimental results even though the pressure dependence is not well reproduced. The ignition delay times are underpredicted when Wagnon et al. (230) and Pelucchi et al. (240) mechanisms are used. Besides that, the Pelucchi et al. (240) model can well reproduce the apparent activation energy, i.e. , the slope of the dependence of ignition delay times versus the inverse of T. The authors remarked that simulated ignition delay times from RCM showed different results using Wagnon et al. and Nowakowska et al. models even though both models were validated in similar conditions. Finally, Büttgen et al. (245) developed the most recent anisole kinetic model. This model was validated using RCM and ST IDT data, new IDTs measurements as well as available data from JSR and flow reactor, in a range of temperatures from 850 to 1315 K. The model is overall in good agreement with the experimental results; and at low temperatures, the results match with the previous simulation using the Nowakowska et al. (236) model and at high temperatures, the model shows better agreement with the model proposed by Wagon et al. (230). Table 9 introduces a summary of the published works.

Table 9 - Synthesis of anisole previous work and experimental conditions.

Reference	Type of study		Operational conditions
Büttgen et al., 2020 (245)	Oxidation Experimental study of autoignition	Rapid Compression Machine Numerical simulation	T: 870 – 1100 K P: 10, 20 and 40 bar Φ: 0.5, 1.0 and 2.0
Yuan et al., 2019 (239)	Pyrolysis	Flow reactor Numerical simulation	T: 850 - 1160K P: 0.04 - 1.0 bar
Büttgen et al., 2019 (243)	Oxidation Experimental study of autoignition	Rapid Compression Machine Numerical simulation	T: 870 – 1100 K P: 10 and 20 bar Φ: 1.0
Pelucchi et al., 2018 (235)	Pyrolysis, Oxidation	Flow reactor Numerical simulation	-
Herzler et al., 2017 (241)	Experimental study of autoignition	Shock Tube	T: 770 – 1600 K P: 10,20 and 40 bar Φ: 0.5 and 1.0

Wagnon et al., 2018 (230)	Pyrolysis, oxidation	Jet-stirred reactor Numerical simulation Laminar Burning Velocity	T: 675 – 1275 K P: 1.0 bar Φ: 0.5 – 2.0
Tian, 2016 (130)	Experimental study of autoignition	IQT - Ignition Quality Tester Spark ignition engine Volvo T5	T: 625 – 1000 K P: 10 bar
Nowakowska, 2014 (115)	Pyrolysis, oxidation	Jet-stirred reactor Numerical simulation	T: 673 – 1098 K P: 1.1 bar Φ: 1.0
Hemings, 2011 (238)	Pyrolysis, oxidation	Numerical simulation	-
Pecullan,1997 (246)	Pyrolysis, oxidation	Flow reactor Numerical simulation	T: 999 – 1003 K P: 1.0 bar Φ: 0.62 – 1.71

2.2.3.2. *O*-cresol previous works

Cresol is an aromatic that has three isomers: o-cresol, p-cresol and *m*-cresol. It can be obtained from biomass through a platinum catalysed hydrodeoxygenation of guaiacol (247). This last one is a substituted phenol present in the bio-oil which is derived from biomass fast pyrolysis (240). In addition, *o*-cresol is also produced by the MgO-based catalytic process of gas-phase alkylation of phenol with methanol (248). Due to its high expected RON value, characteristic of aromatics (249), it is a potential candidate to formulate fuels as an antiknock blendstock. The decomposition of many aromatics yield cresols, e.g., toluene can react with O-atoms, at low temperature, producing cresols or cresoxy radicals (250). Likewise, a recent study on low-temperature toluene and toluene-blends combustion model encourages the investigation of cresol combustion to better understand the antagonistic effect of toluene on more reactive components, inside a surrogate fuel (251). As mentioned in the anisole section, Nowakowsa et al. (115) studied the pyrolysis and the oxidation of anisole and reported the formation of cresol in the anisole oxidation and pyrolysis via reaction of phenoxy and methyl radical. This was first reported by Pecullan et al. (252), the proposed formation pathway being included in the modeling efforts by Nowakowska et al. Cavallotti et al. (253) also suggest the formation of *o*-cresol by ipso-substitution in the case of catechol and guaiacol:

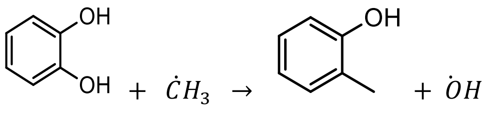

(41)

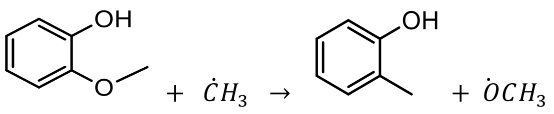

(42)

Concerning the global combustion parameters, a recent study performed by Zhang et al. (123), investigated the anti-knock tendency of six substituted phenols, including *o*-cresol, by simulating the ignition delay times of blends of these compounds in *n*-butane. The used mechanism has 1465 species and 27428 reactions and was built using the Reaction Mechanism Generator (RMG). Based on that, authors concluded that the order of increasing reactivity of the studied additives is 2,4-xylenol, *p*-cresol=*o*-cresol, *m*-cresol, 2-ethylphenol and guaiacol. *o*-Cresol being more volatile than 2,4-xylenol and *p*–cresol, it was judged a stronger potential fuel blendstock for SI engines.

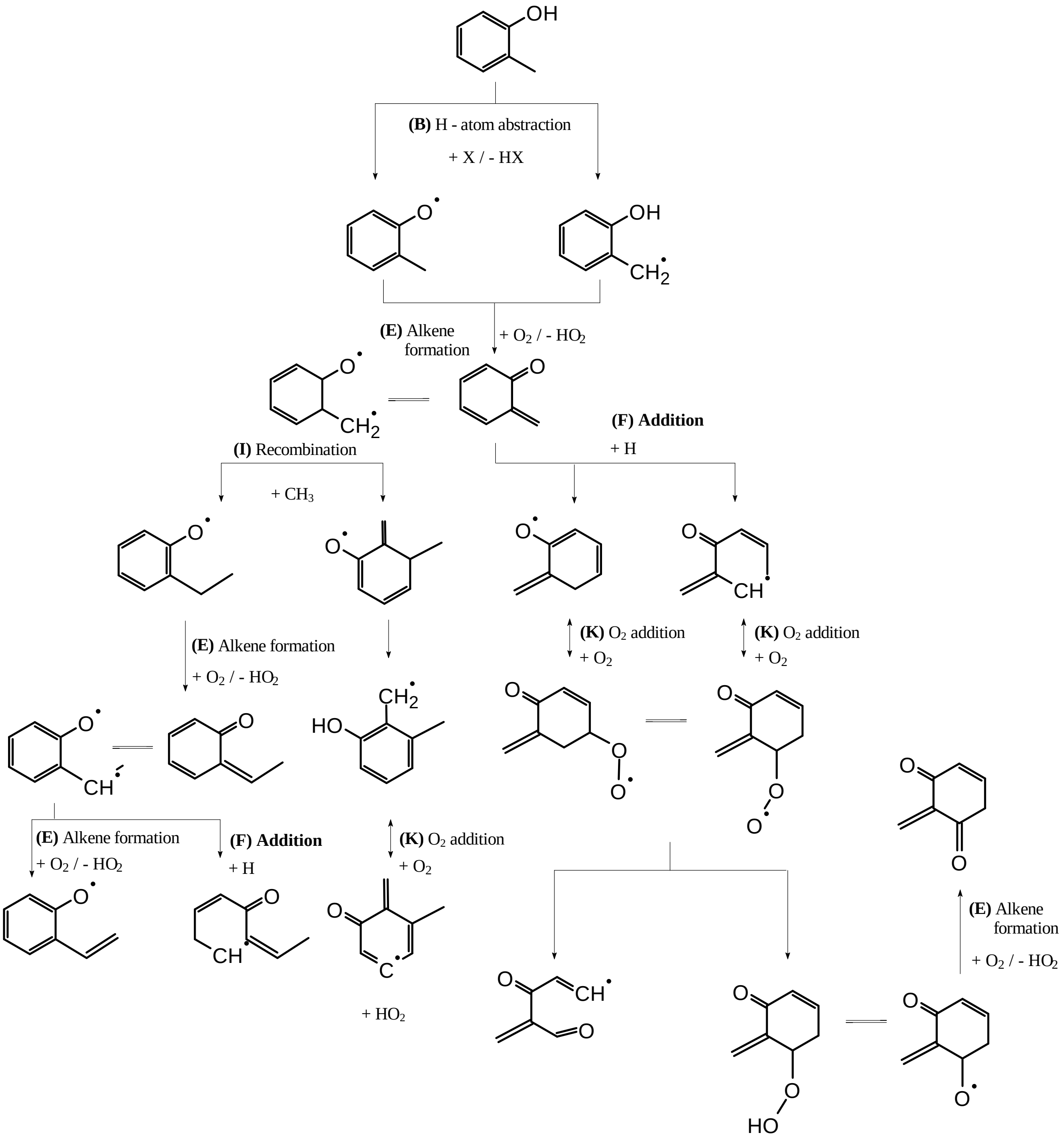

Figure 19 - Example of potential routes for o-cresol oxidation (123).

The effect of *o*-cresol as a diesel-like fuel additive was studied by Singaravelan et al. (254), three different *o*-cresol contents being added to diesel and tested in a Kirloskar AV1 four-stroke single cylinder diesel engine. In order to measure the engine performance, the brake specific fuel consumption and the brake thermal efficiency were measured in relation to brake power. The brake specific fuel consumption decreases with an increase of the *o*-cresol composition, except for the full-load condition. Concerning the emissions, a decrease of HC, NO_X and smoke emissions was also observed with the increase of additive. Problems related to corrosion and lack of solubility in hydrocarbons were however reported with o-cresol. They could however be adequately improved using low concentrations of additives.

The importance to atmospheric chemistry of *o*-cresol OH oxidation was reported by Schwantes et al. (255), special attention being dedicated to the low-volatility oxygenated products formed during this process. According to the authors, cresol can be produced from toluene after OH addition to the aromatic ring followed by O_2 addition and HO_2 elimination. To perform this study, *o*-cresol atmospheric simulation chamber experiments were conducted at low and high NO conditions, and chemical ionization mass spectrometry and offline direct analysis in real-time mass spectrometry were used to analyze the products in the gas and particle phase, respectively. The main products identified in this study are mono-, di- and trihydroxy-methyl-benzoquinones and di-, tri-, tetra- and pentahydroxy-toluenes. These last products are suggested as particularly relevant to secondary organic aerosol formation which contributes to an important amount of ambient tropospheric aerosol. Table 10 summarizes the relevant studies on *o*-cresol.

Table 10 - Synthesis of o-cresol previous work and experimental conditions.

Reference	**Type of study**		**Operational conditions**
Zhang et al., 2018 (123)	Blending ignition delay times	Numerical simulation	T: 650 – 1000 K P: 20 bar Φ: 1.0
Singaravelan et al., 2015 (254)	Engine performance Emissions such as NO_X, HC, CO and smoke	Experimental study in Kirloskar AV1 engine	-

2.2.4. Alcohols

As an alternative to fossil fuels, alcohols, and especially ethanol have been used around the world in the past decades (256). Different published studies point out that ethanol can cause a reduction of soot emissions in diesel engines, and an increase of the octane number in spark ignition engines (257). This effect is known to originate at least partly from the evaporative charge cooling effect, where the higher boiling point and heat of vaporization of ethanol cause a reduction in the temperature of the charge in the engine conditions

(258). Although this benefit in terms of resistance to knock is well-known, the use of alcohols can also promote the formation of hazardous species, such as aldehydes (259), which are expected to be converted by the three-way catalyst. Alcohols can be obtained from lignocellulosic biomass through the gasification process producing ethanol, from “syngas” or methanol (82). They can also be obtained from starches such as corn grains or sugar cane by fermentation processes, yielding ethanol, propanol and butanol (260). Lastly, a biochemical pathway has also been suggested to produce alcohols from algae (261).

The kinetics of combustion of ethanol have been widely studied (113,262–266). They proceed initially likewise alkanes through unimolecular decompositions (A) and H-atom abstractions (B). As for alkanes, at high temperatures, the role of atomic H is predominant whereas at low temperatures, $\dot{O}H$ and $H\dot{O}_2$ prevail (135).

Due to its weaker bond dissociation energy, the abstraction from the α carbon adjacent to the OH group is favored over the β-position and beyond (8). Comparing against analogue hydrocarbons, the H-atom abstraction in the β-position is more difficult than in the secondary carbon position of a hydrocarbon due to its higher bond energy dissociation, as shown in Figure 20. After addition to O_2, the resulting α radical can very easily yield a carbonyl and an $H\dot{O}_2$ radical, especially in the case of a terminal hydroxyl group (8).

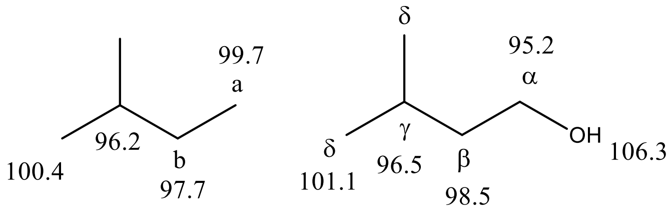

isopentane iso-pentanol

Figure 20 - Bond energy dissociation in kcal/mol; adapted – isopentane (267) *and iso-pentanol* (268,269).

Prenol will be used next to describe the potential oxidation pathways of unsaturated alcohols. Previous works concerning the combustion of prenol will be also summarized.

2.2.4.1. Prenol previous works

Prenol (3-methyl-2-buten-1-ol) is an unsaturated alcohol that belongs to the isoprenoids family and can be synthetized industrially by the chemical interaction between isobutene and formaldehyde and subsequent catalytic isomerization of isoprene (270). It is also possible to produce prenol from renewable sugar, using a microbial fermentation process with Escherichia coli with a yield of around 12% (271,272). The boiling point of prenol is 140°C, making it a good candidate to formulate gasoline-like fuels (233,273). In addition, it is miscible with most common organic solvents (274). This C_5 alcohol is commonly used as flavoring ingredient or in the perfume industry and has low toxicity (275). Its autoignition temperature, lower flammability limit, and flashpoint are higher than gasoline and therefore, it has a good storage quality and transportation stability (124). The lower heating value of prenol is 34.04 MJ/kg which is around 24 % higher than ethanol (276), therefore leading to potential fuel economy.

In the case of alkanes, the decomposition of the initial radical can produce another radical and an alkene. However, in the case of alcohols, an enol or a carbonyl can be produced. At low temperatures, after $\mathrm{O_2}$ addition at the α position, internal $\dot{\mathrm{H}}$ atom transfer from $\dot{\mathrm{O}}\mathrm{H}$ to the peroxy group can form an aldehyde and $H\dot{O}_2$ radical, as showed in the follow reaction for the prenol case:

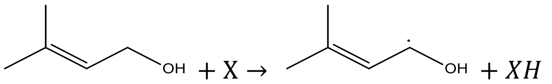

(43)

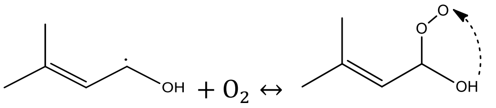

(44)

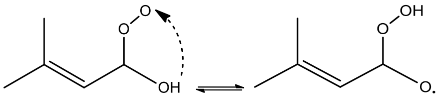

(45)

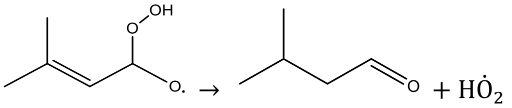

(46)

In a recent study, Monroe et al. (12) demonstrated an octane hyperboosting effect of prenol on different gasoline surrogates. This corresponds to the mixture presenting higher values of RON than the pure components in the mixture. Furthermore, compounds with similar structure as 2-methyl-1-butanol, 3-methyl-1-butanol, 3-methyl-3-buten-1-ol and 2-methyl-3- buten-2-ol were also evaluated. Despite of structural similarities, with exception of prenol, none of these compounds presented similar octane hyperboosting effect. This could therefore result from a synergistic effect of both hydroxyl and alkenyl functional groups on the resistance to pre-ignition. These results strongly encourage the investigation on the kinetics of combustion of prenol.

Ninnemann et al. (124) measured the ignition delay times and carbon monoxide time-histories during the ignition delay, as well as the laminar burning velocities of prenol. The ignition delay times were measured using a heated shock tube at temperatures from 1269 K to 1472 K, at pressure near 9.4 atm and with a mixture composition of 0.05% fuel/0.35% O2/99.6% Ar. A constant-volume spherical chamber was used to perform laminar burning velocity measurements at an initial temperature of 428 K, atmospheric pressure and an equivalence ratio from 0.75 to 1.50. The authors found that the maximum laminar burning velocity of prenol corresponds to slightly lean conditions and is equal to 0.72 m/s. A comparison with LBV of ethanol at the same conditions was also performed and showed that in lean conditions ethanol and prenol present similar LBV, while the maximum LBV of ethanol (0.82 m/s) corresponds to an equivalence ration of 1.1.

De Bruycker et al. (277) investigated the reactivity of prenol and isoprenol experimentally and numerically. An isothermal jet-stirred quartz reactor was used to study the pyrolysis and oxidation of the unsaturated alcohols at temperatures from 500 to 1100 K, a pressure of 0.107 MPa, and a residence time of 2 s. The oxidation experiments were performed at equivalence ratios 0.5 and 1.0. The formed intermediate products were identified and quantified using gas-chromatographic techniques and a kinetic model was developed using the Genesys mechanism generator (278). The isobutene oxidation mechanism developed by Zhou et al. (222) was used as a submechanism for the oxidation of small species such as hydrogen, methane, ethane, propene, methanol, ethanol and acetaldehyde. Thermodynamic data for prenol, isoprenol, their radicals and related peroxy species was calculated using the CBS-QB3 level of theory. It was found that prenol and isoprenol have completely different oxidation pathways even though the only difference between these two species is the position of the double bond. While prenol reacts predominantly by initial H-abstraction and addition, isoprenol forms formaldehyde and isobutene by unimolecular decomposition. At the investigated conditions no NTC behaviour was observed for prenol oxidation. The reactivity of enols was also investigated by Taatjes et al. (279). However, in this case the double bond is adjacent to hydroxyl group. It was found that these compounds can isomerize to form aldehydes. To the author's knowledge no previous studies in the literature are available concerning the co-oxidation of prenol by alkanes. The available works about prenol are listed in Table 11 below.

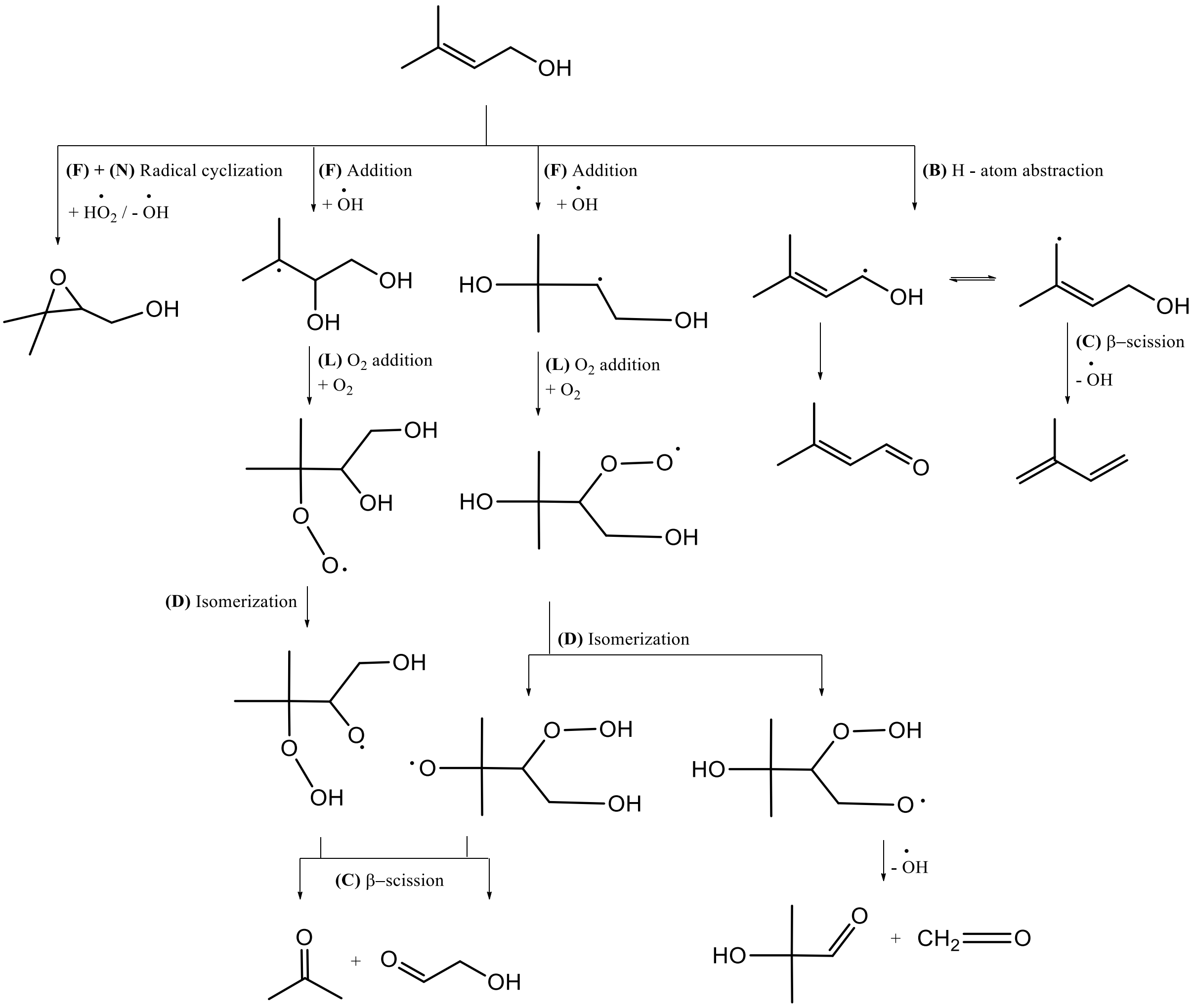

Figure 21 – Example of potential routes for prenol oxidation.

Table 11 - Synthesis of prenol previous work and experimental conditions.

Reference	**Type of study**		**Operational conditions**
Ninnemann et al., 2019 (124)	Carbon monoxide time-histories, ignition delay times, and laminar burning velocity	Constant-volume spherical combustion chamber, shock tube	T: 1269 – 472 K P: 9.5 bar 0.05% fuel/0.35% O_2/99.6% Ar
Monroe et al., 2019 (12)	Octane rating (RON and MON)	ASTM D2699 and ASTM D2700	-
De Bruycker et al., 2016 (277)	Pyrolysis and oxidation	Isothermal jet stirred quartz reactor	T: 500 to 1100 K P: 1.1 bar Φ: 0.5, 1.0 and ∞

2.2.5. Ketones

Characterized by the presence of a carbonyl group on the molecule, ketones have not received so much attention as other oxygenated fuels like alcohols. The exception is acetone, the smallest ketone, that had its combustion properties investigated since the early 1960s (280). Ketones are intermediate and final products in most of hydrocarbon combustion process (281), and several research groups investigated these type of oxygenated molecules in the context of their use as fluorescent tracers for fuel-concentrated visualization in laser diagnostic techniques (282). Besides that, ketone fuels are, in general, strongly knock resistant (283–285), and have potential to reduces the soot production by the presence of the carbonyl group on the carbon chain, inside a fuel mixture (286,287), which has recently raised interest.

The kinetics of ketone oxidation follows the same rules discussed before for other chemical families, with a special similarity to alcohol mechanisms. A detailed description of such classes of reactions is given by Burke et al. (284) in the case of butanone oxidation. The authors indicated that at high temperatures the major oxidation pathways are fuel unimolecular decomposition, H-atom abstraction from the fuel and β-scission decompositions. The low temperature mechanism was based on the work of Curran et al. (288), in which 20 reaction classes from the original model were considered, and the reaction between the fuel (RH) and the peroxyl radical $(\dot{R}O_2)$, forming alkyl hydroperoxide $(ROOH)$ was added.

Most recent, Fenard et al. (285) proposed a detailed kinetic model for the oxidation of pentanone isomers. In this work, important new classes of reactions were added, such as bimolecular decomposition reactions, by adding oxygen to the fuel, at high temperature; and at low temperatures, the primary radical oxidation class, forming alkenes and the hydroperoxyl radical. The main classes of reactions governing the combustion of cyclic ketones are exemplified in Figure 22 for cyclopentanone, as well as the potential routes of its oxidation.

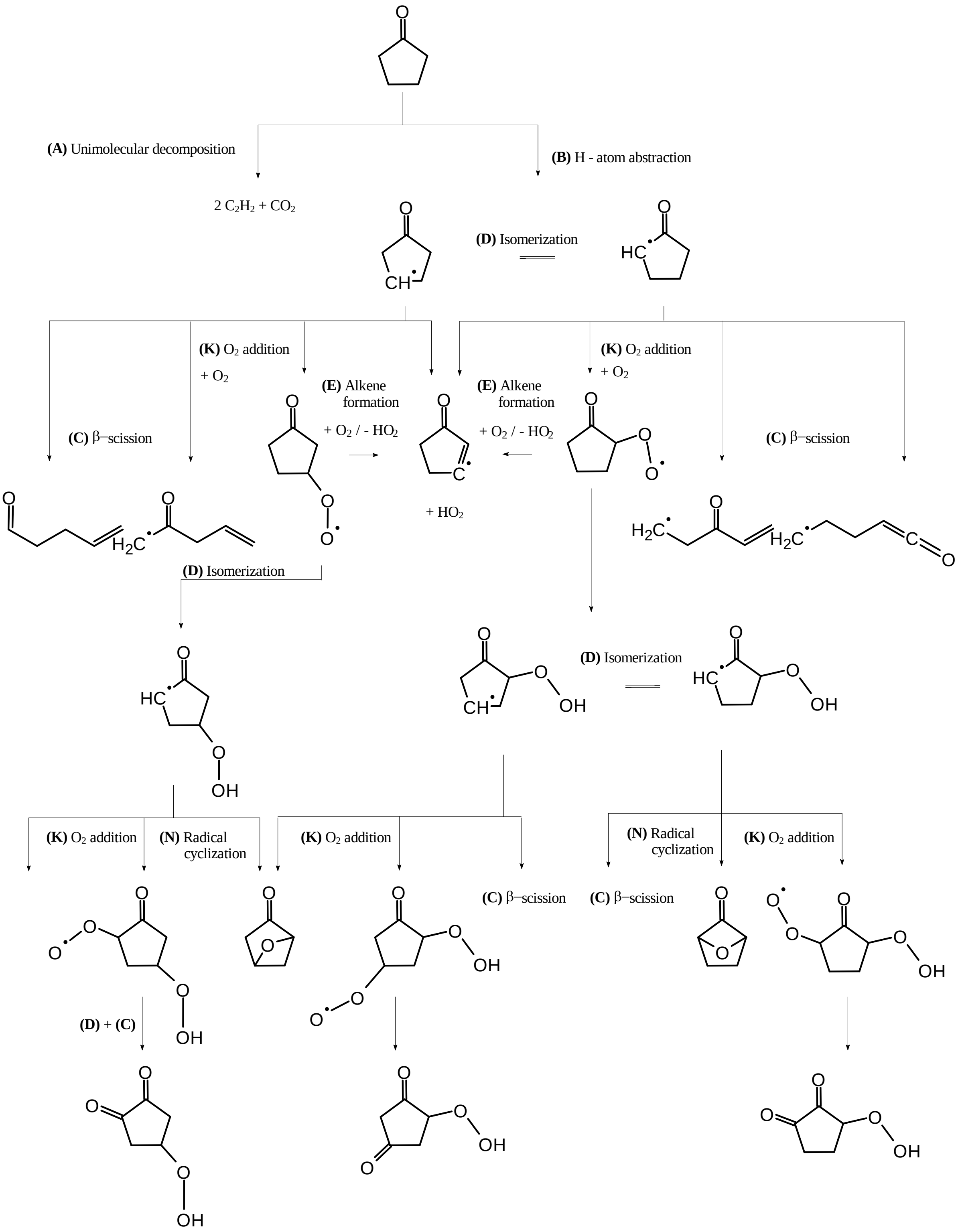

Figure 22 – Example of potential routes for cyclopentanone oxidation adapted from (289).

Small hydrocarbons can be produced, at high temperatures, by H-atom abstraction or unimolecular decomposition. The unimolecular decomposition of cyclopentanone leads to the formation of smaller olefins such as ethylene, and CO_2 (290,291). Meanwhile, H-atom abstraction from aldehydes and ketones is facilitated by the presence of oxygen and the preferential pathway is the abstraction at the α position due the weakest C-H bond, shown in Figure 23.

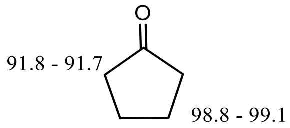

Figure 23 – Molecular structure and C-H bond dissociation energies (kcal/mol) of cyclopentanone (290).

In the case of cyclopentanone, the formation of radicals at the β position has however been reported as the preferential route for hydrogen abstraction (289), forming 3-oxo-cyclopentyl. This radical can undergo a ring opening forming an unsaturated aldehyde or ketone, or it can react via O_2 addition. This radical can undergo a ring opening forming an unsaturated aldehyde or ketone, or it can react via O_2 addition.

Even though, reactions such as isomerization of fuel peroxyl radicals to hydroperoxyalkyl radicals have been proved to have an important contribution to the reactivity of ketones, the competition from other reactions such as the formation of cyclic ethers or olefins and hydroperoxyl radicals or, the decomposition of hydroperoxyl alkyl radicals via β-scission reactions inhibits the low temperature reactivity. Besides that, the reaction of radicals stabilized by resonance on molecular oxygen are not favored, which also contributes to inhibit the reactivity at this condition. Furthermore, the formation of 2-cyclopentenone has been reported as important pathways for α fuel radical consumption (289,290).

2.2.5.1. Cyclopentanone previous works

Cyclopentanone is a cyclic ketone largely used to produce fragrances, drugs, pesticides, rubber and other chemicals (292,293). However, its use as a potential fuel or additive has not been extensively investigated. It can be obtained by lignocellulose hydrodeoxygenation over Ni-base catalysts (294). This process has been demonstrated on an industrial scale by selective catalytic conversion of furfural with a good yield of 84%, using agriculture waste and forest residues as primary sources (295,296). Moreover, the production of cyclopentanone can also be achieved through biomass pyrolysis (297), the thermal decomposition of nylon 66 (298) or by breaking down of cellulose by fungi in a biochemical route (299). Due its high density of 0.866 g mL^{-1} and the net heat of combustion of 42.6 MJ kg^{-1} - 37.0MJL^{-1} it can be used as a fuel or as additive to bio-jet fuels (296). This cyclic ketone has RON and MON values of 101 and 89 (300), respectively and thus a high value of S, make it interesting as a SI engine fuel and blendstocks (301).

Thion et al. (290) developed a kinetic model for cyclopentanone in which theoretical calculations and experimental measurements were performed. The model was validated using species profile data from JSR at equivalence ratio of 0.5, 1.0 and 2.0, at temperatures from 730 to 1280 K and at pressures of 1 and 10 atm. It was based on the previous works concerning butenes (302) and 2-butanone (303). The model was overall able to predict the experimental results. However, some discrepancies were observed in mole fraction simulations of 1,3-butadiene and acetylene, which are underestimated. Besides that, ethylene showed high concentrations in all studied equivalence ratios, being mostly formed by fuel unimolecular decompositions at high temperatures, as discussed before.

Zhang et al. (289) recently measured cyclopentanone IDTs in a range of temperature from 794 to 1368 K, and at compressed pressure from 15 to 30 bar, using a high-pressure shock tube and a Rapid Compression Machine. In the studied conditions, no two-stage ignition was observed in the RCM experiments. The CO-time histories were measured using the shock tube, and the reaction rates for the olefin + $H\dot{O}_2$ elimination reactions, from cyclopentanone peroxyl radicals, were also calculated. A detailed kinetic model based on the *n*-heptane mechanism (304) was proposed for cyclopentanone and it was validated using the experimental data provided in this work. The developed model showed a considerable improvement in comparison to the Thion et al. (290) model for the prediction of IDTs, especially at 6 atm and stoichiometric conditions.

Furthermore, additional works considering reaction rate calculations (291,305–307) and laminar flame characteristics (308), also contribute to the better understanding of the kinetics of cyclopentanone oxidation. The most relevant previous studies to this work concerning the oxidation of cyclopentanone are summarized in Table 12.

Table 12 - Synthesis of cyclopentanone previous work and experimental conditions.

Reference	**Type of study**		**Operational conditions**
Zhang et al., 2019 (289)	Oxidation Ignition delay times detailed Kinetic model Reaction rate calculation	Rapid Compression Machine Shock tube Numerical simulation	T: 794 – 1368 K P: 15 – 30 bar Φ: 0.5, 1.0, 2.0
Thion et al., 2017 (290)	Oxidation Mole fraction profiles Reaction rate calculation Kinetic modeling	Jet-Stirred Reactor	T: 730−1280 K P: 1 and 10 bar Φ: 0.5, 1.0, 2.0

2.2.6. Combustion of gasoline surrogates – co-oxidation

In order to build a reaction mechanism for a surrogate fuel, it is necessary to include the sub-mechanisms of several hydrocarbon families, as discussed before. During the simultaneous oxidation of various hydrocarbons, some interaction may appear; therefore, their behavior differs from that they would show separately, thus mixture studies must be part of the validation base of the mechanisms. There are two possible theories related to the interaction between different compounds during the oxidation of mixtures (7). The first theory proposes that said interaction is limited to the effects derived from sharing the same radical pool (309), while the second one defends the existence of cross reactions with significant effects on the reactivity of the mixture (310). Various research works have considered cross reactions between different compounds and their intermediates, reaching different conclusions depending on the type of species present in the mixture. Although, such cross reactions are often neglected in alkane mixtures, and mildly important in mixtures containing alkenes and/or aromatics (7).

Therefore, due to the importance of modeling the autoignition process, mechanisms have been developed for mixtures of hydrocarbons, known as reference fuels, which have in turn motivated the study of co-oxidation reactions in alkane mixtures. The most studied gasoline surrogate fuels were the Primary Reference Fuels (PRF), i.e binary blends of isooctane *n*-heptane used to represent a variable octane number fuel. Ternary mixtures as isooctane, *n*-heptane and toluene have also been proposed to study the effect of fuel composition on combustion properties such as emissions, but also to represent fuels with various octane number sensitivities (9). Studies of mixtures including bio-derived components have been limited mostly to ethanol/gasoline mixtures (117). However a recent work showed the potential of cyclopentanone to improve the oxidation of alkenes inside a mixture (311).

The first work concerning the co-oxidation of hydrocarbon fuels was performed by Ray et al. in 1971. Several alkenes and 1,3-butadiene have been investigated inside mixtures with acetaldehyde in a flow reactor at 357 K. The species formed during the combustion were analyzed by gas chromatography analysis and mass spectrometry. The evidence of cross reactions is confirmed by the adduct formed by the acetaldehyde in the presence of alkenes, which lead to the formation of epoxides.

Mixtures of aromatic and alkanes are also considered in surrogate fuels studies due the remarkable presence of aromatics in commercial fuels and their essential role in soot formation. When analyzing mixtures of alkanes with aromatics, Davidson et al. (182) and Naik et al. (312) considered dehydrogenation reactions of toluene with alkyl and peroxyalkyl radicals. It was found that the importance of these reactions is more significant than in the case of interaction between alkanes and may explain the formation of some experimentally detected reaction intermediates (204).

Furthermore, a recent work identified ten promising Bio-Blendstocks for spark ignition engines (300). This study was realized under the Co-Optima project which reveals biomass derived fuels with potential to improve efficiency in currently available engines, the challenge in their production and commercialization, their potential to reduce emissions and the needs in future research. Cyclopentanone and prenol, two of the lignocellulosic derived fuels studied in the current work, were considered by the authors to have a strong potential to be used as blendstocks, especially due their synergetic blending for octane and octane sensitivity.

Finally, a recent extensive review of the chemical kinetic modeling of gasoline surrogate fuel combustion can be found in (234). The results given in this work are consistent with other recent works (12,313–315), which observed that most studies of kinetic modeling of biofuels had been carried out for pure components. Consequently, systematic studies on multiple component biofuel blends are needed to develop new alternative fuels, reaffirming the importance of the current work.

3. Experimental Facility & Methods

In this chapter, the experimental facility and the methodologies employed in this work are presented. These include the experimental devices used to study the autoignition propensity of the lignocellulosic biomass derived compounds, as well as the sampling and the analysis system. Finally, the numerical approach used to simulate the experimental data is discussed.

Introduction

The previous Chapters have discussed the importance of precisely characterizing the performance and the emissions resulting from the usage of novel fuels, in order to facilitate their implementation. This can be done through kinetic models; which together with CFD simulations can lead to reduce the impact of practical combustion engines. Kinetic models are constructed by knowing the molecular structure of the fuel and suggesting relevant reaction pathways, and validated using experimental data from different devices. Figure 24 summarizes the most commonly used devices and their operating regimes.

Regardless of the interest of such facilities, which are designed to simulate realistic combustion environments, the interpretation of the data obtained in these experimental devices is often complex, due to potential fluid mechanics-chemistry interactions and their effects on the observed phenomena (316). Therefore, the choice of the apparatus to be used to this aim stems from the need for ensuring feasibility and controlling the combustion environment over a wide range of experimental conditions.

Speciation data is commonly provided by flow and jet-stirred reactors; these continuous reactors enable physical sampling and due to the well-controlled mixing and dilution conditions inside the combustion chamber, gradients of temperature, pressure and species concentration can be neglected. However, only diluted conditions are reachable using jet-stirred reactors, while non-diluted conditions and ignition delay measurements can also be performed in plug-flow reactors.

Shock Tubes (STs) and Rapid Compression Machines (RCMs) are transient single-shot reactors, commonly used to measure Ignition Delay Times (IDTs). Shock tubes are used to investigate very short reaction times by using the compressive heating of a shock wave to provide the suitable compressed, high temperature conditions. On the other hand, the operating principle of modern RCMs is based on a fast compression of the reactive mixture, using a piston that is blocked at the end of stroke, thus maintaining the volume constant. The first RCM was built in 1906 and was initially used to measure minimum ignition temperatures, considering an instantaneous autoignition (317). However, the existence of an ignition delay between the end of compression and the onset of autoignition was observed for the first time by Dixon (318).

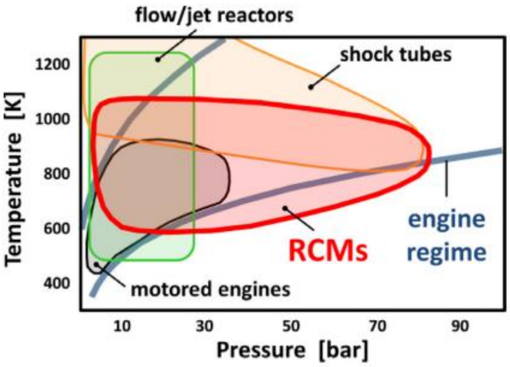

Figure 24 - Experimental devices typical used in the combustion kinetic studies and their operational conditions (175).

Currently, there are more than 20 laboratories around the world using RCMs to study gaseous phase autoignition, relevant to technologies such as homogeneous charge compression ignition (HCCI) and spark-assisted compression ignition (SACI). Table 13 shows a selection of different laboratories in the world which use RCMs, and studies in which the detailed characteristics of each machine can be found. A more extensive review of existing RCMs for kinetic studies is provided in Goldsborough et al. (175).

Table 13 - Different laboratories around the world using an RCM.

Facility	P_{max} (kPa)	T_{max} (K)	Compression Time (ms)	Reference
Université de Lille	3000	1000	20 - 80	(319)
Argonne National Laboratory	2100	Not specified	< 20	(320)
University of Michigan	> 2000	2000	~ 100	(321)
Colorado State University	5000	Not specified	~ 20	(322)
University of Akron	10000	Not specified	30	(323,324)
M.I.T.	7000	1200	10 - 30	(325)
UCONN – University of Connecticut	11000	Not specified	10 - 40	(326)
National University of Ireland, Galway	4000	1060	< 22	(327)
Leeds University	2000	1000	22	(328)
University of Sheffield	2200	Not specified	25 - 35	(329)
Institut Pprime – Institut de recherche de Poitiers	4000	Not specified	29	(330)
PRISME	Not specified	Not specified	35	(331)
DNV KEMA Energy & SustainabilitY	5000	1100	20	(332,333)
RWTH Aachen	10000	1000	Not specified	(334)

KAUST	4000	1200	< 22	(335)
PUC-Rio – Catholic University of Rio de Janeiro	Not specified	Not specified	Not specified	(336)
Keio University	3000	Not specified	200	(337)

The University of Lille Rapid Compression Machine (ULille RCM) was used in the current work and its operating set-up and specific features will be discussed further. Figure 25 summarizes the present chapter and illustrates the approach used in order to present a benchmark of potential new biofuels and/or additives to SI engines, as well as provide useful kinetic discussions on the co-oxidation of these compounds along with conventional fuels.

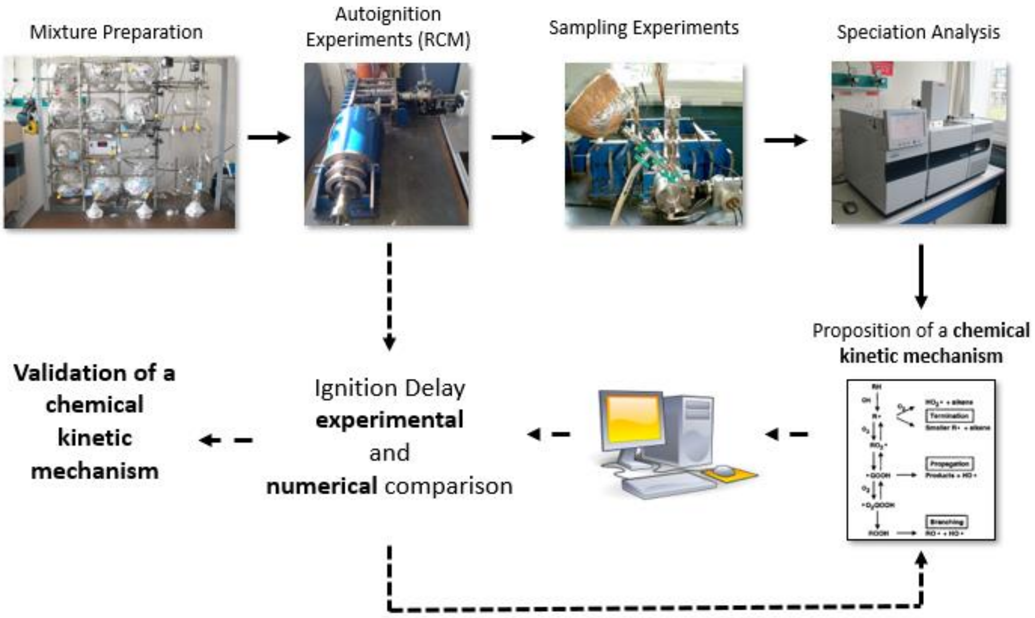

Figure 25 - Diagram of the process used for the development/validation of kinetic mechanisms using experimental RCM data.

The IDTs of mixtures of isooctane/LDC/O_2/inert were measured using the ULille RCM in stoichiometric fuel-in-air conditions. The influence of three parameters on the IDTs were evaluated: the mixture composition, compressed pressure and temperature. The LDC blending effect was investigated by varying its amount into the surrogate. For each different composition the compressed pressure was also varied allowing the definition of an ignition range. After these preliminary results, the surrogates were formulated at stoichiometric condition and prepared until the LDC fraction reached the maximum allowed value within the mixture preparation bench, with regards to their vaporization properties. This choice reflects the constraints in volatility of potential biofuels, since LDCs with too high a boiling point cannot be incorporated in SI fuels with a high content. Table 14 summarizes the work done for each studied surrogate.

Table 14 - Project plan by fuel.

	Isooctane	Isooctane/ anisole	Isooctane/ o-cresol	Isooctane/ prenol	Isooctane/ cyclopentanone
RCM experiments	✓	✓	✓	✓	✓
Sampling experiments	literature	✓	X	X	✓
Chemical kinetic modeling	literature	development / validation	X	testing	testing

In the following sections, the mixture preparation, IDT measurement, sampling experiments, speciation analysis, analysis of the experimental uncertainties and the numerical approach used to simulate the experimental data are described in detail.

3.1. Mixture preparation

The gas mixtures tested in the RCM were prepared using the partial pressure method. Two experimental benches were used: one operates at room temperature while the second is heated. The unheated dilution bench, presented in Figure 26, includes 10 Pyrex bulbs of 10L and 3 of 15L, all externally coated with aluminium paper, to avoid the decomposition of photosensitive compounds; two MKS Baratron pressure gauges, model 627D12TDC1B (0 - 100 torr) and model 627D13TDC1B (0 -1000 torr); and a vacuum pump. A glass flask is filled with the liquid hydrocarbon, which is introduced into the bench by evaporation. Before that, each liquid compound is purified from potential dissolved gases with three freezing/pumping cycles using liquid nitrogen. The hydrocarbons with the lowest vapor pressure are introduced first, then oxygen and finally inert gases. The mixtures prepared using the unheated dilution bench are prepared 24 hours before being used to ensure their homogeneity.

Figure 26 - Gas mixture preparation bench (unheated). 1: 0-100 torr pressure gauge, 2: 0-1000 torr pressure gauge, 3: pressure reader, 4: vacuum pump access valve, 5: 15 L balloon, 6: 10 L balloon, 6: product introduction valve, 7: RCM access valve.

The second bench, illustrated in Figure 27, is a dilution bench composed by 3 Pyrex balloons of 15L, placed in a thermostatically controlled environment, in order to avoid condensation of mixtures with low vapor pressures. This was described in detail before (231) and the elements of this device will be briefly discussed here. The temperature can vary from 50 °C to 90 °C and is measured by a K type thermocouple placed on the bulb wall. A PID regulator controls the temperature and a thin resistor (1000 W) is placed under a fan that allows homogeneous heat distribution inside the bench. The connection between this bench and the RCM is ensured by a heated gas line. Two MKS Baratron type 628 F gauges (0-100 Torr and 0-1000 Torr), heated to 100°C, measure the pressure. Liquid hydrocarbons are also introduced using glass flasks using the procedure described above.

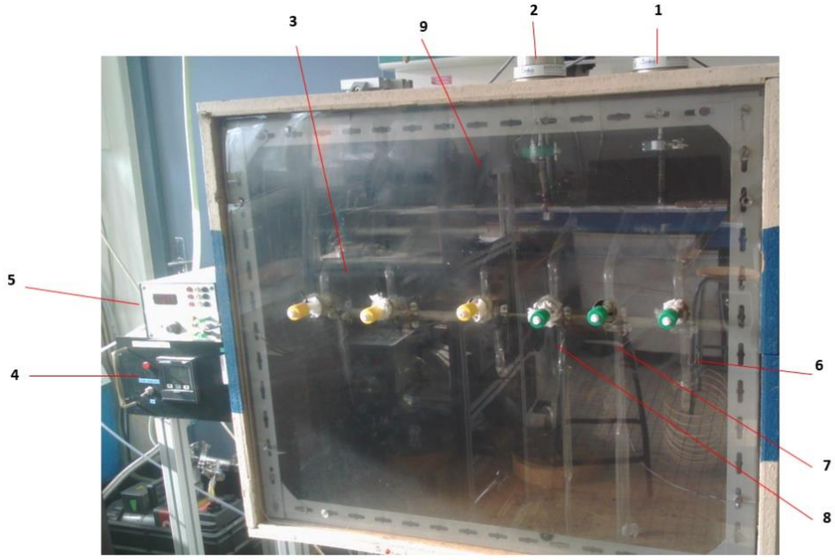

Figure 27 - Thermostatic gas mixture preparation bench. 1: 0-100 torr pressure gauge, 2: 0-1000 torr pressure gauge, 3: 15 L balloon, 4: temperature reader, 5: pressure reader, 6: gas bulb/preheater, 7: vacuum pump, 8: external gases, 9: fan.

After mixture preparation, a homogenization time is needed before introducing it into the RCM. If the mixture is kept for too long in the heated bench with an elevated temperature, fuel conversion can also take place and must be prevented. The studied fuels have different physical-chemistry properties, as diffusivity and vapor pressure, thus the homogenization tests were performed for each studied fuel. These tests consist of varying the homogenization time and then analysing the gas mixture using gas chromatography and mass spectrometry techniques, and also measuring IDTs. The comparison between the calculated and the theoretical mole fractions of the hydrocarbons provides information about the effect of the time on the fuel conversion and mixture homogenization. A time of one hour was observed as the minimum homogenization time for all investigated fuels, i.e., no considerable fuel conversion was observed in any of the cases, yet the IDTs were found to be reproducible.

Figure 28 and Figure 29 show the pressure profiles and the chromatograms respectively, of the aforementioned test using isooctane/cyclopentanone 60/40 /O_2/N_2 mixture. It was prepared two times using the homogenization time of one hour for mixture 1 and two hours for mixture 2. The highest observed difference in IDT was 3 ms. Moreover, the quantified mole fractions of both mixtures are found in Table 15, and it shows a maximum difference of 0.1 % in the conversion between mixture 1 and 2 for both isooctane and cyclopentanone.

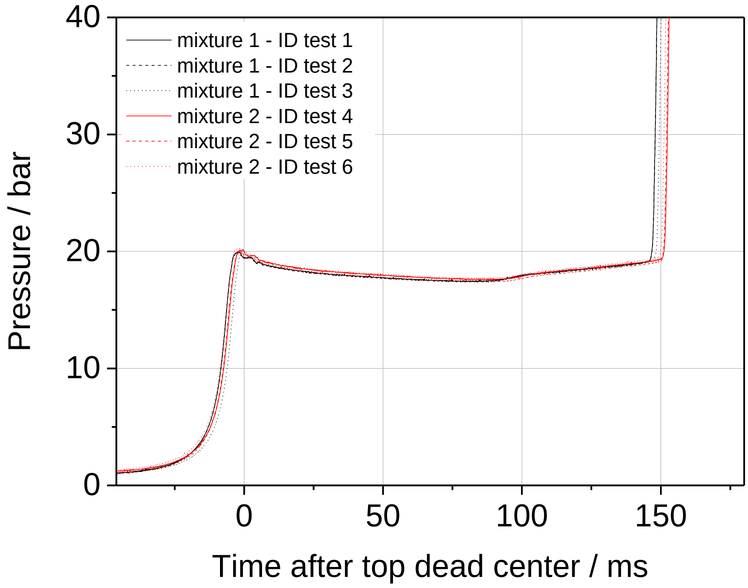

Figure 28 – Comparison of pressure profiles from mixture 1, black lines, using a homogenization time of 1 hour and mixture 2, red lines, using a homogenization time of 2 hours.

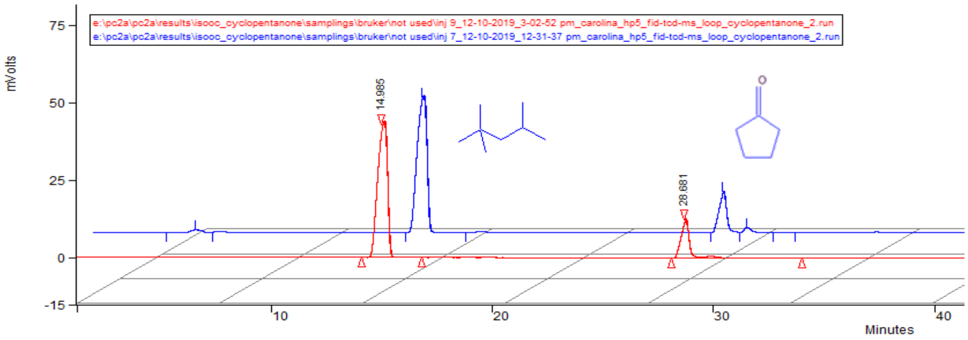

Figure 29 - Chromatograms of the mixture 1 in red and mixture 2 in blue.

Table 15 - Comparison of calculated mole fractions within different homogenization times.

	Mixture 1	Conversion (%)	Mixture 2	Conversion (%)
$x_{isooctane}$	0.01180	1.6	0.01178	1.7
$x_{cyclopentanone}$	0.00790	1.2	0.00789	1.3

Besides that, the temperature of the heated bench, RCM and the gas lines were set to ensure that the fuel partial pressure was inferior to its vapor pressure by a factor of two (116), and the temperatures of the RCM and the gas lines was chosen as superior to the heated bench by 5 K to prevent condensation of the mixture during the transfer to the RCM. The gas lines and sampling chamber temperatures are detailed, for each fuel, in the appendices.

The composition of the reactive gas mixtures is defined according to the desired equivalence ratio. This last one is calculated according to the following equation:

$$C_nH_m + \left(n + \frac{m}{4}\right)O_2 + pZ \rightarrow nCO_2 + \left(\frac{m}{2}\right)H_2O + pZ \tag{47}$$

$$\varphi = \frac{\left(\frac{\sum x_{fuel}}{\sum oxidizer}\right)_{mixture}}{\left(\frac{\sum x_{fuel}}{\sum x_{oxidizer}}\right)_{stoichiometric}} \tag{48}$$

Where Z is the inert, ϕ the equivalence ratio and x the mole fractions. The composition of the reactive gas mixtures is defined according to the desired TDC temperature which depends on the ratio of the heat capacities γ of the gas mixture. Once the RCM compression ratio is fixed, the composition of the inert is modified in order to reach a wide range of temperatures in the end of the compression; Nitrogen and CO_2 are used for the lowest temperatures, and Argon for the highest temperatures.

Non-reactive mixtures are prepared according to the same method presented above, replacing oxygen by nitrogen. These are used to enable the modeling of the compression phase and heat losses in the RCM in a zero-dimensional framework, as described in section 3.6.1.

3.2. Rapid Compression Machine (RCM)

The ULille RCM was developed between 1988 and 1992, analogue to existing machines (338) dedicated to the measurement of ignition delay times at temperatures between 600 and 1000 K and at pressures range from 1 to 30 bar, under nearly adiabatic conditions (177). For the past 30 years, work has been undergone with the ULille RCM to describe the autoignition of pure hydrocarbons and mixtures, as well as engine-relevant combustion phenomena such as cool flames, the negative temperature coefficient and knock. A review of the work carried out at the ULille RCM can be found in the table below.

Table 16 - Previous works on Lille RCM.

Author	Year	Studied compounds	Reference
Marc Ribaucour	1992	*n*-butane, *n*-pentane, *n*-heptane, neopentane, isooctane, *n*-pentane/neopentane, *n*-pentane/neopentane and *n*-heptane/isooctane	(177)
Anne Roubaud-Bernard	1999	toluene, xylenes, trimethylbenzenes, ethylbenzene, *n*-propyl benzene, *n*-butylbenzene and 2-ethyltoluene	(231)
Olivier Lemaire	2001	cyclohexane, cyclohexene, cyclohexa-1,3-diene, cyclohexane/cyclohexene	(339)
Guillaume Vanhove	2004	1-hexene, 2-hexene, 3-hexene and isooctane/toluene isooctane/1-hexene, toluene/1-hexene and ternary surrogate	(179)
Kamal Hadj Ali	2007	dimethyl ether and methyl esters	(340)
Moïse Crochet	2008	*n*-butylbenzene, *n*-propyl cyclohexane, *n*-decane, binary mixtures and ternary surrogate	(341)

Yi Yu	2012	methane, natural gas/hydrogen mixtures and tetrahydrofuran	(342)
Mohamed A. Boumehdi	2016	*n*-heptane and *n*-butane plasma ignition	(343)
Yann Fenard	2017 - 2018	2-methyltetrahydrofuran, ferrocene, real fuels and blendstocks	(344–347)
Hwasup Song	2017 - 2020	2,5-dimetyltetrahydrofuran, 2-methyl-1-butene, 2-methyl-2-butene, and 3-methyl-1-butene, DIB isomers and fuel blends	(346,347)

3.2.1. RCM operating set-up

The ULille RCM is equipped with two pistons: the driving piston and the compression piston. These are connected by a cam which allows the coupling between both pistons, thereby ensuring a right-angle connection. Compressed air propels the driving piston, which is attached to the cam. The displacement of the cam drives the compression piston and thus compresses the gas mixture inside the combustion chamber. This RCM specific design prevents piston rebound after the compression, keeping the volume strictly constant, inside the combustion chamber during the ignition delay period. It also allows changing the compression time while keeping the compression ratio constant. The combustion chamber is heated using three heating elements, covering the stroke of the compression piston. The initial temperature can vary from 30 to 90°C and the maximum deviation along the axial direction is 1 °C. The mechanical coupling between the two pistons is shown in Figure 30.

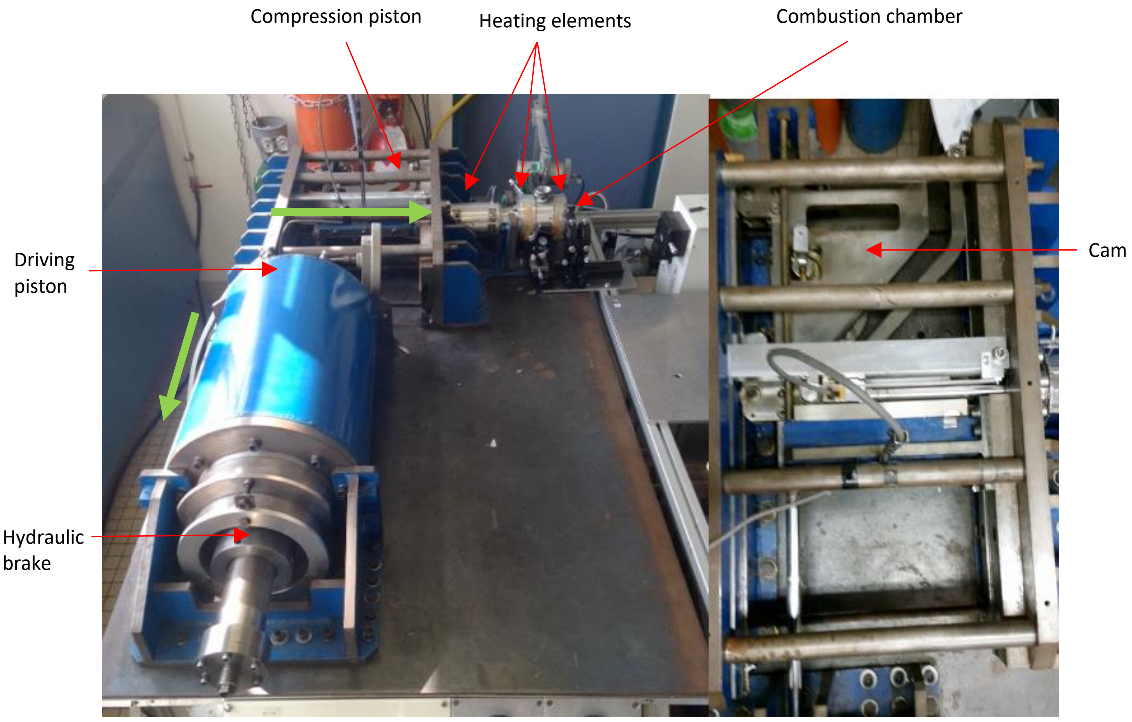

Figure 30 - Left, ULille RCM and right, detailed view of the cam shape.

Figure 31 illustrates the profile of the combustion chamber. It was designed in stainless steel, with a diameter of 50 mm, a height at top dead center of 17 mm, while the piston stroke is 200 mm and the volume at top dead center 33 cm^3. The combustion chamber is equipped with a removable end-plate, two lateral optical ports that are plugged by two stainless steel fittings in the case of high-pressure studies, a sampling orifice, a gas introduction valve, and two piezoelectric sensors. Different end-plates permit variation of the compression ratio by changing the reactor volume. During the current work the volumetric compression ratio was fixed at 10.29 for all studied LDCs.

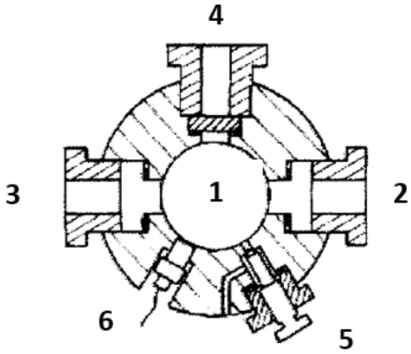

Figure 31 - Diagram of the combustion chamber (348)*. 1: combustion chamber end-plate, 2, 3: side window, 4: sampling port, 5: gas introduction valve, 6: piezoelectric pressure sensor.*

When the piston moves, a vortex can be formed if the piston scrapes the thermal boundary layer present near the walls of the combustion chamber. As a consequence, cold gases from the wall and hot gases in the chamber are mixed, resulting in a non-uniformity of the reacting core. The ULille RCM piston was built according to the recommendations of Lee et al. (349) and has a crevice that captures the thermal boundary layer during compression, minimizing the temperature heterogeneities inside the combustion chamber. However, the mass transfer to the crevice can lead to longer ignition delay times (350), especially for two-stage ignition cases where the first-stage leads to strong heat release. This additional dead volume also must be taken into account during speciation experiments. It is done by considering the dilution correction caused by the crevice volume and it will be discussed in detail in section 3.4.2.

3.2.2. Adiabatic core gas temperature (T_C)

The compressed temperature is calculated from experimental data according to the adiabatic core gas model, previously described (349,351). This model was validated using several experimental techniques such as micro thermocouples (352), Rayleigh scattering (353) and mid-IR absorption spectroscopy (354). Although effective, these techniques are either intrusive or not compliant for routine application, justifying the calculation of the temperature. Using the isentropic law, the adiabatic core model allows calculation of the temperature at the top dead center (T_C), assuming that there exists an adiabatic core of gas in the combustion chamber which is not affected by heat losses to the walls. Hence, considering the conservation of energy, and an isentropic compression:

$$dU = -PdV + dQ \;\; (dQ = 0) \tag{49}$$

Assuming that the test gas mixture is a mixture of ideal gases, with C_P-C_v = R and C_p / C_v = γ, γ being the ratio of heat capacities, and for one mole of gas:

$$dU = -PdV = C_v dT \tag{50}$$

$$-P\frac{dV}{T} = C_V\frac{dT}{T} \tag{51}$$

$$\frac{P}{T} = \frac{R}{V} = \frac{C_P - C_V}{V} \tag{52}$$

$$\frac{dT}{T} = -\left(\frac{C_P}{C_V} - 1\right)\frac{dV}{V} \tag{53}$$

$$\frac{1}{1-\gamma}\frac{dT}{T} = \frac{dP}{P} \tag{54}$$

The adiabatic core temperature T_C is then calculated by an iterative method:

$$\int_{T0}^{TC}\frac{1}{1-\gamma}\frac{dT}{T} = \int_{P0}^{PC}\frac{dP}{P} \tag{55}$$

where P_0 and T_0 are the initial pressure and temperature respectively and P_c the pressure at top dead center. The NASA formalism, based on a polynomial expression, is used to calculate the ratio of molar heat capacities

$$\frac{1}{1-\gamma} = a_1T^0 + a_2T^1 + a_3T^2 + a_4T^3 + a_5T^4 \tag{56}$$

Softwares as THERM, which uses the theory of additivity of Benson groups (355), and RMG, which also uses an on-the-fly quantum mechanics (QM) method (356), can be used to calculate the coefficients a_i when they are not available in the literature.

3.2.3. RCM data acquisition

The RCM data is recorded using a data acquisition system controlled by Labview 8.5. The recording of the pressure and the displacement of the piston are achieved with a step of 40 µs during and after the compression, for an acquisition time of 2 s. Dynamic pressure measurements, during and after compression, are obtained from two Kistler 601-CA and 6052 piezoelectric pressure sensors protected from thermal shock effects. Charge amplifiers (Kistler 5018 and 5007) are connected to these pressure sensors, converting the charge signal into voltage. The initial pressure in the combustion chamber is measured using the capacitive pressure gauges installed in the mixture dilution benches. A type K thermocouple, penetrating 1 mm into the combustion chamber, allows the measurement of the initial temperature.

A HOA 20001-001 Honeywell, optocoupler, attached to the compressing piston, is used to measure the position of the compressing piston during the compression phase with help from an optical comb, with a 1 mm resolution.

3.2.4. Ignition delay time definition

Ignition delay times are determined from the experimental pressure profiles. The time between the end of compression and the autoignition time is the definition of the ignition delay time. In the current work, the autoignition time is defined as the time corresponding to the overall maximum of the pressure derivative. In the case where the autoignition takes place in two stages, the cool flame delay (or first-stage ignition delay time) is defined as the time between the TDC and the first maximum of the pressure derivative. Figure 32 is an example of the pressure profile time history in the case of two-stage ignition. The compression time is defined as the time between the first up- or downward step of the optocoupler signal, and the TDC.

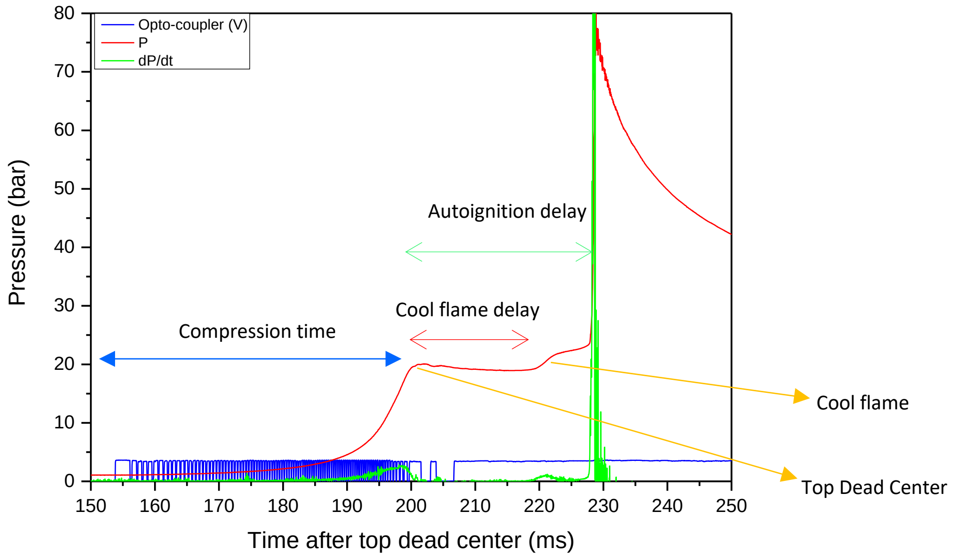

Figure 32 - Representative pressure and optocoupler profiles during a two-stage ignition delay experiment. Mixture isooctane/O_2/N_2, $\varphi = 1.0$, Tc = 682 K et Pc = 20 bar..

3.3. Sampling set-up

The ULille RCM allows physical sampling during the ignition delay in order to perform chemical analysis of the reacting mixture. Currently, only three RCMs around the world have this possibility, which makes it a useful tool for the detailed validation of combustion kinetic models in “realistic” engine conditions (177). The sampling system is fixed on the combustion chamber upper port, Figure 31, and an aluminum diaphragm separates both. A metal needle is held in the high position by an electromagnet before the sampling event. At this time, the sampling chamber, with a volume of 1530 cm^3, is under vacuum.

Figure 33 presents a diagram of the sampling system as well as five phases, highlighted in the figure, illustrating the sampling methodology (339). Phase 1 represents the electromagnet which retains the metal needle and at the settled time, enables its release. This is driven by the spring (phase 2) which, by propelling the needle, enable the perforation of the aluminum membrane (phase 3). In phase 4, the reacting gas mixture expands to the sampling chamber and hence, the sampling chamber is filled with the gas mixture which is then isolated for subsequent analysis (phase 5). The original RCM sampling system is similar to that previously described in various studies (328,357,358). and has been heavily modified and optimized on the basis of these principles.

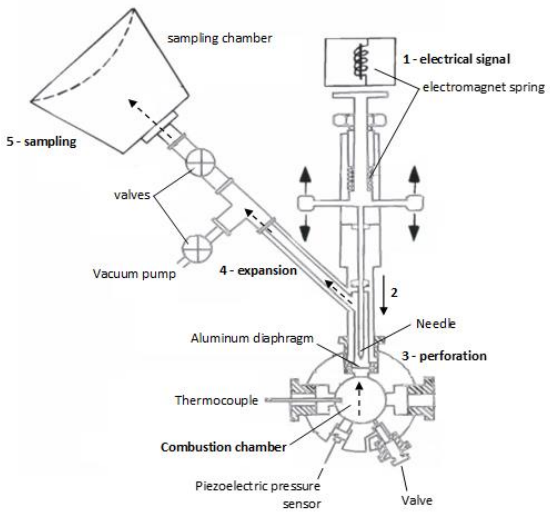

Figure 33 - RCM sampling system (339)*, adapted.*

The comparison of pressure profiles of a typical RCM IDT and sampling experiment, is shown in Figure 34. It reveals the sudden decrease in pressure during the diaphragm perforation. The pressure drops by 50% in less than 0.5 ms, because of the volumetric ratio between the combustion chamber and the sampling chamber of approximately 1/40, thereby ensuring the instantaneous quenching of chemical reactivity.

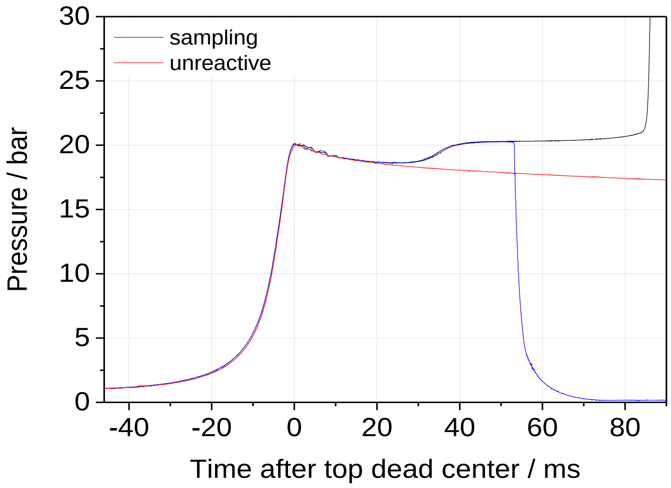

Figure 34 - Pressure profiles for isooctane/ anisole 60/40 /O_2/N_2 stoichiometric mixtures, P_c = 20.06 bar and T_c = 685 K. Blue line: pressure profile during a sampling experiment; red line: non-reactive mixture; black line: reactive mixture.

Each point in a species mole fraction time-history profile corresponds to a different compression experience; however challenging, the unique contribution of knowing the species formed during the combustion is extremely useful for kinetic model development. In order to guarantee the reproducibility of the experiments, between each sampling experiment the reaction chamber is filled with pure nitrogen to limit the entry of oxygen inside the combustion chamber. Before being analyzed, the test gas mixture can be concentrated by slow compression in a heated cylinder, before being injected into the gas chromatographs (GC).

3.4. Speciation system

3.4.1. Qualitative and quantitative speciation

The chemical analysis of the sampled products is done by GC technique, coupled to a mass spectrometer (MS) and to a TCD (Thermal Conductivity Detector) / FID (Flame Ionization Detector) line in the Bruker Scion 456 -GC, or to a TCD / FID line in the Agilent 6890. The first of these devices is used to perform qualitative and quantitative analysis of products ranging from C_2 to C_{10}, and its configuration is presented in Figure 35. The sample are injected into two columns and then split in two lines leading to FID/TCD detectors and the MS. The separation columns used in the current work are described in Table 17.

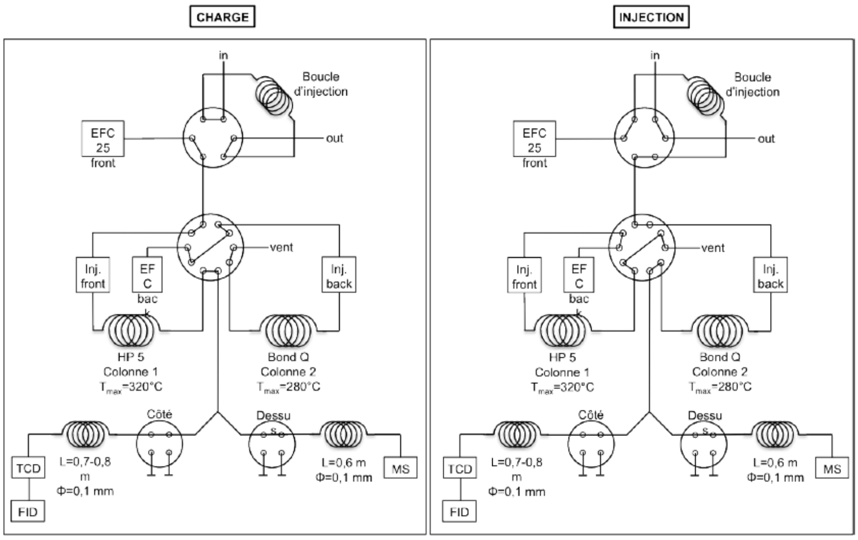

Figure 35 - Bruker Scion 456 -GC chromatography charging and injection configuration (343).

The recent previous works using ULille RCM and its analytical system, used the BR5 – MS capillary column to separate the sampled gas mixtures (343,346). However, the first surrogate to be studied was isooctane/anisole and its analysis revealed trace of aromatics. In order to better quantify these small amounts of aromatics, the BR5 – MS was replaced by a second column, UptiBond UB5P, which the maximum operating temperature is 300 °C, and it has a thicker stationary phase and therefore longer retention times. Figure 36 shows two examples of chromatograms using the BR5 column and sampled at 71.7 ms after TDC and using the UB5P at 71.1 ms. The peaks are better separated in the second case especially in the first 10 minutes of the analysis. The RT bond Q and the UptiBond UB5P columns were used to separate the sampled gas mixtures for all LDCs surrogates studied.

Table 17 - Capillary columns properties.

Column	**RT bond Q**	**UptiBond UB5P**
Products analyzed	from C_2 to C_6	From C_5 to C_{12}
Length	30 m	30 m
Internal diameter	0.25 mm	0.25 mm
Stationary phase	8 µm	1.00 µm
Composition	100% divinylbenzene	5% phenyl – 95% dimethyl arylene siloxane

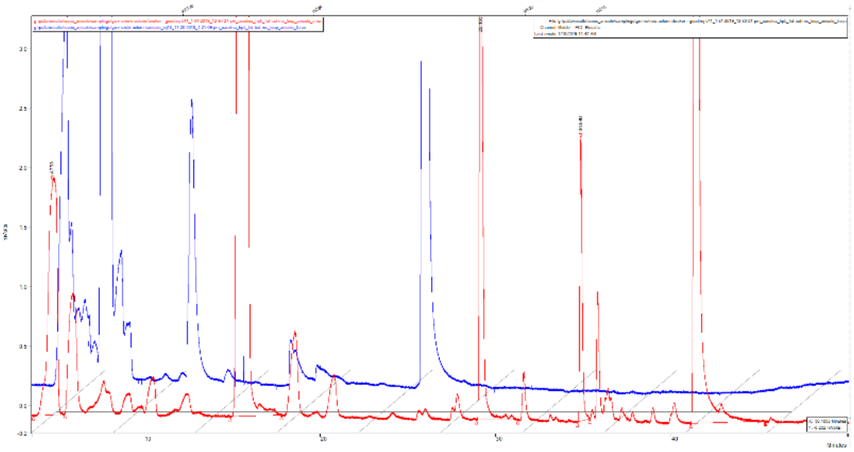

Figure 36 - Comparison chromatograms with BR5 column at 71.7 ms after top dead center (blue) and using UptiBond UB5P at 71.1 ms after top dead center (red).

The fuel-specific experimental set-ups, such as GC oven temperature programs can be found in the appendices. The injection mode was also altered by changing the injection liners, using liners that are specifically designed for splitless injection and analysis of very polar molecules. The identification of intermediates was performed using their mass spectrum, by comparison using NIST2011 mass spectral library or by studying their fragmentation scheme and detailed analysis of the mass spectra (359).

After the separation of the samples by the GC, the quantitative analysis of the products is done using the signal from the FID and TCD detector. The principle of FID detection is based on an increase in the electrical conductivity between two electrodes which are located around the hydrogen/air flame; when an organic species, leaving the chromatographic column, is introduced into the flame, electrically charged species are formed. This results in an increase in the electrical conductivity which is proportional to the amount of the species. The resulting current is amplified by an electrometer and transformed by the software into a chromatographic peak. The condition for the detection of a component of the sample is the creation of temporary intermediate carbon-radical ions which are finally oxidized to CO_2 and H_2O. However, certain species, such as formaldehyde do not form intermediate carbon-radical ions (360) and therefore cannot be quantified by FID. This is problematic for these works, formaldehyde being a species largely formed during the combustion of low temperatures.

The operating principle of the TCD is based on the thermal conductivity difference between the pure carrier gas and the mixture of carrier gas and analyte. In a thermostatically controlled detection cell, a filament is heated by an electric current and is continuously rinsed by the carrier gas which absorbs the heat emitted by the filament, thus decreasing its temperature. This filament, arranged within an electrical assembly known as "Wheatstone Bridge", has its electrical resistance changed if the thermal conductivity of the gas circulating in the cell changes, which results in a variation of the measured voltage and a measured signal.

In order to calculate the concentration of the identified species, the response factor of the FID is necessary. For commercially available products, mixtures of a known molar fraction are prepared by the partial pressure method, then are injected into the GC in order to obtain calibration factors. The response factors for species i were calculated using the value of the peak areas A_i, provided by the chromatogram, the injection pressure P_{inj} and the known molar fraction x_i, from Equation (71). To prevent uncertainties due to evolution of the FID signal, calibration of key species was repeated before sampling experiments of the studied LDCs surrogates. A summary of all calculated response factors, used during the study of each LDC surrogate, is found in the appendices.

$$F_i = \frac{A_i}{x_i . P_{inj}} \tag{57}$$

The Agilent 6890 TCD detector was replaced between the isooctane/o-cresol and isooctane/prenol experiments. The first CO response factor was used to measure mole fraction profiles of isooctane/anisole experiments and the second one, was used during isooctane/cyclopentanone sampling experiments.

Knowing the response factors, the species formed during the combustion can be quantified. For species not commercially available and quantified using the FID, the effective carbon number method was used (361). This is based on the fact that species with the same number of carbon atoms and the same functional groups have a similar FID response.

3.4.2. Crevice dilution correction

As previously mentioned, the use of a creviced piston, in RCM studies, may suppress the formation of the roll-up vortex and thus promote the homogenization of the gas mixture temperature. The dilution of the samples by gases trapped in the crevice is taken into account during species quantification. Considering an ideal mixture and the test volume as the sum of the RCM (V_{RCM} = 33 cm^3) and the crevice volume ($V_{crevice}$ = 3.3 cm^3), as seen in Figure 37. The gases trapped in the crevice are considered to not have reacted, which is consistent with the fact that the expected temperature in the crevice is quite low (362). The measured mole fraction of each species is:

$$x_i = \frac{n_i}{n_{total}} = \frac{n_i}{\frac{pV}{RT}} \qquad (58)$$

$$x_{i,measured} = \frac{n_{i,RCM} + n_{i,crevice}}{n_{total,RCM} + n_{total,crevice}} = \frac{n_{i,RCM} + n_{i,crevice}}{\frac{pV_{RCM}}{T_C} + \frac{PV_{crevice}}{T_{crevice}}} \qquad (59)$$

There is only the initial gas mixture (fuel/O$_2$/inert) inside the combustion chamber at the beginning of the test. Thus, the corrected mole fraction of the reactants and the species formed during the combustion process is provided by two different equations. For the reactants, the corrected mole fraction $x_{i(reactants),RCM}$, is given by:

$$x_{i,measured\ (reactants:\, n_{i,crevice}=n_{i,0})} = \frac{x_{i(reactants),RCM}\left(\frac{V_{RCM}}{T_C}\right) + x_{i,0}\left(\frac{V_{crevice}}{T_{crevice}}\right)}{\left(\frac{V_{RCM}}{T_C} + \frac{V_{crevice}}{T_{crevice}}\right)} \qquad (60)$$

$$x_{i(reactants),RCM} = \frac{x_{i,mesured}\left(\frac{V_{RCM}}{T_C} + \frac{V_{crevice}}{T_{crevice}}\right) - x_{i,0}\left(\frac{V_{crevice}}{T_{crevice}}\right)}{\frac{V_{RCM}}{T_C}} \qquad (61)$$

And for the products:

$$x_{i,measured\ (products:\, n_{i,crevice}=0)} = \frac{\frac{p_{i,RCM}V_{RCM}}{RT_C}}{\frac{p}{R}\left(\frac{V_{RCM}}{T_C} + \frac{V_{crevice}}{T_{crevice}}\right)} = \frac{x_{i,RCM}\left(\frac{V_{RCM}}{T_C}\right)}{\left(\frac{V_{RCM}}{T_C} + \frac{V_{crevice}}{T_{crevice}}\right)} \qquad (62)$$

$$x_{i(products),RCM} = x_{i,mesured}\left(1 + \frac{\frac{V_{crevice}}{T_{crevice}}}{\frac{V_{RCM}}{T_C}}\right) \qquad (63)$$

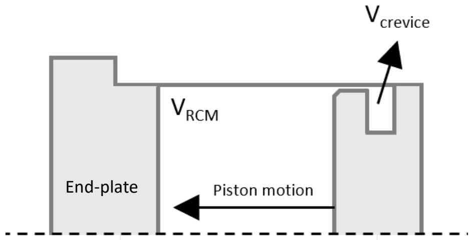

Figure 37 – Transversal section of the endplate, combustion chamber and creviced piston of the ULille RCM.

In order to minimize the uncertainties, the corrected mole fractions, in both cases, reactants and products, were calculated considering the temperature extremes, i.e., $(T_{crevice})$ was replaced by the initial temperature (T_0) and the compressed temperature (T_C), leading to two different results. The reported mole fraction is the average between these results. The total uncertainty associated to the reported mole fractions is estimated in 10% for the calibrated species and 20% for the species using the effective carbon number method.

3.5. Experimental data uncertainty analysis

Since experimental data are used to validate kinetic models, it is important to evaluate their associated uncertainties in order to ensure their reliability and estimate the model accuracy. The sources of uncertainty are dependent on different parameters and have to be taken into account at each experimental stage. They include, in RCM experiments: p_0, T_0, P_c and T_C measurements; compression time, cool flame time, autoignition time definition and test gas mixture composition. On the other hand, the uncertainties associated to speciation analysis may consider: injection pressure measurements, response factors, sampling time definition, chromatographic peaks resolution and potential species condensation.

The measurements of the initial conditions inside the combustion chamber has been reported as one of the major sources of uncertainties during RCM experiments, especially the pressure (p_0) (363). As mentioned in section 3.1, four MKS Baratron pressure gauges, two in the heated bench and two in the non-heated bench, are used to measure the pressure at the bottom dead center. The accuracy of these pressure gauges is 0.25% of reading, i.e., for a 1000 Torr Full Scale manometer, which means that the error could be up to 2.5 Torr (364).

Estimating the uncertainties associated to the ignition delay measurements is a challenging task due the numerous non-linear effects that lead to ignition. Instead of reporting arbitrary error bars, the repeatability of the experiment is presented by reproducing all of the experimentally observed data points in the Figures. All of the experimental conditions have been repeated a minimum of three times. However, uncertainty in the calculated core gas temperature has been previous discussed (365) inferring that the associated error is mainly due to the uncertainties in the initial temperature measurements. In the current work, an uncertainty on T_C of ± 5 K is considered.

As mentioned in section 3.2.3 the pressure inside the combustion chamber is measured using two KISTLER pressure sensors; both have been calibrated at the start of this work. The maximal relative error reported by the manufacturer associated with the pressure sensor is 0.05% of the measured pressure.

As stated in the previous section, the uncertainty associated with the mole fractions measurements is dependent on the used quantification method. When it is made through measured calibration factors, the estimated uncertainty is 10%. On the other hand, if the effect carbon number method is used, its estimated value is 20% (366). All the chemical products used in this work and their respective purities and suppliers, are shown in the appendices.

The inability to quantify formaldehyde and potential condensed heavy products, as mentioned in section 3.4.1, can also lead to some source of errors. In order to estimate that, the verification of the experimental results was carried out by taking a balance of carbon atoms, i.e., by comparing the moles of carbon entering the RCM and the moles of carbon quantified for each sampling time during isooctane/anisole and isooctane/cyclopentanone sampling experiments. The reactive mixture and the moles of carbon ($n_{C,in}$) entering in the RCM are:

$$\sum_i x_i C_{a_i} H_{b_i} O_{c_i} \tag{64}$$

$$n_{C,in} = \sum_i x_i a_i \tag{65}$$

On the other hand, the number of carbon moles coming out of the machine ($n_{C,out}$), for each sampling time is:

$$\sum_i y_i C_{d_i} H_{e_i} O_{f_i} \tag{66}$$

$$n_{C,out} = \sum_i y_i d_i \tag{67}$$

Finally, the relation between $n_{C,in}$ and $n_{C,out}$ can be calculated. The graphics showing the evolution of calculated carbon balances during the ignition delay are illustrated in the appendices.

3.6. Kinetic modeling

In this section the numerical approach used to simulate the experimental results will be introduced. Detailed chemical kinetic models are developed to reproduce the fuel's combustion in which all the possible elementary chemical reactions between relevant species are included. The design of the kinetic mechanism mainly consists of defining the key reactions taking place during the chemical transformation. Then, for each reaction, kinetic parameters must be determined. It is also essential to introduce the thermodynamic properties for all the compounds which appear in the model.

3.6.1. RCM experiments modeling

The open source solver Cantera (367) is herein used to solve the system of ODEs that describes the mole fractions of species and the energy. This suite of object-oriented software provides a tool to include complex chemistry in combustion simulations. In order to calculate the ignition delay times and to account for heat losses, Cantera uses an isentropic reactor in which a volumetric compression of the gas mixture is triggered by the movement of an adiabatic wall. A Python script, which includes the initial conditions (p_0, T_0 and mixture composition) is required as input file, along with: the non-reactive volume profile (.csv) acquired in the Lille RCM, and the kinetic mechanism in Cantera format (.cti). The non-reactive volume profiles are initially computed from non-reactive pressure histories on the basis of the isentropic law, also including a Savitzky-Golay filter which removes high frequency noise from data. The numerical approach used to generate the volume profiles is depicted in Figure 38. Figure 39 illustrates the physical model used by Cantera to simulate an RCM.

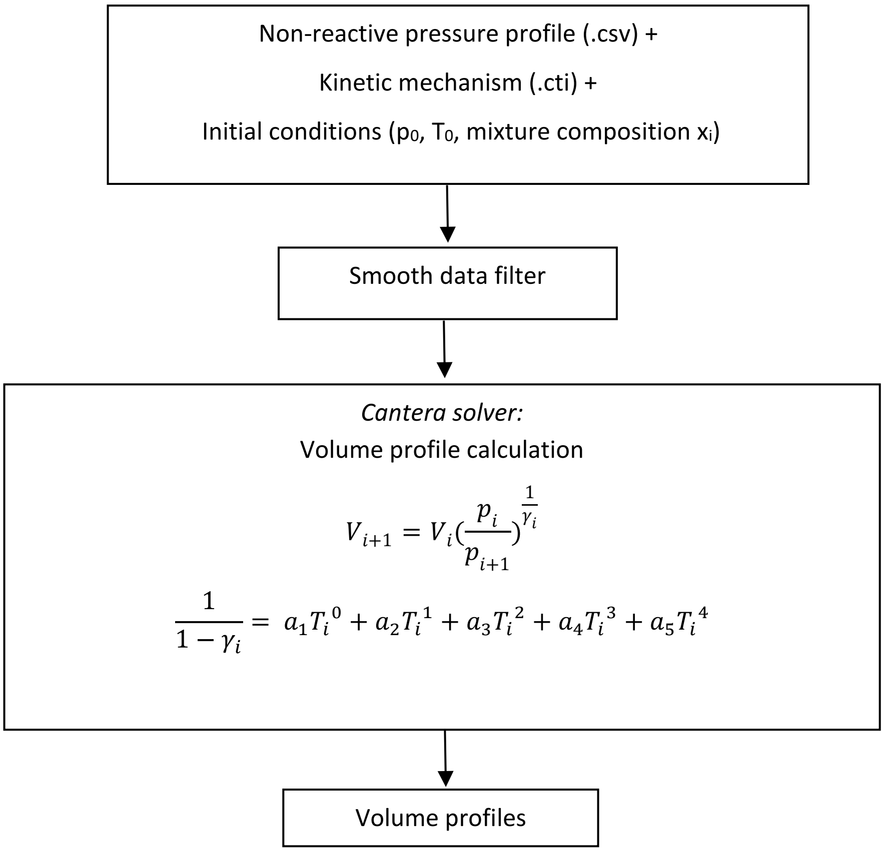

Figure 38 - Volume profile generation.

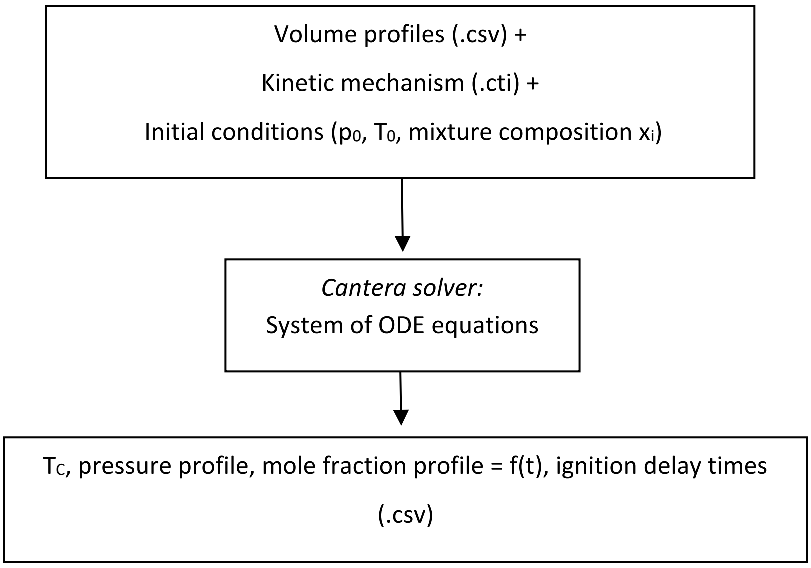

Figure 39 - Scheme of numerical simulation used by Cantera.

The definition of the ignition delay times depends on the user's choice: Either the maximum of the derivative of pressure or the maximum in the mole fraction of a user-specified species can be used. In the simulations performed in this thesis, results, the first stage ignition delay time is calculated from the occurrence of the maximum of a C_3 ketohydroperoxide mole fraction, and the total ignition delay time is calculated from the occurrence of the peak in the OH radical.

The aforementioned adiabatic wall has its movement direction limited by the volume profile, which is used to calculate the wall's velocity. Two parameters limit the test duration, the final temperature (end_temp) and the simulation time (Sim_time) both defined by the user. The simulation stops when the temperature exceeds (end_temp), or the time exceeds (Sim_time). If after a simulation the autoignition is not achieved, (Sim_time) can be increased in order to give enough time to reach ignition.

3.6.2. Kinetic mechanism

To develop a kinetic mechanism, all the species must be reported in the mechanism: reactants, intermediates (molecules, atoms and free radicals) and products. In addition, all thermodynamically possible relevant reactions should be added. The development is therefore done following a hierarchical methodology, successively adding the reactions of the species containing an increasing number of carbon atoms.

The isooctane/anisole surrogate mechanism was developed using the aforementioned hierarchical methodology. The model base was built by Lawrence Livermore National Laboratory (LLNL) research group and included a detailed model for isooctane. The sub-mechanism describing the kinetics of anisole, developed in the current work, was added. The kinetic mechanism in Cantera format herein used is composed of three parts: species list, species data, and reaction data.

An ideal gas mixture is assumed to simulate the experimental results. In this first part the user defines the "*name*" identifying the species; "*elements*" including all the chemical elements used in the model; and "*species*" declaring all the chemical species. Commonly, sub-mechanisms from different research groups are added into a base. Therefore, in this case the species declaration has to be done carefully in order to ensure that the species appearing simultaneously in the base and in the sub-mechanism have the same name.

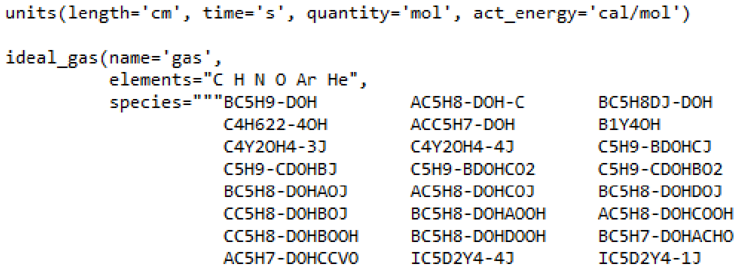

```
units(length='cm', time='s', quantity='mol', act_energy='cal/mol')

ideal_gas(name='gas',
          elements="C H N O Ar He",
          species="""BC5H9-DOH         AC5H8-DOH-C       BC5H8DJ-DOH
                     C4H622-4OH        ACC5H7-DOH        B1Y4OH
                     C4Y2OH4-3J        C4Y2OH4-4J        C5H9-BDOHCJ
                     C5H9-CDOHBJ       C5H9-BDOHCO2      C5H9-CDOHBO2
                     BC5H8-DOHAOJ      AC5H8-DOHCOJ      BC5H8-DOHDOJ
                     CC5H8-DOHBOJ      BC5H8-DOHAOOH     AC5H8-DOHCOOH
                     CC5H8-DOHBOOH     BC5H8-DOHDOOH     BC5H7-DOHACHO
                     AC5H7-DOHCCVO     IC5D2Y4-4J        IC5D2Y4-1J
```

Figure 40 - Structure of .cti input file - species list.

The thermodynamic data is included in the mechanism through 14 coefficients, 7 for the low temperature and 7 for the high temperature. These parameters correspond to the coefficients of the NASA polynomial, showed in Equation (70), and they are used to compute the heat capacity at constant pressure ($c^{\circ}_{p,i}$), the standard enthalpy of formation ($\Delta_f H^{\circ}_i$) and the standard entropy (S°_i), shown in the equations below. Figure 41 illustrates the structure of the species data in the model used in this work. The blue arrow indicates the low temperature range in which the seven first coefficients can be used and the red arrow indicates the high temperature range.

$$\frac{c_{p,i}^{\circ}(T)}{R} = a_{1,i}T^0 + a_{2,i}T^1 + a_{3,i}T^2 + a_{4,i}T^3 + a_{5,i}T^4 \tag{68}$$

$$\frac{\Delta_f H_i^{\circ}(T)}{RT} = a_{1,i}T^0 + a_{2,i}\frac{T^1}{2} + a_{3,i}\frac{T^2}{3} + a_{4,i}\frac{T^3}{4} + a_{5,i}\frac{T^4}{5} + \frac{a_{6,i}}{T} \tag{69}$$

$$\frac{S_i^{\circ}(T)}{RT} = a_{1,i}\ln T + a_{2,i}T^1 + a_{3,i}\frac{T^2}{2} + a_{4,i}\frac{T^3}{3} + a_{5,i}\frac{T^4}{4} + a_{7,i} \tag{70}$$

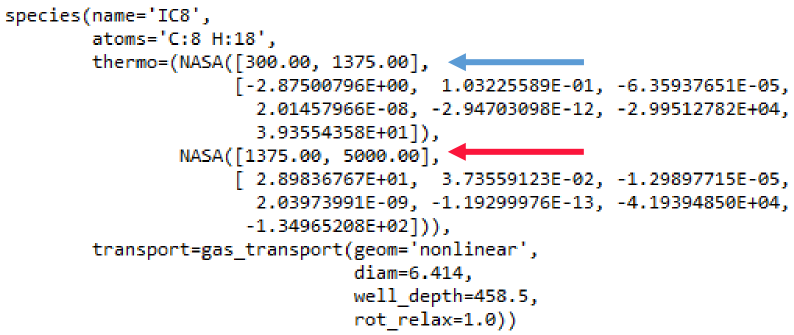

```
species(name='IC8',
        atoms='C:8 H:18',
        thermo=(NASA([300.00, 1375.00],
                     [-2.87500796E+00,  1.03225589E-01, -6.35937651E-05,
                       2.01457966E-08, -2.94703098E-12, -2.99512782E+04,
                       3.93554358E+01]),
                NASA([1375.00, 5000.00],
                     [ 2.89836767E+01,  3.73559123E-02, -1.29897715E-05,
                       2.03973991E-09, -1.19299976E-13, -4.19394850E+04,
                      -1.34965208E+02])),
        transport=gas_transport(geom='nonlinear',
                                diam=6.414,
                                well_depth=458.5,
                                rot_relax=1.0))
```

Figure 41 - Structure of .cti input file - species data.

Considering that an ideal gas mixture is used to simulate the experimental results, the heat capacities of the studied mixtures are calculated according to the following equation:

$$c_p = \sum_i x_i c_{p,i} \tag{71}$$

Figure 42 shows the third part of the kinetic mechanism. The kinetic data required in this part are the pre-exponential factor (A), the coefficient (n) and the activation energy (E_a). These coefficients are used to represent the variation of the reaction rate constant (k) with temperature, according to Reaction (12).

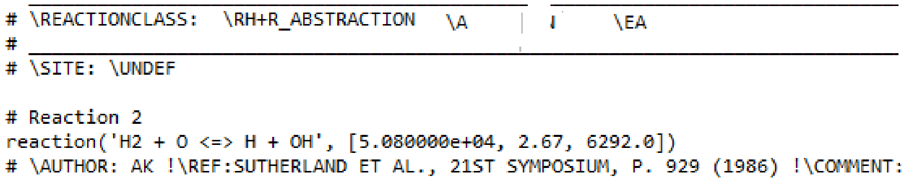

```
# \REACTIONCLASS:  \RH+R_ABSTRACTION   \A    |       \EA
#
# \SITE: \UNDEF

# Reaction 2
reaction('H2 + O <=> H + OH', [5.080000e+04, 2.67, 6292.0])
# \AUTHOR: AK !\REF:SUTHERLAND ET AL., 21ST SYMPOSIUM, P. 929 (1986) !\COMMENT:
```

Figure 42 - Structure of .cti input file - reaction data.

Moreover, knowing the standard enthalpy of formation and the standard entropy, the Gibbs Energy can be calculated, and also the equilibrium constants as a function of the pressure following the equations introduced in section 2.1.1.

3.6.3. Mechanism validation and optimization

The comparison of simulations and experimental results from different experimental devices and research groups, allows the validation of a comprehensive mechanism (60). In the current work the RCM experimental results are used to evaluate the model accuracy. In the case of the isooctane/anisole surrogate, previous Laminar burning velocity (LBV) and Jet-stirred reactor (JSR) data from different research groups were also used to validate the model.

In general, the predictive quality of a model is evaluated considering the agreement of the simulated results with the experimental data. The necessary computing time required to perform the simulations is also an important factor, however during the development of a detailed kinetic model, exhaustivity is sought, and reduction of the models is usually performed later. A rough estimation can be made to calculate the "computational costs", i.e., the time needed to solve a set of ordinary differential equations (ODE) in order to simulate a phenomenon by considering it proportional to the square of the species number (60).

Despite the increasing computational resources, the implementation of an increasingly complex, representative and predictive chemistry, quickly showed the restrictions of industrial calculation codes and made it difficult to couple a detailed description of the physics with detailed kinetics, due to a large number of species and reactions. Therefore, it is necessary to simplify the detailed models. The initial operation, essential before any simplification of a detailed kinetic scheme, involves a meticulous selection of the operating conditions that the model should be able to reproduce, keeping in mind that the reduced scheme obtained cannot show better performance than the original. This choice strongly influences the size of the final model through the species and associated reactions, but also the simulation time in comparison to the original model. However, the wider the set of experimental conditions, the more the size of the reduced diagram will approach that of the detailed one and the less the gain in computation time will be interesting. In order to optimize the model, sensitivity analysis and reaction path analysis can be performed (145).

The first one evaluates how each rate coefficient affects the overall reaction rate, the production of a certain species, or a global measurement, such as the ignition delay time. This method allows the user to identify reactions that have the largest influence on the reproduction of the experiments. Relating this information to the uncertainty of the relevant rate parameters allows optimization of the mechanism, while keeping in mind that the model should still be able to reproduce its initial validation base. Reaction pathway analysis describes the importance of certain paths in the mechanism under specified conditions. It is achieved through the calculation of the transfer rate of certain atoms such as C, O, and H. This allows identifying the most important reactions for the formation and consumption of a set of species.

4. Experimental Results & Modeling of the Oxidation by Fuel

In this chapter a framework of the reactivity of the studied LDCs is presented. For each surrogate, RCM experiments were performed at low to intermediate temperatures. When a model was available, with the aid of kinetic modeling a discussion is proposed regarding the possible oxidation pathways of these compounds and the differences in their reactivity.

Introduction

In order to investigate the reactivity of the studied LDCs, RCM experiments were performed at the operating conditions showed in Table 18. As mentioned before, biofuels are rarely found pure inside a commercial fuel. Therefore, the antiknock blending effect of these components was studied inside a surrogate. The effect of three factors on the auto-ignition delay of isooctane and the four LDCs surrogates were settled as the starting point for this work, which are: temperature at the end of compression, top dead center pressure, and the mixture composition. Parts of the results shown in this chapter, concerning isooctane and isooctane/anisole surrogate have been submitted to *Proceedings of the European Combustion Meeting (ECM) 2019* and to *Proceedings of the Combustion Institute* (232). The next sections present the experimental and modeling results separately for each studied fuel.

Table 18 - Summary of the experimental conditions in this study.

	Temperature (T_c)	**Pressure (p_c)**	**Mole fraction**
Isooctane	**T_C = 676 – 848 K** 20 bar	**20 – 14 bar** T_C = 680 ± 3 K T_C = 846 ± 2 K	-
Isooctane/anisole	**T_C = 670 – 850 K** 20 bar Isooctane/anisole 60/40	**20 – 14 bar** 0 – 40 % anisole T_C = 683 ± 4 K T_C = 850 ± 6 K	**0 – 40 % anisole** 20 bar T_C = 682 ± 4 K T_C = 849 ± 5 K
Isooctane/*o*-cresol	**T_C = 739 – 849 K** 20 bar Isooctane/*o*-cresol 80/20	**20 – 14 bar** 0 – 40 % *o*-cresol T_C = 686 ± 7 K T_C = 849 ± 5 K	**0 – 40 % *o*-cresol** 20 bar T_C = 688 ± 6 K T_C = 849 ± 5 K
Isooctane/prenol	**T_C = 675 – 852 K** 20,18 and 16 bar Isooctane/prenol 50/50	**20 – 14 bar** 0 – 50 % prenol T_C = 683 ± 3 K T_C = 850 ± 5 K	**0 – 50 % prenol** 20 bar T_C = 682 ± 1 K T_C = 850 ± 3 K
Isooctane/cyclopentanone	**T_C = 695 – 867 K** 20 and 25 bar Isooctane/CPN 60/40	**25 – 14 bar** 0 – 100 % CPN T_C = 693 ± 4 K T_C = 865 ± 13 K	**0 – 100 % CPN** 25 and 20 bar T_C = 693 ± 3 K (25 bar) T_C = 869 ± 10 K (25 bar) T_C = 693 ± 3 K (20 bar) T_C = 867 ± 12 K (20 bar)
Cyclopentanone	**T_C = 832 – 879 K** 25 bar	-	-

4.1. Isooctane

As previously discussed, results from different RCMs can differ depending on the operational conditions used and due to the complexity of this type of experiment. Isooctane was therefore studied over a wide range of thermodynamic conditions to precisely quantify the blending effect of investigated LDCs. A comparison of the ignition delay results with previous results from the ULille RCM and from different RCMs was also performed.

4.1.1. RCM experiments

The isooctane delay measurements were performed at three different pressures p_c = 20, 16 and 14 bar with initial pressures in a range of p_0 = 668 to 807 Torr. The core gas temperatures varied from T_C = 676 to 848 K. In order to validate the RCM experiments, a comparison with previous isooctane ignition delay measurements using the same machine by Minetti et al. (153) and UCONN RCM (166) is shown in Figure 43. In the current work the abbreviation IDT is used to represent the total ignition delay time and FSIDT to represent the first stage ignition delay time.

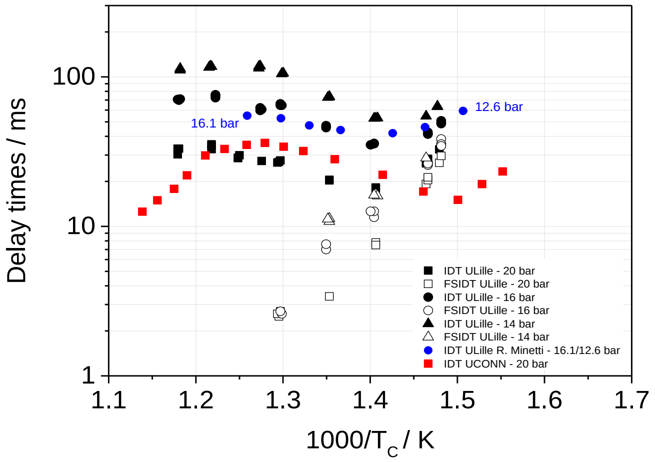

Figure 43 - Isooctane delay time measurements from different RCMs.

During the Minetti et al. (153) experiments, the pressure at top dead center was not constant, and covered a range from p_c = 12.6 to 16.1 bar. Overall, a good agreement can be observed with the results of this study. The current ignition delay times however appear to be slightly superior to comparable conditions. This can be explained by 1) the shorter compression time in the current work conditions: historical measurements in the Univ. Lille RCM were performed with a 60 ms compression time, increasing the possibility for reactivity during the compression phase, and 2) possibility of mass transfer to the crevice, since the Minetti et al. experiments were performed with a flat piston; this mass transfer results in mitigation of the temperature increase during the first stage of ignition, and therefore longer second stage and total ignition delay. The slight discrepancy observed with the UCONN measurements can be explained by considerations on the used diluents. The UCONN group uses N_2 as diluent, modifying the compression ratio of their RCM to vary the core gas temperature. The ignition delays at the highest temperatures are slightly longer in the ULille RCM, which uses pure Ar as a diluent in these conditions. This is due to the superior cooling effect of Argon, which leads to higher heat losses in the post compression period [29]. In the lowest temperature region, N_2/CO_2 mixtures are used as a diluent in the ULille RCM, increasing the heat capacity of the mixture and reducing the thermal diffusivity of the mixture, therefore reducing the heat losses to the walls. This procedure in favored in ULille in order to preserve the surface/volume and crevice volume/chamber volume ratios of the combustion chamber. All these effects are however routinely taken into account during the kinetic modeling of RCM experiments, allowing reconciliation of the datasets.

Pressure profiles for the ignition of isooctane/O_2/inert mixtures are shown in Figure 44 at different core gas temperatures from T_C = 676 to 848 K. A typical two stage ignition is observed with NTC behavior between T_C = 711 and 821 K. This non-Arrhenius behavior, in which the reactivity decreases with the increasing of temperature is attributed to the competition between chain branching reactions which produce ketohydroperoxides and chain propagation reactions that lead to the formation of alkenes and cyclic ethers (7), as discussed in chapter 2. As the temperature increases, transition towards single-stage ignition is observed.

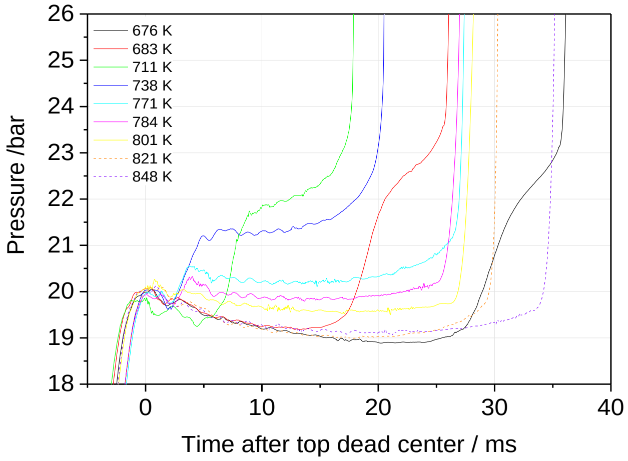

Figure 44 - Pressure profiles for stoichiometric isooctane/O_2/inert mixtures at pc = 20 bar and at different core gas temperatures (T_C).

4.1.2. Kinetic modeling

The previously acquired isooctane ignition delay results were simulated using two mechanisms from the literature and a new mechanism, shown in Figure 45.

- Atef et al. (166), including 9220 reactions and 2768 chemical species;
- Mehl's mechanism described by Mehl et al. (161), including 8000 reactions and 1550 chemical species;
- The currently under development Co-Optima model (368) developed by Lawrence Livermore National Laboratory, including 15985 reactions and 3690 chemical species.

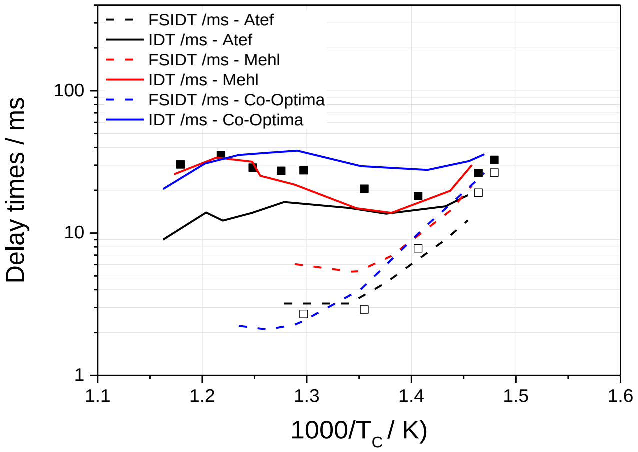

Figure 45 - Evolution of both experimental first-stage (white squares) and total ignition delays (black squares) of isooctane/O_2/inert, as a function of temperature. P_C = 20 bar, Φ = 1. Lines correspond to simulated DTs using Atef et al. (166)*, Mehl et al.* (369)*, and Co-Optima* (368) *models.*

The total ignition delay time measurements show a better agreement using the mechanism from Mehl et al. (161) than using the mechanism from Atef et al. (166). However, both models are not able to reproduce the temperature dependence of FSIDTs and the NTC region accurately. Following these results, a modeling work was started over as part of collaboration with the Lawrence Livermore National Laboratory. They provided a working version of their Co-Optima model (368), which included submechanisms for isooctane (IC8), anisole (C6H5OCH3), prenol (BC5H9-DOH), and cyclopentanone (CPN). The performance of this model with the isooctane data is better than that showed for both Mehl and Atef models. However, the IDTs are still not perfectly simulated, especially in the intermediate temperature region where the maximum deviation is below a factor of two. The agreement on FSIDT being considered prioritary in the accurate description of the LTC conditions, the Co-optima model was selected for further work.

4.1.3. Conclusions

- The comparison of IDT measurements using different RCMs showed a good agreement considering the complexity of these type of experiments, allowing the validation of the methodology used in the current work;

- Isooctane IDTs measurements provided a base of comparison for further LDCs blending effect study;

- While progress has been accomplished in the prediction of FSIDTs, the inability of the available isooctane models on precisely predicting IDTs in the NTC region reveals the necessity to further improve these models.

4.2. Isooctane/ANISOLE

4.2.1. RCM experiments

Stoichiometric isooctane/anisole/O_2/inert mixtures were compressed at pressures between p_c = 14 and p_c = 20 bar and temperatures from T_C = 670 to T_C = 850 K.

- **Composition effect**

The effect of molar composition of isooctane/anisole mixtures was studied, at p_C = 20 bar and at two different temperatures T_C = 849 ± 5 K and 682 ± 4 K, using argon and nitrogen as inert, respectively, in Figure 46. The mole fraction of anisole mixtures is shown in Table 19.

Table 19 - Mole fraction of isooctane/anisole/O_2/inert mixtures at p_C = 20 bar.

% anisole	$x_{isooctane}$	$x_{anisole}$	x_{O2}	x_{Ar}	x_{N2}	T_C (K)
0	0.0165	0.0000	0.2064	0.7767	0.0000	848
10	0.0153	0.0017	0.2065	0.7765	0.0000	847
20	0.0140	0.0035	0.2064	0.7761	0.0000	850
30	0.0126	0.0054	0.2063	0.7757	0.0000	844
40	0.0112	0.0074	0.2062	0.7752	0.0000	850
50	0.0096	0.0096	0.2061	0.7748	0.0000	717
0	0.0165	0.0000	0.2066	0.0000	0.7768	683
10	0.0153	0.0017	0.2065	0.0000	0.7764	679
20	0.0140	0.0035	0.2064	0.0000	0.7761	682
30	0.0126	0.0054	0.2063	0.0000	0.7757	683
40	0.0112	0.0074	0.2062	0.0000	0.7752	683
50	0.0096	0.0096	0.2060	0.0000	0.7748	688

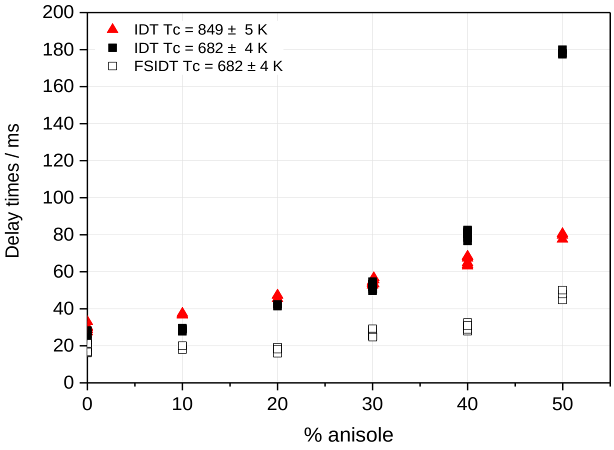

Figure 46 - Ignition delay times of isooctane/anisole/O_2/inert mixtures for an increasing amount of anisole at p_C = 20 bar and two different core gas temperatures: T_C = 849 ± 5 K (triangles) and T_C = 682 ± 4 K (squares).

At T_C = 682 K, the first-stage ignition delays seem unaffected until 20% anisole is added, then increase as anisole is substituted to isooctane. The total ignition delay times however increase monotonically with the proportion of anisole. Figure 47 shows that the addition of anisole reduces the pressure jump, and associated heat release of the first stage of ignition. The temperature reached after the first stage is therefore reduced, leading to a longer second stage of ignition. At 849 K, the ignition delay increases as anisole is added to the mixture. Figure 47 (left) shows that the ignition takes place in one stage for all anisole compositions.

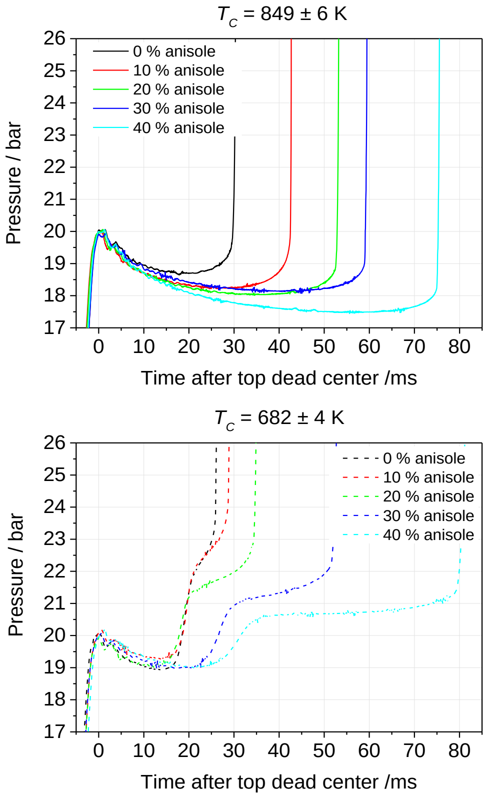

Figure 47 - Pressure profiles for isooctane/anisole/O_2/inert mixtures at stoichiometric condition, p_C = 20 bar.

- **Pressure effect**

The effect of pressure on the total ignition delay of isooctane/anisole mixtures was evaluated for different anisole compositions as a function of the top dead center pressure. The results are shown in Figure 48, at two different temperatures: T_C = 683 ± 4 K and at T_C = 850 ± 6 K.

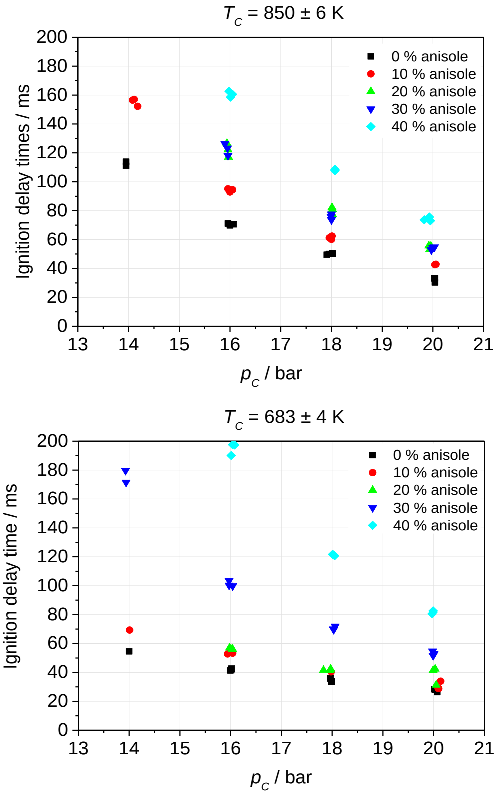

Figure 48 - Evolution of total ignition delays as a function of pressure for isooctane/anisole/O_2/inert mixtures at stoichiometric condition.

The effect of pressure is more pronounced at T_C = 683 K than T_C = 850 K. It can be explained by considering in a first approximation that at low temperatures the major reaction pathway for isooctane oxidation are the addition of the oxygen molecules to alkyl radicals to produce the peroxyalkyl radical, described by Reaction (28), leading to the LTC branching. At lower pressures, the decomposition of RO_2 to $R+O_2$ is faster, as the equilibrium constant of Reaction (28) is reduced. The rise of the pressure causes a shift of the NTC region to lower temperatures, and therefore reduces the temperature reached after first-stage ignition and increases the duration of the second stage of ignition.

- **Temperature effect**

The isooctane/anisole (60/40)/O_2/inert mixture was chosen to perform a detailed study which includes delay time measurements from low- to high-temperatures and sampling experiments. This mixture composition was defined considering that at the experimental conditions of sampling (p_C = 20 bar and T_C = 684 K) the ignition occurs in two stages, as shown in Figure 47. This choice allows the investigation of the reaction pathways relevant to low-temperature combustion, and the transition towards the intermediate temperature range, which are responsible for autoignition in modern engines and are closely related to the fuel's antiknock quality (6). The choice of the mixture composition roughly corresponds to the maximum allowed quantity of aromatics in SI fuels in the EU. The pressure profiles of isooctane/anisole (60/40) mixtures are shown in Figure

49. No direct modification of the ignition phenomenology is observed during the addition of anisole. However, the total heat release associated with first stage ignition is inferior at all temperatures to the pure isooctane cases, as seen by comparing Figure 44 and Figure *49*. Figure 50 illustrates the evolution of the total and first stage ignition delay time as a function of temperature for isooctane/anisole (60/40) mixtures at p_C = 20 bar and a comparison with pure isooctane. The mole fractions used to study the temperature effect on the ignition delay times are shown in the Table 20.

Table 20 - Mole fractions of isooctane/anisole/O_2/inert mixtures at p_C = 20 bar.

$x_{isooctane}$	$x_{anisole}$	x_{O2}	x_{Ar}	x_{N2}	x_{CO2}	T_C (K)
0.0112	0.0074	0.2062	0.7752	0.0000	0.0000	850
0.0111	0.0074	0.2079	0.6960	0.0775	0.0000	829
0.0111	0.0074	0.2061	0.6202	0.1551	0.0000	807
0.0111	0.0074	0.2058	0.5444	0.2313	0.0000	790
0.0111	0.0074	0.2061	0.4651	0.3102	0.0000	769
0.0111	0.0074	0.2061	0.3876	0.3877	0.0000	752
0.0111	0.0074	0.2061	0.3101	0.4652	0.0000	735
0.0111	0.0074	0.2062	0.2327	0.5426	0.0000	723
0.0111	0.0074	0.2062	0.1550	0.6202	0.0000	708
0.0111	0.0074	0.2065	0.0806	0.6943	0.0000	695
0.0111	0.0074	0.2062	0.0000	0.7752	0.0000	676
0.0111	0.0074	0.2062	0.0000	0.7366	0.0387	670
0.0111	0.0074	0.2062	0.0000	0.6977	0.0775	665

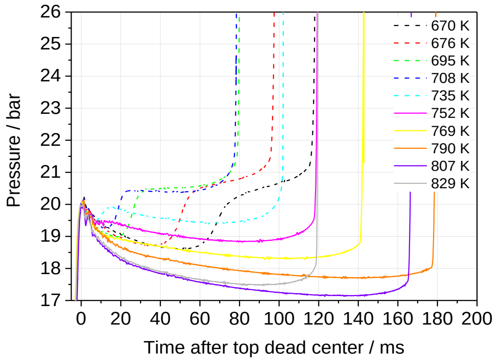

Figure 49 - Pressure profiles of isooctane/anisole (60/40)/O_2/inert mixtures at stoichiometric condition, at p_C = 20 bar and at different core gas temperatures (T_C).

It is observed that the addition of anisole to isooctane decreases the reactivity, and causes a global increase of both first-stage and total ignition delay along the total studied temperature range. The NTC zone is shifted towards lower temperatures in the presence of anisole, which is consistent with the observed reduced first stage ignition heat release in Figure 47. This could be caused by a conjunction of delayed low-temperature branching, and the reaction pathways associated with anisole becoming significant and forming HO_2 radicals and H_2O_2 molecules at lower temperatures than in the case of isooctane. A first interpretation of this effect is that, following the reaction flux diagram proposed by Wagnon et al. (230), at the lowest temperatures and in co-oxidation conditions, abstraction of a hydrogen on the methoxy group is likely, leading to the formation of the anisyl radical, which can form benzaldehyde after internal isomerization into the benzoxy radical. This reaction pathway consumes radicals without leading to the formation of branching agents, and therefore constitutes a radical sink. Anisole can therefore act as a sink for the radical pool formed by isooctane, and therefore slow down the reaction pathways leading to first-stage ignition. This kinetic analysis will however be enhanced using the kinetic model presented in the next section.

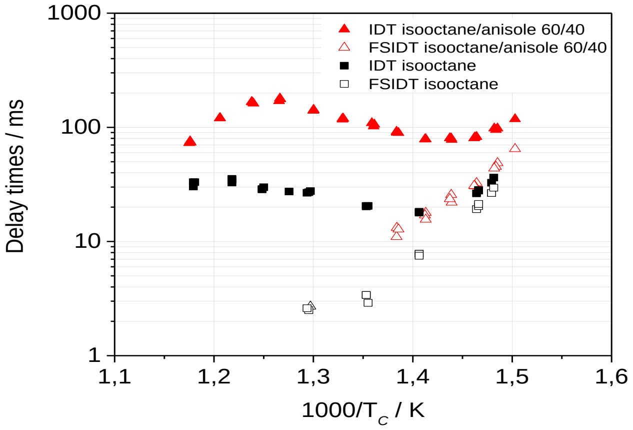

Figure 50 - Comparison of the evolution of first stage ignition delays (open symbols) and total ignition delays (full symbols) of isooctane/anisole (60/40)/O_2/inert mixtures (black symbols) and isooctane/O_2/inert mixtures (red symbols) with temperature, at pc = 20 bar.

Figure 51 shows a comparison of this study and the anisole previous results at stoichiometric and lean conditions. The anisole ignition delay times from Herzler and Shu at equivalence ratio 0.5 agree very well with each other. On the other hand, the results from Herzler and Büttgen present a discrepancy especially in the region from 1000 to 833 K. To the author´s knowledge, there are no published anisole autoignition experimental studies at low temperature, which makes a quantitative comparison of this work and the previous impossible. Besides that, the comparison of ignition delay times data from different Rapid Compression Machines or shock tubes is quite challenging, considering that there are many parameters that could be changed as compression time, type of piston or diluent gas. In addition, discrepancies between experimental results from Rapid Compression Machines at high temperature and from Shock Tubes at low temperature have been reported (175,370). They can primarily be explained by the fact that both reactors show deviations from ideal behavior in their common temperature range. Shock tubes have difficulties operating at test times superior to 1 ms, mostly because of interactions with the boundary layer causing a steady increase of the pressure in the test section, and resulting in shorter ignition delay times than in ideal conditions (371). As discussed previously, heat loss takes place during ignition delays in RCMs, and results in longer measured ignition delay measurements than in ideal conditions.

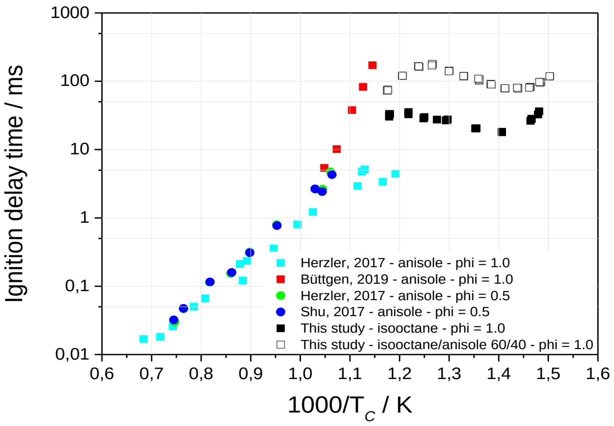

Figure 51 - Comparison of evolution of total ignition delay time of this study and anisole previous works at different equivalence ratio and at p_C = 20 bar.

4.2.2. Sampling/speciation

A total of 18 samples were taken at different times during the ignition delay as shown in Figure 52. The sampling times were chosen in order to cover all the phases of the ignition delay time and to be able to identify the potential different species formed before the first stage of ignition, during the cool flame, between the cool flame and the total ignition delay and during the ignition.

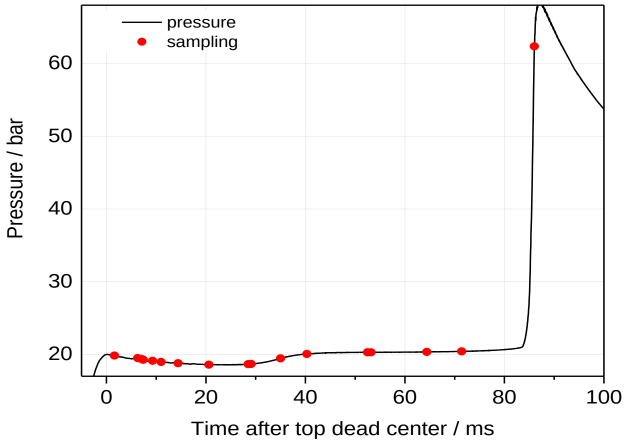

Figure 52 - Sampling experiment times and pressure profile of the mixture isooctane/anisole (60/40)/O_2/N_2 at stoichiometric condition, p_C = 20 bar and at T_C = 684 K.

Figure 53 shows an example of the chromatogram using the UB5P column and at 71.4 ms after top dead center. All the 27 products identified during the 18 samples, using the same column, are listed in the Table 21 including their structure and the retention time.

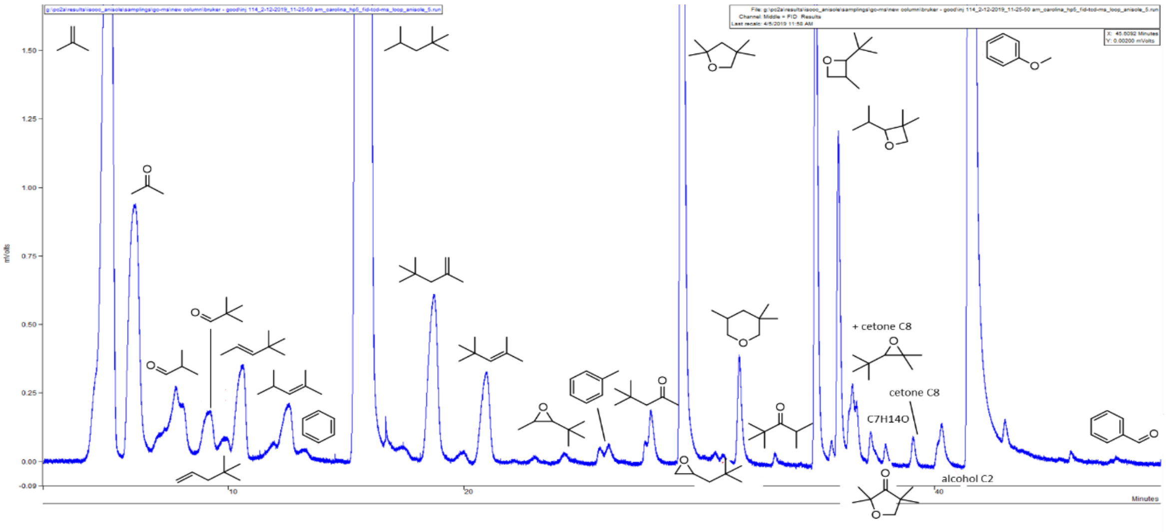

Figure 53 - Chromatogram of isooctane/anisole (60/40) sampling at 71.4 ms using UB5P column and the FID detector.

Table 21 - Oxidation products identified during sampling experiments of the stoichiometric mixture isooctane/anisole (60/40)/O_2/N_2 using UB5P column. Black: isooctane products, blue: anisole products and red: isooctane and anisole products.

Retention time	Nomenclature	Structure	Retention time	Nomenclature	Structure
4.746	2-methyl-1-propene	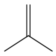	29.024	2,2,4,4-tetramethyltetrahydrofuran	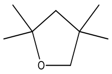
5.736	acetone	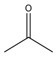	30.726	2,2-dimethylpropyl-oxirane	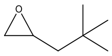
7.308	2-methyl-propanal	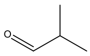	31.422	3,3,5-trimethyltetrahydro-2H-pyran	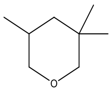
8.781	2,2-dimethyl-propanal	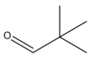	32.941	2,2,4-trimethyl-3-pentanone	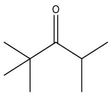
9.486	4,4-dimethyl-1-pentene	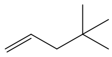	34.714	2-tert-butyl-3-methyloxetane	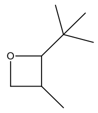
10.224	4,4-dimethyl-2-pentene	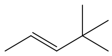	35.056	ethylbenzene	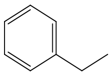
12.233	2,4-dimethyl-2-pentene	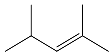	35.673	3,3-dimethy-2-isopropyloxetane	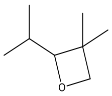
12.784	benzene	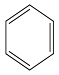	36.004	*o*-xylene	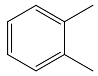
15.725	isooctane	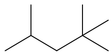	36.227	3-tert-butyl-2,2-dimethyloxirane +cetone C8	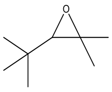
18.314	2,4,4-trimethyl-1-pentene	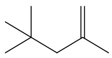	37.632	Dihydro-2,2,4,4-tetramethyl-3(2H)-furanone	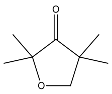
20.605	2,4,4-trimethyl-2-pentene	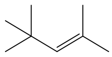	41.318	anisole	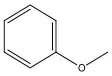
23.951	2-tert-butyl-3-methyl-oxirane	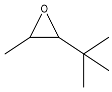	47.263	benzaldehyde	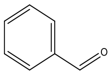

25.541	toluene	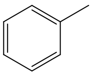	51.569	1,3-benzodioxole	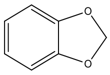
27.398	4,4-dimethyl-2-pentanone	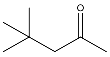			

Figure 54 shows a chromatogram from a sample obtained at 71.4 ms using the PBQ column for the mixture isooctane/anisole (60/40)/O_2/N_2. Even though the column is appropriated to products from C_2 to C_6, some species can be identified in both columns, these results being used to validate as complementary results. All the 37 species identified using this column are listed in Table 22.

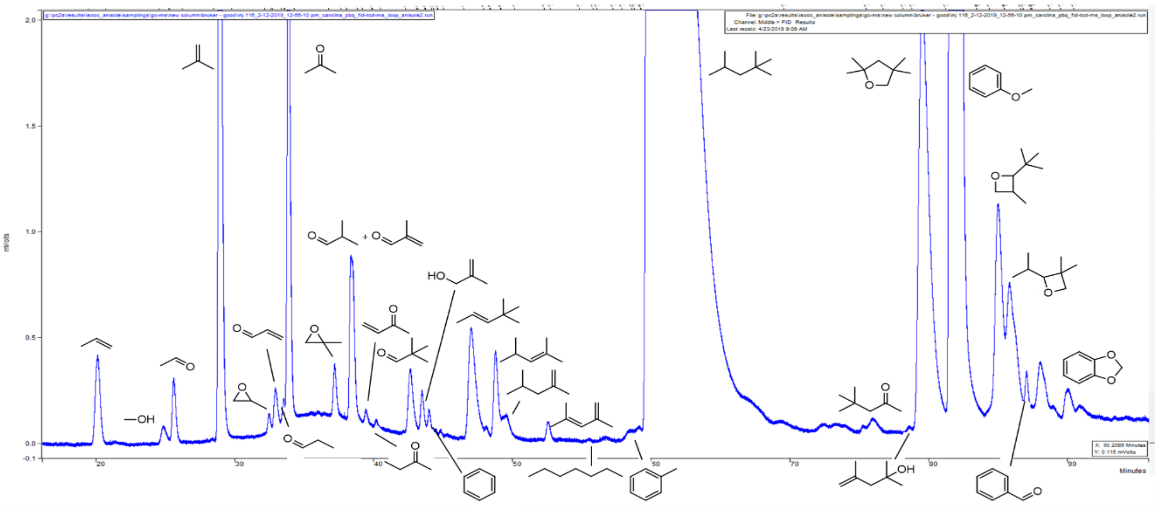

Figure 54 - Chromatogram of isooctane/anisole 60/40 sampling at 71.4 ms using PBQ column.

Table 22 - Oxidation products identified during sampling experiments of the stoichiometric mixture isooctane/anisole (60/40)/O_2/N_2 using PBQ column. Black: isooctane products, blue: anisole products and red: isooctane and anisole products.

Retention time	Nomenclature	Structure	Retention time	Nomenclature	Structure
19.649	propene	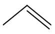	43.646	benzene	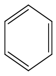
20.852	allene (propadiene)	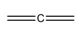	49.355	2,4-dimethyl-1-pentene	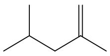
21.411	propyne	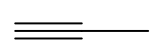	52.154	2,4-dimethyl-1,3-pentadiene	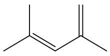
24.457	methanol	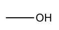	54.978	heptane	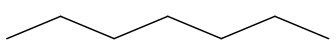
25.228	acetaldehyde	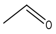	58.317	toluene	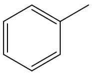
28.634	2-methyl-1-propene	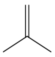	60.741	isooctane	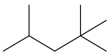
32.093	methyl oxirane	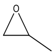	75.708	4,4-dimethyl-2-pentanone	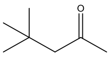
32.555	2-propenal +furan	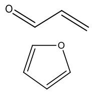	78.26	2,4-dimethyl-4-penten-2-ol	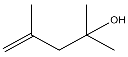
33.185	propanal	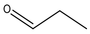	78.35	ethylbenzene	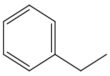
33.62	acetone	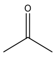	79.042	2,2,4,4-tetramethyltetrahydrofuran	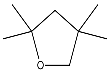

36.824	2,2-dimethyl-oxirane	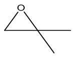	79.367	*o*-xylene	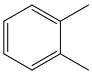
38.217	2-methyl-propanal + methacrolein	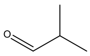 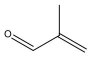	81.861	anisole	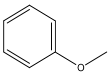
39.71	methyl vinyl ketone	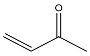	83.832	2,4-dimethyl-1-heptene	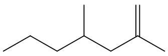
40.509	2-butanone	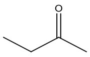	84.822	2-tert-butyl-3-methyloxetane	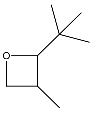
42.301	2,2-dimethyl-propanal	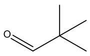	85.651	3,3-dimethy-2-isopropyloxetane	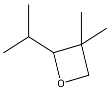
43.108	2-methyl-2-propen-1-ol	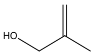	86.816	benzaldehyde	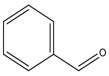
46.728	4,4-dimethyl-2-pentene	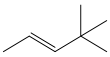	89.295	1,3-benzodioxole	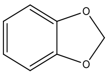
48.545	2,4-dimethyl-2-pentene	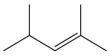			

4.2.3. Kinetic modeling

On the basis of the Co-Optima model presented in section 4.1, a kinetic model for the co-oxidation of anisole was developed, in collaboration between U. Zaragoza and Lawrence Livermore National Laboratory. In this purpose, reaction rate coefficients for the H-atom abstraction reactions of the principal pool radicals on both the methoxy group and the ortho position of anisole were evaluated from ab initio methods. The potential energy surfaces for the addition of oxygen to both the anisyl and the ortho-methoxyphenyl radicals were also explored, the relevant reaction rate coefficients being evaluated. The development of this mechanism being a collaborative work, it is not reproduced here, but is described in detail in (232). This model will however be used to understand the most relevant pathways for anisole co-oxidation in the following pages.

Figure 55 displays the simulated and the experimentally obtained delay times, shown previously in Figure 46. The model captures well the increase in ignition delay at the low temperature condition, the simulations being in very good agreement with the experiments. It is however not the case at the higher temperature condition, where the effect of anisole addition is underestimated.

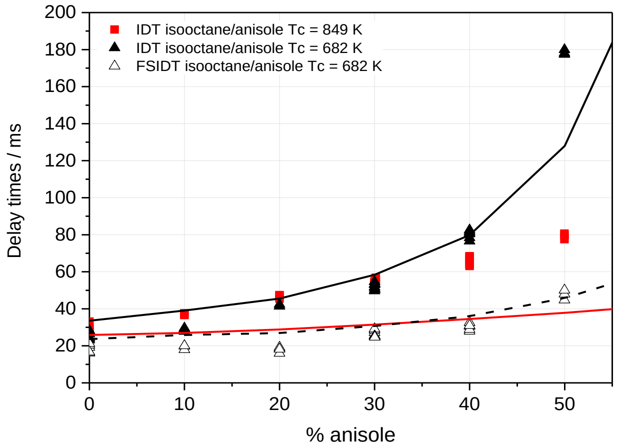

Figure 55 - Evolution of the modeled (lines) and experimental (symbols) first-stage and total ignition delay times of isooctane/anisole/O_2/inert mixtures at two temperatures relevant to low-temperature and intermediate temperature combustion, as a function of anisole molar content in the fuel. p_{TDC} = 20 bar, Φ = 1.

Similarly, Figure 56 displays the comparison of the evolution of the first-stage and total ignition delays with temperature for the isooctane/anisole (60/40)/O_2/inert and pure isooctane. The model captures these features, the agreement being very good at the low temperatures, and within a factor of two at the highest temperatures.

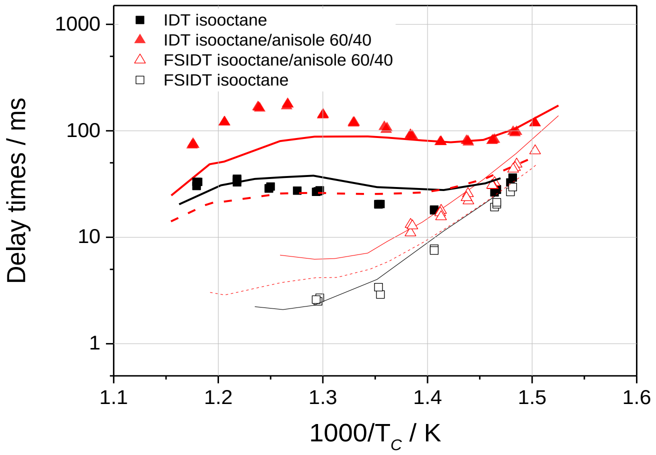

Figure 56 - Evolution of first-stage and total ignition delays of isooctane/O_2/inert (black triangles) and isooctane/anisole (60/40)/O_2/inert mixtures (red squares), as a function of temperature. P_{TDC} = 20 bar, Φ = 1. Full lines correspond to the updated model, dashed lines the initial model.

Figure 57 shows the results of the sampling experiments as well as the model predictions. It can be observed that both fuels are converted during the first-stage ignition, to the extent of about one third for isooctane, and one fourth for anisole. The current isooctane model seems to overestimate the conversion of isooctane during the first-stage, while the one of anisole is captured accurately. It should be noted that the presented mole fraction profiles were not normalized in time on the total ignition delay duration. This shows the good performance of the model in capturing both the first-stage and total ignition delay in these conditions.

The overestimated conversion of isooctane can however be correlated to the too high reactivity of the model in the intermediate temperature region. It results in a deviation on the isooctane-specific C_8 intermediates of approximately a factor of two, the branching between the different products being however accurate, as shown in Figure 57. Very low quantities of aromatic products were detected during the sampling experiments, but small amounts of benzaldehyde, benzene and toluene were however quantified. Trace amounts of benzodioxole were also detected, being however too small to yield reliable quantification. The model accurately predicts the low quantities of aromatic products that were detected, given the experimental uncertainty.

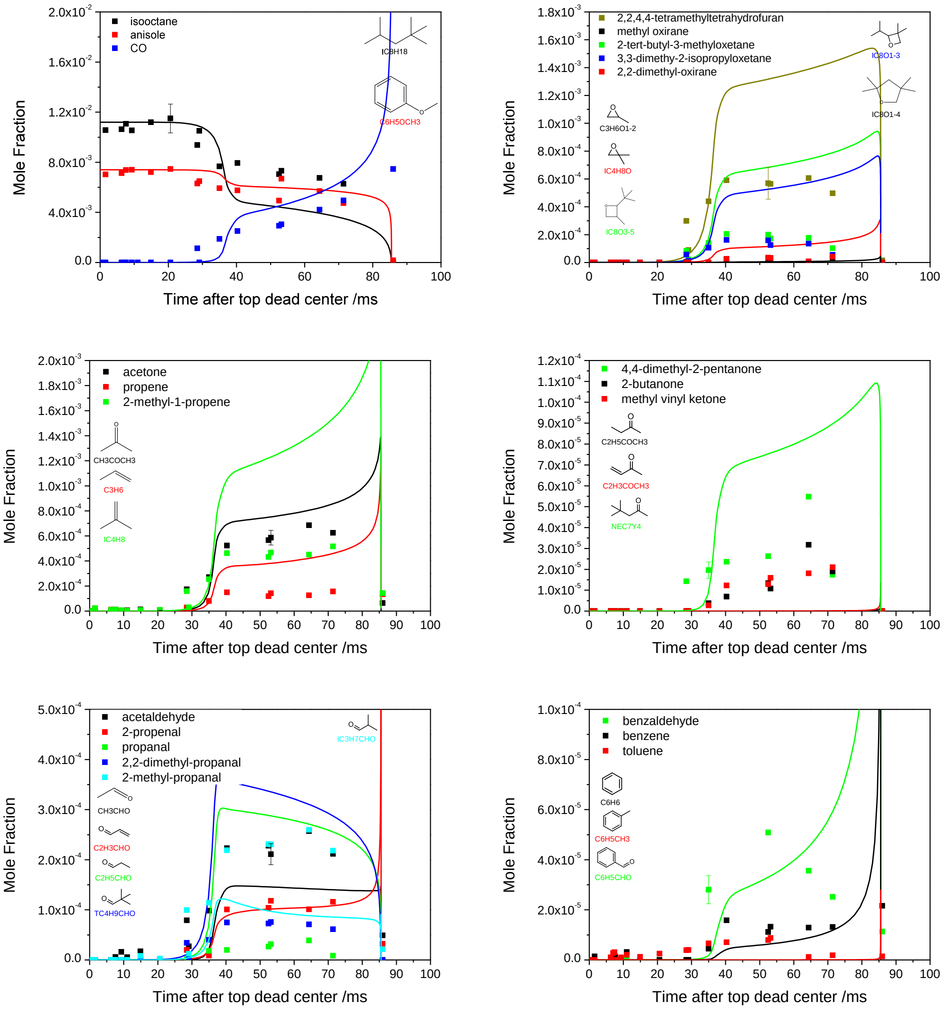

Figure 57 - Experimental and simulated (lines) mole fraction profiles of the fuels and intermediates formed during two-stage ignition of isooctane/anisole (60/40)/air mixture at p_C = 20 bar, and T_C = 684 K.

The conversions of anisole and isooctane start around 30 ms after the top dead center time, which coincides with the first-stage ignition, as shown in Figure 52. They increase along with the time after top dead center and around 85 ms, the total ignition delay time, the mole fraction of anisole and isooctane are respectively 0.00099 and 0.0012, i.e. a conversion of 87% of anisole and of 90% of isooctane. Carbon monoxide starts to be formed at around 25 ms and its mole fraction increases monotonically until the total ignition delay time. The most abundant stable intermediates of oxidation formed are acetone, 2-methyl-1-propene and 2,4,4-

trimethyl-pentene. The carbon balance associated with the sampling results presented in Figure 57 can be found in the annexes, and shows a maximum deviation of about 20 % before the ignition, corresponding to samples acquired after the first-stage ignition. The main reason for the deviation in the carbon balance are expected to be formaldehyde and CO_2, which are not detectable with the FID. Both isooctane and anisole are indeed expected to yield large quantities of formaldehyde.

A reaction pathway analysis has been performed in the conditions relevant to the sampling experiments, i.e. p_C = 20 bar, T_C = 684 K, phi = 1, after a conversion of 5% of anisole. H-abstraction on anisole represents the largest contribution to anisole conversion, leading mostly to the anisyl radical and to a smaller extent to the ortho-methoxyphenyl radical. The resulting ortho-methoxyphenyl radical is mostly converted to a methoxycyclopentadienyl and the ortho-methoxyphenoxy radical. These pathways mainly form a methoxycyclopentadienyl dimer and ortho-hydroxy-methoxybenzene (see Figure 58), whose boiling points and polarities probably render detection difficult through GC techniques. These would then result in deposits, which could be detrimental to engine performance. The anisyl radical mostly adds to O_2, yielding the peroxyphenyl radical or hydroperoxyanisyl. Both can form the phenoxy radical, which in turn converts to cyclohexadienone or phenol, but most of the peroxyphenyl radical reacts into a non-cyclic C_5 species.

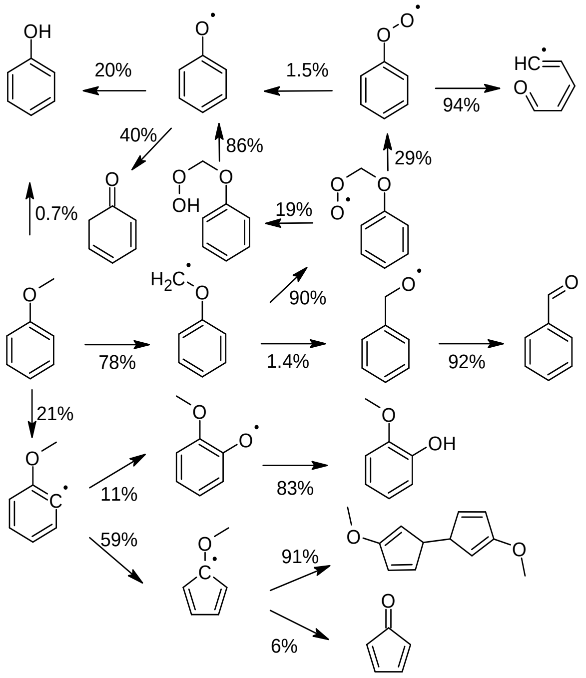

Figure 58 - Reaction Pathway Analysis of anisole co-oxidation in the conditions of the sampling experiments.

In order to identify the most sensitive reactions on the IDTs prediction of two-stage ignition of isooctane/anisole blends, dual brute-force sensitivity analysis was performed on the first-stage, second-stage and total ignition delay. The second-stage ignition delay is defined as the length of time between the first-stage and final ignition events. This method allows unraveling the reactions that are most relevant to the first-stage ignition event. It is therefore a stronger tool than sensitivity analysis on the total ignition delay, which is integrated over the whole duration (and temperature/composition trajectory) of the ignition delay. The focus of this work being the co-oxidation of anisole, this sensitivity analysis was limited to the anisole sub-mechanism reactions. Figure 59 shows the results of this analysis. The results highlight the high sensitivity of the H-atom abstraction reactions by ȮH on the prediction of the FSIDT and IDT, having a large sensitivity on both first-stage and second-stage ignition delay. Both H-atom abstraction reactions from anisole have a positive sensitivity factor on the first-stage ignition delay, which indicates that the increase of the first-stage ignition delay caused by the addition of anisole is correlated to a competition with isooctane on the reactivity with ȮH. It is also of importance that 10 of the 11 most important reactions in terms of sensitivity on both ignition delays are part of the elementary reactions that have been investigated ab initio for the development of the current model, the pathways relevant to O_2 addition on anisyl and ortho-methoxyphenyl radicals being largely represented.

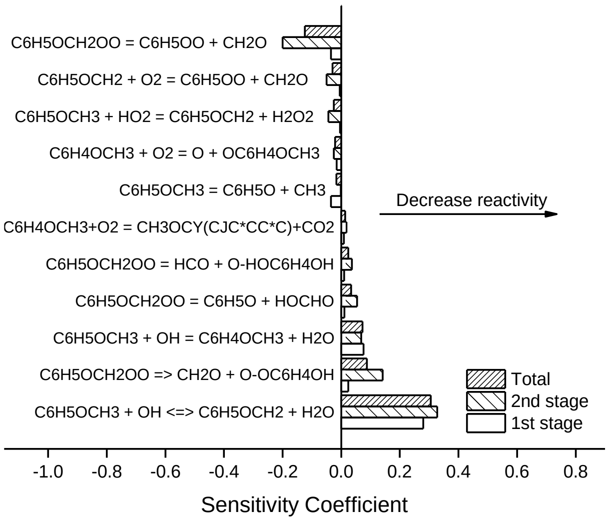

Figure 59 - «Brute-force» sensitivity analysis to first-stage, second-stage and total ignition delay times. p_C = 20 bar, Φ = 1, T_C = 684 K.

4.2.4. Conclusions

In an attempt to clarify the kinetic effect of the addition of anisole to practical fuels, an experimental and kinetic modeling study of anisole co-oxidation with isooctane has been performed. This study showed that:

- Addition of anisole leads to a pronounced increase in both the first-stage and total ignition delays of isooctane,

- While the ignition delays increase over the whole temperature range, a 60/40 isooctane/anisole blend still shows Negative Temperature Coefficient behavior,

- Anisole is partly converted during the first-stage ignition, but yields limited amounts of aromatic products,

- A new model, based on previous literature and newly calculated rate constants, shows good agreement with the experimental data, and helps understanding the most important reaction pathways involved in the co-oxidation of anisole,

- The model also allowed identifying the most sensitive reactions in the prediction of both stages of the ignition delay.

On a more general note, this study demonstrates the importance of co-oxidation reaction pathways in the ignition of anisole as part of a fully-blended fuel. While the high RON of anisole (103, as reported in (372)) suggests it could be an interesting blendstock, one should however note that in co-oxidation conditions, two-stage ignition and NTC behavior are still observed.

4.3. Isooctane/*O*-CRESOL

4.3.1. RCM experiments

The *o*-cresol co-oxidation experiments were conducted at stoichiometric conditions and likewise anisole studies, the effect of three parameters on ignition delay times were evaluated: the temperature at the end of the compression, the compressed pressure and the *o*-cresol composition.

- **Composition effect**

Reactant mole fractions for isooctane/*o*-cresol blends used to investigate the effect of *o*-cresol addition into isooctane mixtures are given in Table 23, together with the associated compressed temperature.

Table 23 - Mole fraction of isooctane/o-cresol/O₂/inert mixtures at p_C = 20 bar.

% *o*-cresol	$x_{isooctane}$	$x_{o\text{-}cresol}$	x_{O2}	x_{Ar}	x_{N2}	***Tc* (K)**
0	0.0165	0.0000	0.2064	0.7767	0.0000	848
10	0.0153	0.0017	0.2065	0.7765	0.0000	848
20	0.0140	0.0035	0.2064	0.7765	0.0000	849
30	0.0126	0.0054	0.2063	0.7765	0.0000	849
35	0.0119	0.0064	0.2062	0.7755	0.0000	849
40	0.0111	0.0074	0.2062	0.7765	0.0000	853
0	0.0165	0.0000	0.2066	0.0000	0.7768	683
10	0.0153	0.0017	0.2065	0.0000	0.7769	687
20	0.0140	0.0035	0.2064	0.0000	0.7761	687
30	0.0126	0.0054	0.2063	0.0000	0.7757	687
35	0.0119	0.0064	0.2062	0.0000	0.7755	687

The effect on the ignition delay times of *o*-cresol addition to isooctane is shown in Figure 60 at two different temperatures.

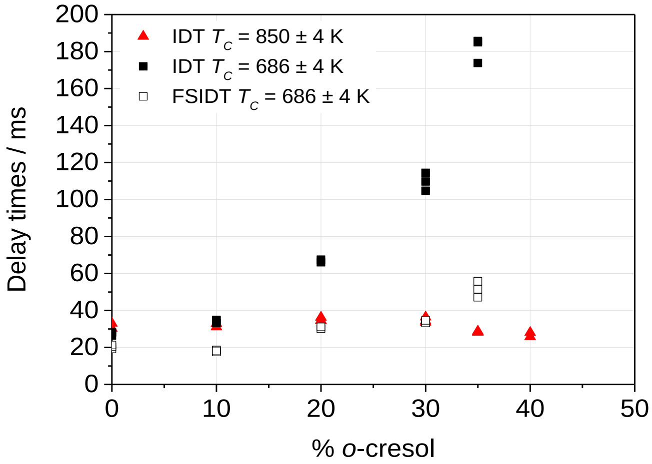

Figure 60 - Ignition delay times of isooctane/o-cresol/O$_2$/inert mixtures for an increasing amount of o-cresol at p_C = 20 bar and two different core gas temperatures: T_C = 850 ± 4 K (triangles) and T_C = 686 ± 4 K (squares).

The associated pressure profiles are shown in Figure 61. *o*-Cresol appears to influence the reactivity in a similar way to anisole: while the ignition phenomenology is unaltered, the extent of first stage of ignition is reduced when *o*-cresol is blended in. However, the effect of replacing isooctane by the LDC on the first-stage of ignition is observed earlier, i.e., only 20% of *o*-cresol is already enough to reduces the pressure jump, and associated heat release of the first stage of ignition.

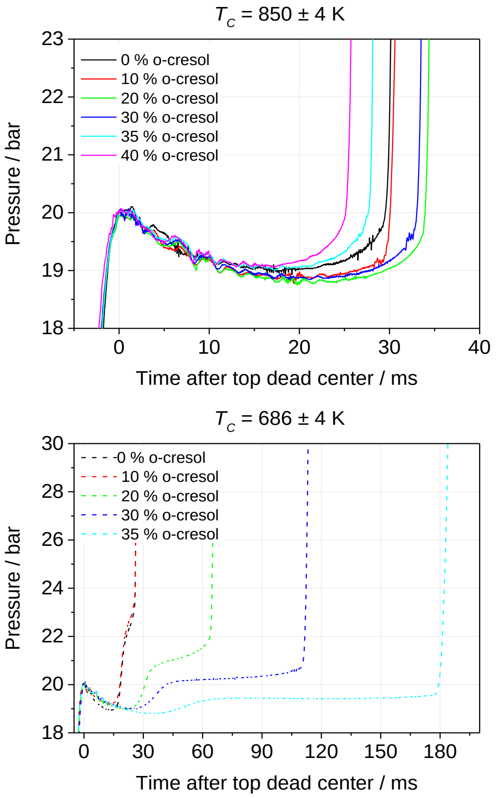

Figure 61 - Pressure profiles for isooctane/o-cresol/O$_2$/inert mixtures at stoichiometric condition and at p_C = 20 bar.

- **Pressure effect**

The effect of the pressure on the total ignition delay was studied at high and low temperature for five different *o*-cresol compositions.

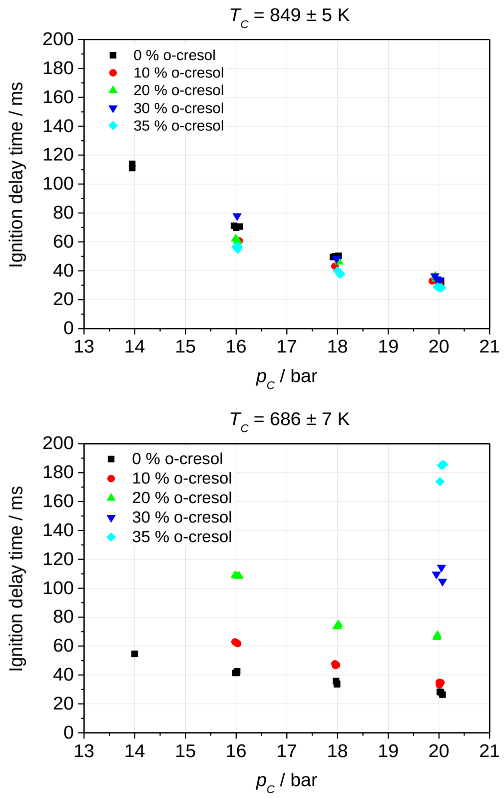

Figure 62 - Evolution of total ignition delays as a function of pressure for isooctane/o-cresol/O_2/inert mixtures at stoichiometric condition.

Figure 62 depicts the effect of the pressure at the end of the compression on the total ignition delay times, at two different temperatures. As it was seen for the isooctane/anisole mixtures, the effect of pressure is more pronounced at low temperatures and longer IDTs are observed as the pressure decreases. At all temperatures the total ignition delay times are strongly pressure-dependent. This behavior can be explained by the same reaction pathway for isooctane oxidation at low temperatures mentioned in the isooctane/anisole mixtures section. Unlike to isooctane/anisole mixtures, the isooctane/*o*-cresol mixtures are not affected by the substitution of isooctane by *o*-cresol at high temperature, until 35 % of *o*-cresol. Finally, at low temperatures even a low concentration of *o*-cresol is enough to inhibit the reactivity of this surrogate.

- **Temperature effect**

The compositions of the isooctane/*o*-cresol mixtures used in the study of the dependency of the ignition delay with temperature are included in Table 24 as well as the calculated temperature at the end of the compression.

Table 24 - Mole fractions of isooctane/o-cresol/O_2/inert mixtures at p_C = 20 bar.

$x_{isooctane}$	$x_{o\text{-}cresol}$	x_{O2}	x_{Ar}	x_{N2}	x_{CO2}	*Tc* (K)
0.0140	0.0035	0.2064	0.7765	0.0000	0.0000	849
0.0140	0.0035	0.2064	0.6985	0.0776	0.0000	826

0.0140	0.0035	0.2064	0.6209	0.1552	0.0000	805
0.0140	0.0035	0.2064	0.5433	0.2328	0.0000	786
0.0140	0.0035	0.2064	0.4657	0.3104	0.0000	769
0.0140	0.0035	0.2064	0.3880	0.3880	0.0000	752
0.0140	0.0035	0.2064	0.3104	0.4657	0.0000	740
0.0140	0.0035	0.2064	0.0000	0.7761	0.0000	688

Figure 63 shows the comparison of the isooctane and isooctane/*o*-cresol 80/20 mixtures pressure profiles at different studied temperatures. The 80/20 composition was imposed by the low volatility of *o*-cresol.

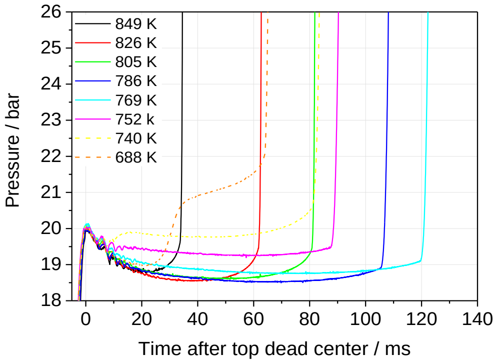

Figure 63 - Pressure profiles for isooctane/o-cresol (80/20)/O_2/inert mixtures (right) at p_C = 20 bar and in stoichiometric conditions.

A transition from two-stage ignition at low temperatures and single-stage ignition at high temperatures is also observed. This transition occurs around 740 K where a shallow cool flame can be detected. Figure 64 shows a comparison of the ignition delay times as a function of the inverse of the temperature for isooctane/*o*-cresol (80/20) and isooctane mixtures.

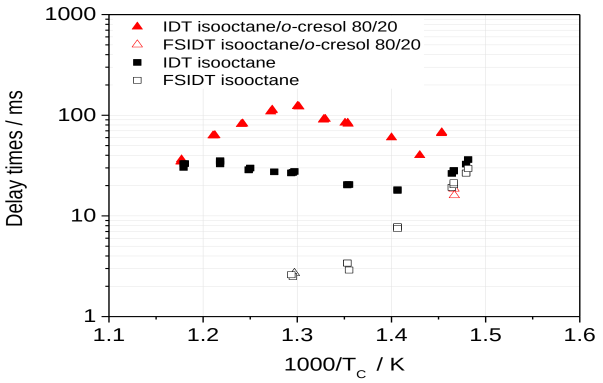

Figure 64 - Comparison of the evolution of first stage ignition delays (open symbols) and total ignition delays (full symbols) of isooctane/o-cresol (80/20)/O_2/inert mixtures (squares) and isooctane/O_2/inert mixtures (triangles) with temperature, at p_c = 20 bar.

The trend of the isooctane/*o*-cresol total ignition delay time curve recalls the phenomenology of ignition of pure isooctane with a slight shift of the NTC region towards lower temperatures, as well as a reduction of the temperature range associated with NTC behavior. Moreover, it appears that the presence of *o*-cresol increases the slope in this region, making the reactivity more dependent on the temperature. As shown the Figure 63 (right) the first stage of ignition is only well defined at 688 K. As a consequence of that, it is represented by a single triangle in Figure 64 and it makes a comparison of the apparent activation energy (or slope) against pure isooctane not possible. The reduction of the NTC region, and the limited cases where first-stage ignition could be observed, for a such low concentration of *o*-cresol make it apparently a good candidate to blend it into a gasoline as an antiknock additive, considering that fuels with high reactivity at high temperatures and low reactivity at low temperatures are desirable for modern spark ignition engines. However, during the *o*-cresol experiments a considerable amount of soot was observed inside the combustion chamber, raising concern about addition of this compound to commercial gasolines, and also increasing the uncertainties associated with these measurements. Therefore, it was decided not to proceed further with sampling experiments and kinetic modeling for this fuel.

4.3.2. Conclusions

- Addition of *o*-cresol decreases the isooctane reactivity without changing drastically the phenomenology of ignition of pure isooctane;

- The temperature range at which first-stage ignition and NTC behaviour can be observed is however reduced, even with 20% content of *o*-cresol, therefore demonstrating interesting properties in the suppression of LTC chain-branching which is sought;

- Soot deposition inside the combustion chamber raises concerns about the use of this compound as a bioblendstock;

- The interest in investigating the reactivity of this molecule to develop kinetic models for LDCs, remains due to the formation of a large amount of cresol during the combustion of other aromatics as anisole.

- Finally, the results presented here provide data for further validation of o-cresol combustion models in engine-relevant conditions.

4.4. Isooctane/PRENOL

4.4.1. RCM experiments

Stoichiometric isooctane/prenol/O_2/inert mixtures were compressed at pressures between p_c = 14 and p_c = 20 bar and temperatures from T_C = 675 to T_C = 852 K.

- **Composition effect**

The compositions of the mixtures used in the study of the effect of the mixture composition on the reactivity are shown in Table 25.

Table 25 - Mole fractions of isooctane/prenol/O_2/inert mixtures at p_C = 20 bar.

% prenol	$x_{isooctane}$	x_{prenol}	x_{O2}	x_{Ar}	x_{N2}	***Tc* (K)**
0	0.0165	0.0000	0.2064	0.7767	0.0000	847
10	0.0155	0.0017	0.2065	0.7763	0.0000	851
20	0.0144	0.0036	0.2063	0.7763	0.0000	850
30	0.0131	0.0056	0.2061	0.7763	0.0000	848
40	0.0118	0.0078	0.2060	0.7763	0.0000	851

50	0.0103	0.0103	0.2058	0.7763	0.0000	851
0	0.0165	0.0000	0.2066	0.0000	0.7768	682
10	0.0155	0.0017	0.2065	0.0000	0.7763	683
20	0.0144	0.0036	0.2063	0.0000	0.7763	681
30	0.0131	0.0056	0.2061	0.0000	0.7763	682
40	0.0118	0.0078	0.2060	0.0000	0.7763	682
50	0.0103	0.0103	0.2058	0.0000	0.7763	683

Figure 65 shows the relation between the ignition delay and the fraction of prenol blended into isooctane mixtures. At high temperatures, the reactivity slightly increases with the addition of prenol but at low temperatures, prenol displays a strong inhibiting effect on the reactivity of isooctane. For a given set of P_C and T_C, the results show that the reactivity of these mixtures is much more sensitive to the prenol concentration at low temperatures than at high temperatures.

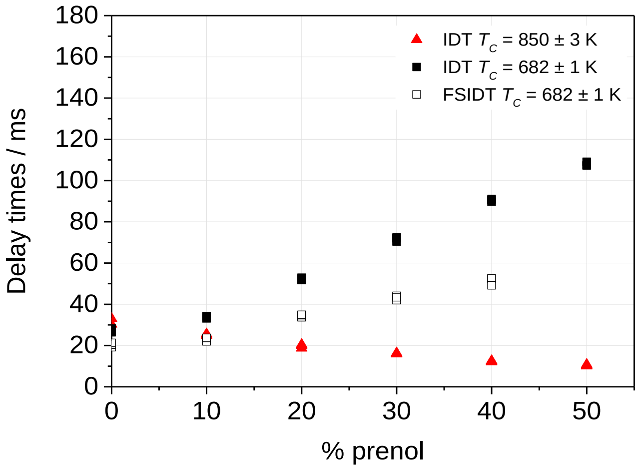

Figure 65 - Ignition delay times of isooctane/prenol/O_2/inert mixtures for increasing amounts of prenol at p_C = 20 bar and two different core gas temperatures: T_C = 850 ± 3 K (triangles) and T_C = 682 ± 1K (squares).

The pressure profiles at all prenol compositions investigated at 20 bar are shown in Figure 66 at two different temperatures. Similar to the pure isooctane, a transition from two stage ignition at low temperatures toward single-stage ignition is observed. The increase in prenol content inside the mixture results in a decrease of the pressure jump after the first stage of ignition and consequently, the total ignition delay time are longer at low temperature. Unlike the isooctane/anisole and isooctane/*o*-cresol case, even a low prenol concentration, i.e. 10 %, can affect the first stage of ignition. The heat release associated to the first stage of ignition is monotonically reduced along with prenol addition and, therefore longer total ignition delay times are observed. In addition, the ignition delay of the blend with more than 50 % of prenol, were limited to the high temperature region, as further decrease in the compressed temperature resulted in ignition delay times longer than 200 ms, the commonly accepted limit for the adiabatic core hypothesis.

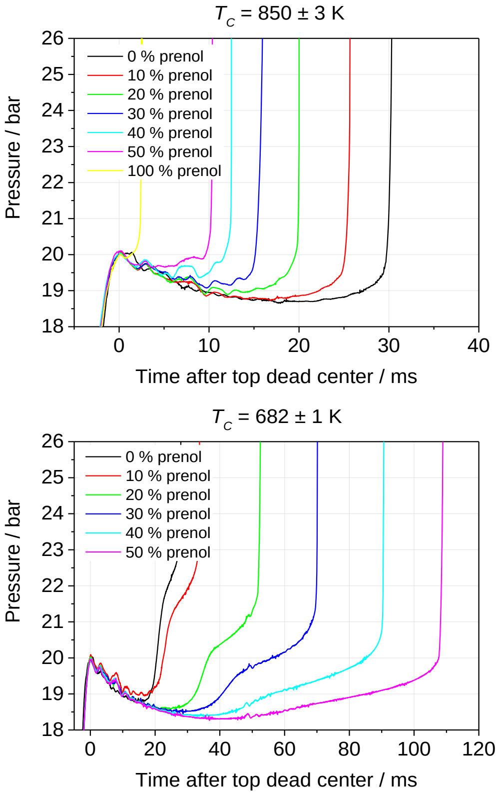

Figure 66 - Pressure profiles for isooctane/prenol/O_2/inert mixtures at stoichiometric condition and at p_C = 20 bar.

- **Pressure effect**

The evolution of the total ignition delay times as a function of the pressure for isooctane/prenol mixtures at all studied prenol compositions are shown in Figure 67.

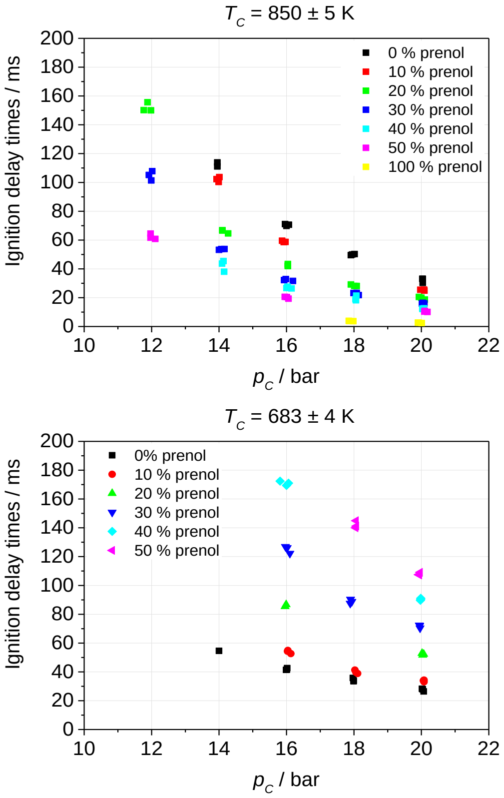

Figure 67 - Evolution of total ignition delays as a function of pressure for isooctane/prenol/O_2/inert mixtures at stoichiometric conditions.

Overall, at all studied temperatures the total ignition delay times decrease as the pressure increases. However, this effect is limited by prenol addition at high temperatures as a consequence of the reaction pathway for isooctane oxidation, Equation (42), as discussed in the anisole section.

- **Temperature effect**

The composition of the isooctane/prenol (50/50) mixtures used to perform this study are summarized in Table 26.

Table 26 - Mole fractions of isooctane/prenol/O_2/inert mixtures at p_C = 20 bar.

$x_{isooctane}$	x_{prenol}	x_{O2}	x_{Ar}	x_{N2}	x_{CO2}	T_C (K)
0.0103	0.0103	0.2058	0.7763	0.0000	0.0000	852
0.0103	0.0103	0.2058	0.6963	0.0774	0.0000	830
0.0103	0.0103	0.2058	0.6189	0.1547	0.0000	808
0.0103	0.0103	0.2058	0.5416	0.2321	0.0000	787
0.0103	0.0103	0.2058	0.4642	0.3095	0.0000	770
0.0103	0.0103	0.2058	0.3868	0.3868	0.0000	753
0.0103	0.0103	0.2058	0.3095	0.4642	0.0000	724
0.0103	0.0103	0.2058	0.2321	0.5416	0.0000	722
0.0103	0.0103	0.2058	0.1547	0.6189	0.0000	708
0.0103	0.0103	0.2058	0.0774	0.6963	0.0000	696
0.0103	0.0103	0.2058	0.0000	0.7763	0.0000	682

0.0103	0.0103	0.2058	0.0000	0.7350	0.0387	675

The pressure profile of and 50/50 isooctane/prenol mixtures are shown in Figure 68, and can be compared to Figure 44. As discussed before, pure isooctane displays transition from single-stage to two-stage ignition as a function of temperature. This feature can also be observed for isooctane/prenol mixture, the pressure increases related to the cool flame being much fainter.

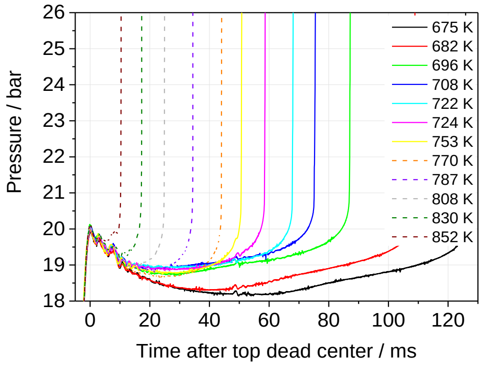

Figure 68 - Pressure profile of isooctane/prenol (50/50)/O_2/inert mixtures (right) at p_C = 20 bar and in stoichiometric conditions.

The total and first stage of ignition of the 50/50 isooctane/prenol mixtures were measured between 675 and 852 K and are shown in Figure 69.

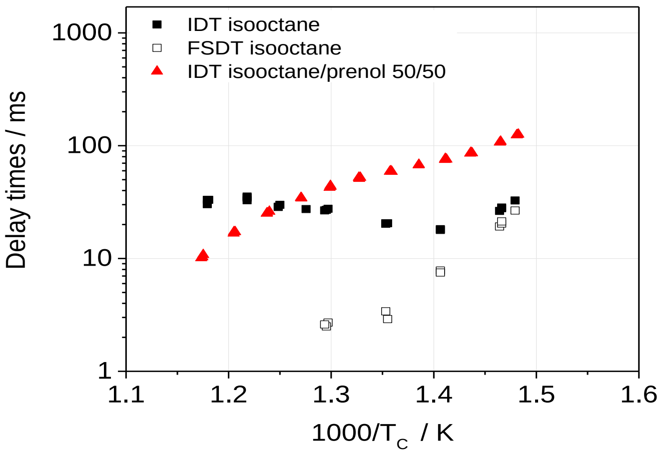

Figure 69 - Comparison of the evolution of first stage ignition delays (open symbols) and total ignition delays (full symbols) of isooctane/prenol (50/50)/O_2/inert mixtures (red symbols) and isooctane/O_2/inert mixtures (black symbols) with temperature, at p_C = 20 bar.

Figure 69 shows that there is an inhibiting effect of prenol at low to intermediate temperature i.e., from 675 to 787 K. On the other hand, at high temperatures the reactivity is increased with comparison to pure isooctane. No NTC was observed, a monotonic decrease of the temperature coefficient (slope) is observed in the region from 689 to 800 K and a subsequent increase of the slope at high temperature (>800 K). This reactivity feature demonstrates large benefits of the addition of prenol to a fuel blend, and is consistent with the observed octane hyperboosting effect. In modern turbocharged engines, high octane sensitivity is sought:

Therefore, a high ignition delay at low temperatures, and low ignition delay at high temperatures is a very positive aspect.

This important effect of prenol on the reactivity of isooctane can be discussed as follows: The relative position of the double bond and the hydroxyl group in the prenol molecule suggest that after an H-atom abstraction reaction, the formation of the conjugated aldehyde (3-methyl-2-butenal) or the diene (2-methyl-1,3-butadiene) would be favoured, as shown in Figure 21. Both of these products form radicals stabilised by resonance, reducing reactivity in the low-temperature regime. Their formation will hence constitute a radical sink that will not contribute to overall chain branching in the low temperature region. Their formation can however be an important source of HO_2 and H_2O_2, which can result in fast ignition in the intermediate temperature regime, as mentioned in chapter 2. Preliminary sampling experiments demonstrated that these species are indeed formed in large quantities during the ignition delay of an isooctane/prenol 50/50 mixture.

4.4.2. Model testing

A comparison of simulated and experimentally obtained ignition delay times, as a function of the core gas temperature are shown in Figure 70. The CoOptima model was used to perform the simulations.

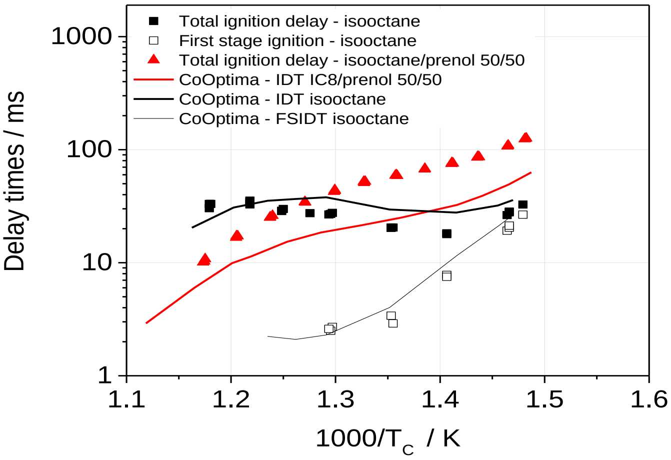

Figure 70 - Evolution of first-stage and total ignition delays of isooctane/O_2/inert (black triangles) and isooctane/prenol (50/50)/O_2/inert mixtures (red squares), as a function of temperature. P_{TDC} = 20 bar, Φ = 1. Full lines correspond to the simulated results.

The model overestimates the reactivity of the isooctane/prenol (50/50)/O_2/inert mixture, for all temperature range. The ignition phenomenology is, therefore, maintained, i.e., with no presence of NTC region. This results in a constant underprediction of the IDTs of isooctane/prenol mixture of about a factor of two. These are encouraging results, but further modeling work should aim at reducing the global reactivity f these mixtures.

4.4.3. Conclusions

The study of prenol co-oxidation with isooctane showed that:

- Addition of prenol leads to a pronounced increase in the total ignition delays of isooctane at low temperatures but a decrease at high temperatures. This shows that the addition of prenol to commercial fuels is likely to result in an increase of octane sensitivity;

- Negative Temperature Coefficient behavior is not observed for isooctane/prenol (50/50) mixtures;

- No first-stage of ignition was identified from 770 to 852 K, however slight cool flames are produced from 675 to 753 K;

- It is believed that this effect is due to the fast formation of 3-methyl-2-butenal and 2-methyl-1,3-butadiene by prenol, constituting a radical sink at low temperatures and facilitating the ignition at intermediate temperatures by the formation of HO_2 and H_2O_2;

- The Co-optima model is able to reproduce the temperature dependence of the IDTs, but underpredicts the IDTs by a factor of two in the whole investigated temperature range.

Overall, this study demonstrates that prenol is an excellent candidate to formulate new biofuels and/or additives to gasoline-like fuels. Further experimental and modeling work could help elucidate the modus operandi for this effect.

4.5. Isooctane/CYCLOPENTANONE

4.5.1. RCM experiments

Cyclopentanone co-oxidation experiments were conducted at stoichiometric conditions and the results of the study of the three parameters mentioned previously are depicted in the following sections.

- **Composition effect**

The compositions of the isooctane/cyclopentanone blends used to investigate the effect of cyclopentanone addition into isooctane mixtures are given in Table 27, as well as the associated compressed temperature.

Table 27 - Mole fraction of isooctane/cyclopentanone/O_2/inert mixtures at p_C = 20 bar.

% CPN	**$x_{isooctane}$**	**x_{CPN}**	**x_{O2}**	**x_{Ar}**	**x_{N2}**	***Tc* (K)**
0	0.0165	0.0000	0.2044	0.7684	0.0000	866
10	0.0155	0.0017	0.2065	0.7763	0.0000	865
20	0.0145	0.0036	0.2063	0.7756	0.0000	863
30	0.0133	0.0057	0.2061	0.7749	0.0000	864
40	0.0120	0.0080	0.2059	0.7741	0.0000	867
50	0.0105	0.0105	0.2057	0.7733	0.0000	866
60	0.0089	0.0134	0.2054	0.7723	0.0000	865
70	0.0071	0.0166	0.2051	0.7712	0.0000	866
80	0.0051	0.0202	0.2048	0.7699	0.0000	868
90	0.0155	0.0017	0.2065	0.7763	0.0000	865
100	0.0000	0.0291	0.2040	0.7669	0.0000	878
0	0.0165	0.0000	0.2044	0.0000	0.7684	693
10	0.0155	0.0017	0.2065	0.0000	0.7763	692
20	0.0145	0.0036	0.2063	0.0000	0.7756	691
30	0.0133	0.0057	0.2061	0.0000	0.7749	691

40	0.0120	0.0080	0.2059	0.0000	0.7741	696

The effect of cyclopentanone addition to isooctane on the ignition delay times is shown in Figure 71 at two different temperatures and at p_C = 25 bar (left) and p_C = 20 bar (right). In order to examine both the influence of isooctane and cyclopentanone on the reactivity of their mixture, IDTs were measured for increasing proportion of cyclopentanone and at stoichiometric conditions, likewise the other LDCs studied previously. Because of the low reactivity of cyclopentanone, compared to isooctane, the IDTs were measured at two compressed pressures of 25 and 20 bar, at low and high temperatures. Overall, at low temperatures the addition of cyclopentanone inhibits the reactivity of isooctane. On the other hand, at higher temperatures, in both 25 and 20 bar cases, the reactivity seems to decrease along with the addition of cyclopentanone until 60% of cyclopentanone are blended with isooctane. For mixtures with higher contents in cyclopentanone the IDTs do not appear to be affected by the addition of this cyclic ketone.

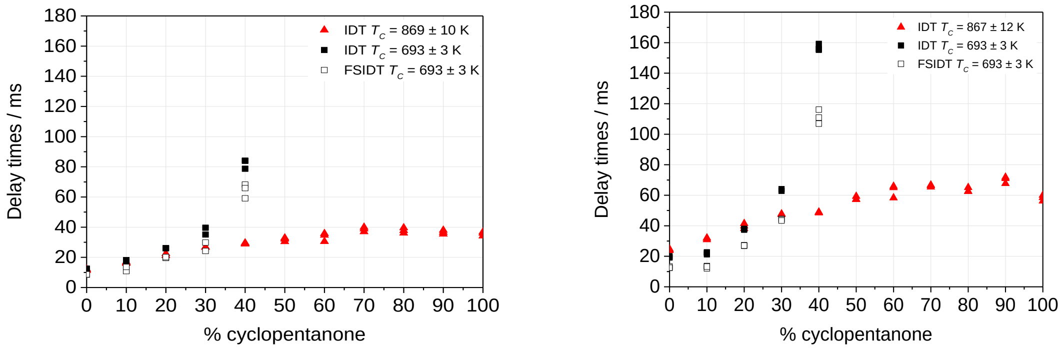

Figure 71 - Ignition delay times of isooctane/cyclopentanone/O_2/inert mixtures for increasing amount of CPN at p_C = 25 bar (left) and p_C = 20 bar (right).

The pressure profiles obtained during the experiments at p_C = 20 bar are shown in Figure 72 at two temperatures.

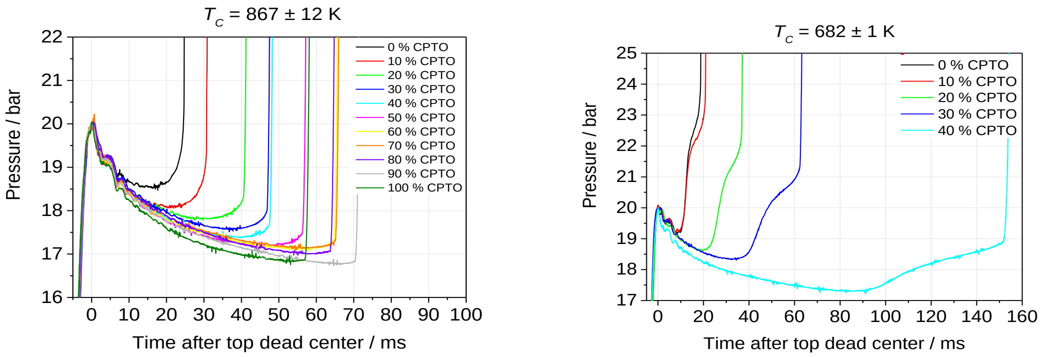

Figure 72 - Pressure profiles for isooctane/cyclopentanone/O_2/inert mixtures at stoichiometric condition and at p_C = 20 bar.

In the same manner as the previous studied LDCs, the isooctane/cyclopentanone mixtures showed a transition from two-stage ignition at low temperatures to single stage ignition at high temperatures. Likewise *o*-cresol, only 20% of cyclopentanone addition is enough to affect the first-stage of ignition and reduce the amplitude of the associated pressure jump. It is also relevant to note that the reduction in the pressure jump associated with the first-stage of ignition is strong when 40% of cyclopentanone is added, leading to longer IDTs, at the same condition. Besides that, both the duration of the first-stage of ignition and the time between the beginning of this stage and the ignition increase with the addition of the cyclopentanone. At high temperatures, as shown in Figure 71, the IDTs increase monotonically as the mole fraction of cyclopentanone increases inside a mixture until 60% of cyclic ketone content. At higher blending ratios of cyclopentanone, however, this evolution is not linear anymore, the 90% cyclopentanone mixture being consistently less reactive than pure cyclopentanone.

- **Pressure effect**

Figure 73 illustrates the modification of the ignition delays over the whole pressure range at two different compressed temperatures 865 and 693 K.

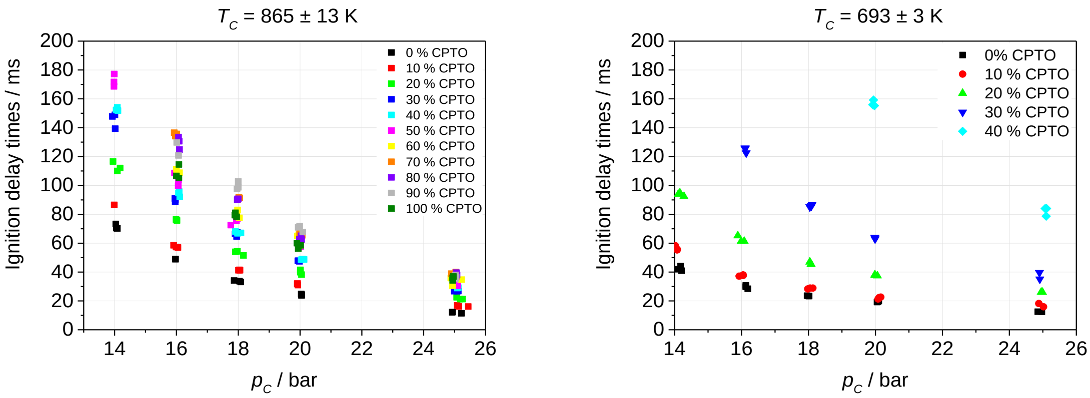

Figure 73 - Evolution of total ignition delays as a function of pressure for isooctane/cyclopentanone/O₂/inert mixtures at stoichiometric conditions.

Overall, the reactivity increase as the compressed pressure increases. This is true until 60% of cyclopentanone added to isooctane, at high temperature and in all range of studied pressure. Again, the 90% cyclopentanone mixture is the least reactive mixture at the highest temperatures, as shown in.

- **Temperature effect**

In addition to volatility concerns, the isooctane/cyclopentanone (60/40) mixture was chosen to perform the study of the autoignition temperature dependency because of the strong effect for this mixture composition on both the first-stage and total ignition delay time. Table 28 depict the isooctane/cyclopentanone (60/40) mixtures composition used in this study as well as the calculated temperature at the end of the compression.

Table 28 - Mole fractions of isooctane/cyclopentanone/O_2/inert mixtures at p_C = 20 bar.

$x_{isooctane}$	x_{CPN}	x_{O2}	x_{Ar}	x_{N2}	x_{CO2}	***Tc* (K)**
0.0120	0.0080	0.2059	0.7741	0.0000	0.0000	867
0.0120	0.0080	0.2059	0.6967	0.0774	0.0000	843
0.0120	0.0080	0.2059	0.6193	0.1548	0.0000	823
0.0120	0.0080	0.2059	0.5419	0.2322	0.0000	802
0.0120	0.0080	0.2059	0.4645	0.3097	0.0000	783
0.0120	0.0080	0.2059	0.3871	0.3871	0.0000	767

0.0120	0.0080	0.2059	0.3097	0.4645	0.0000	750
0.0120	0.0080	0.2059	0.2322	0.5419	0.0000	735
0.0120	0.0080	0.2059	0.1548	0.6193	0.0000	720
0.0120	0.0080	0.2059	0.0774	0.6967	0.0000	708
0.0120	0.0080	0.2059	0.0000	0.7741	0.0000	696

Figure 74 shows the pressure profiles for isooctane/cyclopentanone (60/40) mixtures at P_c = 20 bar. At high temperatures and both pressures, the reactivity of pure cyclopentanone is too low to be measured, i.e., the ignition delay times are longer than 200 ms, which exceed the accepted limit for IDTs measurements. This is also true for the 20 bar isooctane/cyclopentanone experiments. However, the reproducibility of these results being good, as seen in Figure 75, they are displayed in the following figures.

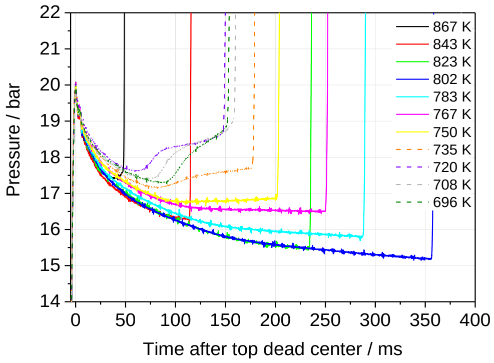

Figure 74 - Pressure profile of isooctane/O_2/inert mixtures (left) and isooctane/cyclopentanone (60/40)/O_2/inert mixtures (right) both at p_C = 20 bar and at stoichiometric condition.

The comparison of the pressure profiles for isooctane (Figure 44) and isooctane/cyclopentanone (60/40) mixtures (Figure 74), indicates that the temperature range, where the first stage of ignition is observed, is reduced when 40% of isooctane is replaced by cyclopentanone, i.e., for pure isooctane cool flames can be observed from 676 to 801 K, while for isooctane/cyclopentanone mixtures the first stage of ignition is observed from 696 to 735 K. From 696 to 720 K the first stage seems to be considerably affected, longer FSIDTs are observed along with the temperature decrease. Figure 75 shows the comparison of the evolution of first stage ignition delays and total ignition delays of isooctane/cyclopentanone (60/40)/O_2/inert mixtures, cyclopentanone/O_2/inert mixtures and isooctane/O_2/inert mixtures with temperature.

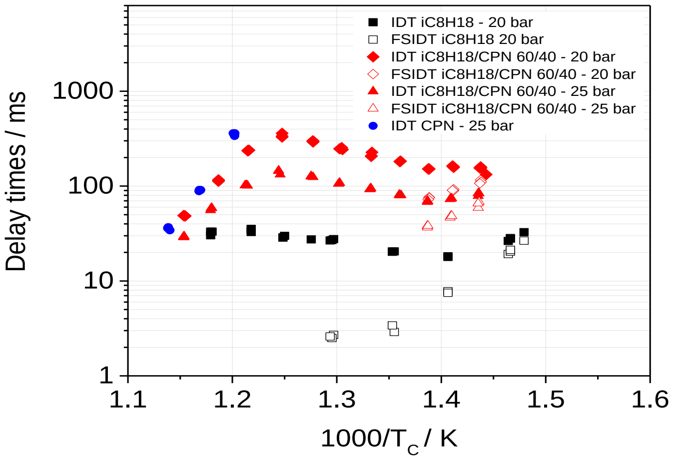

Figure 75 - Comparison of the evolution of first stage ignition delays (open symbols) and total ignition delays (full symbols) of isooctane/cyclopentanone (60/40)/O_2/inert mixtures (triangles), cyclopentanone/O_2/inert mixtures (circles) and isooctane/O_2/inert mixtures (squares) with temperature.

Isooctane/cyclopentanone (60/40) IDT measurements shown in Figure 75 illustrate the resistance to autoignition, with the shortest IDT measured being 48.5 ms at p_C = 20 bar. The presence of the NTC at both 25 and 20 bar, suggests that despite of its important effect in delaying the first-stage of ignition, cyclopentanone could still take part in LTC oxidation pathways through the formation of peroxyalkyl radicals and subsequent isomerization. However, one can note that the addition of cyclopentanone mainly results in an increased first-stage ignition delay (about a factor of 4), the duration of the second stage of ignition remaining comparable to the pure isooctane case. It is therefore possible that cyclopentanone is competitive with isooctane in the H-atom abstraction reactions at low temperatures, but results in longer LTC chain branching than isooctane.

4.5.2. Sampling/speciation

During sampling experiments 12 samples were taken during the ignition delay time of isooctane/cyclopentanone (60/40)/O_2/inert, shown in Figure 76.

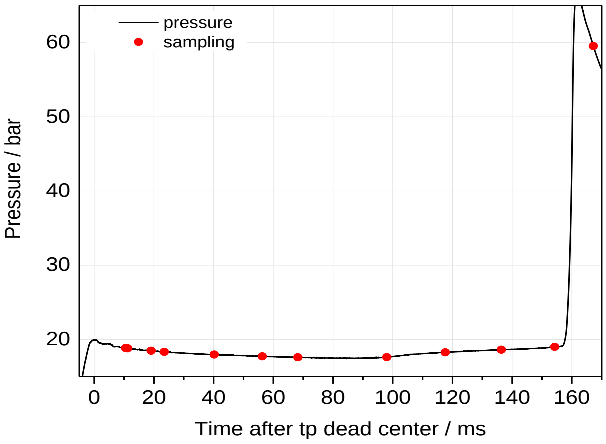

Figure 76 - Sampling experiment times and pressure profile of the mixture isooctane/cyclopentanone (60/40)/O_2/N_2 at stoichiometric condition, p_C = 20 bar and at T_C = 694 ± 3 K.

An example of the chromatogram using the PBQ column and at 136.4 ms after top dead center is shown in Figure 77 . Within the 12 samples, 26 products were identified from the analyses using this column, which are listed in the Table 29 along with their structure and retention time.

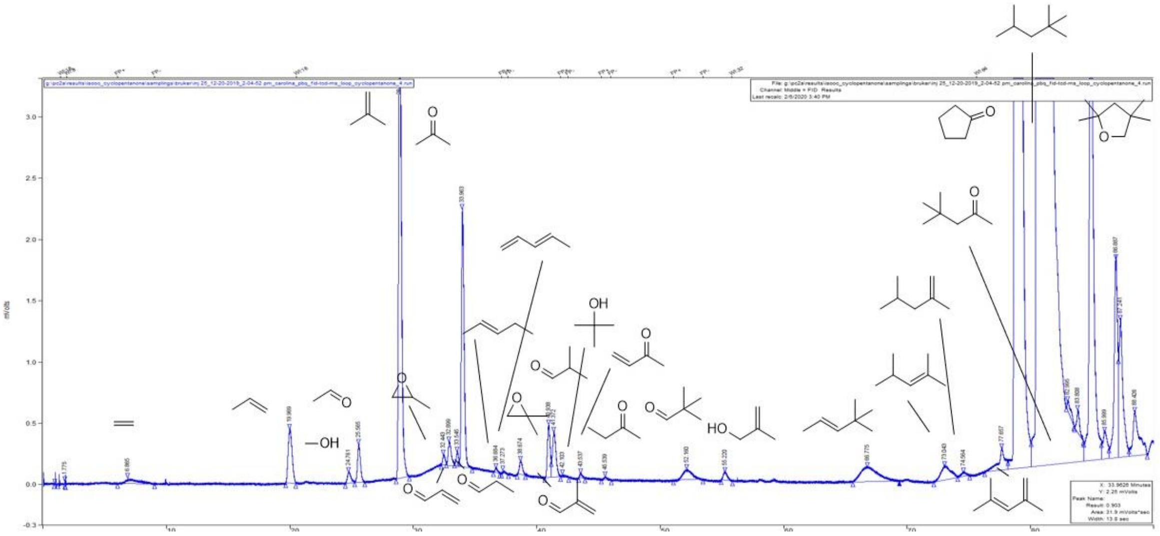

Figure 77 - Chromatogram of isooctane/cyclopentanone (60/40) sampling at 136.4 ms using PBQ column.

Table 29 - Oxidation products identified during sampling experiments of the stoichiometric mixture isooctane/cyclopentanone (60/40)/O_2/N_2 using the PBQ column. Black: isooctane products, blue: cyclopentanone products and red: isooctane and cyclopentanone products.

Retention time	Nomenclature	Structure	Retention time	Nomenclature	Structure
7.131	ethylene		42.204	2-methyl-2-propanol	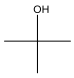
24.461	methanol	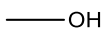	43.492	methyl vinyl ketone	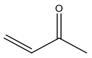
25.652	acetaldehyde	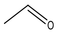	45.225	2-butanone	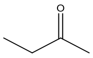
28.959	2-methyl-1-propene	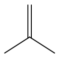	51.966	2,2-dimethyl-propanal	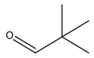
32.504	methyl oxirane	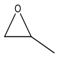	54.889	2-methyl-2-propen-1-ol	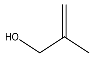
32.958	2-propenal	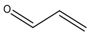	66.487	4,4-dimethyl-2-pentene	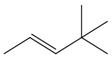
33.654	propanal	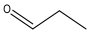	73.104	2,4-dimethyl-2-pentene	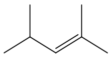
34.063	acetone	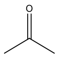	74.186	2,4-dimethyl-1-pentene	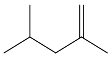
36.745	2-pentene	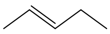	77.671	2,4-dimethyl-1,3-pentadiene	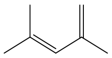
38.778	2,2-dimethyl-oxirane	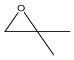	79.96	Isooctane	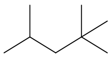
41.013	methacrolein	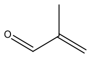	78.213	cyclopentanone	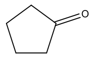
41.438	2-methyl-propanal	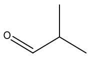	83.839	4,4-dimethyl-2-pentanone	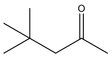
			84.914	2,2,4,4-tetramethyltetrahydrofuran	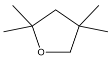

The use of the UB5P column allowed the identification of 19 species, shown in Table 30, from the samples taken during the ignition delay time. Figure 78 shows a chromatogram from a sample obtained at 136.4 ms using the UB5P column for the same mixture.

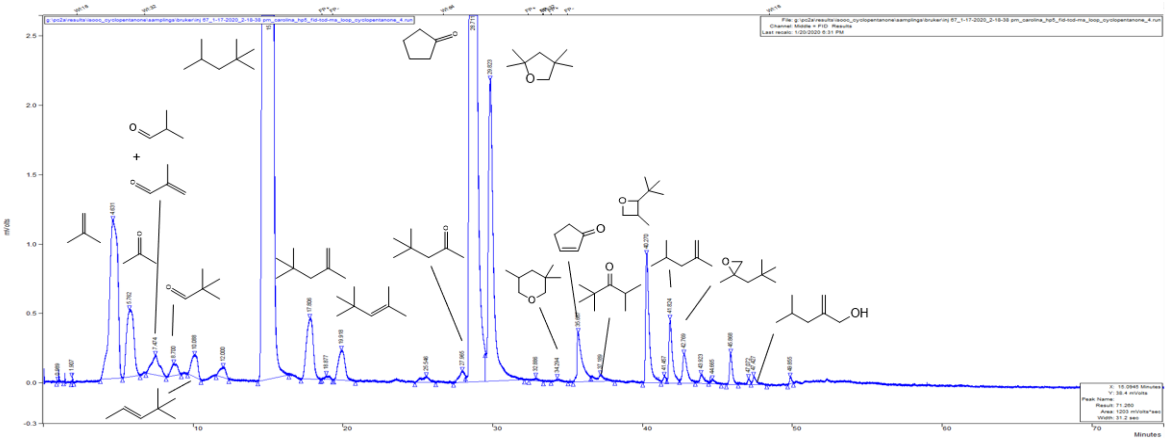

Figure 78 - Chromatogram of isooctane/cyclopentanone (60/40) sampling at 136.4 ms using UB5P *column.*

Table 30 - Oxidation products identified during sampling experiments of the stoichiometric mixture isooctane/cyclopentanone (60/40)/O_2/N_2 using UB5P column. Black: isooctane products, blue: cyclopentanone products and red: isooctane and cyclopentanone products.

Retention time	Nomenclature	Structure	Retention time	Nomenclature	Structure
4.543	2-methyl-propene	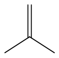	28.335	cyclopentanone	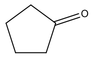
5.654	acetone	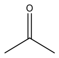	29.415	2,2,4,4-tetramethyltetrahydrofuran	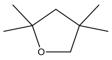
7.348	2-methyl-propanal + methacrolein	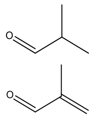	32.886	2,2-dimethylpropyl-oxirane	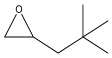
8.56	2,2-dimethyl-propanal	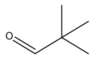	42.403	2,2-dimethyl-propyl-methyloxirane	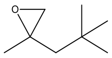
9.912	4,4-dimethyl-2-pentene	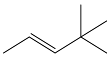	36.731	2,2,4-trimethyl-3-pentanone	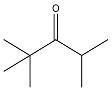
14.812	isooctane	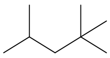	33.844	3,3,5-trimethyltetrahydro-2H-pyran	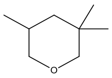
17.448	2,4,4-trimethyl-1-pentene	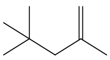	41.474	3,3-dimethyl-2-isopropyloxetane	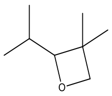
19.513	2,4,4-trimethyl-2-pentene	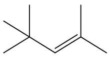	35.21	2-cyclopenten-1-one	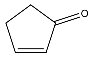
23.386	2-tert-butyl-3-methyl-oxirane	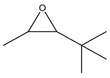	45.545	ketone C8	-
27.557	4,4-dimethyl-2-pentanone	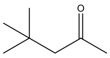	47.125	4-methyl-2-methylene-1-pentanol	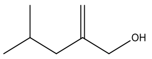

4.5.3. Model testing

The experimentally obtained isooctane/cyclopentanone ignition delay results were simulated using the Co-Optima model, shown in Figure 79 for the study of the effect of composition and, in Figure 80 for the study of the effect of temperature. The non-reactive pressure profiles used to calculate the volume profile used in these simulations are available in the appendices.

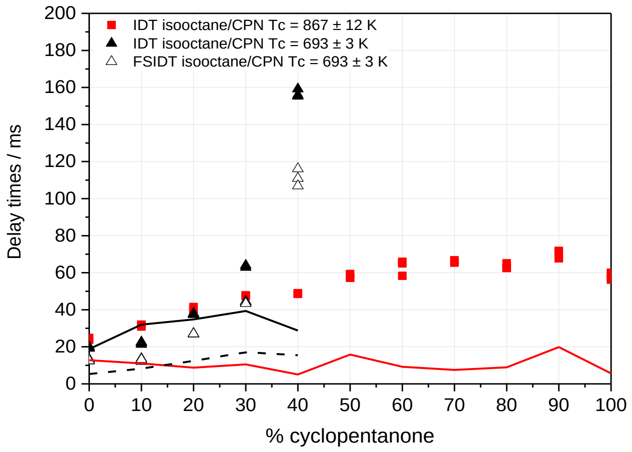

Figure 79 - Evolution of the modeled (lines) and experimental (symbols) first-stage and total ignition delay times of isooctane/cyclopentanone/O_2/inert mixtures at two temperatures relevant to low-temperature and intermediate temperature combustion, as a function of cyclopentanone molar content in the fuel. p_C = 20 bar, Φ = 1.

At high temperatures, the IDTs are underestimated by the model, especially for high concentrations of cyclopentanone. At low temperatures the model is able to predict the IDTs until 20% of cyclopentanone, for higher mole fractions the IDTs are underestimated.

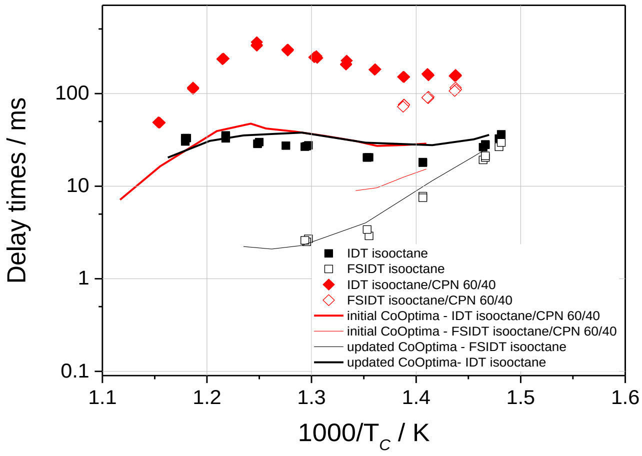

Figure 80 - Evolution of first-stage and total ignition delays of isooctane/O_2/inert (black triangles) and isooctane/cyclopentanone (60/40)/O_2/inert mixtures (red squares), as a function of temperature. P_{TDC} = 20 bar, Φ = 1. Full lines correspond to the simulated results.

In all the studied range of temperature, the delay times for both first-stage and total ignition, are underestimated using the Co-Optima mechanism. However, the "shape" of the NTC region and the cool flames are well captured. Overall, the model is unable to capture the important effect of the addition of cyclopentanone on reactivity. The measured mole fraction profiles for the experimentally detected products are shown in Figure 80. As the IDT is not correctly reproduced by the model, the simulated profiles were adjusted in time to correspond with the observed IDT.

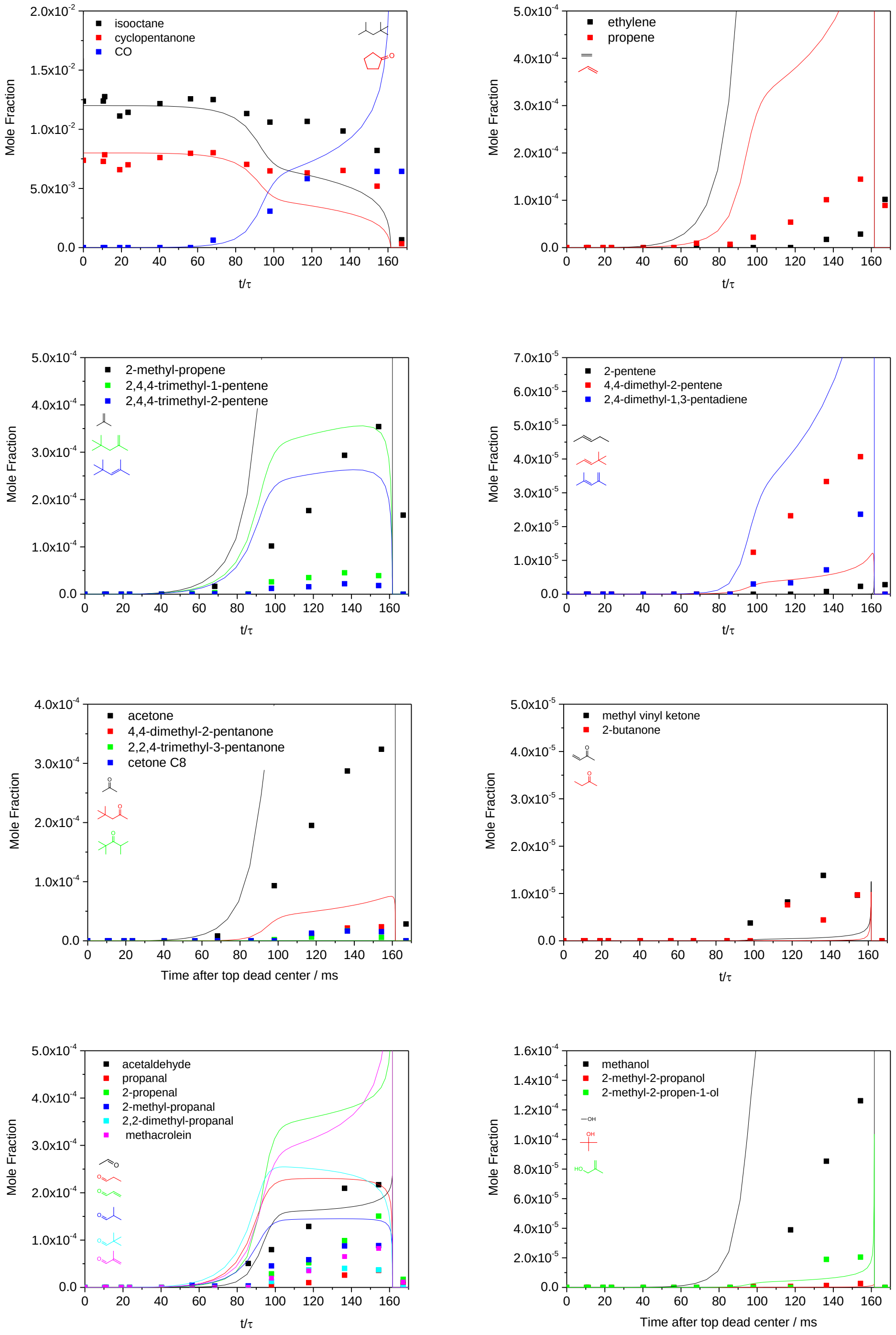

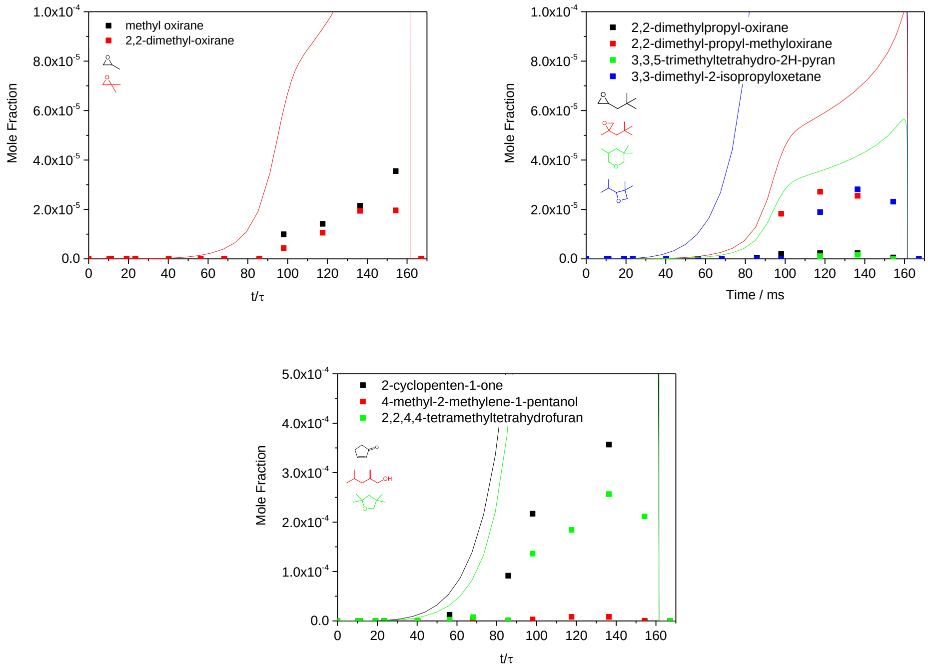

Figure 81 - Experimental and simulated (lines) mole fraction profiles of the fuels and intermediates formed during two-stage ignition of isooctane/cyclopentanone (60/40)/air mixture at p_C = 20 bar, and T_C = 694 ± 3 K and, CO mol fraction profile.

The cyclopentanone and isooctane conversions start around 80 ms after the top dead center time, which coincides with the beginning of the first-stage ignition event, as shown in Figure 76. The consumption of cyclopentanone and isooctane increases along with the time after top dead center and around 156 ms, the total autoignition delay time, the mole fraction of cyclopentanone is 0.0052 and isooctane is 0.00821, i.e. a conversion of 76% of cyclopentanone and of 83% of isooctane. The carbon monoxide starts to be formed around 68 ms and its mole fraction increases until the total ignition delay time.

The species formed in relevant amounts are mostly found in the case of pure isooctane. All identified products are overestimated by the model, with the exception of 4,4-dimethyl-2-pentene and 2-methyl-2-propen-1-ol. This is also true for the conversion of both fuels during the first-stage ignition event, which is overestimated by about a factor of two. Along the identified products, only two can be specific to cyclopentanone: 2-cyclopenten-1-one, and ethylene, which have been identified as major products of cyclopentanone oxidation in Chapter 2. Both are largely overestimated by the model. It should be noted that no quantifiable amounts of ethylene were detected in the isooctane/anisole experiments. While the formation of 2-cyclopenten-1-one is observed first during the first-stage ignition event and therefore corresponds to co-oxidation in the LTC regime, the formation of ethylene is gradual during the second stage of ignition, consistently with its formation through ring opening reactions with higher activation energy.

In their experimental and modeling study of cyclopentanone, Thion et al. (290) demonstrated that the formation of the 2-cyclopentanonyl radical after H-abstraction by $\dot{\mathrm{O}}$H takes place after the formation of a Van der Waals complex between cyclopentanone and the OH radical, rendering the formation of the 3-

cyclopentanonyl radical more favourable. The formation of this complex could result in artificial “fixation” of OH radicals, which means that these OH radicals will not be able to take part in H-atom abstraction reactions with isooctane, therefore delaying first-stage ignition.

In order to shed light on means to improve the kinetic model, and similarly to the anisole study, dual brute-force sensitivity analysis was performed on the first-stage, second-stage and total ignition delay, and is shown in Figure 82. Because of the nature of the disagreement between experiments and model, special attention is given to reaction having a positive coefficient on the first-stage ignition delay, and a smaller absolute sensitivity coefficient on the second stage of ignition (i.e., the time difference between the first-stage ignition and the total ignition). This is true for the two reactions of hydrogen abstraction on cyclopentanone. Both their first-stage sensitivity coefficients are positive, indicating that their competition on OH radicals results in an inhibition of the reactivity of isooctane. Another such reaction is a decomposition pathway of CPNOOH3-5O2R yielding a hydroperoxycyclopentenone CPND2-4OOH. The concerted elimination pathways of RO2 both have positive sensitivity coefficients.

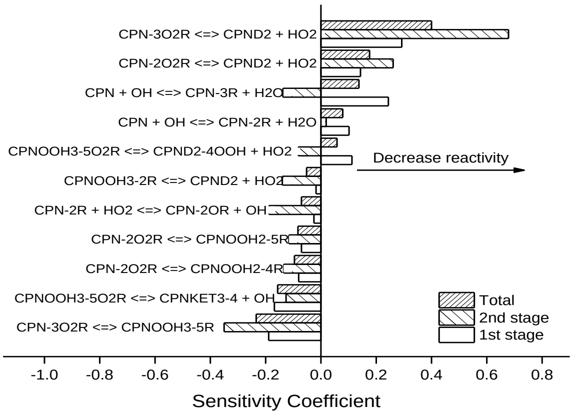

Figure 82 – «Brute-force» sensitivity analysis to first-stage, second-stage and total ignition delay times. Cyclopentanone/O_2/N_2 mixture at p_C = 20 bar, Φ = 1, T_C = 698 K.

A Reaction pathway analysis was performed in the conditions of the sampling experiments and is shown in Figure 83. It demonstrates that the most expected species (2-cyclopenten-1-one, 2-propenal, ethylene and carbon monoxide) were observed experimentally. Other postulated species, including bycyclic ethers or cyclodiones, may not be stable of volatile enough to be detected by GC techniques. The model, as suggested by Thion et al. (290), demonstrates that the formation of the 3-cyclopentanonyl radical is preferential, mostly leading to the formation of 2-cyclopenten-1-one. A more detailed analysis of these results would however be risky, given the poor performance of the model in the prediction of the experimental IDTs.

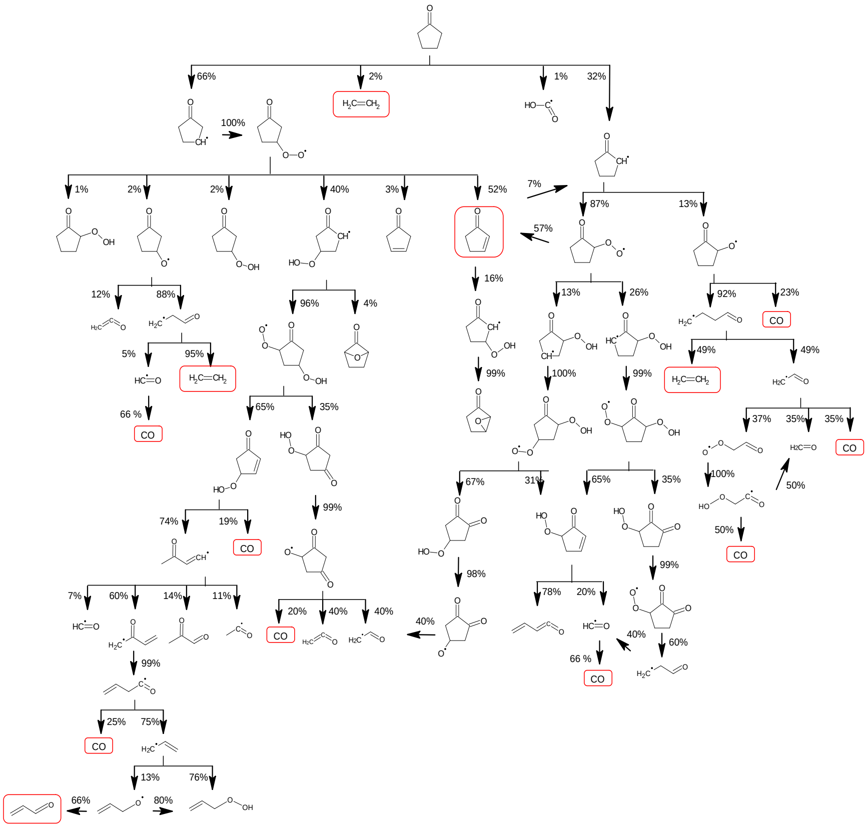

Figure 83 - Reaction Pathway Analysis of cyclopentanone oxidation in the conditions of the sampling experiments and 5% conversion. Red squares: species identified by GC-MS.

4.5.4. Conclusions

The co-oxidation of cyclopentanone with isooctane has been investigated experimentally by measuring ignition delay times and performing sampling experiments over a wide range of conditions. These results show:

- Addition of cyclopentanone leads to a clear increase in both the first-stage and total ignition delays of isooctane. This is mostly due to a dramatic increase of the first-stage ignition delays rather than a suppression of LTC reactivity;

- Isooctane/cyclopentanone (60/40) blend still shows Negative Temperature Coefficient behavior;

- It is believed that this effect on reactivity is due to competition with isooctane on the H-abstraction reactions, where abstraction on cyclopentanone would be favoured, cyclopentanone however resulting in delayed low-temperature chain branching;

- Chemical analysis of samples acquired during the ignition delay show the formation of low concentrations of the expected products from cyclopentanone;

- The Co-Optima model is currently unable to accurately reproduce the observed effects. Ways to improve the agreement include a re-evaluation of the reaction rate parameters for the H-atom abstraction reactions by $\dot{O}H$, as well as a deeper investigation of the Potential Energy Surface of the relevant $R\dot{O}_2$ radicals.

4.6. Syntheses of main results

A qualitative comparison of the results from studied LDCs blended with isooctane is proposed in this section. Figure 84 shows a comparison of the pressure profiles at low temperature.

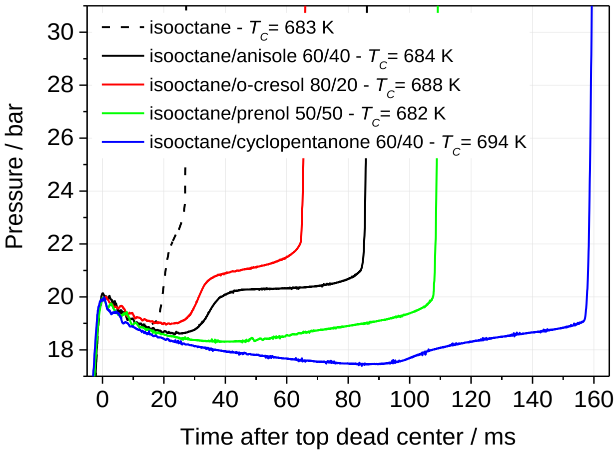

Figure 84 – Evolution of the pressure as a function of the time after top dead center for all studied LDCs and isooctane at low temperature.

The addition of the studied LDC has an effect of inhibit the reactivity of isooctane, at low temperatures, i.e., the ignition delay time of all mixtures are longer than pure isooctane. On the other hand, prenol is the only one capable to suppress the first stage of ignition, at these conditions. Cyclopentanone demonstrates the highest potential to increase the ignition delay at low temperatures.

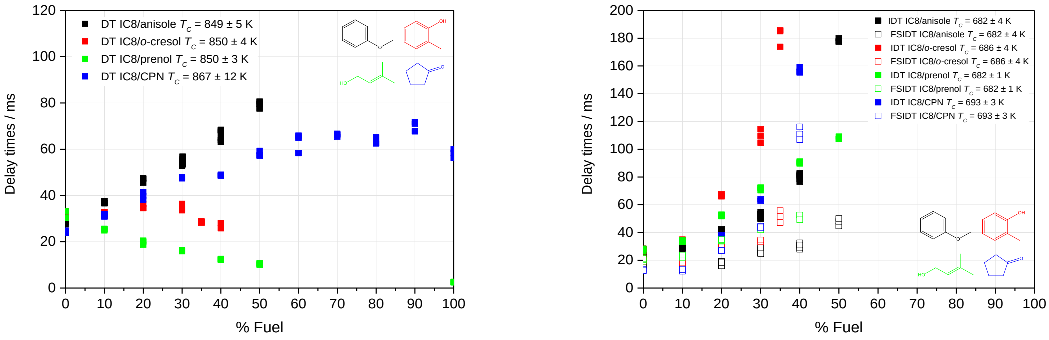

Figure 85 - Ignition delay times of all surrogates studied for increasing amount of additive at p_C = 20 bar and two different core gas temperatures.

The effect of isooctane substitution by the studied fuel on ignition delay times is more pronounced at low temperatures for the three studied compounds, as shown in Figure 85. While prenol and o-cresol mixtures show a decrease of ignition delay times at high temperature and an increase at low temperature with increasing blending, the addition of anisole results in an increase of the IDT at low and high temperature. At high temperatures, anisole-containing mixtures show the longest ignition delay times and prenol-containing mixtures depict the shortest ignition delay times. On the other hand, at low temperature, isooctane/o-cresol mixtures have the longest ignition delay times. Comparing prenol and anisole mixtures, until 40 % of isooctane substitution, prenol mixtures have the longest delay times but an inversion of this behavior is observed for mixtures with a higher concentration on the studied fuels. The first stage of ignition is longer for isooctane/anisole mixtures for all compositions and isooctane/prenol mixtures seem to have the shortest cool flame delay times until 40% of isooctane substitution. A qualitative comparison of the evolution of the ignition delay times with temperature for isooctane and all the studied surrogates is shown in Figure 86.

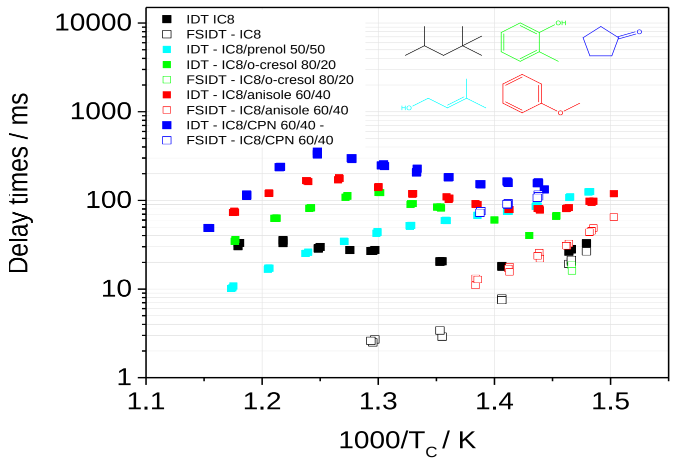

Figure 86 - Comparison of the evolution of first stage ignition delays (open symbols) and total ignition delays (full symbols) of all surrogates studied) with temperature, at p_C = 20 bar.

Even though the blending ratios are different for each mixture, Figure 86 shows that the 50/50 isooctane/prenol mixtures are the only blends which show no NTC behavior. It is also interesting that this mixture has the longest ignition delay times in the region from 675 to 787 K, i.e., at low temperature and the shortest ignition delay times at high temperatures in the region from 787 to 852 K. This result suggests that the prenol is a good candidate to formulate gasoline-like biofuels considering that in the modern spark ignition engines a high octane sensitivity is required (11,117). On the other hand, while not suppressing first-stage ignition events, cyclopentanone demonstrates great potential in increasing the ignition delays at all temperatures.

5. Conclusions & Outlook

A summary of experimental results and a discussion from a global point of view is presented in this chapter as well as suggestions for future research.

5.1. Summary

In the current context of increasing energy demand and concern for climate change, internal combustion engines still account for a large portion of the global mobility. Short-term options to reduce the impact of transport on the climate therefore rely on the incorporation of short-carbon cycle compounds inside commercial fuels. Among the currently considered fuels, many originate from thermochemical treatment of the biomass. While a number of studies have been dedicated to the investigation of the reactivity of these compounds, it has also been shown in the past that in co-oxidation conditions, numerous reaction pathways can become important, while they would be negligible in pure conditions.

This study aimed at addressing the potential of several of these advanced biofuels for incorporation into commercial gasolines through an extensive study of the mechanisms responsible for the auto-ignition in co-oxidation conditions. Anisole, *o*-cresol, prenol and cyclopentanone were selected as biofuels of interest after an exhaustive literature study of their physico-chemical properties as well as their means of production. Isooctane was chosen as the preferred matrix to represent such fuels and a source of OH radicals during its low-temperature ignition, because of its representability of a large fraction of these fuels, as well as the number of studies that have been performed in the past on its oxidation. A detailed experimental study of the ignition of mixtures of isooctane with the selected biofuels was therefore conducted with help from the ULille RCM, an experimental device dedicated to the study of low-temperature combustion kinetics in the high-pressure, low-temperature conditions representative of internal combustion engines.

Firstly, the measurement of the ignition delays of isooctane has demonstrated the validity of this method, as well as the reliability of the results obtained on this complex experimental device, through the comparison of the newly acquired data with historical results, both from the literature and the same RCM. They allowed the selection of a kinetic model which aided in the interpretation of the experimental data for anisole, prenol and cyclopentanone.

A study of anisole demonstrated its ability to increase both first-stage and total ignition delay. Samples acquired during the ignition delay demonstrated that while it is not reactive when considered pure in these conditions, anisole is converted during first-stage ignition, yielding a variety of products. A kinetic model was developed, validated and used to interpret the data. It allowed to demonstrate that the effect of anisole mainly proceeds through competition with isooctane on the reaction with OH radicals, the further reaction pathways for anisole being non-chain branching.

The investigation of the effect of *o*-cresol on the ignition of isooctane demonstrated that while it shows an important increasing effect on the ignition delays, its volatility properties as well as its propensity to form soot particles are an obstacle to its widespread incorporation into commercial gasolines.

Prenol demonstrated an impressive ability to reduce the extent of the first-stage ignition and cancel the NTC behavior. This effect is believed to originate from the quick formation of 2-methyl-1,3-butadiene and 3-methyl-2-butenal, acting as a sink for OH radicals, and facilitating the formation of HO_2 and H_2O_2 in the intermediate temperature region. The Co-optima model is able to reproduce the IDTs, and their evolution with temperature with a constant underestimation of a factor of 2.

Finally, cyclopentanone demonstrated the highest ability to increase the ignition delay at all temperatures, resulting in a multiplication of first-stage ignition delays by a factor of 4. The mole faction profiles of the formed species during two-stage ignition show the formation of 2-cyclopentenone to be the largest consumption pathway. The effect on reactivity could be due to the formation of a Van der Waals complex between the fuel and the OH radical, thereby constituting a radical sink. The Co-optima model is however unable to reproduce these results, and suggestions for future improvements of this model have been made.

5.2. Suggestions for future research

Among the studied biofuels, prenol and cyclopentanone demonstrated the highest potential in terms of improving the knock resistance of gasoline fuels. Developing kinetic models that are able to accurately describe their blending behavior should therefore be sought. In the case of prenol, additional sampling experiments would be a valuable source of detailed validation data. In the case of cyclopentanone, the current Co-optima model is far from being able to capture the observed increase of the ignition delays, and a careful kinetic modeling work should be undertaken.

Another observation that could be made also concerns the isooctane model. While it shows the best performance, among the models available from the literature, the reactivity in the intermediate temperature range still seems to be overestimated, as witnessed by the overestimation of the conversion by a factor of two or more that is observed when trying to model the hereby acquired mole fraction profiles. This would indeed require an extensive work, including additional sampling experiments.

References

1. Kalghatgi G. Is it really the end of internal combustion engines and petroleum in transport? Appl Energy . 2018;225:965–74. Available from: https://www.sciencedirect.com/science/article/abs/pii/S0306261918307955
2. Kumar S, Sani RK. Biorefining of biomass to biofuels : opportunities and perception. 2017. 382 p.
3. Alalwan HA, Alminshid AH, Aljaafari HAS. Promising evolution of biofuel generations. Subject review. Renew Energy Focus . 2019;28:127–39. Available from: https://www.sciencedirect.com/science/article/abs/pii/S1755008418303259
4. Darda S, Papalas T, Zabaniotou A. Biofuels journey in Europe: Currently the way to low carbon economy sustainability is still a challenge. J Clean Prod . 2019;208:575–88. Available from: https://www.sciencedirect.com/science/article/abs/pii/S0959652618331639
5. Leduc P, Dubar B, Ranini A, Monnier G. Downsizing of gasoline engine: An efficient way to reduce CO2 emissions. Oil Gas Sci Technol . 2003;58(1):115–27. Available from: https://doi.org/10.2516/ogst:2003008
6. Boot MD, Tian M, Hensen EJM, Mani Sarathy S. Impact of fuel molecular structure on auto-ignition behavior – Design rules for future high performance gasolines. Prog Energy Combust Sci . 2017;60:1–25. Available from: http://www.sciencedirect.com/science/article/pii/S0360128516300570
7. Battin-Leclerc F. Detailed chemical kinetic models for the low-temperature combustion of hydrocarbons with application to gasoline and diesel fuel surrogates. Prog Energy Combust Sci . 2008;34(4):440–98. Available from: https://www.sciencedirect.com/science/article/abs/pii/S0360128507000627
8. Zádor J, Taatjes CA, Fernandes RX. Kinetics of elementary reactions in low-temperature autoignition chemistry. Prog Energy Combust Sci . 2011;37(4):371–421. Available from: http://dx.doi.org/10.1016/j.pecs.2010.06.006
9. Farrell JT, Cernansky NP, Dryer FL, Law CK, Friend DG, Hergart CA, et al. Development of an Experimental Database and Kinetic Models for Surrogate Diesel Fuels. SAE Tech Pap . 2007; Available from: http://papers.sae.org/2007-01-0201/
10. Demirbas A, Balubaid MA, Basahel AM, Ahmad W, Sheikh MH. Octane Rating of Gasoline and Octane Booster Additives. Pet Sci Technol . 2015 Jun;33(11):1190–7. Available from: https://doi.org/10.1080/10916466.2015.1050506
11. Abdul-Manan AFN, Kalghatgi G, Babiker H. Exploring Alternative Octane Specification Methods for Improved Gasoline Knock Resistance in Spark-Ignition Engines. Front Mech Eng . 2018;4(December):1–13. Available from: https://www.frontiersin.org/articles/10.3389/fmech.2018.00020/full
12. Monroe E, Gladden J, Albrecht KO, Bays JT, McCormick R, Davis RW, et al. Discovery of novel octane hyperboosting phenomenon in prenol biofuel/gasoline blends. Fuel . 2019;239(October 2018):1143–8. Available from: https://doi.org/10.1016/j.fuel.2018.11.046
13. Global Warming of 1.5°C. An IPCC Special Report on the impacts of global warming of 1.5°C above pre-industrial levels and related global greenhouse gas emission pathways, in the context of strengthening the global response to the threat of climate changeM MT, (eds.) TW. Global Warming of 1.5°C. An IPCC Special Report on the impacts of global warming of 1.5°C above pre-industrial levels and related global greenhouse gas emission pathways, in the context of strengthening the global response to the threat of climate change. 2018.
14. Blunden J, Arndt DS, editors. State of the Climate in 2019. Bull Am Meteorol Soc . 2020;101(8):S1–429. Available from: https://doi.org/10.1175/2020BAMSStateoftheClimate.1
15. Ripple WJ, Wolf C, Newsome TM, Barnard P, Moomaw WR. Corrigendum: World Scientists' Warning of a Climate Emergency. Bioscience . 2020; Available from: https://doi.org/10.1093/biosci/biz088
16. Richard W. Boubel; Donald L. Fox; D. Bruce Turner; Arthur C. Stern . Fundamentals of Air Pollution. 3rd ed. Academic Press; 1994. 996 p.
17. Health Effects Institute. State of Global Air 2018 . Boston, MA:Health Effects Institute; 2018. Available from: https://www.stateofglobalair.org/sites/default/files/soga-2018-report.pdf
18. European Environment Agency (EEA). Convention on Long-range Transboundary Air Pollution (LRTAP Convention) . 2018 [cited 2018 Aug 20]. Available from: https://www.eea.europa.eu/data-and-maps/indicators/transport-emissions-of-air-pollutants-8/transport-emissions-of-air-pollutants-5
19. Climate Transparency. the G20 Transition Towards a Net-Zero Emissions Economy . Vol. 53, Climate Transparency. 2019. Available from: http://www.climate-transparency.org/g20-climate-performance/g20report2019
20. Siano A, Vollero A, Conte F, Amabile S. "More than words": Expanding the taxonomy of greenwashing after the Volkswagen scandal. J Bus Res . 2017;71:27–37. Available from: http://dx.doi.org/10.1016/j.jbusres.2016.11.002
21. Continental-automotive (Powertrain). Worldwide Emission Standards and Related Regulations . 2019. Available from: www.continental-automotive.com
22. ACEA. Paving the way to carbon-neutral transport 10-point plan to help implement the European Green Deal . 2020. Available from: https://www.acea.be/uploads/publications/ACEA_10-point_plan_European_Green_Deal.pdf
23. Greenhouse gas emission trend projections and target — European Environment Agency . [cited 2020 Aug 21]. Available from: https://www.eea.europa.eu/data-and-maps/figures/greenhouse-gas-emission-trend-projections

24. Kitamura T, Ito T, Senda J, Fujimoto H. Mechanism of smokeless diesel combustion with oxygenated fuels based on the dependence of the equivalence ration and temperature on soot particle formation. Int J Engine Res . 2002;3(4):223–48. Available from: https://doi.org/10.1243/146808702762230923

25. Dec JE. Advanced compression-ignition engines - Understanding the in-cylinder processes. Proc Combust Inst . 2009;32 II(2):2727–42. Available from: http://dx.doi.org/10.1016/j.proci.2008.08.008

26. Chen Y, Ma J, Han B, Zhang P, Hua H, Chen H, et al. Emissions of automobiles fueled with alternative fuels based on engine technology: A review. J Traffic Transp Eng (English Ed . 2018;5(4):318–34. Available from: http://www.sciencedirect.com/science/article/pii/S209575641830343X

27. Musculus MPB, Miles PC, Pickett LM. Conceptual models for partially premixed low-temperature diesel combustion . Vol. 39, Progress in Energy and Combustion Science. Elsevier Ltd; 2013. 246–283 p. Available from: http://dx.doi.org/10.1016/j.pecs.2012.09.001

28. Heywood JB. Internal Combustion Engine Fundementals. Vol. 21, McGrawHill series in mechanical engineering. 1988. 930 p.

29. McAllister S, Chen J, Fernandez-Pello AC. Fundamentals of Cumbustion Processes. 2011. 15–47 p.

30. Wang Z, Qi Y, He X, Wang J, Shuai S, Law CK. Analysis of pre-ignition to super-knock: Hotspot-induced deflagration to detonation. Fuel . 2015;144:222–7. Available from: http://dx.doi.org/10.1016/j.fuel.2014.12.061

31. Stein RA, Polovina D, Roth K, Foster M, Lynskey M, Whiting T, et al. Effect of Heat of Vaporization, Chemical Octane, and Sensitivity on Knock Limit for Ethanol - Gasoline Blends. SAE Int J Fuels Lubr . 2012;5(2):2012-01–1277. Available from: http://papers.sae.org/2012-01-1277/

32. Comité des Constructeurs Français d'Automobiles (CCFA). Analyse et Statistique 2019 - L'industrie Automobile Française . 2019. Available from: http://temis.documentation.developpement-durable.gouv.fr/document.html?id=Temis-0000921

33. Zhao H. HCCI and CAI engines for the automotive industry. Woodhead Publishing Limited and CRC Press LLC; 2007. 544 p.

34. Reitz RD, Duraisamy G. Review of high efficiency and clean reactivity controlled compression ignition (RCCI) combustion in internal combustion engines. Prog Energy Combust Sci . 2015;46:12–71. Available from: http://www.sciencedirect.com/science/article/pii/S0360128514000288

35. Lin W, Sterniak J, Bohac S V. NOX emissions characterization during transient spark assisted compression ignition (SACI) engine operation. Proc ASME 2013 Intern Combust Engine Div Fall Tech Conf . 2013;1–9. Available from: https://doi.org/10.1115/ICEF2013-19099

36. Skyactiv-X . [cited 2020 Sep 6]. Available from: https://www.mazda.fr/adn-mazda/skyactiv-x/

37. Skyactiv-X M Hybrid . [cited 2020 Sep 6]. Available from: https://www.mazda.co.nz/imagination-drives-us/Skyactiv-x/#:~:text=The M Hybrid component is,plug or charging is required.

38. Search begins for ecopreneurs with big ideas for cutting carbon | Shell United Kingdom . [cited 2020 Aug 21]. Available from: https://www.shell.co.uk/media/2010-media-releases/search-begins-for-ecopreneurs-with-ideas-for-cutting-carbon.html

39. Willand J, Jelitto C, Jakobs J. The GCI Combustion Process from Volkswagen. MTZ Worldw . 2008;69(4):56–61. Available from: https://doi.org/10.1007/BF03226906

40. Kang J-M, Chang C-F, Chen J-S, Chang M-F. Concept and Implementation of a Robust HCCI Engine Controller. SAE Tech Pap . 2009; Available from: https://doi.org/10.4271/2009-01-1131

41. Wu HW, Wang RH, Ou DJ, Chen YC, Chen T yu. Reduction of smoke and nitrogen oxides of a partial HCCI engine using premixed gasoline and ethanol with air. Appl Energy . 2011;88(11):3882–90. Available from: http://dx.doi.org/10.1016/j.apenergy.2011.03.027

42. Bahri B, Aziz AA, Shahbakhti M, Muhamad Said MF. Understanding and detecting misfire in an HCCI engine fuelled with ethanol. Appl Energy . 2013;108:24–33. Available from: https://doi.org/10.1016/j.apenergy.2013.03.004

43. Saxena S, Schneider S, Aceves S, Dibble R. Wet ethanol in HCCI engines with exhaust heat recovery to improve the energy balance of ethanol fuels. Appl Energy . 2012;98:448–57. Available from: http://dx.doi.org/10.1016/j.apenergy.2012.04.007

44. Polat S. An experimental study on combustion, engine performance and exhaust emissions in a HCCI engine fuelled with diethyl ether–ethanol fuel blends. Fuel Process Technol . 2016;143:140–50. Available from: http://www.sciencedirect.com/science/article/pii/S0378382015302472

45. Shibata G, Ogawa H. HCCI Combustion Control by DME-Ethanol Binary Fuel and EGR. SAE Tech Pap . 2012; Available from: https://doi.org/10.4271/2012-01-1577

46. Saisirirat P, Foucher F, Chanchaona S, Mounaïm-Rousselle C. Spectroscopic Measurements of Low-Temperature Heat Release for Homogeneous Combustion Compression Ignition (HCCI) n-Heptane/Alcohol Mixture Combustion. Energy & Fuels . 2010;24(10):5404–9. Available from: https://doi.org/10.1021/ef100938u

47. Vuilleumier D, Kozarac D, Mehl M, Saxena S, Pitz WJ, Dibble RW, et al. Intermediate temperature heat release in an HCCI engine fueled by ethanol/n-heptane mixtures: An experimental and modeling study. Combust Flame . 2014;161(3):680–95. Available from: http://www.sciencedirect.com/science/article/pii/S0010218013003829

48. Yang D, Wang Z, Wang J-X, Shuai S. Experimental study of fuel stratification for HCCI high load extension. Appl Energy . 2011;88(9):2949–54. Available from: http://www.sciencedirect.com/science/article/pii/S0306261911001590

49. Maurya RK, Agarwal AK. Experimental investigations of performance, combustion and emission characteristics of ethanol and methanol fueled HCCI engine. Fuel Process Technol . 2014;126:30–48. Available from: http://www.sciencedirect.com/science/article/pii/S0378382014001271

50. Maurya RK, Agarwal AK. Statistical analysis of the cyclic variations of heat release parameters in HCCI combustion of methanol and gasoline. Appl Energy . 2012;89(1):228–36. Available from: http://www.sciencedirect.com/science/article/pii/S0306261911004478

51. Uyumaz A. An experimental investigation into combustion and performance characteristics of an HCCI gasoline engine fueled with n-heptane, isopropanol and n-butanol fuel blends at different inlet air temperatures. Energy Convers Manag . 2015;98:199–207. Available from: http://www.sciencedirect.com/science/article/pii/S0196890415002617

52. Mack JH, Schuler D, Butt RH, Dibble RW. Experimental investigation of butanol isomer combustion in Homogeneous Charge Compression Ignition (HCCI) engines. Appl Energy . 2016;165:612–26. Available from: http://www.sciencedirect.com/science/article/pii/S0306261915016785

53. Kalghatgi G, Stone R. Fuel requirements of spark ignition engines. Proc Inst Mech Eng Part D J Automob Eng . 2017;232(1):22–35. Available from: https://doi.org/10.1177/0954407016684741

54. Wilson D, Allen C. A comparison of sensitivity metrics for two-stage ignition behavior in rapid compression machines. Fuel . 2017;208:305–13. Available from: http://www.sciencedirect.com/science/article/pii/S0016236117308578

55. Leppard WR. The chemical origin of fuel octane sensitivity. Sae . 1990;16. Available from: https://www.sae.org/publications/technical-papers/content/902137/

56. Zhao N, Li BX. The effect of sodium chloride on the pyrolysis of rice husk. Appl Energy . 2016;178:346–52. Available from: http://dx.doi.org/10.1016/j.apenergy.2016.06.082

57. Bridgwater A V. Renewable fuels and chemicals by thermal processing of biomass. Chem Eng J . 2003;91(2–3):87–102. Available from: https://doi.org/10.1016/S1385-8947(02)00142-0

58. Bridgwater T, Maniatis K. The production of biofuels by the thermochemical processing of biomass. In: Molecular to Global Photosynthesis . 2004. p. 521–611. (Series on Photoconversion of Solar Energy; vol. Volume 2). Available from: https://doi.org/10.1142/9781860945496_0010

59. Cuypers MP. Rapport d'information . 2019. Available from: https://www.senat.fr/rap/r19-136/r19-136_mono.html#toc40

60. Westbrook CK, Curran HJ. Detailed kinetics of fossil and renewable fuel combustion. In: Faravelli T, Manenti F, Ranzi EBT-CACE, editors. Mathematical Modelling of Gas-Phase Complex Reaction Systems: Pyrolysis and Combustion . Elsevier; 2019. p. 363–443. Available from: http://www.sciencedirect.com/science/article/pii/B9780444640871000073

61. Herrmann R, Jumbe C, Bruentrup M, Osabuohien E. Competition between biofuel feedstock and food production: Empirical evidence from sugarcane outgrower settings in Malawi. Biomass and Bioenergy . 2018;114:100–11. Available from: http://www.sciencedirect.com/science/article/pii/S0961953417302866

62. Shrestha DS, Staab BD, Duffield JA. Biofuel impact on food prices index and land use change. Biomass and Bioenergy . 2019;124:43–53. Available from: http://www.sciencedirect.com/science/article/pii/S0961953419300911

63. Negash M, Swinnen JFM. Biofuels and food security: Micro-evidence from Ethiopia. Energy Policy . 2013;61:963–76. Available from: http://www.sciencedirect.com/science/article/pii/S0301421513005168

64. Riera O, Swinnen J. Household level spillover effects from biofuels: Evidence from castor in Ethiopia. Food Policy . 2016;59:55–65. Available from: http://www.sciencedirect.com/science/article/pii/S0306919215001487

65. Pontes R, Romaní A, Michelin M, Domingues L, Teixeira J, Nunes J. Comparative autohydrolysis study of two mixtures of forest and marginal land resources for co-production of biofuels and value-added compounds. Renew Energy . 2018;128:20–9. Available from: http://www.sciencedirect.com/science/article/pii/S0960148118305767

66. Feng Q, Chaubey I, Engel B, Cibin R, Sudheer KP, Volenec J. Marginal land suitability for switchgrass, Miscanthus and hybrid poplar in the Upper Mississippi River Basin (UMRB). Environ Model Softw . 2017;93:356–65. Available from: http://www.sciencedirect.com/science/article/pii/S136481521730350X

67. Ramakrishna W, Rathore P, Kumari R, Yadav R. Brown gold of marginal soil: Plant growth promoting bacteria to overcome plant abiotic stress for agriculture, biofuels and carbon sequestration. Sci Total Environ . 2020;711:135062. Available from: http://www.sciencedirect.com/science/article/pii/S0048969719350545

68. Mehmood MA, Ibrahim M, Rashid U, Nawaz M, Ali S, Hussain A, et al. Biomass production for bioenergy using marginal lands. Sustain Prod Consum . 2017;9:3–21. Available from: http://www.sciencedirect.com/science/article/pii/S2352550916300197

69. Ibarra-Gonzalez P, Rong B-G. A review of the current state of biofuels production from lignocellulosic biomass using thermochemical conversion routes. Chinese J Chem Eng . 2019;27(7):1523–35. Available from: http://www.sciencedirect.com/science/article/pii/S1004954118305779

70. Bhatia SK, Kim S-H, Yoon J-J, Yang Y-H. Current status and strategies for second generation biofuel production using microbial systems. Energy Convers Manag . 2017;148:1142–56. Available from: http://www.sciencedirect.com/science/article/pii/S0196890417306180

71. Stephen JL, Periyasamy B. Innovative developments in biofuels production from organic waste materials: A review. Fuel . 2018;214:623–33. Available from: http://www.sciencedirect.com/science/article/pii/S0016236117314436

72. Fatih Demirbas M, Balat M, Balat H. Biowastes-to-biofuels. Energy Convers Manag . 2011;52(4):1815–28. Available from: http://www.sciencedirect.com/science/article/pii/S0196890410005157

73. Sikarwar VS, Zhao M, Fennell PS, Shah N, Anthony EJ. Progress in biofuel production from gasification. Prog Energy Combust Sci . 2017;61:189–248. Available from: https://www.sciencedirect.com/science/article/pii/S036012851630106X

74. Amidon TE, Liu S. Water-based woody biorefinery. Biotechnol Adv . 2009;27(5):542–50. Available from: https://www.sciencedirect.com/science/article/abs/pii/S0734975009000706

75. Beis SH, Onay Ö, Koçkar ÖM. Fixed-bed pyrolysis of safflower seed: Influence of pyrolysis parameters on product yields and compositions. Renew Energy . 2002;26(1):21–32. Available from: https://www.sciencedirect.com/science/article/abs/pii/S0960148101001094

76. Bridgwater A V. Principles and practice of biomass fast pyrolysis processes for liquids. J Anal Appl Pyrolysis . 1999;51(1):3–22. Available from: https://www.sciencedirect.com/science/article/abs/pii/S0165237099000054

77. Zakzeski J, Bruijnincx PCA, Jongerius AL, Weckhuysen BM. The Catalytic Valorization of Lignin for the Production of Renewable Chemicals. Chem Rev . 2010;110(6):3552–99. Available from: https://pubs.acs.org/doi/10.1021/cr900354u

78. Drummond ARF, Drummond IW. Pyrolysis of Sugar Cane Bagasse in a Wire-Mesh Reactor. Ind Eng Chem Res . 1996;35(4):1263–8. Available from: https://pubs.acs.org/doi/abs/10.1021/ie9503914#

79. Wang K, Kim KH, Brown RC. Catalytic pyrolysis of individual components of lignocellulosic biomass. Green Chem . 2014;16(2):727–35. Available from: https://pubs.rsc.org/en/content/articlelanding/2014/gc/c3gc41288a#!divAbstract

80. Amutio M, Lopez G, Aguado R, Artetxe M, Bilbao J, Olazar M. Kinetic study of lignocellulosic biomass oxidative pyrolysis. Fuel . 2012;95:305–11. Available from: http://www.sciencedirect.com/science/article/pii/S0016236111006259

81. Limayem A, Ricke SC. Lignocellulosic biomass for bioethanol production: Current perspectives, potential issues and future prospects. Prog Energy Combust Sci . 2012;38(4):449–67. Available from: http://dx.doi.org/10.1016/j.pecs.2012.03.002

82. Wang S, Dai G, Yang H, Luo Z. Lignocellulosic biomass pyrolysis mechanism: A state-of-the-art review. Prog Energy Combust Sci . 2017;62:33–86. Available from: http://dx.doi.org/10.1016/j.pecs.2017.05.004

83. Kabir G, Hameed BH. Recent progress on catalytic pyrolysis of lignocellulosic biomass to high-grade bio-oil and bio-chemicals. Renew Sustain Energy Rev . 2017;70(March 2015):945–67. Available from: http://dx.doi.org/10.1016/j.rser.2016.12.001

84. Guedes RE, Luna AS, Torres AR. Operating parameters for bio-oil production in biomass pyrolysis: A review. J Anal Appl Pyrolysis . 2018;129(November 2017):134–49. Available from: https://doi.org/10.1016/j.jaap.2017.11.019

85. Gasson JR, Forchheim D, Sutter T, Hornung U, Kruse A, Barth T. Modeling the lignin degradation kinetics in an ethanol/formic acid solvolysis approach. Part 1. Kinetic model development. Ind Eng Chem Res . 2012;51(32):10595–606. Available from: https://pubs.acs.org/doi/10.1021/ie301487v

86. Ragauskas AJ, Beckham GT, Biddy MJ, Chandra R, Chen F, Davis MF, et al. Lignin valorization: Improving lignin processing in the biorefinery. Science (80-) . 2014;344(6185). Available from: https://science.sciencemag.org/content/344/6185/1246843

87. Kumar CR, Anand N, Kloekhorst A, Cannilla C, Bonura G, Frusteri F, et al. Solvent free depolymerization of Kraft lignin to alkyl-phenolics using supported NiMo and CoMo catalysts. Green Chem . 2015;17(11):4921–30. Available from: https://pubs.rsc.org/en/content/articlelanding/2015/gc/c5gc01641j#!divAbstract

88. Ong HC, Chen W-H, Singh Y, Gan YY, Chen C-Y, Show PL. A state-of-the-art review on thermochemical conversion of biomass for biofuel production: A TG-FTIR approach. Energy Convers Manag . 2020;209:112634. Available from: http://www.sciencedirect.com/science/article/pii/S0196890420301722

89. Callegari A, Bolognesi S, Cecconet D, Capodaglio AG. Production technologies, current role, and future prospects of biofuels feedstocks: A state-of-the-art review. Crit Rev Environ Sci Technol . 2020;50(4):384–436. Available from: https://doi.org/10.1080/10643389.2019.1629801

90. Bertero M, De La Puente G, Sedran U. Fuels from bio-oils: Bio-oil production from different residual sources, characterization and thermal conditioning. Fuel . 2012;95:263–71. Available from: http://dx.doi.org/10.1016/j.fuel.2011.08.041

91. Zakzeski J, Bruijnincx PCA, Jongerius AL, Weckhuysen BM. The Catalytic Valorization of Ligning for the Production of Renewable Chemicals. Chem Rev . 2010;110:3552–99. Available from: https://pubs.acs.org/doi/10.1021/cr900354u

92. Huber GW, Iborra S, Corma A. Synthesis of Transportation Fuels from Biomass: Chemistry, Catalysts, and Engineering. Chem Rev . 2006;106(9):4044–98. Available from: https://doi.org/10.1021/cr068360d

93. Hassan MH, Kalam MA. An Overview of Biofuel as a Renewable Energy Source: Development and Challenges. Procedia Eng . 2013;56:39–53. Available from: http://www.sciencedirect.com/science/article/pii/S1877705813004414

94. Tuck CO, Pérez E, Horváth IT, Sheldon RA, Poliakoff M. Valorization of Biomass: Deriving More Value from Waste. Science (80-) . 2012;337(6095):695 LP – 699. Available from: http://science.sciencemag.org/content/337/6095/695.abstract

95. Zakzeski J, Jongerius AL, Bruijnincx PCA, Weckhuysen BM. Catalytic Lignin Valorization Process for the Production of Aromatic Chemicals and Hydrogen. ChemSusChem . 2012;5(8):1602–9. Available from: https://doi.org/10.1002/cssc.201100699

96. International Renewable Energy Agency (IRENA). Advanced biofuels. What holds them back? . 2019. Available from: https://www.irena.org/publications/2019/Nov/Advanced-biofuels-What-holds-them-back

97. Reference Regulatory Framework | EU Science Hub . [cited 2020 Aug 8]. Available from:

https://ec.europa.eu/jrc/en/jec/reference-regulatory-framework

98. Eurostat - Data Explorer . [cited 2020 Jul 17]. Available from: http://appsso.eurostat.ec.europa.eu/nui/submitViewTableAction.do

99. Fagerström A, Anderson S, Lindblom H. The contribution of advanced renewable transport fuels to transport decarbonization in Sweden - 2030 and beyong . 2019. Available from: https://www.ivl.se/download/18.20b707b7169f355daa77ae0/1561538469463/C416.pdf

100. Biofuels in the time of Covid-19: Staying the course on clean transport fuels in Latin America – Analysis - IEA . [cited 2020 Aug 20]. Available from: https://www.iea.org/commentaries/biofuels-in-the-time-of-covid-19-staying-the-course-on-clean-transport-fuels-in-latin-america

101. RenovaBio: Biocombustíveis 2030 . [cited 2020 Aug 20]. Available from: http://www.mme.gov.br/documents/36224/460139/EPE_NT1_PAPEL+DOS+BIOCOMBUSTÍVEIS.pdf/d0387687-b3a6-0543-6a70-03e8f750d1e9?version=1.0

102. National energy and climate plans (NECPs) | European Commission . [cited 2020 Aug 10]. Available from: https://ec.europa.eu/info/energy-climate-change-environment/overall-targets/national-energy-and-climate-plans-necps_en

103. Bioenergie B. EU climate law and climate protection legislation call for effective climate protection measures in transport . 2020. Available from: https://www.ufop.de/files/2515/9480/2390/200702_Position_paper_EU_climate_law_and_climate_protection_legislation_call_for_effec-tive_climate_protection_measures_in_transport.pdf

104. IEA (2020). Renewable Energy Market Update, IEA, Paris . 2020. Available from: https://www.iea.org/reports/renewable-energy-market-update

105. International Renewable Energy Agency (IRENA). Renewable Energy and Jobs: Annual Review 2019 . 2019. Available from: www.irena.org

106. Cristalco - COVID-19: CRISTAL union group is being mobilized . [cited 2020 Aug 21]. Available from: https://cristalco.com/en/article/137-covid-19-cristal-union-group-is-being-mobilized

107. Le Groupe Cristal Union annonce l'arrêt temporaire d'une unité de production de bioéthanol au profit de la production d'alcool éthylique. - Cristal Union . [cited 2020 Aug 21]. Available from: https://www.cristal-union.fr/actualites/le-groupe-cristal-union-annonce-larret-temporaire-dune-unite-de-production-de-bioethanol-au-profit-de-la-production-dalcool-ethylique/

108. Oil Bailouts Force POET to Lower Production - POET . [cited 2020 Aug 21]. Available from: https://poet.com/pr/oil-bailouts-force-poet-to-lower-production

109. Ethanol Producer Magazine – The Latest News and Data About Ethanol Production . [cited 2020 Aug 21]. Available from: http://ethanolproducer.com/articles/17061/biofuel-producers-face-continued-economic-hardship-from-covid-19

110. International Renewable Energy Agency (IRENA). The post-COVID recovery: An agenda for resilience, development and equality . 2020. Available from: https://www.irena.org/-/media/Files/IRENA/Agency/Publication/2020/Apr/IRENA_GRO_Regional_Factsheets.pdf?la=en&hash=3F56F17BF240485E636A852588759185FEAA7B58

111. Fuels – Sustainable Recovery – Analysis - IEA . [cited 2020 Sep 7]. Available from: https://www.iea.org/reports/sustainable-recovery/fuels#abstract

112. Cortez LAB, Nogueira LAH, Leal MRVL, Baldassin RJ. 40 Years of the Brazilian Ethanol Program (Proálcool): Relevant Public Policies and Events Throughout Its Trajectory and Future Perspectives. 22nd Int Symp Alcohol Fuels – 22nd ISAF 40 . 2016;1–13. Available from: http://bioenfapesp.org/gsb/lacaf/documents/papers/05_ISAF_2016_Cortez_et_al.pdf

113. Natarajan K, Bhaskaran KA. Experimental and analytical investigation of high temperature ignition of ethanol . United States; 1981. Available from: https://www.osti.gov/biblio/6171078

114. Morgan N, Smallbone A, Bhave A, Kraft M, Cracknell R, Kalghatgi G. Mapping surrogate gasoline compositions into RON/MON space. Combust Flame . 2010;157(6):1122–31. Available from: http://www.sciencedirect.com/science/article/pii/S0010218010000337

115. Nowakowska M. Conversion thermique des goudrons provenant de la gazéification de la biomasse . Université de Lorraine; 2014. Available from: http://www.theses.fr/2014LORR0092/document

116. Yaws CL. The Yaws Handbook of Vapor Pressure. Elsevier Inc.; 2015. 327 p.

117. Wang C, Zeraati-Rezaei S, Xiang L, Xu H. Ethanol blends in spark ignition engines: RON, octane-added value, cooling effect, compression ratio, and potential engine efficiency gain. Appl Energy . 2017;191:603–19. Available from: http://www.sciencedirect.com/science/article/pii/S0306261917300946

118. Jiang Y, Xu H, Ma X, Bao X, Wang B. Laminar burning characteristics of 2-MTHF compared with ethanol and isooctane. Fuel . 2017;190:10–20. Available from: http://www.sciencedirect.com/science/article/pii/S0016236116311371

119. Elfasakhany A. Exhaust emissions and performance of ternary iso-butanol–bio-methanol–gasoline and n-butanol–bio-ethanol–gasoline fuel blends in spark-ignition engines: Assessment and comparison. Energy . 2018;158:830–44. Available from: http://www.sciencedirect.com/science/article/pii/S0360544218309460

120. McCormick RL, Fioroni G, Fouts L, Christensen E, Yanowitz J, Polikarpov E, et al. Selection Criteria and Screening of Potential

Biomass-Derived Streams as Fuel Blendstocks for Advanced Spark-Ignition Engines. SAE Int J Fuels Lubr . 2017;10(2):442–60. Available from: https://doi.org/10.4271/2017-01-0868

121. Ma X, Jiang C, Xu H, Ding H, Shuai S. Laminar burning characteristics of 2-methylfuran and isooctane blend fuels. Fuel . 2014;116:281–91. Available from: http://dx.doi.org/10.1016/j.fuel.2013.08.018

122. Isooctane - Registration Dossier - ECHA . [cited 2019 Oct 10]. Available from: https://echa.europa.eu/registration-dossier/-/registered-dossier/26046/4/9

123. Zhang P, Yee NW, Filip S V, Hetrick CE, Yang B, Green WH. Modeling study of the anti-knock tendency of substituted phenols as additives: an application of the reaction mechanism generator (RMG). Phys Chem Chem Phys . 2018;20(16):10637–49. Available from: http://dx.doi.org/10.1039/C7CP07058F

124. Ninnemann E, Kim G, Laich A, Almansour B, Terracciano AC, Park S, et al. Co-optima fuels combustion: A comprehensive experimental investigation of prenol isomers. Fuel . 2019;254:115630. Available from: http://www.sciencedirect.com/science/article/pii/S0016236119309822

125. Chen Z, Ai Y, Qin T, Luo F. Quantitative evaluation of n-butane concentration on knock severity of a natural gas heavy-duty SI engine. Energy . 2019;189:116244. Available from: http://www.sciencedirect.com/science/article/pii/S0360544219319395

126. Curran HJ. Developing detailed chemical kinetic mechanisms for fuel combustion. Proc Combust Inst . 2019;37(1):57–81. Available from: http://www.sciencedirect.com/science/article/pii/S1540748918302372

127. Battin-Leclerc F. Chimie de la combustion: Auto-inflammation des carburants. Tech l'ingénieur . 2009;BE8318(0):1–19. Available from: http://cat.inist.fr/?aModele=afficheN&cpsidt=22122497

128. Ó Conaire M, Curran HJ, Simmie JM, Pitz WJ, Westbrook CK. A comprehensive modeling study of hydrogen oxidation. Int J Chem Kinet . 2004;36(11):603–22. Available from: https://doi.org/10.1002/kin.20036

129. Marinov NM, Westbrook CK, Pitz WJ. Detailed and Global Chemical Kinetics Model for Hydrogen. In: 8th International Symposium on Transport Properties . San Francisco: Taylor & Francis; 1995. Available from: https://digital.library.unt.edu/ark:/67531/metadc794810/

130. Tian M. Lignocellulosic Octane Boosters . Eindhoven University of Technology; 2016. Available from: https://research.tue.nl/en/publications/lignocellulosic-octane-boosters

131. Curran HJ. Detailed Chemical Kinetic Mechanisms for Combustion. In: Proceedings of the European Combustion Meeting 2009 . 2009. Available from: http://citeseerx.ist.psu.edu/viewdoc/download?doi=10.1.1.596.35&rep=rep1&type=pdf

132. Vanhove G, Boumehdi M-A, Shcherbanev S, Fenard Y, Desgroux P, Starikovskaia SM. A comparative experimental kinetic study of spontaneous and plasma-assisted cool flames in a rapid compression machine. In: Proceedings of the Combustion Institute . 2017. p. 4137–43. Available from: http://www.sciencedirect.com/science/article/pii/S1540748916304837

133. Pilling MJ. Low Temperature Combustion and Autoignition. Elsevier Science; 1997. 793 p.

134. Westbrook CK, Mehl M, Pitz WJ, Sjöberg M. Chemical kinetics of octane sensitivity in a spark-ignition engine. Combust Flame . 2017;175:2–15. Available from: http://www.sciencedirect.com/science/article/pii/S0010218016301146

135. Sarathy SM, Oßwald P, Hansen N, Kohse-Höinghaus K. Alcohol combustion chemistry. Prog Energy Combust Sci . 2014;44:40–102. Available from: http://www.sciencedirect.com/science/article/pii/S0360128514000240

136. GRI-Mech 3.0 . [cited 2020 Apr 16]. Available from: http://combustion.berkeley.edu/gri-mech/version30/text30.html

137. Xue J, Xi S, Wang F. An extensive study on skeletal mechanism reduction for the oxidation of C0–C4 fuels. Combust Flame . 2020;214:184–98. Available from: http://www.sciencedirect.com/science/article/pii/S0010218019305930

138. Guo J, Li S, Tang S, Xiao L, Tan N. Influence of Different Core Mechanisms on Low-Temperature Combustion Characteristics of Large Hydrocarbon Fuels. Energy & Fuels . 2019;33(8):7835–51. Available from: https://doi.org/10.1021/acs.energyfuels.9b01365

139. Lawrence Livermore National Laboratory - Mechanisms . [cited 2020 Apr 26]. Available from: https://combustion.llnl.gov/mechanisms

140. Chemical Mechanism: Combustion Research Group at UC San Diego . [cited 2020 Apr 26]. Available from: http://web.eng.ucsd.edu/mae/groups/combustion/mechanism.html

141. CRECK Modeling - Detailed kinetic mechanisms . [cited 2020 Apr 26]. Available from: http://creckmodeling.chem.polimi.it/menu-kinetics/menu-kinetics-detailed-mechanisms

142. Li Y, Zhou C-W, Somers KP, Zhang K, Curran HJ. The oxidation of 2-butene: A high pressure ignition delay, kinetic modeling study and reactivity comparison with isobutene and 1-butene. In: Proceedings of the Combustion Institute . 2017. p. 403–11. Available from: http://www.sciencedirect.com/science/article/pii/S1540748916300529

143. Norrish RGW, Foord SG. The kinetics of the combustion of methane. Proc R Soc London Ser A - Math Phys Sci . 1936;157(892):503–25. Available from: https://doi.org/10.1098/rspa.1936.0211

144. Simmie JM. Detailed chemical kinetic models for the combustion of hydrocarbon fuels. Prog Energy Combust Sci . 2003;29(6):599–634. Available from: http://www.sciencedirect.com/science/article/pii/S0360128503000601

145. Battin-Leclerc F, Simmie JM, Blurock E. Cleaner Combustion. London: Springer; 2013. 657 p.

146. Mehl M, Vanhove G, Pitz WJ, Ranzi E. Oxidation and combustion of the n-hexene isomers: A wide range kinetic modeling study. Combust Flame . 2008;155(4):756–72. Available from: http://www.sciencedirect.com/science/article/pii/S0010218008002150

147. Maurya RK. Characteristics and Control of Low Temperature Combustion Engines. Springer International Publishing AG; 2018. 544 p.

148. Westbrook CK. Chemical Kinetics of Hydrocarbon Ignition in Pratical Combustion Systems. In: Proceedings of the Combustion Institute . 2000. p. 1563–77. Available from: https://doi.org/10.1016/S0082-0784(00)80554-8

149. Mehl M, Pitz WJ, Westbrook CK, Yasunaga K, Conroy C, Curran HJ. Autoignition behavior of unsaturated hydrocarbons in the low and high temperature regions. In: Proceedings of the Combustion Institute . 2011. p. 201–8. Available from: http://www.sciencedirect.com/science/article/pii/S154074891000101X

150. Curran HJ, Gaffuri P, Pitz WJ, Westbrook CK. A comprehensive modeling study of iso-octane oxidation. Combust Flame . 2002;129(3):253–80. Available from: http://www.sciencedirect.com/science/article/pii/S001021800100373X

151. Walsh AD. Processes in the oxidation of hydrocarbon fuels.—I. Trans Faraday Soc . 1946;42(0):269–79. Available from: http://dx.doi.org/10.1039/TF9464200269

152. Wang Z, Sarathy SM. Third O2 addition reactions promote the low-temperature auto-ignition of n-alkanes. Combust Flame . 2016;165:364–72. Available from: http://www.sciencedirect.com/science/article/pii/S0010218015004630

153. Minetti R, Ribaucour M, Carlier M, Sochet LR. Autoignition Delays of a Series of Linear and Branched Chain Alkanes in the Intermediate Range of Temperature. Combust Sci Technol . 1996;113(1):179–92. Available from: https://doi.org/10.1080/00102209608935493

154. Beerer DJ, McDonell VG. An experimental and kinetic study of alkane autoignition at high pressures and intermediate temperatures. In: Proceedings of the Combustion Institute . 2011. p. 301–7. Available from: http://www.sciencedirect.com/science/article/pii/S1540748910000477

155. Jarrosson F, Fenard Y, Vanhove G, Dauphin R. Gasoline and Combustion: Relationship between Molecular Structure and Performance. SAE Tech Pap . 2018; Available from: https://doi.org/10.4271/2018-01-0906

156. Wallington TJ, Kaiser EW, Farrell JT. Automotive fuels and internal combustion engines: A chemical perspective. Chem Soc Rev . 2006;35(4):335–47. Available from: https://doi.org/10.1039/B410469M

157. Knox JH. A New Mechanism for the Low Temperature Oxidation of Hydrocarbons in the Gas Phase. Combust Flame . 1965; Available from: https://doi.org/10.1016/0010-2180(65)90095-7

158. Fish A, Read IA, Affleck WS, Haskell WW. The controlling role of cool flames in two-stage ignition. Combust Flame . 1969;13(1):39–49. Available from: http://www.sciencedirect.com/science/article/pii/0010218069900261

159. Westbrook CK, Warnatz J, Pitz WJ. A detailed chemical kinetic reaction mechanism for the oxidation of iso-octane and n-heptane over an extended temperature range and its application to analysis of engine knock. In: Symposium (International) on Combustion . 1989. p. 893–901. Available from: http://www.sciencedirect.com/science/article/pii/S0082078489800980

160. Chen J-S, Litzinger TA, Curran HJ. The Lean Oxidation of Iso-Octane in the Intermediate Temperature Regime at Elevated Pressures. Combust Sci Technol . 2000;156(1):49–79. Available from: https://doi.org/10.1080/00102200008947296

161. Mehl M, Curran HJ, Pitz WJ, Westbrook CK. Detailed Kinetic Modeling of Gasoline Surrogate Mixtures. In United States; 2009. Available from: https://www.osti.gov/biblio/953312

162. Mehl M, Pitz WJ, Westbrook CK, Curran HJ. Kinetic modeling of gasoline surrogate components and mixtures under engine conditions. Proc Combust Inst . 2011;33(1):193–200. Available from: http://www.sciencedirect.com/science/article/pii/S1540748910000787

163. Sarathy SM, Kukkadapu G, Mehl M, Wang W, Javed T, Park S, et al. Ignition of alkane-rich FACE gasoline fuels and their surrogate mixtures. In: Proceedings of the Combustion Institute . 2015. p. 249–57. Available from: http://www.sciencedirect.com/science/article/pii/S1540748914001254

164. Vuilleumier D, Selim H, Dibble R, Sarathy M. Exploration of Heat Release in a Homogeneous Charge Compression Ignition Engine with Primary Reference Fuels. SAE Tech Pap . 2013; Available from: https://doi.org/10.4271/2013-01-2622

165. Hwang W, Dec J, Sjöberg M. Spectroscopic and chemical -kinetic analysis of the phases of HCCI autoignition and combustion for single- and two-stage ignition fuels. Combust Flame . 2008;154(3):387–409. Available from: http://www.sciencedirect.com/science/article/pii/S0010218008000977

166. Atef N, Kukkadapu G, Mohamed SY, Rashidi M Al, Banyon C, Mehl M, et al. A comprehensive iso-octane combustion model with improved thermochemistry and chemical kinetics. Combust Flame . 2017;178:111–34. Available from: http://www.sciencedirect.com/science/article/pii/S0010218016304059

167. Fang R, Kukkadapu G, Wang M, Wagnon SW, Zhang K, Mehl M, et al. Fuel molecular structure effect on autoignition of highly branched iso-alkanes at low-to-intermediate temperatures: Iso-octane versus iso-dodecane. Combust Flame . 2020;214:152–66. Available from: http://www.sciencedirect.com/science/article/pii/S0010218019305954

168. Zhang K, Banyon C, Burke U, Kukkadapu G, Wagnon SW, Mehl M, et al. An experimental and kinetic modeling study of the oxidation of hexane isomers: Developing consistent reaction rate rules for alkanes. Combust Flame . 2019;206:123–37. Available from: http://www.sciencedirect.com/science/article/pii/S0010218019301567

169. Di H, He X, Zhang P, Wang Z, Wooldridge MS, Law CK, et al. Effects of buffer gas composition on low temperature ignition of iso-

octane and n-heptane. Combust Flame . 2014;161(10):2531–8. Available from: http://dx.doi.org/10.1016/j.combustflame.2014.04.014

170. Zhang P, Ji W, He T, He X, Wang Z, Yang B, et al. First-stage ignition delay in the negative temperature coefficient behavior: Experiment and simulation. Combust Flame . 2016;167:14–23. Available from: http://www.sciencedirect.com/science/article/pii/S0010218016300098

171. Mittal G, Chomier M. Effect of crevice mass transfer in a rapid compression machine. Combust Flame . 2014;161(2):398–404. Available from: http://www.sciencedirect.com/science/article/pii/S0010218013003404

172. Mittal G, Sung C-J. Homogeneous charge compression ignition of binary fuel blends. Combust Flame . 2008;155(3):431–9. Available from: http://www.sciencedirect.com/science/article/pii/S0010218008001557

173. Mittal G, Sung C-J. A Rapid Compression Machine for chemical kinetics studies at elevated pressures and temperatures. Combust Sci Technol . 2007;179(3):497–530. Available from: https://doi.org/10.1080/00102200600671898

174. Wu Y, Yang M, Tang C, Liu Y, Zhang P, Huang Z. Promoting "adiabatic core" approximation in a rapid compression machine by an optimized creviced piston design. Fuel . 2019;251:328–40. Available from: http://www.sciencedirect.com/science/article/pii/S001623611930585X

175. Goldsborough SS, Hochgreb S, Vanhove G, Wooldridge MS, Curran HJ, Sung C-J. Advances in rapid compression machine studies of low- and intermediate-temperature autoignition phenomena. Prog Energy Combust Sci . 2017;63:1–78. Available from: http://www.sciencedirect.com/science/article/pii/S0360128516300776

176. He X, Donovan MT, Zigler BT, Palmer TR, Walton SM, Wooldridge MS, et al. An experimental and modeling study of iso-octane ignition delay times under homogeneous charge compression ignition conditions. Combust Flame . 2005;142(3):266–75. Available from: https://doi.org/10.1016/j.combustflame.2005.02.014

177. Ribaucour M. Autoinflammation et cliquetis dans les moteurs : étude en machine à compression rapide de l'influence de la structure de l'hydrocarbure sur les délais d'autoinflammation . 1992. Available from: http://www.theses.fr/1992LIL10012

178. Minetti R, Carlier M, Ribaucour M, Therssen E, Sochet LR. Comparison of oxidation and autoignition of the two primary reference fuels by rapid compression. In: Symposium (International) on Combustion . 1996. p. 747–53. Available from: http://www.sciencedirect.com/science/article/pii/S0082078496802839

179. Vanhove G. Oxydation , co-oxydation et auto-inflammation à basses températures d'alcènes et aromatiques type. Etude expérimentale des interactions au sein d'un carburant-modèle . Université Des Sciences et Technologies de Lille; 2004. Available from: http://ori-nuxeo.univ-lille1.fr/nuxeo/site/esupversions/ec6260f2-ea19-4353-8da3-98c60a66ba48

180. Fieweger K, Blumenthal R, Adomeit G. Self-ignition of S.I. engine model fuels: A shock tube investigation at high pressure. Combust Flame . 1997;109(4):599–619. Available from: http://www.sciencedirect.com/science/article/pii/S0010218097000497

181. Davidson DF, Oehlschlaeger MA, Herbon JT, Hanson RK. Shock tube measurements of iso-octane ignition times and OH concentration time histories. In: Proceedings of the Combustion Institute . 2002. p. 1295–301. Available from: http://www.sciencedirect.com/science/article/pii/S1540748902801596

182. Davidson DF, Gauthier BM, Hanson RK. Shock tube ignition measurements of iso-octane/air and toluene/air at high pressures. In: Proceedings of the Combustion Institute . 2005. p. 1175–82. Available from: http://www.sciencedirect.com/science/article/pii/S0082078404000566

183. Shen H-PS, Vanderover J, Oehlschlaeger MA. A shock tube study of iso-octane ignition at elevated pressures: The influence of diluent gases. Combust Flame . 2008;155(4):739–55. Available from: http://www.sciencedirect.com/science/article/pii/S0010218008001879

184. Hartmann M, Gushterova I, Fikri M, Schulz C, Schießl R, Maas U. Auto-ignition of toluene-doped n-heptane and iso-octane/air mixtures: High-pressure shock-tube experiments and kinetics modeling. Combust Flame . 2011;158(1):172–8. Available from: http://www.sciencedirect.com/science/article/pii/S0010218010002312

185. Malewicki T, Comandini A, Brezinsky K. Experimental and modeling study on the pyrolysis and oxidation of iso-octane. Proc Combust Inst . 2013;34(1):353–60. Available from: http://www.sciencedirect.com/science/article/pii/S1540748912002453

186. Fieweger K, Blumenthal R, Adomeit G. Shock-tube investigations on the self-ignition of hydrocarbon-air mixtures at high pressures. In: Symposium (International) on Combustion . 1994. p. 1579–85. Available from: http://www.sciencedirect.com/science/article/pii/S0082078406808039

187. D'anna A, Mercoguano R, Barbella R, Ciajolo A. Low Temperature Oxidation Chemistry of iso-Octane under High Pressure Conditions. Combust Sci Technol . 1992;83(4–6):217–32. Available from: https://doi.org/10.1080/00102209208951833

188. Lignola PG, Di Maio FP, Marzocchella A, Mercogliano R, Reverchon E. JSFR combustion processes of n-heptane and isooctane. In: Symposium (International) on Combustion . 1989. p. 1625–33. Available from: http://www.sciencedirect.com/science/article/pii/S0082078489801742

189. Dagaut P, Reuillon M, Cathonnet M. High Pressure Oxidation of Liquid Fuels From Low to High Temperature. 1. n-Heptane and iso-Octane. Combust Sci Technol . 1993;95(1–6):233–60. Available from: https://doi.org/10.1080/00102209408935336

190. Galmiche B, Halter F, Foucher F. Effects of high pressure, high temperature and dilution on laminar burning velocities and Markstein lengths of iso-octane/air mixtures. Combust Flame . 2012;159(11):3286–99. Available from: http://www.sciencedirect.com/science/article/pii/S0010218012001885

191. van Lipzig JPJ, Nilsson EJK, de Goey LPH, Konnov AA. Laminar burning velocities of n-heptane, iso-octane, ethanol and their binary and tertiary mixtures. Fuel . 2011;90(8):2773–81. Available from: http://www.sciencedirect.com/science/article/pii/S0016236111002365

192. Kumar K, Freeh JE, Sung CJ, Huang Y. Laminar Flame Speeds of Preheated iso-Octane/O2/N2 and n-Heptane/O2/N2 Mixtures. J Propuls Power . 2007;23(2):428–36. Available from: https://doi.org/10.2514/1.24391

193. Huang Y, Sung CJ, Eng JA. Laminar flame speeds of primary reference fuels and reformer gas mixtures. Combust Flame . 2004;139(3):239–51. Available from: http://www.sciencedirect.com/science/article/pii/S0010218004001750

194. Kwon OC, Hassan MI, Faeth GM. Flame/Stretch Interactions of Premixed Fuel-Vapor/O/N Flames. J Propuls Power . 2000;16(3):513–22. Available from: https://doi.org/10.2514/2.5598

195. Ji C, Sarathy SM, Veloo PS, Westbrook CK, Egolfopoulos FN. Effects of fuel branching on the propagation of octane isomers flames. Combust Flame . 2012;159(4):1426–36. Available from: http://www.sciencedirect.com/science/article/pii/S0010218011004019

196. Davis SG, Law CK. Laminar flame speeds and oxidation kinetics of iso-octane-air and n-heptane-air flames. In: Symposium (International) on Combustion . 1998. p. 521–7. Available from: http://www.sciencedirect.com/science/article/pii/S0082078498804426

197. Bradley D, Hicks RA, Lawes M, Sheppard CGW, Woolley R. The Measurement of Laminar Burning Velocities and Markstein Numbers for Iso-octane–Air and Iso-octane–n-Heptane–Air Mixtures at Elevated Temperatures and Pressures in an Explosion Bomb. Combust Flame . 1998;115(1):126–44. Available from: http://www.sciencedirect.com/science/article/pii/S0010218097003490

198. Liu N, Mani Sarathy S, Westbrook CK, Egolfopoulos FN. Ignition of non-premixed counterflow flames of octane and decane isomers. In: Proceedings of the Combustion Institute . 2013. p. 903–10. Available from: http://www.sciencedirect.com/science/article/pii/S1540748912000417

199. Blouch JD, Law CK. Non-premixed ignition of n-heptane and iso-octane in a laminar counterflow. In: Proceedings of the Combustion Institute . 2000. p. 1679–86. Available from: http://www.sciencedirect.com/science/article/pii/S0082078400805676

200. Ning H, Gong C, Li Z, Li X. Pressure-Dependent Kinetics of Initial Reactions in Iso-octane Pyrolysis. J Phys Chem A . 2015;119(18):4093–107. Available from: https://doi.org/10.1021/acs.jpca.5b02013

201. Snitsiriwat S, Bozzelli JW. Thermochemical Properties for Isooctane and Carbon Radicals: Computational Study. J Phys Chem A . 2013;117(2):421–9. Available from: https://doi.org/10.1021/jp3041154

202. Auzmendi-Murua I, Bozzelli JW. Thermochemistry, Reaction Paths, and Kinetics on the Secondary Isooctane Radical Reaction with 3O2. Int J Chem Kinet . 2014;46(2):71–103. Available from: https://doi.org/10.1002/kin.20825

203. Walton SM, He X, Zigler BT, Wooldridge MS, Atreya A. An experimental investigation of iso-octane ignition phenomena. Combust Flame . 2007;150(3):246–62. Available from: http://www.sciencedirect.com/science/article/pii/S0010218006002008

204. Vanhove G, Petit G, Minetti R. Experimental study of the kinetic interactions in the low-temperature autoignition of hydrocarbon binary mixtures and a surrogate fuel. Combust Flame . 2006;145(3):521–32. Available from: http://www.sciencedirect.com/science/article/pii/S0010218006000277

205. He X, Zigler BT, Walton SM, Wooldridge MS, Atreya A. A rapid compression facility study of OH time histories during iso-octane ignition. Combust Flame . 2006;145(3):552–70. Available from: http://www.sciencedirect.com/science/article/pii/S0010218006000101

206. Tipler S, Mergulhão CS, Vanhove G, Van Haute Q, Contino F, Coussement A. Ignition study of an oxygenated and high-alkene light petroleum fraction produced from automotive shredder residues. Energy and Fuels . 2019;33(6):5664–72. Available from: https://pubs.acs.org/doi/10.1021/acs.energyfuels.9b00649

207. Westbrook CK, Pitz WJ, Mehl M, Glaude P-A, Herbinet O, Bax S, et al. Experimental and Kinetic Modeling Study of 2-Methyl-2-Butene: Allylic Hydrocarbon Kinetics. J Phys Chem A . 2015;119(28):7462–80. Available from: https://doi.org/10.1021/acs.jpca.5b00687

208. Kumar K, Mittal G, Sung C-J, Law CK. An experimental investigation of ethylene/O2/diluent mixtures: Laminar flame speeds with preheat and ignition delays at high pressures. Combust Flame . 2008;153(3):343–54. Available from: http://www.sciencedirect.com/science/article/pii/S0010218008000412

209. Colket MB, Spadaccini LJ. Scramjet Fuels Autoignition Study. J Propuls Power . 2001;17(2):315–23. Available from: https://doi.org/10.2514/2.5744

210. Kopp MM, Donato NS, Petersen EL, Metcalfe WK, Burke SM, Curran HJ. Oxidation of Ethylene–Air Mixtures at Elevated Pressures, Part 1: Experimental Results. J Propuls Power . 2014;30(3):790–8. Available from: https://doi.org/10.2514/1.B34890

211. Burke SM, Burke U, Mc Donagh R, Mathieu O, Osorio I, Keesee C, et al. An experimental and modeling study of propene oxidation. Part 2: Ignition delay time and flame speed measurements. Combust Flame . 2015;162(2):296–314. Available from: http://www.sciencedirect.com/science/article/pii/S0010218014002387

212. Wang K, Villano SM, Dean AM. Fundamentally-based kinetic model for propene pyrolysis. Combust Flame . 2015;162(12):4456–70. Available from: http://www.sciencedirect.com/science/article/pii/S0010218015002734

213. Choi J-H, Shin W-J, Lee W-J, Choi BC. Autoignited laminar lifted flames of propene in heated coflow jets: Dependence on ignition

delay time. Fuel . 2017;206:307–17. Available from: http://www.sciencedirect.com/science/article/pii/S0016236117306920

214. Minetti R, Roubaud A, Therssen E, Ribaucour M, Sochet LR. The chemistry of pre-ignition of n-pentane and 1-pentene. Combust Flame . 1999;118(1):213–20. Available from: http://www.sciencedirect.com/science/article/pii/S0010218098001515

215. Cheng Y, Hu E, Deng F, Yang F, Zhang Y, Tang C, et al. Experimental and kinetic comparative study on ignition characteristics of 1-pentene and n -pentane. FUEL . 2016;172:263–72. Available from: http://dx.doi.org/10.1016/j.fuel.2016.01.008

216. Ribaucour M, Minetti R, Sochet LR. Autoignition of n-pentane and 1-pentene: Experimental data and kinetic modeling. In: Symposium (International) on Combustion . 1998. p. 345–51. Available from: http://www.sciencedirect.com/science/article/pii/S0082078498804220

217. Cheng Y, Hu E, Lu X, Li X, Gong J, Li Q, et al. Experimental and kinetic study of pentene isomers and n-pentane in laminar flames. Proc Combust Inst . 2017;36(1):1279–86. Available from: http://www.sciencedirect.com/science/article/pii/S1540748916304151

218. Vanhove G, Ribaucour M, Minetti R. On the influence of the position of the double bond on the low-temperature chemistry of hexenes. In: Proceedings of the Combustion Institute . 2005. p. 1065–72. Available from: http://www.sciencedirect.com/science/article/pii/S0082078404000955

219. Fan X, Wang G, Li Y, Wang Z, Yuan W, Zhao L. Experimental and kinetic modeling study of 1-hexene combustion at various pressures. Combust Flame . 2016;173:151–60. Available from: http://www.sciencedirect.com/science/article/pii/S0010218016301985

220. Blanksby SJ, Ellison GB. Bond Dissociation Energies of Organic Molecules. Acc Chem Res . 2003;36(4):255–63. Available from: https://doi.org/10.1021/ar020230d

221. Stark MS, Waddington DJ. Oxidation of propene in the gas phase. Int J Chem Kinet . 1995;27(2):123–51. Available from: https://onlinelibrary.wiley.com/action/showCitFormats?doi=10.1002%2Fkin.550270205

222. Zhou C-W, Li Y, O'Connor E, Somers KP, Thion S, Keesee C, et al. A comprehensive experimental and modeling study of isobutene oxidation. Combust Flame . 2016;167:353–79. Available from: http://www.sciencedirect.com/science/article/pii/S0010218016000365

223. Song H, Dauphin R, Vanhove G. Low-temperature Combustion of Methylbutene Isomers under Engine-relevant Conditions. Proc Eur Combust Meet. 2019;

224. Zhong B-J, Zeng Z-M, Peng H-S. The pressure dependence of laminar flame speed of 2-methyl-2-butene/air flames in the 0.1–1.0 MPa range. Combust Sci Technol . 2018;190(11):1886–99. Available from: https://doi.org/10.1080/00102202.2018.1467406

225. Ruwe L, Moshammer K, Hansen N, Kohse-Höinghaus K. Consumption and hydrocarbon growth processes in a 2-methyl-2-butene flame. Combust Flame . 2017;175:34–46. Available from: http://www.sciencedirect.com/science/article/pii/S001021801630178X

226. León L, Ruwe L, Moshammer K, Seidel L, Shrestha KP, Wang X, et al. Chemical insights into the larger sooting tendency of 2-methyl-2-butene compared to n-pentane. Combust Flame . 2019;208:182–97. Available from: http://www.sciencedirect.com/science/article/pii/S0010218019302883

227. Ruwe L, Moshammer K, Hansen N, Kohse-Höinghaus K. Influences of the molecular fuel structure on combustion reactions towards soot precursors in selected alkane and alkene flames. Phys Chem Chem Phys . 2018;20(16):10780–95. Available from: http://dx.doi.org/10.1039/C7CP07743B

228. Butler A, Sobotowski R, Hoffmann G, Machiele P. Influence of Fuel PM Index and Ethanol Content on Particulate Emissions from Light-Duty Gasoline Vehicles. SAE Tech Pap . 2015;2015-01–10. Available from: https://doi.org/10.4271/2015-01-1072

229. Boot M. Biofuels from lignocellulosic biomass: innovation beyond bioethanol . Wiley-VCH; 2016. 214 p. Available from: https://www.wiley.com/en-us/Biofuels+from+Lignocellulosic+Biomass%3A+Innovations+beyond+Bioethanol-p-9783527338139

230. Wagnon SW, Thion S, Nilsson EJK, Mehl M, Serinyel Z, Zhang K, et al. Experimental and modeling studies of a biofuel surrogate compound: laminar burning velocities and jet-stirred reactor measurements of anisole. Combust Flame . 2018;189:325–36. Available from: https://doi.org/10.1016/j.combustflame.2017.10.020

231. Roubaud-Bernard A. Étude de l'oxydation et la combustion de quelques hydrorcabures aromatiques entrant dans la composition des carburants automobiles . Université des sciences et technologies de Lille; 1999. Available from: http://ori-nuxeo.univ-lille1.fr/nuxeo/site/esupversions/904613a4-9fce-48a3-8ff5-85da97fed494

232. Mergulhão CS, Carstensen H-H, Song H, Wagnon SW, Pitz WJ, Vanhove G. Probing the antiknock effect of anisole through an ignition, speciation and modeling study of its blends with isooctane. Proc Combust Inst . 2020; Available from: http://www.sciencedirect.com/science/article/pii/S1540748920305976

233. McCormick RL, Ratcliff MA, Christensen E, Fouts L, Luecke J, Chupka GM, et al. Properties of Oxygenates Found in Upgraded Biomass Pyrolysis Oil as Components of Spark and Compression Ignition Engine Fuels. Energy & Fuels . 2015;29(4):2453–61. Available from: https://doi.org/10.1021/ef502893g

234. Sarathy SM, Farooq A, Kalghatgi GT. Recent progress in gasoline surrogate fuels. Prog Energy Combust Sci . 2018;65:67–108. Available from: https://doi.org/10.1016/j.pecs.2017.09.004

235. Pelucchi M, Faravelli T, Frassoldati A, Ranzi E, SriBala G, Marin GB, et al. Experimental and Kinetic Modeling Study of Pyrolysis

and Combustion of Anisole. AIDIC . 2018;26(9):5550–68. Available from: http://pubs.acs.org/doi/abs/10.1021/ef3011965#.VyjHXwc2I8U.mendeley

236. Nowakowska M, Herbinet O, Dufour A, Glaude PA. Detailed kinetic study of anisole pyrolysis and oxidation to understand tar formation during biomass combustion and gasification. Combust Flame . 2014;161(6):1474–88. Available from: http://dx.doi.org/10.1016/j.combustflame.2013.11.024

237. Shu B, Herzler J, Peukert S, Fikri M, Schulz C. A Shock Tube and Modeling Study about Anisole Pyrolysis Using Time-Resolved CO Absorption Measurements. Int J Chem Kinet . 2017;49(9):656–67. Available from: https://onlinelibrary.wiley.com/action/showCitFormats?doi=10.1002%2Fkin.21105

238. Barker Hemings E, Bozzano G, Dente M, Ranzi E. Detailed Kinetics of the Pyrolysis and Oxidation of Anisole. Chem Eng Trans . 2011;24:61-66 SE-Research Articles. Available from: https://www.cetjournal.it/index.php/cet/article/view/CET1124011

239. Yuan W, Li T, Li Y, Zeng M, Zhang Y, Zou J, et al. Experimental and kinetic modeling investigation on anisole pyrolysis: Implications on phenoxy and cyclopentadienyl chemistry. Combust Flame . 2019;201:187–99. Available from: http://www.sciencedirect.com/science/article/pii/S0010218018305455

240. Pelucchi M, Cavallotti C, Cuoci A, Faravelli T, Frassoldati A, Ranzi E. Detailed kinetics of substituted phenolic species in pyrolysis bio-oils. React Chem Eng . 2019;4(3):490–506. Available from: https://doi.org/10.1039/C8RE00198G

241. Herzler J, Fikri M, Schulz C. Ignition Delay Time Study of Aromatic LIF Tracers in a Wide Temperature and Pressure Range. In: 26th International Colloquium on the Dynamics of Explosions and Reactive Systems . 2017. Available from: http://www.icders.org/ICDERS2017/abstracts/ICDERS2017-0795.pdf

242. Ranzi E, Frassoldati A, Grana R, Cuoci A, Faravelli T, Kelley AP, et al. Hierarchical and comparative kinetic modeling of laminar flame speeds of hydrocarbon and oxygenated fuels. Prog Energy Combust Sci . 2012;38(4):468–501. Available from: http://www.sciencedirect.com/science/article/pii/S0360128512000196

243. Büttgen RD, Maffei LP, Pelucchi M, Faravelli T, Frassoldati A, Heufer KA. Towards a better understanding of the combustion of oxygenated aromatic hydrocarbons . Comparing benzene , toluene , phenol and anisole with ignition delay times in a rapid compression machine. Proc Eur Combust Meet. 2019;1–7.

244. Nowakowska M, Herbinet O, Dufour A, Glaude P-A. Detailed kinetic study of anisole pyrolysis and oxidation to understand tar formation during biomass combustion and gasification. Combust Flame . 2014;161(6):1474–88. Available from: http://www.sciencedirect.com/science/article/pii/S0010218013004379

245. Büttgen RD, Tian M, Fenard Y, Minwegen H, Boot MD, Heufer KA. An experimental, theoretical and kinetic modelling study on the reactivity of a lignin model compound anisole under engine-relevant conditions. Fuel . 2020;269(October 2019):117190. Available from: https://doi.org/10.1016/j.fuel.2020.117190

246. Pecullan MS. Pyrolyisis and Oxidation Kinetics of Anisole and Phenol . Princeton University; 1997. Available from: https://apps.dtic.mil/dtic/tr/fulltext/u2/a349061.pdf

247. Verma AM, Kishore N. Platinum catalyzed hydrodeoxygenation of guaiacol in illumination of cresol production: a density functional theory study. R Soc Open Sci . 2020;4(11):170650. Available from: https://doi.org/10.1098/rsos.170650

248. Sad ME, Padró CL, Apesteguía CR. Synthesis of cresols by alkylation of phenol with methanol on solid acids. Catal Today . 2008;133–135(1–4):720–8. Available from: https://doi.org/10.1016/j.cattod.2007.12.074

249. Roubaud A, Minetti R, Sochet LR. Oxidation and combustion of low alkylbenzenes at high pressure: comparative reactivity and auto-ignition. Combust Flame . 2000;121(3):535–41. Available from: http://www.sciencedirect.com/science/article/pii/S0010218099001698

250. Herbinet O, Husson B, Ferrari M, Glaude P-A, Battin-Leclerc F. Low temperature oxidation of benzene and toluene in mixture with n-decane. Proc Combust Inst . 2013;34(1):297–305. Available from: http://www.sciencedirect.com/science/article/pii/S1540748912001137

251. Zhang Y, Somers KP, Mehl M, Pitz WJ, Cracknell RF, Curran HJ. Probing the antagonistic effect of toluene as a component in surrogate fuel models at low temperatures and high pressures. A case study of toluene/dimethyl ether mixtures. In: Proceedings of the Combustion Institute . Elsevier Inc.; 2017. p. 413–21. Available from: http://dx.doi.org/10.1016/j.proci.2016.06.190

252. Pecullan M, Brezinsky K, Glassman I. Pyrolysis and Oxidation of Anisole near 1000 K. J Phys Chem A . 1997;101(18):3305–16. Available from: https://doi.org/10.1021/jp963203b

253. Cavallotti C, Cuoci A, Faravelli T, Frassoldati A, Ranzi E. Detailed Kinetics of Pyrolysis and Combustion of Catechol and Guaiacol , as Reference Components of Bio-Oil from Biomass. Chem Eng Trans . 2018;65(2017):2–7. Available from: http://hdl.handle.net/11311/1057473

254. Singaravelan K, Dhivakar AK, Sivananth M, Sivasankaralingam V, Balasubramanian KA. Effect of oxygenated additives on the characteristics of a diesel engine. In: International Journal of Applied Engineering Research . 2015. Available from: http://www.ripublication.com/ijaer.htm

255. Schwantes RH, Schilling KA, McVay RC, Lignell H, Coggon MM, Zhang X, et al. Formation of highly oxygenated low-volatility products from cresol oxidation. Atmos Chem Phys . 2017;17(5):3453–74. Available from: https://acp.copernicus.org/articles/17/3453/2017/

256. Pachiannan T, Zhong W, Rajkumar S, He Z, Leng X, Wang Q. A literature review of fuel effects on performance and emission characteristics of low-temperature combustion strategies. Appl Energy . 2019;251(301):113380. Available from:

https://doi.org/10.1016/j.apenergy.2019.113380

257. Awad OI, Mamat R, Ibrahim TK, Hammid AT, Yusri IM, Hamidi MA, et al. Overview of the oxygenated fuels in spark ignition engine: Environmental and performance. Renew Sustain Energy Rev . 2018;91(April 2017):394–408. Available from: https://doi.org/10.1016/j.rser.2018.03.107

258. Kasseris E, Heywood J. Charge cooling effects on knock limits in SI di engines using gasoline/ethanol blends: Part 1-quantifying charge cooling. SAE Tech Pap . 2012; Available from: https://doi.org/10.4271/2012-01-1275

259. Jacobson MZ. Effects of ethanol (E85) versus gasoline vehicles on cancer and mortality in the United States. Environ Sci Technol . 2007;41(11):4150–7. Available from: https://doi.org/10.1021/es062085v

260. Menon V, Rao M. Trends in bioconversion of lignocellulose: Biofuels, platform chemicals & biorefinery concept. Prog Energy Combust Sci . 2012;38(4):522–50. Available from: http://dx.doi.org/10.1016/j.pecs.2012.02.002

261. Dong C, Wang Y, Wang H, Lin CSK, Hsu H-Y, Leu S-Y. New Generation Urban Biorefinery toward Complete Utilization of Waste Derived Lignocellulosic Biomass for Biofuels and Value-Added Products. Energy Procedia . 2019;158:918–25. Available from: http://www.sciencedirect.com/science/article/pii/S1876610219302425

262. Cooke DF, Dodson MG, Williams A. A shock-tube study of the ignition of methanol and ethanol with oxygen. Combust Flame . 1971;16(3):233–6. Available from: http://www.sciencedirect.com/science/article/pii/S0010218071800937

263. Marinov N. A Detailed Chemical Kinetic Model for Ethanol Oxidation, report . California; 1997. Available from: https://digital.library.unt.edu/ark:/67531/metadc690213/

264. Leplat N, Dagaut P, Togbé C, Vandooren J. Numerical and experimental study of ethanol combustion and oxidation in laminar premixed flames and in jet-stirred reactor. Combust Flame . 2011;158(4):705–25. Available from: http://www.sciencedirect.com/science/article/pii/S0010218010003627

265. Barraza-Botet CL, Wagnon SW, Wooldridge MS. Combustion Chemistry of Ethanol: Ignition and Speciation Studies in a Rapid Compression Facility. J Phys Chem A . 2016;120(38):7408–18. Available from: https://doi.org/10.1021/acs.jpca.6b06725

266. Cancino LR, Fikri M, Oliveira AAM, Schulz C. Measurement and Chemical Kinetics Modeling of Shock-Induced Ignition of Ethanol−Air Mixtures. Energy & Fuels . 2010;24(5):2830–40. Available from: https://doi.org/10.1021/ef100076w

267. Bugler J, Somers KP, Silke EJ, Curran HJ. Revisiting the Kinetics and Thermodynamics of the Low-Temperature Oxidation Pathways of Alkanes: A Case Study of the Three Pentane Isomers. J Phys Chem A . 2015;119(28):7510–27. Available from: https://doi.org/10.1021/acs.jpca.5b00837

268. Tsujimura T, Pitz WJ, Gillespie F, Curran HJ, Weber BW, Zhang Y, et al. Development of Isopentanol Reaction Mechanism Reproducing Autoignition Character at High and Low Temperatures. Energy & Fuels . 2012;26(8):4871–86. Available from: https://doi.org/10.1021/ef300879k

269. Luo Y-R. Comprehensive Handbook of Chemical Bond Energies. CRC Press; 2007. 1684 p.

270. Kogan SB, Kaliya M, Froumin N. Liquid phase isomerization of isoprenol into prenol in hydrogen environment. Appl Catal A Gen . 2006;297(2):231–6. Available from: http://www.sciencedirect.com/science/article/pii/S0926860X0500709X

271. Zheng Y, Liu Q, Li L, Qin W, Yang J, Zhang H, et al. Metabolic engineering of Escherichia coli for high-specificity production of isoprenol and prenol as next generation of biofuels. Biotechnol Biofuels . 2013;6:57. Available from: https://doi.org/10.1186/1754-6834-6-57

272. George KW, Thompson MG, Kang A, Baidoo E, Wang G, Chan LJG, et al. Metabolic engineering for the high-yield production of isoprenoid-based C5 alcohols in E. coli. Sci Rep . 2015;5(1):11128. Available from: https://doi.org/10.1038/srep11128

273. McGinty D, Jones L, Letizia CS, Api AM. Fragrance material review on 3-methyl-2-buten-1-ol. Food Chem Toxicol . 2010;48:S64–9. Available from: http://www.sciencedirect.com/science/article/pii/S0278691509005298

274. 3-Methyl-2-buten-1-ol, 99%, ACROS Organics™ . [cited 2020 Sep 27]. Available from: https://www.fishersci.se/shop/products/3-methyl-2-buten-1-ol-99-acros-organics-2/10153950/en

275. Organisation for Economic Co-operation and Development. 3-Methylbut-2-en-1-ol, CAS No: 556-82-1. SIDS Initial Assessment Report For SIAM 16. 2003;1–85. Available from: https://hpvchemicals.oecd.org/ui/handler.axd?id=4c28be17-2537-4139-8b1c-ed3cf6e02b6f

276. FuelEngineCoOptimization (fuelsdb.nrel.gov) . [cited 2019 Oct 3]. Available from: https://fuelsdb.nrel.gov/fmi/webd/FuelEngineCoOptimization

277. De Bruycker R, Herbinet O, Carstensen HH, Battin-Leclerc F, Van Geem KM. Understanding the reactivity of unsaturated alcohols: Experimental and kinetic modeling study of the pyrolysis and oxidation of 3-methyl-2-butenol and 3-methyl-3-butenol. Combust Flame . 2016;171:237–51. Available from: https://doi.org/10.1016/j.combustflame.2016.06.009

278. Vandewiele NM, Van Geem KM, Reyniers M-F, Marin GB. Genesys: Kinetic model construction using chemo-informatics. Chem Eng J . 2012;207–208:526–38. Available from: http://www.sciencedirect.com/science/article/pii/S1385894712009059

279. Taatjes CA, Hansen N, Miller JA, Cool TA, Wang J, Westmoreland PR, et al. Combustion Chemistry of Enols: Possible Ethenol Precursors in Flames. J Phys Chem A . 2006;110(9):3254–60. Available from: https://doi.org/10.1021/jp0547313

280. Barnard JA, Honeyman TW, Linnett JW. The gaseous oxidation of acetone - I. The high-temperature reaction. Proc R Soc London Ser A Math Phys Sci . 1964;279(1377):236–47. Available from: https://doi.org/10.1098/rspa.1964.0101

281. Hemken C, Burke U, Lam K, Davidson DF, Hanson RK, Alexander K, et al. Toward a better understanding of 2-butanone oxidation : Detailed species measurements and kinetic modeling. Combust Flame . 2017;184:195–207. Available from: http://dx.doi.org/10.1016/j.combustflame.2017.06.007

282. Fikri M, Cancino LR, Hartmann M, Schulz C. High-pressure shock-tube investigation of the impact of 3-pentanone on the ignition properties of primary reference fuels. Proc Combust Inst . 2013;34(1):393–400. Available from: http://dx.doi.org/10.1016/j.proci.2012.05.101

283. Cartlidge J, Tipper CFH. Knock resistance and anti-knock with hydrocarbon fuels. Combust Flame . 1961;5:87–91. Available from: http://www.sciencedirect.com/science/article/pii/0010218061900785

284. Burke U, Beeckmann J, Kopp WA, Uygun Y, Olivier H, Leonhard K, et al. A comprehensive experimental and kinetic modeling study of butanone. Combust Flame . 2016;168:296–309. Available from: http://www.sciencedirect.com/science/article/pii/S0010218016300086

285. Fenard Y, Pieper J, Hemken C, Minwegen H, Büttgen RD, Kohse-Höinghaus K, et al. Experimental and modeling study of the low to high temperature oxidation of the linear pentanone isomers: 2-pentanone and 3-pentanone. Combust Flame . 2020;216:29–44. Available from: http://www.sciencedirect.com/science/article/pii/S001021802030078X

286. Westbrook CK, Pitz WJ, Curran HJ. Chemical Kinetic Modeling Study of the Effects of Oxygenated Hydrocarbons on Soot Emissions from Diesel Engines. J Phys Chem A . 2006;110(21):6912–22. Available from: https://doi.org/10.1021/jp056362g

287. Minwegen H, Burke U, Heufer KA. An experimental and theoretical comparison of C3-C5 linear ketones. Proc Combust Inst. 2017;36(1):561–8.

288. Curran HJ, Gaffuri P, Pitz WJ, Westbrook CK. A Comprehensive Modeling Study of n-Heptane Oxidation. Combust Flame . 1998;114(1):149–77. Available from: http://www.sciencedirect.com/science/article/pii/S0010218097002824

289. Zhang K, Lokachari N, Ninnemann E, Khanniche S, Green WH, Curran HJ, et al. An experimental, theoretical, and modeling study of the ignition behavior of cyclopentanone. Proc Combust Inst . 2019;37(1):657–65. Available from: http://www.sciencedirect.com/science/article/pii/S1540748918302803

290. Thion S, Togbé C, Dayma G, Serinyel Z, Dagaut P. Experimental and Detailed Kinetic Modeling Study of Cyclopentanone Oxidation in a Jet-Stirred Reactor at 1 and 10 atm. Energy & Fuels . 2017;31(3):2144–55. Available from: https://doi.org/10.1021/acs.energyfuels.6b02061

291. Giri BR, AlAbbad M, Barker JR, Farooq A. High temperature unimolecular decomposition of cyclopentanone. Proc Combust Inst . 2019;37(1):267–73. Available from: http://www.sciencedirect.com/science/article/pii/S1540748918300774

292. Yang Y, Du Z, Huang Y, Lu F, Wang F, Gao J, et al. Conversion of furfural into cyclopentanone over Ni–Cu bimetallic catalysts. Green Chem . 2013;15(7):1932–40. Available from: http://dx.doi.org/10.1039/C3GC37133F

293. Scognamiglio J, Jones L, Letizia CS, Api AM. Fragrance material review on cyclopentanone. Food Chem Toxicol . 2012;50 Suppl 3:S608-12. Available from: https://doi.org/10.1016/j.fct.2012.03.027

294. Li G, Li N, Wang X, Sheng X, Li S, Wang A, et al. Synthesis of Diesel or Jet Fuel Range Cycloalkanes with 2-Methylfuran and Cyclopentanone from Lignocellulose. Energy & Fuels . 2014;28(8):5112–8. Available from: https://doi.org/10.1021/ef500676z

295. Shen T, Hu R, Zhu C, Li M, Zhuang W, Tang C, et al. Production of cyclopentanone from furfural over Ru/C with Al11.6PO23.7 and application in the synthesis of diesel range alkanes. RSC Adv . 2018;8(66):37993–8001. Available from: http://dx.doi.org/10.1039/C8RA08757A

296. Yang J, Li N, Li G, Wang W, Wang A, Wang X, et al. Synthesis of renewable high-density fuels using cyclopentanone derived from lignocellulose. Chem Commun . 2014;50(20):2572–4. Available from: http://dx.doi.org/10.1039/C3CC46588H

297. Demirbas A. The influence of temperature on the yields of compounds existing in bio-oils obtained from biomass samples via pyrolysis. Fuel Process Technol . 2007;88(6):591–7. Available from: http://www.sciencedirect.com/science/article/pii/S0378382007000252

298. Ballistreri A, Garozzo D, Giuffrida M, Montaudo G. Mechanism of thermal decomposition of nylon 66. Macromolecules . 1987;20(12):2991–7. Available from: https://doi.org/10.1021/ma00178a007

299. Strobel GA, Knighton B, Kluck K, Ren Y, Livinghouse T, Griffin M, et al. The production of myco-diesel hydrocarbons and their derivatives by the endophytic fungus Gliocladium roseum (NRRL 50072). Microbiology . 2008 Nov 1 [cited 2020 Oct 27];154(11):3319–28. Available from: https://www.microbiologyresearch.org/content/journal/micro/10.1099/mic.0.2008/022186-0

300. Gaspar, Daniel J., West, Brian H., Ruddy, Danial, Wilke, Trenton J., Polikarpov, Evgueni, Alleman, Teresa L., George, Anthe, Monroe, Eric, Davis, Ryan W., Vardon, Derek, Sutton, Andrew D., Moore, Cameron M., Benavides, Pahola T., Dunn, Jennifer, Biddy, Ma WJ. Top Ten Blendstocks Derived From Biomass For Turbocharged Spark Ignition Engines: Bio-blendstocks With Potential for Highest Engine Efficiency . 2019. Available from: doi:10.2172/1567705

301. Yang Y, Dec JE, Sjöberg M, Ji C. Understanding fuel anti-knock performances in modern SI engines using fundamental HCCI experiments. Combust Flame . 2015;162(10):4008–15. Available from: http://www.sciencedirect.com/science/article/pii/S0010218015002485

302. Fenard Y, Dagaut P, Dayma G, Halter F, Foucher F. Experimental and kinetic modeling study of trans-2-butene oxidation in a jet-stirred reactor and a combustion bomb. In: Proc Combust Inst . 2015. p. 317. Available from: https://doi.org/10.1016/j.proci.2014.05.007

303. Thion S, Diévart P, Van Cauwenberghe P, Dayma G, Serinyel Z, Dagaut P. An experimental study in a jet-stirred reactor and a comprehensive kinetic mechanism for the oxidation of methyl ethyl ketone. Proc Combust Inst . 2017;36(1):459–67. Available from: http://www.sciencedirect.com/science/article/pii/S1540748916300220

304. Zhang K, Banyon C, Bugler J, Curran HJ, Rodriguez A, Herbinet O, et al. An updated experimental and kinetic modeling study of n-heptane oxidation. Combust Flame . 2016;172:116–35. Available from: http://www.sciencedirect.com/science/article/pii/S0010218016301560

305. AlAbbad MA. Reactivity and Ignition Delay Measurements of Petroleum-based Fuels, Surrogate Fuels and Biofuels . King Abdullah University of Science and Technology; 2018. Available from: http://hdl.handle.net/10754/630104

306. Zhou C-W, Simmie JM, Pitz WJ, Curran HJ. Toward the Development of a Fundamentally Based Chemical Model for Cyclopentanone: High-Pressure-Limit Rate Constants for H Atom Abstraction and Fuel Radical Decomposition. J Phys Chem A . 2016;120(36):7037–44. Available from: https://doi.org/10.1021/acs.jpca.6b03994

307. Zaras AM, Thion S, Dagaut P. Computational kinetic study for the unimolecular decomposition of cyclopentanone. Int J Chem Kinet . 2015;47(7):439–46. Available from: https://onlinelibrary.wiley.com/doi/abs/10.1002/kin.20921

308. Bao X, Jiang Y, Xu H, Wang C, Lattimore T, Tang L. Laminar flame characteristics of cyclopentanone at elevated temperatures. Appl Energy . 2017;195:671–80. Available from: http://www.sciencedirect.com/science/article/pii/S0306261917302490

309. Klotz SD, Brezinsky K, Glassman I. Modeling the combustion of toluene-butane blends. In: Symposium (International) on Combustion . 1998. p. 337–44. Available from: http://www.sciencedirect.com/science/article/pii/S0082078498804219

310. Andrae J, Johansson D, Björnbom P, Risberg P, Kalghatgi G. Co-oxidation in the auto-ignition of primary reference fuels and n-heptane/toluene blends. Combust Flame . 2005;140(4):267–86. Available from: http://www.sciencedirect.com/science/article/pii/S0010218004002330

311. Christensen ED, Kim SA, Fioroni GM, Paton RS, McCormick RL. Experimental and Theoretical Study of Cyclopentanone as a Catalyst for Low Temperature Alkene Oxidation: Preprint. 2019; Available from: https://www.osti.gov/servlets/purl/1566800

312. Naik C V, Pitz WJ, Westbrook CK, Sjöberg M, Dec JE, Orme J, et al. Detailed Chemical Kinetic Modeling of Surrogate Fuels for Gasoline and Application to an HCCI Engine. SAE Tech Pap . 2005; Available from: https://doi.org/10.4271/2005-01-3741

313. Larsson T, Stenlaas O, Erlandsson A. Future Fuels for DISI Engines: A Review on Oxygenated, Liquid Biofuels. SAE Tech Pap . 2019; Available from: https://doi.org/10.4271/2019-01-0036

314. Shirazi SA, Abdollahipoor B, Windom B, Reardon KF, Foust TD. Effects of blending C3-C4 alcohols on motor gasoline properties and performance of spark ignition engines: A review. Fuel Process Technol . 2020;197:106194. Available from: http://www.sciencedirect.com/science/article/pii/S0378382019307519

315. Dooley S, Won SH, Dryer FL. Surrogate fuels and combustion characteristics of liquid transportation fuels . 1st ed. Vol. 45, Mathematical Modelling of Gas-Phase Complex Reaction Systems: Pyrolysis and Combustion. Elsevier B.V.; 2019. 513–602 p. Available from: http://dx.doi.org/10.1016/B978-0-444-64087-1.00010-3

316. Mittal G. A Rapid Compression Machine – Design, Characterization, and autoignition investigations . Case Western Reserve University; 2006. Available from: http://rave.ohiolink.edu/etdc/view?acc_num=case1130184196

317. Falk KG. The ignition temperatures of hydrogen-oxygen mixtures. J Am Chem Soc . 1906;28(11):1517–34. Available from: https://doi.org/10.1021/ja01977a001

318. Dixon HB, Bradshaw L, Campbell C. CLXXXIX.—The firing of gases by adiabatic compression. Part I. Photographic analysis of the flame. J Chem Soc Trans . 1914;105(0):2027–35. Available from: http://dx.doi.org/10.1039/CT9140502027

319. Yu Y, Vanhove G, Griffiths JF, De Ferrières S, Pauwels J-F. Influence of EGR and Syngas Components on the Autoignition of Natural Gas in a Rapid Compression Machine: A Detailed Experimental Study. Energy & Fuels . 2013;27(7):3988–96. Available from: https://doi.org/10.1021/ef400336x

320. Goldsborough SS, Johnson M V., Banyon C, Pitz WJ, McNenly MJ. Experimental and modeling study of fuel interactions with an alkyl nitrate cetane enhancer, 2-ethyl-hexyl nitrate. Proc Combust Inst . 2015;35(1):571–9. Available from: http://dx.doi.org/10.1016/j.proci.2014.06.048

321. Donovan MT, He X, Zigler BT, Palmer TR, Wooldridge MS, Atreya A. Demonstration of a free-piston rapid compression facility for the study of high temperature combustion phenomena. Combust Flame . 2004;137(3):351–65. Available from: https://doi.org/10.1016/j.combustflame.2004.02.006

322. Dumitrache C, Baumgardner M, Boissiere A, Maria A, Roucis J, Marchese AJ, et al. A study of laser induced ignition of methane-air mixtures inside a Rapid Compression Machine. Proc Combust Inst . 2017;36(3):3431–9. Available from: http://dx.doi.org/10.1016/j.proci.2016.05.033

323. Foong TM. On the autoignition of ethanol/gasoline blends in spark-ignition engines . University of Melbourne; 2013. Available from: https://minerva-access.unimelb.edu.au/bitstream/handle/11343/38517/304387_20131121_thesis_Foong_final.pdf?sequence=1&isAllowed=y

324. Mittal G, Bhari A. A rapid compression machine with crevice containment. Combust Flame . 2013;160(12):2975–81. Available from: http://www.sciencedirect.com/science/article/pii/S0010218013002526

325. Park P, Keck JC. Rapid Compression Machine Measurements of Ignition Delays for Primary Reference Fuels. SAE Int . 1990; Available from: https://www.jstor.org/stable/44580365

326. Kukkadapu G, Kumar K, Sung C-J, Mehl M, Pitz WJ. Experimental and surrogate modeling study of gasoline ignition in a rapid compression machine. Combust Flame . 2012;159(10):3066–78. Available from: http://www.sciencedirect.com/science/article/pii/S0010218012001733

327. Healy D, Curran HJ, Simmie JM, Kalitan DM, Zinner CM, Barrett AB, et al. Methane/ethane/propane mixture oxidation at high pressures and at high, intermediate and low temperatures. Combust Flame . 2008;155(3):441–8. Available from: https://doi.org/10.1016/j.combustflame.2008.07.003

328. Beeley P, Griffiths JF, Gray P. Rapid compression studies on spontaneous ignition of isopropyl nitrate Part II: Rapid sampling, intermediate stages and reaction mechanisms. Combust Flame . 1980;39(3):269–81. Available from: https://doi.org/10.1016/0010-2180(80)90023-1

329. Nyong OE. Development of a Rapid Compression Machine for Screening Alternative Fuel for Gas Turbines . University of Sheffield; 2017. Available from: http://etheses.whiterose.ac.uk/17855/

330. Guibert P, Keromnes A, Legros G. Development of a Turbulence Controlled Rapid Compression Machine for HCCI Combustion. SAE Tech Pap . 2007;1086–96. Available from: http://papers.sae.org/2007-01-1869/

331. Pochet M, Dias V, Moreau B, Foucher F, Jeanmart H, Contino F. Experimental and numerical study, under LTC conditions, of ammonia ignition delay with and without hydrogen addition. Proc Combust Inst . 2019;37(1):621–9. Available from: http://www.sciencedirect.com/science/article/pii/S1540748918301445

332. Gersen S, Darmeveil H, Levinsky H. The effects of CO addition on the autoignition of H2, CH4 and CH4/H2 fuels at high pressure in an RCM. Combust Flame . 2012;159(12):3472–5. Available from: http://dx.doi.org/10.1016/j.combustflame.2012.06.021

333. Gersen S, Mokhov A V., Darmeveil JH, Levinsky HB. Ignition properties of n-butane and iso-butane in a rapid compression machine. Combust Flame . 2010;157(2):240–5. Available from: http://dx.doi.org/10.1016/j.combustflame.2009.10.012

334. Vranckx S, Beeckmann J, Kopp WA, Lee C, Cai L, Chakravarty HK, et al. An experimental and kinetic modelling study of n-butyl formate combustion. Combust Flame . 2013;160(12):2680–92. Available from: http://dx.doi.org/10.1016/j.combustflame.2013.06.012

335. Javed T, Ahmed A, Lovisotto L, Issayev G, Badra J, Sarathy SM, et al. Ignition studies of two low-octane gasolines. Combust Flame . 2017;185:152–9. Available from: http://dx.doi.org/10.1016/j.combustflame.2017.07.006

336. Zegarra Sanchez F, Leal Braga S, Renata NC de S, Flavio GD. Experimental Study of the Ignition Delay for Ethanol-Powered in a Rapid Compression Machine. SAE Tech Pap Ser . 2014; Available from: https://doi.org/10.4271/2014-36-0127

337. Akiyama H, Nishimura H, Ibaraki Y, Iida N. Study of diesel spray combustion and ignition using high-pressure fuel injection and a micro-hole nozzle with a rapid compression machine: Improvement of combustion using low cetane number fuel. JSAE Rev . 1998;19(4):319–27. Available from: https://doi.org/10.1016/S0389-4304(98)00024-1

338. Guézet J, Kageyama T. Étude aérodynamique dans une machine à compression rapide. Rev Générale Therm . 1997;36(1):17–25. Available from: http://www.sciencedirect.com/science/article/pii/S0035315999800622

339. Lemaire O. Étude experimentale et par modelisation de la cinetique d'oxydation et d'autoinflammation à haute pression d'hydrocarbures alicycliques . Universite des Sciences et Technologies de Lille; 2001. Available from: http://www.theses.fr/fr/2001LIL10084

340. Hadj Ali K. Étude cinétique de l'oxydation et de l'auto-inflammation en milieu gazeux homogène pauvre et ultra pauvre de carburants de substitution issus de la biomasse . Université de Lille 1; 2007. Available from: http://ori-nuxeo.univ-lille1.fr/nuxeo/site/esupversions/52def8cd-1012-4326-9c3e-d6507800d4de

341. Crochet M. Adéquation moteurs propres-carburants en combustion homogène. Etude expérimentale en machine à compression rapide et modélisation de carburants modèles types gazoles en milieu ultra-pauvre . Université des scienes et technologies de Lille; 2008. Available from: http://ori-nuxeo.univ-lille1.fr/nuxeo/site/esupversions/ccec2244-d09d-44ba-aab1-d6399291de3d

342. Yu Y. Cinétiqu d'auto inflammation de carburants gazeaux a haute pression: etude experimentale et de modelisation . Universite des sciences et technologies de lille; 2012. Available from: http://www.theses.fr/2012LIL10098

343. Boumehdi MA. Interaction entre plamas froids et combustion aux températures basses et intermédiaires: approche expérimentale . Université Lille 1; 2016. Available from: https://www.theses.fr/204417244

344. Fenard Y, Gil A, Vanhove G, Carstensen H, Van KM, Westmoreland PR, et al. A model of tetrahydrofuran low-temperature oxidation based on theoretically calculated rate constants. Combust Flame . 2018;191:252–69. Available from: https://doi.org/10.1016/j.combustflame.2018.01.006

345. Fenard Y, Boumehdi MA, Vanhove G. Experimental and kinetic modeling study of 2-methyltetrahydrofuran oxidation under engine-relevant conditions. Combust Flame . 2017;178:168–81. Available from: http://www.sciencedirect.com/science/article/pii/S0010218017300081

346. Fenard Y, Song H, Minwegen H, Parab P, Sampaio Mergulhão C, Vanhove G, et al. 2,5-Dimethyltetrahydrofuran combustion: Ignition delay times at high and low temperatures, speciation measurements and detailed kinetic modeling. Combust Flame . 2019;203:341–51. Available from: http://www.sciencedirect.com/science/article/pii/S0010218019300860

347. Fenard Y, Song H, Dauphin R, Vanhove G. An engine-relevant kinetic investigation into the anti-knock effect of organometallics through the example of ferrocene. Proc Combust Inst . 2019;37(1):547–54. Available from: https://doi.org/10.1016/j.proci.2018.06.135

348. Ribaucour M, Minetti R, Carlier M, Sochet L-R. Autoinflammation à haute pression. conception, réalisation et test d’une machine à compression rapide. J Chim Phys . 1992;89:2127–52. Available from: https://doi.org/10.1051/jcp/1992892127

349. Lee D, Hochgreb S. Rapid compression machines: Heat transfer and suppression of corner vortex. Combust Flame . 1998;114(3–4):531–45. Available from: https://doi.org/10.1016/S0010-2180(97)00327-1

350. Bourgeois N, Goldsborough SS, Jeanmart H, Contino F. CFD simulations of Rapid Compression Machines using detailed chemistry: Evaluation of the ‘crevice containment’ concept. Combust Flame . 2018;189:1339–51. Available from: https://doi.org/10.1016/j.combustflame.2017.10.033

351. Hu H, Keck J. Autoignition of Adiabatically Compressed Combustible Gas Mixtures. SAE Trans . 1987;96:592–604. Available from: http://www.jstor.org/stable/44469171

352. Desgroux P, Minetti R, Sochet LR. Temperature Distribution Induced by Pre-Ignition Reactions in a Rapid Compression Machine. Combust Sci Technol . 1996;113(1):193–203. Available from: https://doi.org/10.1080/00102209608935494

353. Desgroux P, Gasnot L, Sochet LR. Instantaneous temperature measurement in a rapid-compression machine using laser Rayleigh scattering. Appl Phys B . 1995;61(1):69–72. Available from: https://doi.org/10.1007/BF01090974

354. Uddi M, Das AK, Sung C-J. Temperature measurements in a rapid compression machine using mid-infrared H2O absorption spectroscopy near 7.6 µm. Appl Opt . 2012;51(22):5464–76. Available from: http://ao.osa.org/abstract.cfm?URI=ao-51-22-5464

355. Ritter ER. THERM: A Computer Code for Estimating Thermodynamic Properties for Species Important to Combustion and Reaction Modeling. J Chem Inf Comput Sci . 1991;31(3):400–8. Available from: https://doi.org/10.1021/ci00003a006

356. Gao CW, Allen JW, Green WH, West RH. Reaction Mechanism Generator: Automatic construction of chemical kinetic mechanisms. Comput Phys Commun . 2016;203:212–25. Available from: http://www.sciencedirect.com/science/article/pii/S0010465516300285

357. Roblee LHS. A technique for sampling reaction intermediates in a rapid compression machine. Combust Flame . 1961;5(August):229–34. Available from: https://doi.org/10.1016/0010-2180(61)90101-8

358. Moreau RA, Sorenson SC, Hull WL. A technique for time resolved nitric oxide measurements in auto-igniting mixtures. Combust Flame . 1975;25(C):197–205. Available from: https://doi.org/10.1016/0010-2180(75)90085-1

359. Terrence AL. A beginner’s guide to mass spectral interpretation Terrence A. Lee. Vol. 9, Journal of the American Society for Mass Spectrometry. 1998. 200 p.

360. Kaiser R. Gas Phase Chromatography. Springer US; 1963. 207 p.

361. Scanlon JT, Willis DE. Calculation of Flame Ionization Detector Relative Response Factors Using the Effective Carbon Number Concept. J Chromatogr Sci . 1985;23(8):333–40. Available from: https://doi.org/10.1093/chromsci/23.8.333

362. Bourgeois N. Numerical study of multi-dimensional effects in Rapid Compression Machines . Ecole Polytechnique de Louvain; 2017. Available from: http://hdl.handle.net/2078.1/195700

363. Sung C-J, Curran HJ. Using rapid compression machines for chemical kinetics studies. Prog Energy Combust Sci . 2014;44:1–18. Available from: http://www.sciencedirect.com/science/article/pii/S0360128514000148

364. Kurt J. Lesker Company | MKS® 628F Baratron® Temperature Regulated Capacitance Manometer | Vacuum Science Is Our Business . [cited 2020 Jun 2]. Available from: https://www.lesker.com/newweb/gauges/mks-628f-baratron-capacitance-manometer.cfm

365. Weber BW, Sung C, Renfro MW. On the uncertainty of temperature estimation in a rapid compression machine. Combust Flame . 2015;162(6):2518–28. Available from: http://dx.doi.org/10.1016/j.combustflame.2015.03.001

366. Vanhove G, Yu Y, Boumehdi MA, Frottier O, Herbinet O, Glaude P-A, et al. Experimental Study of Tetrahydrofuran Oxidation and Ignition in Low-Temperature Conditions. Energy & Fuels . 2015;29(9):6118–25. Available from: https://doi.org/10.1021/acs.energyfuels.5b01057

367. Cantera . [cited 2019 Nov 21]. Available from: https://cantera.org/

368. Wagnon SW, Pitz WJ. Personal communication. 2019.

369. Mehl M, Curran HJ, Pitz WJ, Westbrook CK. Chemical kinetic modeling of component mixtures relevant to gasoline. In: 4th European Combustion Meeting . 2009. p. 1–6. Available from: https://www.osti.gov/servlets/purl/952084

370. Petersen EL, Lamnaouer M, de Vries J, Curran H, Simmie J, Fikri M, et al. Discrepancies between shock tube and rapid compression machine ignition at low temperatures and high pressures. In: Shock Waves . 2009. p. 739–44. Available from: https://doi.org/10.1007/978-3-540-85168-4_119

371. Chaos M, Dryer FL. Chemical-kinetic modeling of ignition delay: Considerations in interpreting shock tube data. Int J Chem Kinet . 2010;42(3):143–50. Available from: https://doi.org/10.1002/kin.20471

372. Szybist JP, Splitter DA. Understanding chemistry-specific fuel differences at a constant RON in a boosted SI engine. Fuel . 2018;217:370–81. Available from: http://www.sciencedirect.com/science/article/pii/S0016236117316836

Annex A: fuel-specific additional information

Isooctane/anisole study

Calculated response factors

Table 31 - Response factors calculated.

Specie	Response factor	Species	Response factor
2-propenal	225303	pentane	726673
3-buten-2-one	249894	propyne	372214
2-butenal	198647	allene	394837
ethanal	124265	hexane	854136
2,5-dimethyltetrahydrofuran	809539	2-butanone	425789
CO	39.075	isooctane	599455
methane	36.579	anisole	236884
acetone	321310	cis-2-butene	2440436
methanol	77124	benzene	460713
propene	348409	toluene	492235
propane	306704	1-pentene	484009
isobutane	554597	1-hexene	505602
n-butane	571494		

Temperature programming – GC

Table 32 - Capillary columns properties.

RT bond Q	UptiBond UB5P	Agilent 6890
40 °C hold 10 minutes, ramp of 5 °C /min until 130 °C, isotherm for 30 minutes, ramp of 5 °C /min until 250 °C and isotherm for 8 minutes	40 °C hold 5 minutes, ramp of 1 °C /min until 230 °C and isotherm for 30 minutes	40 °C hold 5 minutes and ramp of 5 °C /min until 105 °C

Carbon balance

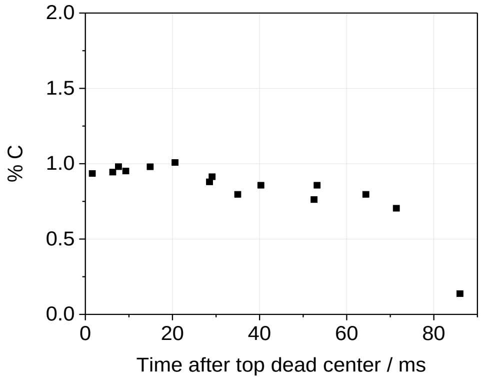

RCM pressure profiles

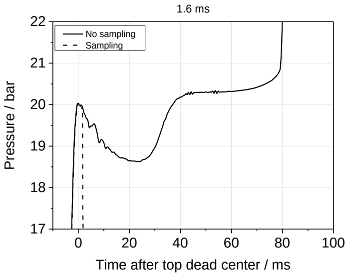

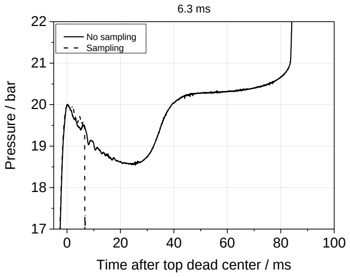

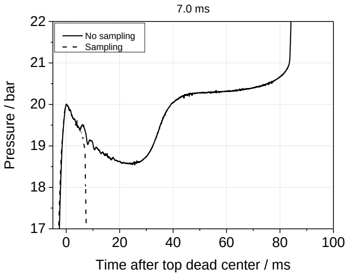

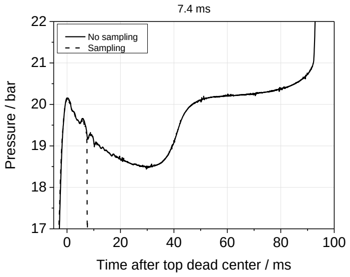

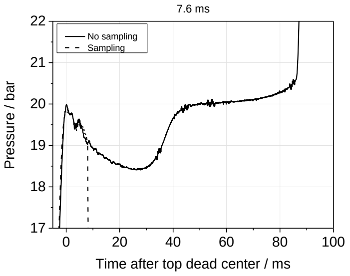

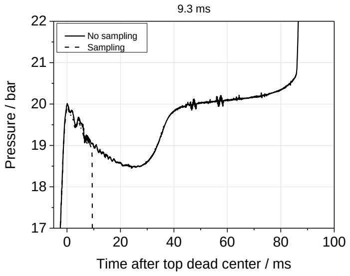

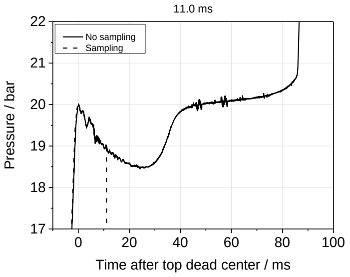

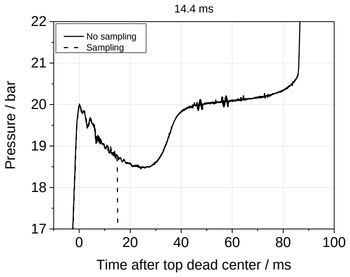

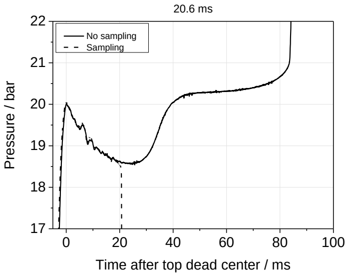

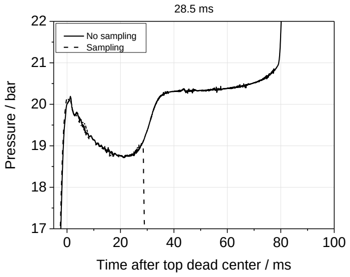

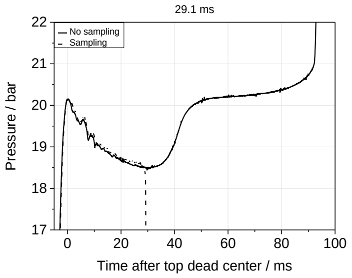

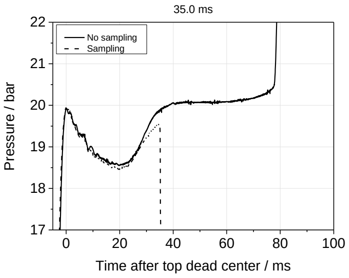

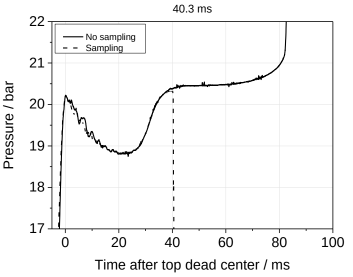

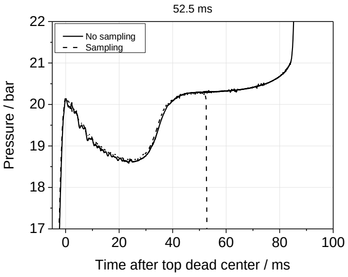

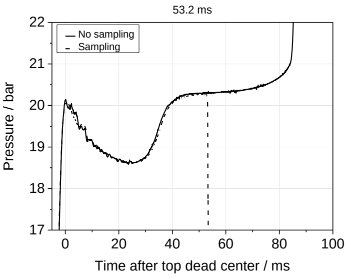

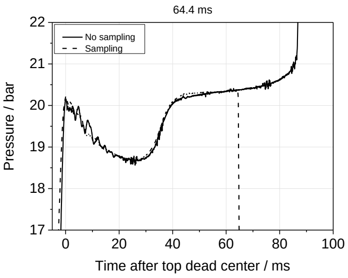

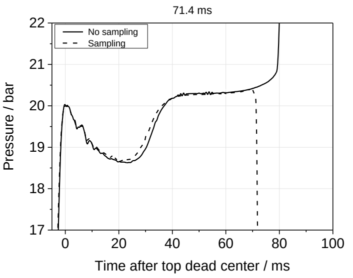

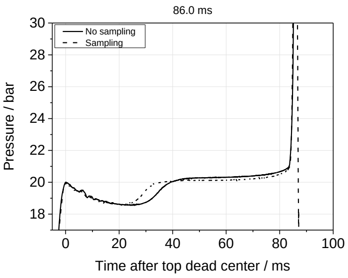

Isooctane/cyclopentanone

Calculated response factors

Table 33 - Response factors calculated

Species	Response factor	Species	Response factor
2-propenal	225303	propyne	372214
3-buten-2-one	249894	allene	394837
2-butenal	198647	hexane	854136
ethanal	124265	2-butanone	425789
2,5-dimethyltetrahydrofuran	809539	isooctane	599455
CO	71.309	anisole	236884
methane	36.579	cis-2-butene	2440436

acetone	321310	benzene	460713
methanol	77124	toluene	492235
propene	348409	1-pentene	484009
propane	306704	1-hexene	505602
isobutane	554597	cyclopentanone	217257
n-butane	571494	cyclopenten-2-one	111278
pentane	726673		

Temperature programming – GC

Table 34 - Capillary columns properties

RT bond Q	**UptiBond UB5P**	**Agilent 6890**
40 °C hold 10 minutes, ramp of 5 °C /min until 150 °C, isotherm for 40 minutes, ramp of 10 °C /min until 250 °C and isotherm for 8 minutes	40 °C hold 20 minutes, ramp of 3 °C /min until 50 °C, isotherm for 9 minutes and ramp of 2 °C /min until 135 °C	40 °C hold 5 minutes and ramp of 5 °C /min until 105 °C

Carbon balance

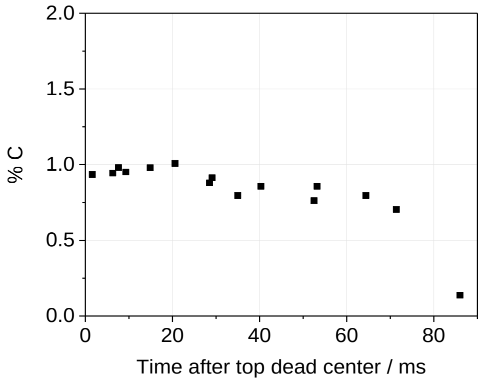

RCM pressure profiles

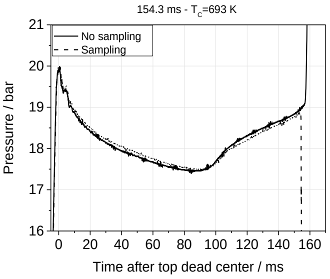

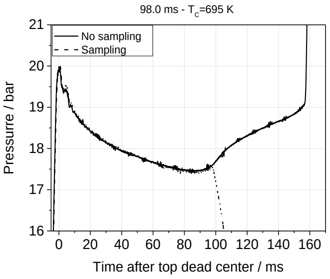

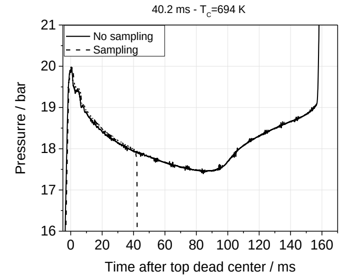
40.2 ms - T_c=694 K

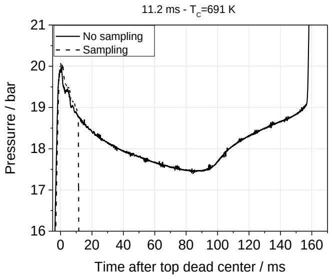
11.2 ms - T_c=691 K

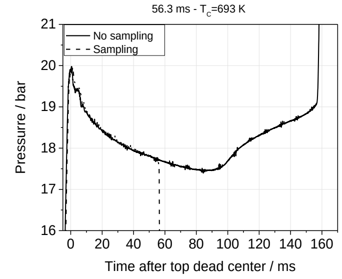
56.3 ms - T_c=693 K

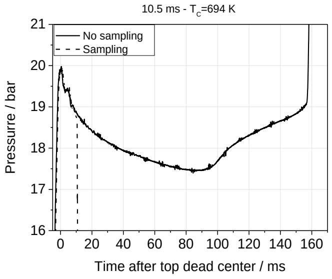
10.5 ms - T_c=694 K

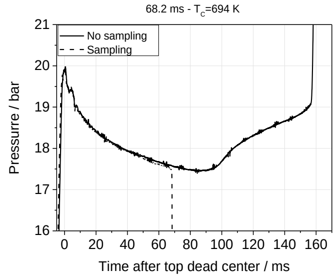
68.2 ms - T_c=694 K

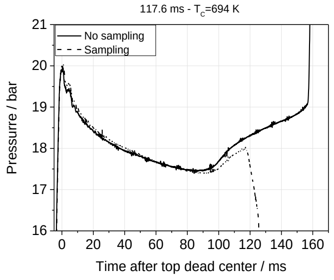
117.6 ms - T_c=694 K

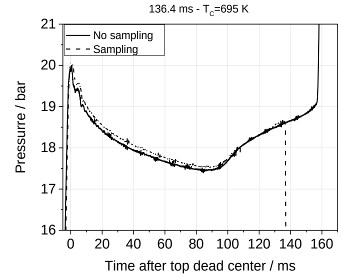
136.4 ms - T_c=695 K

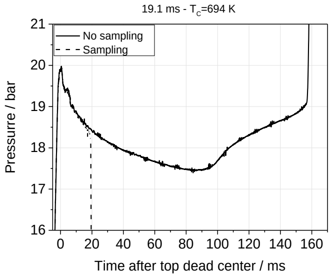
19.1 ms - T_c=694 K

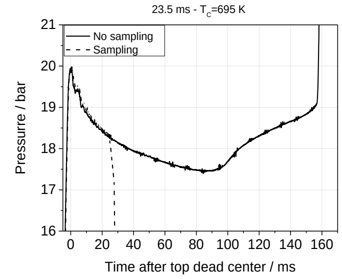
23.5 ms - T_c=695 K

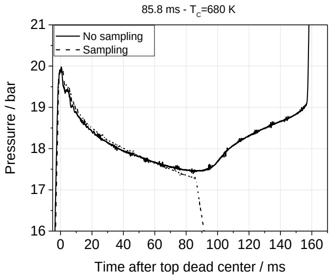
85.8 ms - T_c=680 K

Annex B: purity of used compounds

Table 35 - Purity of used chemical products.

Specie	**Purity**	**Supplier**
	Fuel components	
Oxygen, nitrogen, argon, CO_2 (N45)	Gas - ≥99.99%	Air Liquide
Isooctane	Liquid - ≥99%	Sigma-Aldrich
Anisole	Liquid - ≥99%	Sigma-Aldrich
o-cresol	Liquid - ≥99%	Sigma-Aldrich
prenol	Liquid - ≥99%	Sigma-Aldrich
Cyclopentanone	Liquid - ≥99%	Sigma-Aldrich
	Calibrated species	
cyclopenten-2-one	Liquid - ≥99%	Sigma-Aldrich
2,5-dimethyltetrahydrofuran	Liquid - ≥99%	Sigma-Aldrich
methane	Gas - ≥99%	Air Liquide
CO	Gas - ≥99%	Air Liquide
cis-2-butene, benzene, toluene, 1-pentene, 1-hexene	Standard gas mixture (15ppm)	PraxAir
Propene, propane, isobutane, n-butane, pentane, propyne/methylacetylene, allene/propadiene, hexane	Standard gas mixture (15ppm)	PraxAir
2-butanone	Liquid - ≥99%	Sigma-Aldrich
2-propenal	Liquid - ≥99%	Sigma-Aldrich
3-buten-2-one	Liquid - ≥99%	Sigma-Aldrich
2-butenal	Liquid - ≥99%	Sigma-Aldrich
ethanal	Liquid - ≥99%	Sigma-Aldrich
2-propanone	Liquid - ≥99%	Sigma-Aldrich
methanol	Liquid - ≥99%	Sigma-Aldrich

Annex C: unreactive pressure profiles

Isooctane

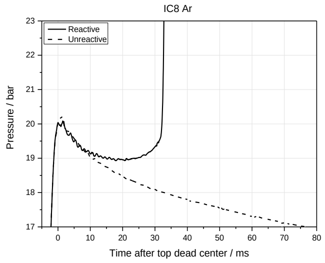

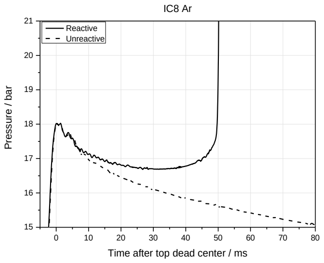

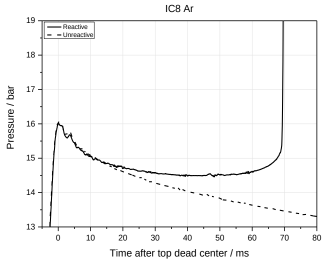

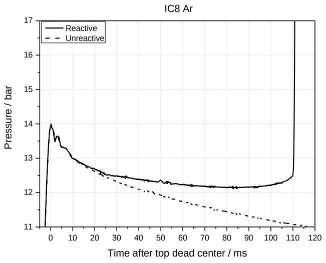

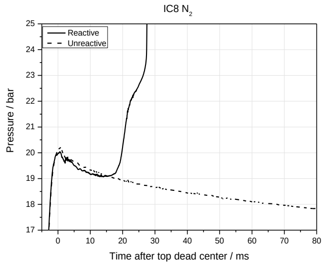

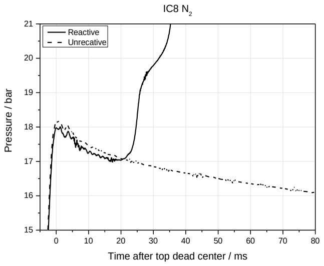

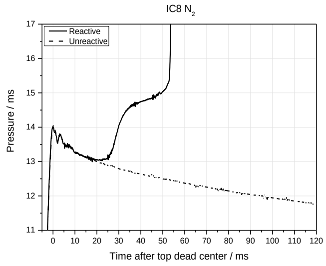

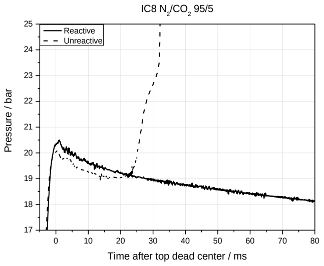

Isooctane/anisole

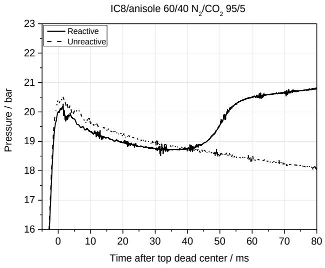

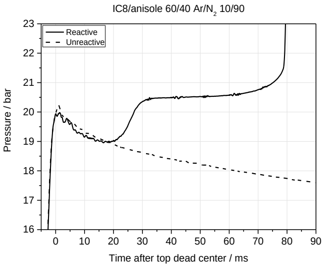

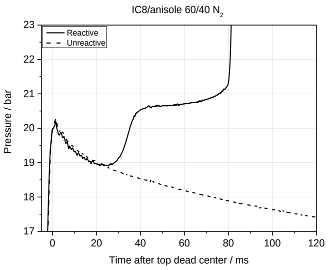
IC8/anisole 60/40 N_2
Reactive
Unreactive
Pressure / bar
17 18 19 20 21 22 23
Time after top dead center / ms
0 20 40 60 80 100 120

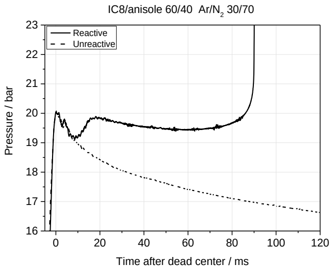
IC8/anisole 60/40 Ar/N_2 30/70
Reactive
Unreactive
Pressure / bar
16 17 18 19 20 21 22 23
Time after dead center / ms
0 20 40 60 80 100 120

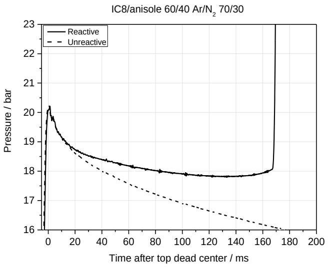
IC8/anisole 60/40 Ar/N_2 70/30
Reactive
Unreactive
Pressure / bar
16 17 18 19 20 21 22 23
Time after top dead center / ms
0 20 40 60 80 100 120 140 160 180 200

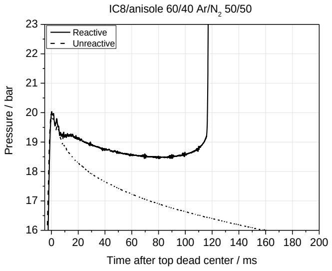
IC8/anisole 60/40 Ar/N_2 50/50
Reactive
Unreactive
Pressure / bar
16 17 18 19 20 21 22 23
Time after top dead center / ms
0 20 40 60 80 100 120 140 160 180 200

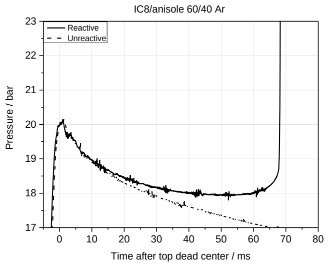
IC8/anisole 60/40 Ar
Reactive
Unreactive
Pressure / bar
17 18 19 20 21 22 23
Time after top dead center / ms
0 10 20 30 40 50 60 70 80

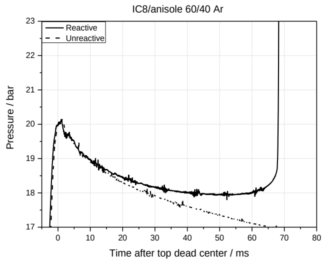
IC8/anisole 60/40 Ar
Reactive
Unreactive
Pressure / bar
17 18 19 20 21 22 23
Time after top dead center / ms
0 10 20 30 40 50 60 70 80

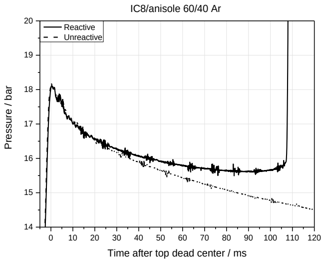
IC8/anisole 60/40 Ar
Reactive
Unreactive
Pressure / bar
14 15 16 17 18 19 20
Time after top dead center / ms
0 10 20 30 40 50 60 70 80 90 100 110 120

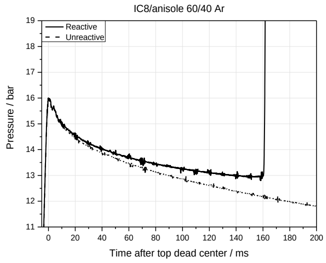
IC8/anisole 60/40 Ar
Reactive
Unreactive
Pressure / bar
11 12 13 14 15 16 17 18 19
Time after top dead center / ms
0 20 40 60 80 100 120 140 160 180 200

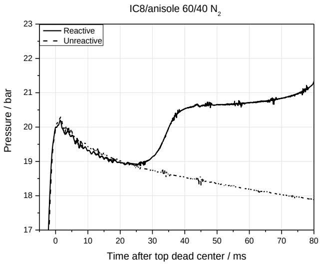
IC8/anisole 60/40 N_2
Reactive
Unreactive
Pressure / bar
17 18 19 20 21 22 23
Time after top dead center / ms
0 10 20 30 40 50 60 70 80

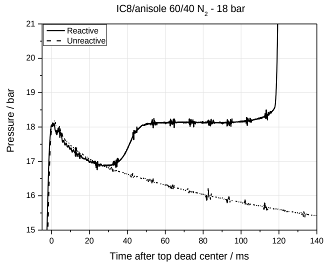
IC8/anisole 60/40 N_2 - 18 bar
Reactive
Unreactive
Pressure / bar
15 16 17 18 19 20 21
Time after top dead center / ms
0 20 40 60 80 100 120 140

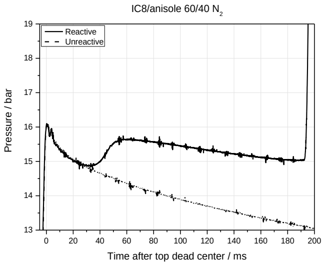
IC8/anisole 60/40 N_2
Reactive
Unreactive
Pressure / bar
13 14 15 16 17 18 19
Time after top dead center / ms
0 20 40 60 80 100 120 140 160 180 200

Isooctane/prenol

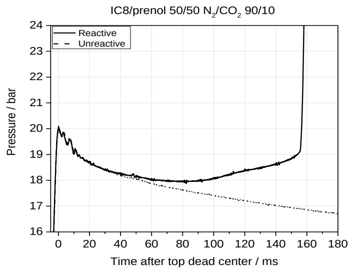

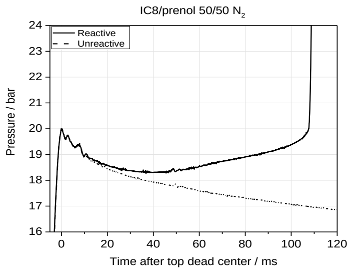

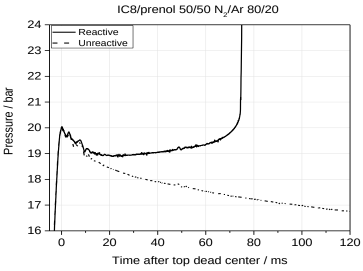

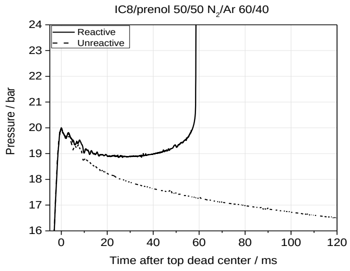

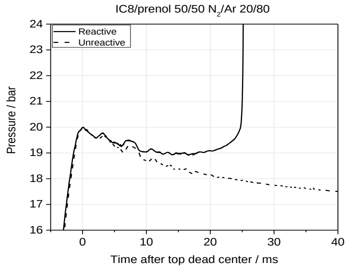

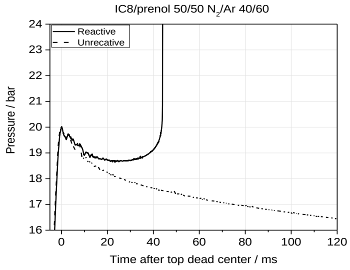

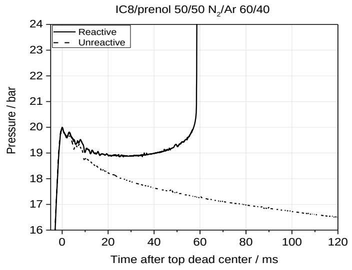

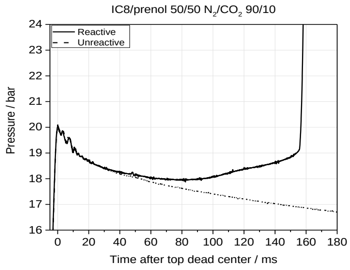

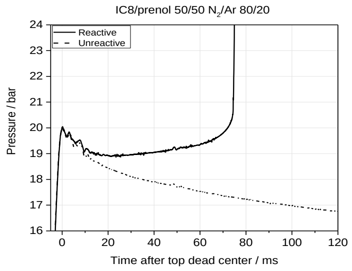

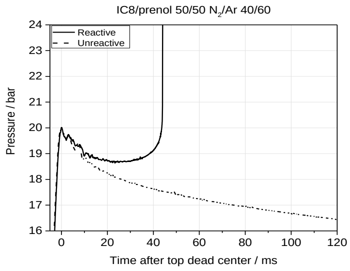

Isooctane/cyclopentanone

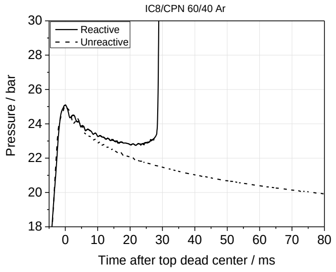

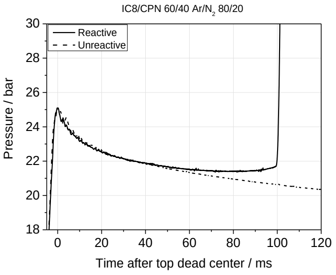

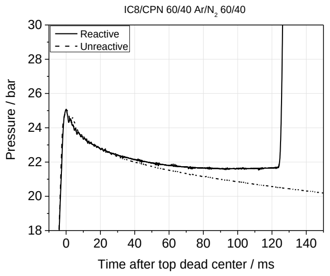
IC8/CPN 60/40 Ar/N2 60/40
Reactive
Unreactive
Pressure / bar
30
28
26
24
22
20
18
0
20
40
60
80
100
120
140
Time after top dead center / ms

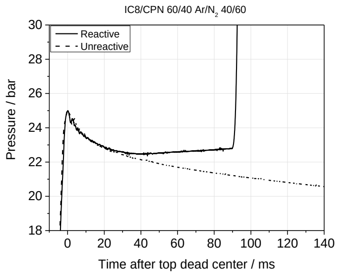
IC8/CPN 60/40 Ar/N2 40/60
Reactive
Unreactive
Pressure / bar
30
28
26
24
22
20
18
0
20
40
60
80
100
120
140
Time after top dead center / ms

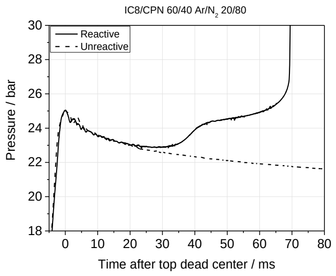
IC8/CPN 60/40 Ar/N2 20/80
Reactive
Unreactive
Pressure / bar
30
28
26
24
22
20
18
0
10
20
30
40
50
60
70
80
Time after top dead center / ms

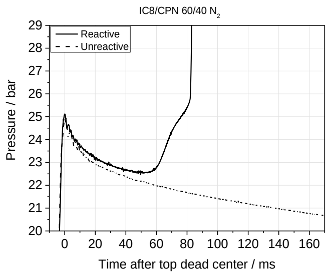
IC8/CPN 60/40 N2
Reactive
Unreactive
Pressure / bar
29
28
27
26
25
24
23
22
21
20
0
20
40
60
80
100
120
140
160
Time after top dead center / ms

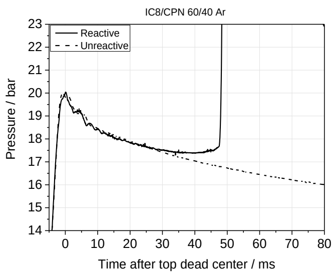
IC8/CPN 60/40 Ar
Reactive
Unreactive
Pressure / bar
23
22
21
20
19
18
17
16
15
14
0
10
20
30
40
50
60
70
80
Time after top dead center / ms

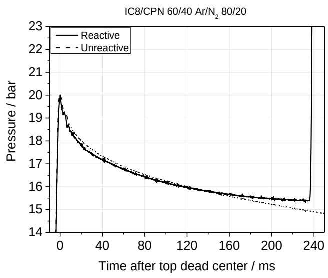
IC8/CPN 60/40 Ar/N2 80/20
Reactive
Unreactive
Pressure / bar
23
22
21
20
19
18
17
16
15
14
0
40
80
120
160
200
240
Time after top dead center / ms

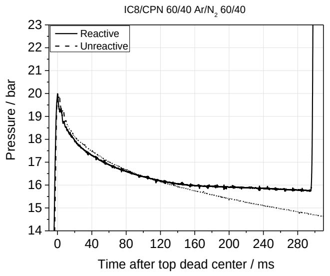
IC8/CPN 60/40 Ar/N2 60/40
Reactive
Unreactive
Pressure / bar
23
22
21
20
19
18
17
16
15
14
0
40
80
120
160
200
240
280
Time after top dead center / ms

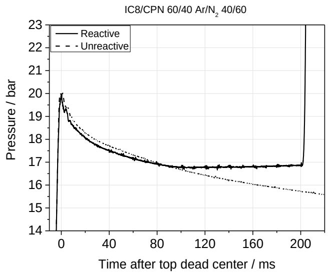
IC8/CPN 60/40 Ar/N2 40/60
Reactive
Unreactive
Pressure / bar
23
22
21
20
19
18
17
16
15
14
0
40
80
120
160
200
Time after top dead center / ms

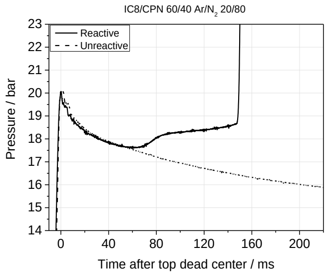
IC8/CPN 60/40 Ar/N2 20/80
Reactive
Unreactive
Pressure / bar
23
22
21
20
19
18
17
16
15
14
0
40
80
120
160
200
Time after top dead center / ms

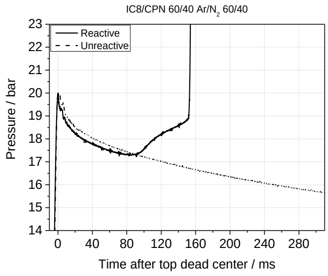
IC8/CPN 60/40 Ar/N2 60/40
Reactive
Unreactive
Pressure / bar
23
22
21
20
19
18
17
16
15
14
0
40
80
120
160
200
240
280
Time after top dead center / ms

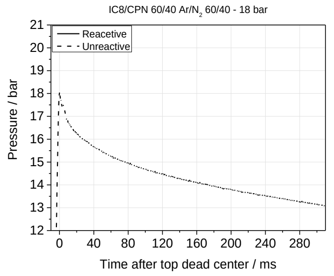
IC8/CPN 60/40 Ar/N2 60/40 - 18 bar
Reactive
Unreactive
Pressure / bar
12 13 14 15 16 17 18 19 20 21
Time after top dead center / ms
0 40 80 120 160 200 240 280

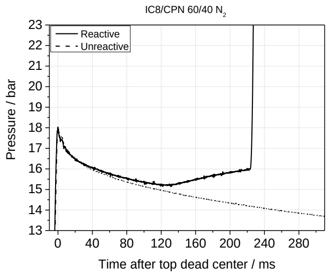
IC8/CPN 60/40 N2
Reactive
Unreactive
Pressure / bar
13 14 15 16 17 18 19 20 21 22 23
Time after top dead center / ms
0 40 80 120 160 200 240 280

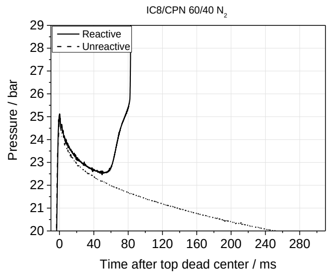
IC8/CPN 60/40 N2
Reactive
Unreactive
Pressure / bar
20 21 22 23 24 25 26 27 28 29
Time after top dead center / ms
0 40 80 120 160 200 240 280

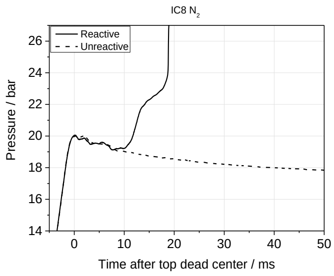
IC8 N2
Reactive
Unreactive
Pressure / bar
14 16 18 20 22 24 26
Time after top dead center / ms
0 10 20 30 40 50

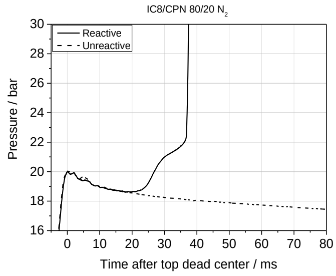
IC8/CPN 80/20 N2
Reactive
Unreactive
Pressure / bar
16 18 20 22 24 26 28 30
Time after top dead center / ms
0 10 20 30 40 50 60 70 80

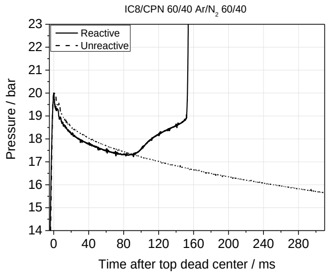
IC8/CPN 60/40 Ar/N2 60/40
Reactive
Unreactive
Pressure / bar
14 15 16 17 18 19 20 21 22 23
Time after top dead center / ms
0 40 80 120 160 200 240 280

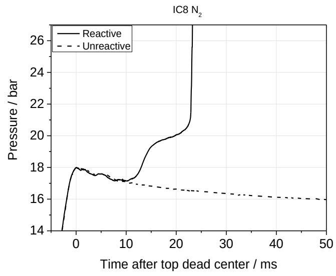
IC8 N2
Reactive
Unreactive
Pressure / bar
14 16 18 20 22 24 26
Time after top dead center / ms
0 10 20 30 40 50

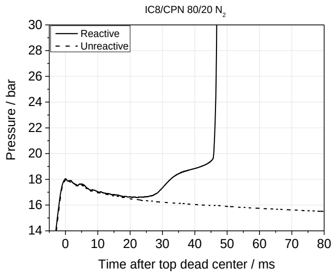
IC8/CPN 80/20 N2
Reactive
Unreactive
Pressure / bar
14 16 18 20 22 24 26 28 30
Time after top dead center / ms
0 10 20 30 40 50 60 70 80

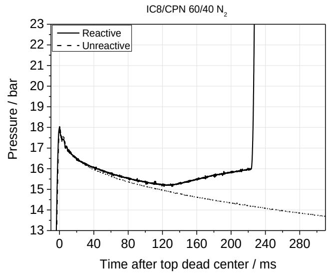
IC8/CPN 60/40 N2
Reactive
Unreactive
Pressure / bar
13 14 15 16 17 18 19 20 21 22 23
Time after top dead center / ms
0 40 80 120 160 200 240 280

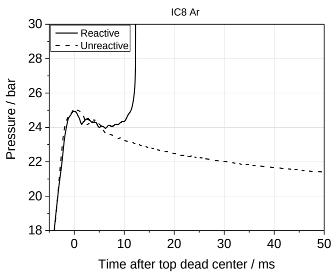
IC8 Ar
Reactive
Unreactive
Pressure / bar
18 20 22 24 26 28 30
Time after top dead center / ms
0 10 20 30 40 50

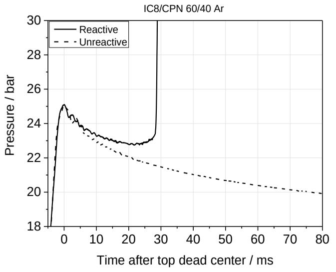
IC8/CPN 60/40 Ar
Reactive
Unreactive
Pressure / bar
Time after top dead center / ms
18 20 22 24 26 28 30
0 10 20 30 40 50 60 70 80

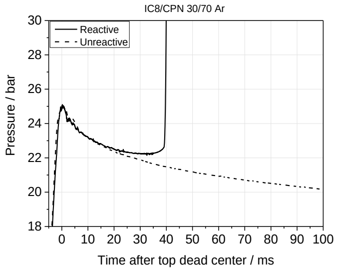
IC8/CPN 30/70 Ar
Reactive
Unreactive
Pressure / bar
Time after top dead center / ms
18 20 22 24 26 28 30
0 10 20 30 40 50 60 70 80 90 100

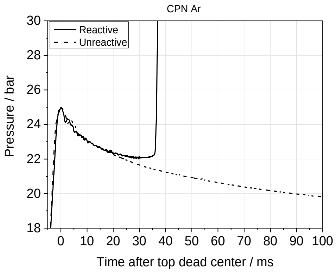
CPN Ar
Reactive
Unreactive
Pressure / bar
Time after top dead center / ms
18 20 22 24 26 28 30
0 10 20 30 40 50 60 70 80 90 100

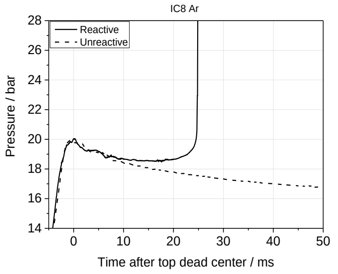
IC8 Ar
Reactive
Unreactive
Pressure / bar
Time after top dead center / ms
14 16 18 20 22 24 26 28
0 10 20 30 40 50

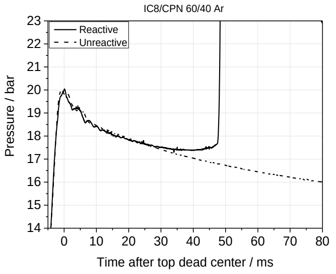
IC8/CPN 60/40 Ar
Reactive
Unreactive
Pressure / bar
Time after top dead center / ms
14 15 16 17 18 19 20 21 22 23
0 10 20 30 40 50 60 70 80

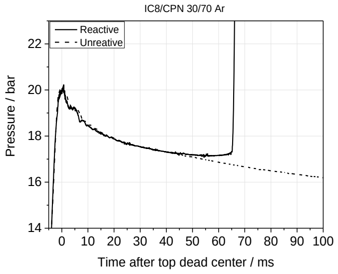
IC8/CPN 30/70 Ar
Reactive
Unreative
Pressure / bar
Time after top dead center / ms
14 16 18 20 22
0 10 20 30 40 50 60 70 80 90 100

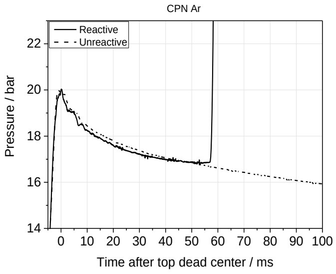
CPN Ar
Reactive
Unreactive
Pressure / bar
Time after top dead center / ms
14 16 18 20 22
0 10 20 30 40 50 60 70 80 90 100

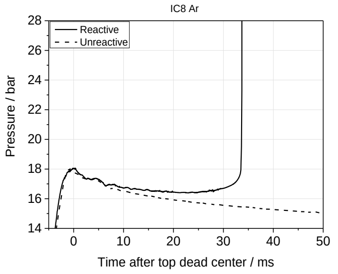
IC8 Ar
Reactive
Unreactive
Pressure / bar
Time after top dead center / ms
14 16 18 20 22 24 26 28
0 10 20 30 40 50

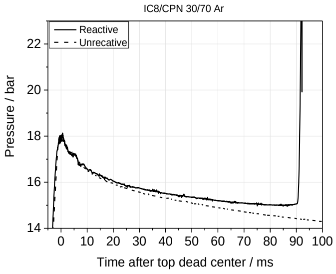
IC8/CPN 30/70 Ar
Reactive
Unrecative
Pressure / bar
Time after top dead center / ms
14 16 18 20 22
0 10 20 30 40 50 60 70 80 90 100

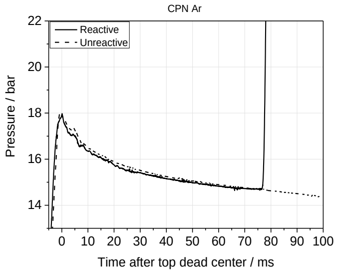
CPN Ar
Reactive
Unrecative
Pressure / bar
Time after top dead center / ms
14 16 18 20 22
0 10 20 30 40 50 60 70 80 90 100

List of publications

- Articles on scientific journals:

- Mergulhão, Carolina S, Hans-Heinrich Carstensen, Hwasup Song, Scott W Wagnon, William J Pitz, and Guillaume Vanhove, 'Probing the Antiknock Effect of Anisole through an Ignition, Speciation and Modeling Study of Its Blends with Isooctane', *Proceedings of the Combustion Institute*, (2020), https://doi.org/10.1016/j.proci.2020.08.013

- Tipler, S., C. S. Mergulhão, G. Vanhove, Q. Van Haute, F. Contino, and A. Coussement, 'Ignition Study of an Oxygenated and High-Alkene Light Petroleum Fraction Produced from Automotive Shredder Residues', *Energy and Fuels*, 33 (2019), 5664–72 https://doi.org/10.1021/acs.energyfuels.9b00649

- Fenard, Y., H. Song, H. Minwegen, P. Parab, C. Sampaio Mergulhao, G. Vanhove, and others, '2,5-Dimethyltetrahydrofuran Combustion: Ignition Delay Times at High and Low Temperatures, Speciation Measurements and Detailed Kinetic Modeling', *Combustion and Flame*, 203 (2019), 341–51 https://doi.org/10.1016/j.combustflame.2019.02.022

- Posters:

- "Experimental Study of the Autoignition of Isooctane/Anisole Mixtures at Low to Intermediate Temperatures". European Combustion Meeting (ECM), 2019. Lisbon / Journée doctorants IRePSE, 2019. Université de Lille.

- "Étude Expérimentale de la Cinétique de Combustion de Carburants Issus de la Biomasse Lignocellulosique à Hautes Pressions". Journée de la recherche, 2019. Université de Lille / Journée doctorants ADEME, 2018. Sophia Antipolis.

- Oral presentations:

- "Auto-inflammation de l'anisole au sein d'un carburant-modèle". Journée François Lacas, 2019. Centrale Supelec (EM2C).

- "Étude Expérimentale de la Cinétique de Combustion de Carburants Issus de la Biomasse Lignocellulosique à Hautes Pressions". Journée doctorants ADEME, 2019. Angers.

Curriculum Vitae

I was born in Rio de Janeiro, Brazil, on October 10, 1989. I obtained my bachelor's degree in chemical engineering in 2016, delivered by the Universidade Católica do Rio de Janeiro (PUC-Rio). During my studies I had the opportunity to work in different research laboratories, therefore revealing my interest in this area. The work in the LABSO-BIO (Organic Synthesis and Coordination Chemistry Lab - PUC-Rio Laboratory) was directed by the professor Nicolás A. Rey and had a duration of one year; it was focused on the synthesis of organic molecules. After that, I worked in the LABSPECTRO (Analysis Laboratory - PUC-Rio Laboratory) during one year, under the supervision of the professors Tatiana Dillenburg Saint'Pierre and Christiane Beatrice Duyck. This work had an emphasis on the analysis of oil samples using chromatographic and spectrometry techniques. It culminated in the publication of the work “Determinação elementar via ICP-MS em frações de óleo cru” (Elementary determination via ICP-MS in crude oil fractions) in the conference “36ª Reunião da Sociedade Brasileira de Química”, 2013, Águas de Lindóia, Brasil. In 2014, I started a research trainee program at PETROBRAS Laboratory (CENPES - Lubricant) in lubricant research and development to Formula 1 and special products; under the supervision of the engineers José André Cavalcante and Luiz Fernando Lastres. In 2015, I started a research trainee in combustion processes at Laboratory of combustion and turbulence (PUC-Rio Laboratory). Under the supervision of the professor Luis Fernando Figueira da Silva, the work “Experimental study of a lean premixed turbulent swirling flame stabilization” was presented in the conference “24th ABCM International Congress of Mechanical Engineering, 2017, Curitiba, Brasil”. Likewise, the final project requested as a prerequisite for obtaining a bachelor's degree, was supervised by the professor Luis Fernando Figueira da Silva and, entitled “Estudo Experimental da Formação de Fuligem em Chamas Laminares de Hidrocarbonetos e Ar” (Experimental Study of Soot Formation in Hydrocarbon/Air Laminar Flames). This project addressed the area of experimental study of soot formation in laminar flames of hydrocarbon and air. From October, 2017 I started a PhD project at Lille University, of which the results are presented in this dissertation.

English • French • Portuguese • Spanish

Acknowledgements

It is a pleasure to acknowledge with gratitude the contribution of several people and institutions towards the completion of this doctoral research. Namely, University of Lille directed by Jean-Christophe Camart, Laboratory PC2A and its directors Laurent Gasnot and Benjamin Hanoune; the Doctoral School SMRE with its coordinators Christoph Van Brussel and director Frédéric Parol; the ADEME and Region Haute de France the co-financers of this research work. Hereby, I would like to thank them.

I would like to thank the members of the committee for their participation and contribution to the public defense of the current thesis: Dr. Frédérique Battin-Leclerc University of Lorraine, Dr. Guillaume Dayma from University of Orléans, Dr. Laurent Gagnepain from ADEME, Dr. Pascale Desgroux from University of Lille, Dr. Mickaël Matrat from IFP *Energies nouvelles* and Dr. Luis Fernando Figueira da Silva from Catholic University of Rio de Janeiro. I feel very fortunate than my work has been approved by such a distinguished committee. I also want to thank Prof. Robert Wojcieszak from University of Lille and Prof. Olivier Herbinet from University of Lorraine, for being part on my *comité de suivi de thèse*.

I would like to express my sincere gratitude to my advisor, Dr. Guillaume Vanhove, for his instruction, encouragement, advice, and support throughout my formation. Thanks for trusting me and my capabilities. Thanks for forming my knowledge, the patience and for instilling in me the researcher way of thinking.

I also thank Dr. Hwasup Song for his patience and for teaching me many useful skills. I have benefited a lot from his broad perspective and expert knowledge. It was a such great pleasure work with you. I want to thank also Dr. Yann Fenard for share with me his knowledge and for helping during the critical moments of this work. I want to extend my gratitude to Dr. Scott W. Wagnon Scott for kindly providing the Co-Optima mechanism used in this work and to Steven Tipler who I had the great opportunity to work with in a contribution work.

Furthermore, I would also like to thank all those who have helped me in the laboratory with the practical life. A very special thanks goes to Sylvie Gosselin, Pascal Demaux, Olivier Hombert, Sadio Soumare and Valerie Vilain without whose expertise in their work at PC2A laboratory and patience this work would not have been possible. The PhD. Students: Eliane, Dora, Jinane, Lucia, Mona, Quan and Thomas, my most sincere thanks for all the time spent together.

I would like to thank all friends who made life easy and very enjoyable in France: Melissa, Débora, Alexandra, Alan, Deise and Tobias, my Brazilian-Venezuela-German crew. Thanks also to Raphael Tavares and all other friends in Brazil for their overseas encouragement. To my Brazilian family I would like to thank for all support the last three years, being far from you was the most difficult part of this work. To my German family my most sincere thanks for all encouragement and for having welcomed so well in your lives. Finally, I want to thank my husband for his endless support and care. Words cannot express my gratitude for everything you have done for me, Danke schön.